Influence of laser irradiated spot size on energetic electron injection and proton acceleration in foil targets

Coury, M.; Carroll, D. C.; Robinson, A. P. L.; Yuan, X. H.; Brenner, C. M.; Burza, Matthias; Gray, R. J.; Quinn, M. N.; Lancaster, K. L.; Li, Y. T.; Lin, X. X.; Tresca, O.; Wahlström, Claes-Göran; Neely, D.; McKenna, P.

Published in:
Applied Physics Letters

DOI:
10.1063/1.3685615

2012

Laser-Driven Particle Acceleration

Improving Performance through Smart Target Design

Matthias Burza

Doctoral Thesis
2012

Lund University

Laser-Driven Particle Acceleration
Improving Performance through Smart Target Design

Printed in Sweden by Media-Tryck, Lund, 2012

Division of Atomic Physics
Department of Physics
Faculty of Engineering, LTH
Lund University
P.O. Box 118
SE–221 00 Lund
Sweden

http://www.atomic.physics.lu.se

ISSN 0281-2762
Lund Reports on Atomic Physics, LRAP-455

ISBN: 978-91-7473-320-4

To those I love and
those who love me

Preface

In the beginning there was nothing. And the Lord said: "Let there be light!" and still there was nothing, but at least you could see it.

Terry Pratchet

People have always been fascinated by the power of light and means of controlling it. This fascination ranges from beautiful the rainbows after thunder storms on a summer's day, laser light shows at public events and binoculars that give us mere mortals eagle's eyes even when only endowed with limited eye sight, to large-scale telescopes that let us look back to the very beginning of the universe. Besides entertainment, the ability to control light has enabled us to address questions of the most basic nature such as "What is the nature of the things around us?" and "Where do we come from?".

Lasers have increased our quality of life through medial applications and optical data transmission, but they can also be used to investigate fundamental questions such as the structure of the matter around us. Even studies on vacuum may well be possible with high-power laser facilities, providing us with an increased understanding of the nature of space and time. With the future in mind, I am proud to present this thesis, which deals with the exposure of ionized matter to laser fields of extremely high intensities and share the joy of discovering an exciting and surprising field of physics where matter behaves quite differently from what we are used to.

While reading this thesis, I hope you will enjoy plunging into the subject of extreme laser fields, employing pulses that are so short that they can be compared to a second like a few milliseconds relative to the age of our solar system, and peak powers equivalent to tens of thousands, even millions, of nuclear power plants. Of course, only a very tiny area within high-power laser physics is addressed in this thesis, namely that of experimental laser-matter interactions focusing on particle acceleration. So, let the tale begin!

Abstract

Laser-driven particle acceleration makes use of sub-picosecond, pulsed, high-power laser systems, capable of producing intensities $\sim 10^{19}\,\mathrm{W/cm^2}$ at the laser focus to form plasmas, and use ultra-relativistic and nonlinear dynamics to produce quasistatic acceleration fields. This allows electrons to be accelerated to $\sim 100\,\mathrm{MeV}$ over sub-centimetre distances, while protons may be accelerated to the $\sim 10\,\mathrm{MeV}$ regime. In addition, novel sources of x-ray radiation become available with these schemes. The topics covered in this thesis focus mainly on target normal sheath acceleration of protons in the overdense plasma regime and laser wakefield acceleration of electrons in the underdense regime. An experimental approach leads to novel acceleration concepts and investigations on properties of new target designs.

In the overdense plasma regime, hollow *microspheres* were found to have the potential to enhance the conversion of laser energy into proton energy. The microscopic structure of the material used as target has impact on electron beam filamentation during electron transport through the target bulk. Long-range order was found to result in smoother beams of TNSA-produced protons as compared to amorphous structures. In addition it was demonstrated that short pulse (fs) laser-solid interactions produce magnetic fields, the strength of which can reach 10 kT, mimicking astrophysical conditions.

In the underdense regime, it was found that when tailored appropriately, density ramps can provide means of dividing the laser wakefield acceleration process into four steps: nonlinear laser evolution, trapping, bunch transfer into the second bucket, and acceleration, resulting in beams with reduced relative energy spread and divergence compared to self-injection by a nonlinear plasma wave. It was further shown that capillaries can be used to improve efficiency by guiding and refocusing the laser light onto the central axis. Short bursts of soft x-rays were produced inside capillaries. Finally, the use of an asymmetric laser field at the focus facilitated off-axis electron injection into the accelerating phase of a plasma wake oscillation and enhanced x-ray emission.

Populärvetenskaplig Sammanfattning

Många forskningsprojekt inom materialvetenskap, medicin eller grundläggande fysik kräver smala strålar av laddade partiklar som fungerar som provtagare för att undersöka materiens egenskaper. Dessa partiklar kan vara protoner, elektroner lättare joner. Relativt ofta, behöver de accelereras nästan upp till ljusets hastighet för att kunna tränga in tillräckligt djupt i provet som ska studeras. Ett rätt intressant exempel på en tillämpning av protonstrålar är att destruera tumörer vid ett visst vävnadsdjup utan att skada omgivande vävnad, jämfört med användandet av röntgenstrålar, som är standarden idag. Alternativt kan strålar av snabba elektroner böjas med hjälp av magneter, vilket leder till emission av ljus i ett väldigt brett färgspektrum som sträcker sig från röntgenstrålning till infrarött med överlägsna strålegenskaper jämfört med alternativa ljuskällor.

Laserdriven partikelacceleration avser att använda sig av extremt starka transversella oscillerande elektriska fält, vilka blir tillgängliga när man fokuserar ljuset hos en modern pulsad högeffektslaser. För partikelacceleration måste dessa dock likriktas på något vis, så att partiklarna utsätts för ett kontinuerligt longitudinellt accelererande fält. Den här omvandlingen sker inuti ett plasma. Plasmat kan bestå av vilket material som helst, då det upphettas till en temperatur så pass hög att elektronerna inte längre är bundna till atomkärnorna och materialet blir joniserat. Detta sker i fokuspunkten när laserljuset träffar målet som t.ex. kan vara en gas eller en tunn folie. Samtidigt kan en sådan växelverkan producera korta pulser av röntgenstrålning eller magnetiska fält, som kan vara av storleksordningen en miljon gånger jordens magnetiska fält. Utöver partikelacceleration kan man dessutom skapa miljöer som liknar astrofysikaliska förhållanden som studieobjekt i ett laboratorium.

Beroende på densiteten av fria elektroner, plöjer en fokuserad ljuspuls genom plasmat, likt en kanonkula av ljus, som knuffar och förflyttar elektroner som kommer i dess väg. Detta fram-

bringar en våg i plasmat efter ljuspulsen, likt kölvattnet bakom en motorbåt. Här finns nu bland annat longitudinella elektriska fält som kan ge upphov till en extremt snabb acceleration, mycket snabbare än vad som är tekniskt möjligt med konventionella högfrekvensacceleratorer som t.ex. används för the Large Hadron Collider vid CERN i Schweiz eller Max IV i Lund i Sverige. Principiellt skulle detta kunna tillåta att acceleratorns längd kan minskas med en faktor ett tusen. Detta innebär att en flera hundra meter lång linjäraccelerator skulle kunna krympas till några centimeter. Oftast kan dessa extrema accelerationsfält inuti plasmat dessvärre endast upprätthållas över några millimeter. Detta innebär att den tillgängliga maximala energin hos elektronerna är begränsad och lösningar måste utvecklas för att utöka denna sträckan.

I ett tätare plasma förflyttar den extremt intensiva laserpulsen fortfarande elektroner, men reflekteras efter att den har överfört delar av sin energi till en del av elektronerna. Kortlivade statiska fält skapas vid kanten av målet, som i sin tur kan accelerera partiklar såsom protoner eller joner på målets yta.

Forskningen, som presenteras i den här avhandlingen, syfter påatt utforska möjligheter inom laser-materieväxelverkan för att förbättra prestanda hos laserdriven partikelacceleration. I synnerhet genom att öka effektiviteten i energiöverföringen från laserenergi till önskad partikelenergi eller genom att förlänga växelverkningslängden med lasern genom utveckling av en *smart target design*. Detta har lett fram till tre nya accelerationsteknier: En metod som använder sig av en ihålig glasmikrosfär, trådinjektionstekniken och användningen av en glaskapillär, vilka presenteras och diskuteras i den här avhandlingen.

Popular Scientific Summary

Many research projects in materials science, medicine and fundamental physics employ narrow beams of charged particles as a probe to investigate the properties of matter. These particles can be electrons, protons or lighter ion species. They often need to be accelerated to velocities close to the speed of light to be able to penetrate deep into the objects to be studied. An interesting example of an application of proton beams is the destruction of tumours at a given tissue depth, without damaging the surrounding tissue, rather than using x-rays, which is currently the standard method of treatment. Beams of fast-moving electrons can be bent by magnets, leading to the emission of light in a very wide colour range, from x-rays to the infrared, not equally well covered by other light sources.

Laser-driven particle acceleration makes use of the extremely strong oscillating transverse electric light fields, attainable when focusing the light from a modern pulsed high-power laser. However, for particle acceleration, this field has to be rectified in some way, so that the particles experience a quasistatic longitudinal accelerating field. This conversion is accomplished inside a plasma, which may be any material heated to a temperature sufficiently high for the electrons to be no longer bound to the core of the atoms, causing the material to become ionized. This happens at focus, when the laser light interacts with the target, which may be a gas or a thin metallic foil. Such an interaction can simultaneously provide short bursts of x-rays, or magnetic fields a million times stronger than the Earth's magnetic field. Thus, besides particle acceleration, environments reminiscent of astrophysical conditions may be created and studied in the laboratory.

Depending of the density of free electrons, the focused light pulse ploughs through the plasma like a bullet of light, pushing and displacing electrons on its way. This stimulates a plasma wake oscillation trailing the laser pulse, similar to the wake behind a speed boat, racing down a river. Here, amongst

others, longitudinal electric fields are created, which allow for an extremely rapid acceleration, much faster than that technically possible with conventional radio frequency accelerators such as those used at the Large Hadron Collider at CERN in Switzerland or MaxIV in Lund, Sweden. In principle, this should enable acceleration lengths to be scaled down by at least three orders of magnitude, which means that a several hundred metre long linear accelerator could be scaled down to a centimetre scale plasma accelerator. However, the extreme acceleration fields inside the plasma can often only be maintained over a few millimetres, thus the available maximum energy of the accelerated electrons is limited and methods must be developed to extend this range.
In the case of a more dense plasma, the extremely intense laser pulse still displaces electrons, but the laser pulse is reflected after transferring part of its energy to some electrons. Short-lived static fields will be created at the edge of the target, which in turn can accelerate particles such as protons or ions adhered to its surface.

The thesis presents research with the goal to investigate means on the laser-matter interaction side to increase performance of laser driven particle acceleration, in particular increasing the conversion efficiency of laser energy to desired particle energy by a *smart target design* leading to the proposal and investigation of three novel acceleration schemes, the hollow glass microsphere postacceleration, the wire injection scheme and the use of a hollow glass capillary, presented and discussed in this thesis.

The thesis presents research on laser-matter interactions aimed at increasing the performance of laser-driven particle acceleration, in particular increasing the conversion efficiency of laser energy to particle energy by a *smart target design*. Three novel acceleration schemes were developed and investigated: the hollow glass *microsphere*, the wire injection scheme and the hollow glass capillary.

List of Publications

This thesis is based on the following papers, which will be referred to in the text by their Roman numerals.

I **Hollow microspheres as targets for staged laser-driven proton acceleration**
M. Burza, A. Gonoskov, G. Genoud, A. Persson, K. Svensson, M. Quinn, P. McKenna, M. Marklund and C.-G. Wahlström.
New Journal of Physics **13**, 013030 (2011).

II **Effect of lattice structure on energetic electron transport in solids irradiated by ultraintense laser pulses**
P. McKenna, A. P. L. Robinson, D. Neely, M. P. Desjarlais, D. C. Carroll, M. N. Quinn, X. H. Yuan, C. M. Brenner, M. Burza, M. Coury, P. Gallegos, R. J. Gray, K. L. Lancaster, Y. T. Li, X. X. Lin, O. Tresca and C.-G. Wahlström.
Physical Review Letters **106**, 185004 (2011).

III **Influence of laser irradiated spot size on energetic electron injection and proton acceleration in foil targets**
M. Coury, D. C. Carroll, A.P.L. Robinson, X. H. Yuan, C. M. Brenner, M. Burza, R. J. Gray, M. N. Quinn, K. L. Lancaster, Y. T. Li, X. X. Lin, O. Tresca, C.-G. Wahlström, D. Neely and P. McKenna.
Applied Physics Letters **100**, 074105 (2012).

IV **Megagauss magnetic field generation at relativistic intensities using 35 femtosecond laser pulses**
A. Gopal, S. Minardi, M. Burza, G. Genoud, I. Tzianaki, A. Karmakar, P. Gibbon, M. Tatarakis, A. Persson and C.-G. Wahlström.
Manuscript.

V **Staged laser wakefield acceleration using double density ramps**
M. Burza, K. Svensson, A. Gonoskov, F. Wojda, A. Persson, O. Lundh, M. Marklund and C.-G. Wahlström.
Manuscript.

VI **Controlling the spectrum of x-rays generated in a laser-plasma accelerator by tailoring the laser wavefront**
S. P. D. Mangles, G. Genoud, S. Kneip, M. Burza, K. Cassou, B. Cros, N. P. Dover, C. Kamperidis, Z. Najmudin, A. Persson, J. Schreiber, F. Wojda and C.-G. Wahlström.
Applied Physics Letters **95**, 181106 (2009).

VII **Self-injection threshold in self-guided laser wakefield accelerators**
S. P. D. Mangles, G. Genoud, M. S. Bloom, M. Burza, Z. Najmudin, A. Persson, K. Svensson, A. G. R. Thomas and C.-G. Wahlström.
Physical Review Special Topics - Accelerators and Beams **15**, 011302 (2012).

VIII **Active control of the pointing of a multi-terawatt laser**
G. Genoud, F. Wojda, M. Burza, A. Persson and C.-G. Wahlström.
Review of Scientific Instruments **82**, 033102 (2011).

IX **Laser-driven plasma waves in capillary tubes**
F. Wojda, K. Cassou, G. Genoud, M. Burza, Y. Glinec, O. Lundh, A. Persson, G. Vieux, E. Brunetti, R. P. Shanks, D. Jaroszynski, N. E. Andreev, C.-G. Wahlström and B. Cros.
Physical Review E **80**, 066403 (2009).

X **Analysis of laser wakefield dynamics in capillary tubes**
N. E. Andreev, K. Cassou, F. Wojda, G. Genoud, M. Burza, O. Lundh, A. Persson, B. Cros, V. E. Fortov and C.-G. Wahlström.
New Journal of Physics **12**, 045024 (2010).

XI **Laser-plasma electron acceleration in dielectric capillary tubes**
G. Genoud, K. Cassou, F. Wojda, H. E. Ferrari, C. Kamperidis, M. Burza, A. Persson, J. Uhlig, S. Kneip, S. P. D. Mangles, A. Lifschitz, B. Cros and C.-G. Wahlström.
Applied Physics B **105**, 309 (2011).

XII **Enhancement of x-rays generated by a guided laser wakefield accelerator inside capillary tubes**
J. Ju, K. Svensson, A. Döpp, H. E. Ferrari, K. Cassou, O. Neveu, G. Genoud, F. Wojda, M. Burza, A. Persson, O. Lundh, C.-G. Wahlström and B. Cros.
Applied Physics Letters **in press**, (2012).

Abbreviations

ASE	Amplified Spontaneous Emission
BSI	Barrier Suppression Ionisation
CCD	Charge-coupled Device
CPA	Chirped Pulse Amplification
cw	continuous wave
DM	Deformable Mirror
DPSS	Diode-Pumped Solid State (laser)
FROG	Frequency-Resolved Optical Gating
FWHM	Full Width at Half Maximum
HeNe	Helium Neon (Gas Laser)
IR	Infra Red
LLC	Lund Laser Centre
LWFA	Laser Wakefield Acceleration
MPI	Multi-Photon Ionization
OAP	Off-Axis Parabola
OPCPA	Optical Parametric Chirped Pulse Amplification
OTR	Optical Transition Radiation
PIC	Particle In Cell
PM	Plasma Mirror
PSD	Position-Sensitive Detector
RCF	Radiochromatic Film
RF	Radio Frequency
RMS	Root Mean Square
SPM	Self-Phase Modulation
SHG	Second-Harmonic Generation
TNSA	Target-Normal Sheath Acceleration
XPW	Cross-Polarized Wave

Nomenclature

A	area [m^2]
$\vec{A}$	vector potential [Vs/m]
$\vec{B}$	magnetic field [T]
$\mathbb{C}$	complex numbers
$\vec{D}$	electric displacement [C/m^2]
E	pulse energy or particle energy [J] (clear by context)
$\vec{E}$	electric field [V/m]
$\vec{H}$	magnetizing field [C/m/s]
I	intensity [W/m^2]
L_d	dephasing length [m]
M_p	proton mass $1.67262171(29) \times 10^{-27}$ kg
$\vec{M}$	magnetization [TN/A^2]
N	particle number
P	power $\frac{dE}{dt}$ [W]
$\vec{P}$	polarization [C/m^2]
$\mathbb{R}$	real numbers
T	temperature [K]
Z_R	Rayleigh length [m]

$\vec{a}$	normalized vector potential
c	speed of light: 299792458 m/s or speed of sound (clear by context)
$\tilde{c}$	contrast $\frac{I_{max}-I_{min}}{I_{max}+I_{min}}$
e	electron charge: $1.60217653(14) \times 10^{-19}$ C
f	focal length or function (clear by context) [m]

i	imaginary unit
$\vec{j}$	current density [A/m^2]
k	Boltzmann constant: $1.3806505(24) \times 10^{-23}$ J/K
$\vec{k}$	wave vector [m^{-1}]
m	electron mass
m_e	electron rest mass: $9.1093826(16) \times 10^{-31}$ kg
n	electron number density [m^{-3}] or particle number density [m^{-3}] (clear by context)
n_c	critical electron density [m^{-3}]
p	pressure [Pa]
q	charge [C]
r	radial coordinate, distance from z axis [m]
r_0	focal spot radius at $\vec{E}_0 e^{-1}$ or $I_0 e^{-2}$[m]
$\vec{r}$	spatial vector
s , s_i	length or path [m]
t	time in laboratory frame [s]
$\vec{v}_g$	group velocity [m/s]
$\vec{v}_p$	phase velocity [m/s]
z	spatial coordinate, commonly along main propagation axis [m]

Φ	electric potential [V]
Ψ	phase $\vec{k}\vec{\xi}$

α	polarisability [A^{2}s^4/kg]
$\vec{\beta}$	reduced velocity $\frac{\vec{v}}{c}$
ϵ	relative permittivity
ϵ_0	vacuum permittivity: $8.854187817 \times 10^{-12}$ F/m
φ	phase
γ	relativistic factor $\sqrt{1 + \frac{\lvert\vec{p}\rvert^2 c^2}{m_0^2 c^4}}$
η	refractive index
λ	wavelength [m] or perturbation factor (clear by context)

λ_p	plasma wavelength [m]
μ	relative permeability
μ_0	magnetic constant: $4\pi \times 10^7$ N/A^2
ϱ	charge density [C/m^3] or mass density [kg/m^3] (clear by context)
τ_l	pulse length (FWHM) [s]
ω	frequency [Hz]
ω_p	plasma frequency [s^{-1}]
ξ	spatial coordinate ($z - v_p t$)

Contents

Papers

Chapter 1

Introduction

This thesis highlights the fast-growing field of *laser-driven particle acceleration*. The goal in many laser-driven acceleration experiments is to rectify the alternating laser field in some way in order to provide a quasistatic field in which particles such as electrons, protons or heavier ions can gain energy. However, most schemes require pulses of extremely high intensities $\gtrsim 10^{19}\,\mathrm{W/cm^2}$ delivered in relatively short times, i.e. in the sub-picosecond range. As a result, increasingly larger laser systems are being built, incorporating novel laser amplification schemes, optics and materials, to push the frontier forward. Available intensities have increased over recent decades as illustrated in Figure 1.1. However, higher laser intensities are associated with higher cost and slower repetition rates.

The title of this thesis "*Laser-Driven Particle Acceleration - Improving Performance through Smart Target Design*" underlines the author's ambition NOT to attempt to increase laser energies to improve the yield of an interaction, but to investigate means of modifying well established acceleration schemes and targets to improve the interaction in such a way that the laser energy is utilized more efficiently, leading towards a *smart target design*. Hollow *microspheres*, hollow glass capillaries or wire-triggered density gradients enabling density gradient injection or ionization injection are examples of the novel targets and schemes investigated and described in this thesis.

It should be mentioned that the intensities applied during the experimental work are commonly described as relativistic. This means that the electrons, when exposed to these fields, behave as relativistic particles. Commonly, all laser interactions in the ultra-intense regime are laser-plasma interactions. A millionth of the peak intensity, irradiated onto the target a few picoseconds before the arrival of the main pulse, is sufficient to form a plasma with

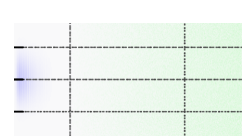

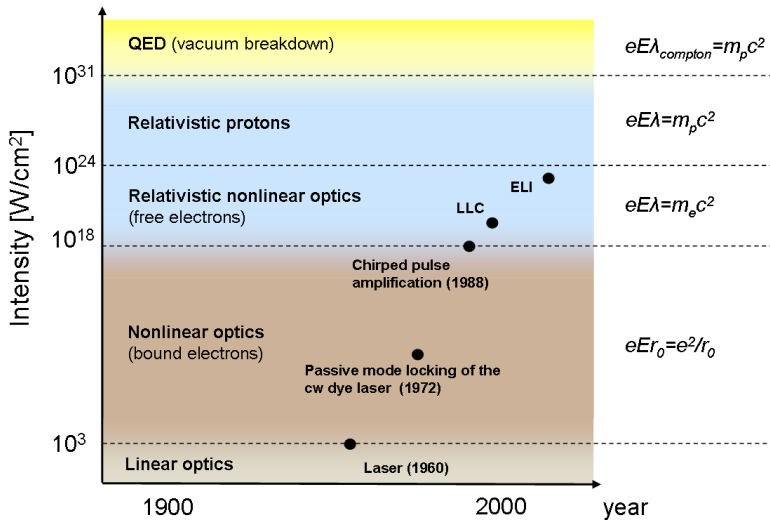

Figure 1.1. *Development of laser intensities and corresponding field strengths over the last decades since the invention of the laser. The colour of the shading indicates the physical regime governing the interaction. (LLC: High Power Laser Facility at the Lund Laser Centre; ELI: The planned Ultra High Field Facility at the Extreme Ligh Infrastructure)*

which the main pulse interacts.

1.1 An Outline of this Thesis

The author investigated and contributed to many experiments both in the underdense and overdense plasma regime of laser-matter interactions at ultra-high intensities. However, most effort was devoted to two experiments: Hollow *microspheres* were investigated (see Figure 1.2) as a novel solid target for laser-driven proton acceleration with the aim of improving laser-to-ion energy conversion efficiency and beam collimation. The density gradient injection mechanism in a laser wakefield accelerator (LWFA) gas jet experiment with double density ramps was also investigated (see Figure 1.3). Here, the laser wakefield acceleration process is divided into 4 steps: laser evolution, injection into the accelerating phase of a plasma wave, bunch transfer to a later bucket, and acceleration, providing improved control and electron beam emittance. The work described here is divided in two main types: laser-solid interactions and laser-gas interactions.

(i) **Investigations of laser-solid interactions:** Investigations were carried out on the effects of laser intensity and

spot size on proton yield in combination with the properties of the bulk material and their influence on electron transport through the target, with the goal of establishing a homogenous charge separation field at the rear surface. These topics are covered in Papers **II** and **III**. During laser interaction with solids, magnetic fields, at strengths similar to those prevailing on white dwarfs, were produced and analysed. This experiment is described in Paper **IV**. These kinds of studies can be seen as investigations to extend our knowledge of the principal interaction mechanisms, necessary in order to design targets with improved performance.
In this interaction regime, the author's major contribution was the first investigation on a novel target geometry using hollow *microspheres*. The results of this study, presented in Paper **I** together with further information provided in Chapter 6, should be regarded as one of the author's major contributions to the field of proton acceleration.

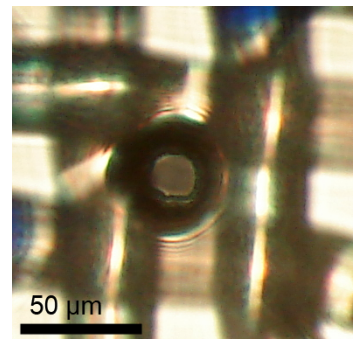

Figure 1.2. *A 50 µm diameter microsphere target in the target fabrication stage after laser micromachining of an opening on one side. The sphere is held by a nylon mesh, which can be seen in the background*

(ii) **Investigations on laser-gaseous interactions:** The topics studied in this field comprise electron acceleration experiments in a laser wakefield accelerator (LWFA) and the production of short (fs-time scale), bright bursts of soft x-rays. The effects of hollow core glass capillaries on laser guiding and driving the plasma wave are reported in Papers **IX**-**XII** together with the possibility of working at reduced gas pressures, resulting in reduced plasma densities, which in turn should allow electron acceleration over larger distances, possibly leading to higher energies of the accelerated electrons.
The main focus of the author's contribution was on a novel acceleration scheme, a staged laser wakefield accelerator that uses double density ramps. Thorough studies by the author on this novel target led to a new understanding of the physical mechanism by which the accelerated electron bunch is transferred to a later plasma bucket, thus isolated from the driving laser pulse. This resulted in electron beams of superb quality and should be regarded as the author's major contribution to the field of electron acceleration. The experiment is presented in Paper **V** with supplemental material in Chapters 4 and 5.

Chapter 2 provides the reader with some fundamentals on electrodynamics, relevant for plasma physics and the experiments discussed in this thesis. The experimental approaches described in the papers are explained and motivated.

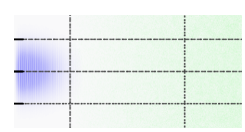

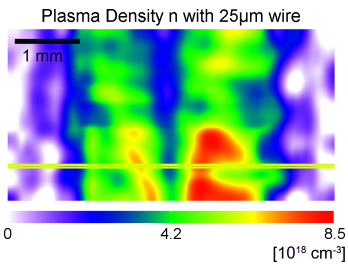

Figure 1.3. *The plasma density in a supersonic flow of H_2 from a 3 mm diameter nozzle, modulated by a 25 µm diameter wire that disturbs the gas flow and produces density ramps. Image resolution is ≈ 100 µm*

Chapter 3 presents the two high-power, short-pulse laser installations, with which the author has been working during his time as a PhD student. Each is representative of a whole class of laser systems commonly used to reach the high field strengths required for ultra-relativistic nonlinear laser-plasma experiments. Furthermore, the issue of sufficient contrast on the target is discussed as this was a key laser parameter in the experiments with hollow *microspheres*.

Chapter 4 describes various diagnostic tools, used during the experimental work to shed some light on the interaction as well as to analyse the results. The focus is on optical diagnostics. In particular, interferometry will be discussed as this represented a key diagnostic method for tailoring the the density modulation, required for the previously mentioned staged LWFA with double ramps.

Chapter 5 shifts the focus on the actual laser-plasma experiments, describing the case of a laser impinging on a gaseous target with density modulations, ramps and shock waves. Detailed background information on the experiment presented in Paper **V** is be given to provide the reader with a deeper understanding of the experimental approach.

Chapter 6 deals with the interaction of a laser with a solid surface producing beams of protons in the ~ 5 MeV range. After general considerations of the principal acceleration process, including its potential and limitations, attention is turned towards the choice of the target material and geometry, both of which influence the quality of the resulting proton beam. In particular, the hollow *microsphere* experiment is discussed. Modified target geometries for possible future experiments are also discussed in this chapter.

Chapter 2

Electrodynamics of Plasma Physics

2.1 Maxwell's Equations

Electric and magnetic fields correlated to charges and currents and their evolution in space-time are described by the Maxwell equations [1]:

Gauss's law: $$\nabla \cdot \vec{E} = \rho/\epsilon_0 \quad (2.1)$$

Faraday's law: $$\nabla \times \vec{E} + \frac{\partial}{\partial t}\vec{B} = 0 \quad (2.2)$$

Maxwell-Ampère's law: $$\nabla \times \vec{B} - \frac{1}{c^2}\frac{\partial}{\partial t}\vec{E} = \mu_0 \vec{j} \quad (2.3)$$

Gauss's law of magnetism: $$\nabla \cdot \vec{B} = 0 \quad (2.4)$$

where $\vec{E}$ and $\vec{B}$ are the electric and magnetic fields, and j and ρ the current and charge density as a function of space $\vec{r}$ and time t, respectively. ϵ_0 and μ_0 are the vacuum permittivity and magnetic constant. To include the reaction of matter, such as charge displacements and induced currents due to local fields in the medium, the polarization and magnetization (density) vectors $\vec{P}$ and $\vec{M}$ are commonly introduced, which may be complicated, nonisotropic, nonlinear functions of the local fields and their frequency ω.

$$\vec{P}(\vec{r},\omega) = f(\vec{E}(\vec{r},\omega)) \qquad \vec{M}(\vec{r},\omega) = f(\vec{B}(\vec{r},\omega)) \quad (2.5)$$

Quite often, these complex relations can be linearized as good approximations leading to the model of linear response in isotropic media:

$$\vec{P}(\vec{r},\omega) = \epsilon_0 \chi_e(\vec{r},\omega)\vec{E}(\vec{r},\omega) \quad \vec{M}(\vec{r},\omega) = \chi_m(\vec{r},\omega)\vec{H}(\vec{r},\omega) \quad (2.6)$$

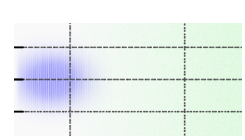

with the fields [2]

$$\vec{D} \equiv \epsilon\epsilon_0\vec{E} = \epsilon_0\vec{E} + \vec{P} \qquad \vec{H} \equiv \vec{B}/(\mu\mu_0) \tag{2.7}$$

which are matter independent. Here, χ_e and χ_m denote the electric and magnetic susceptibility, respectively.
At this stage, averaging over local inhomogeneities is assumed, thus these equations cannot be used to calculate electron trajectories on a microscopic scale. In this context, "microscopic" means atomic scale ($\ll$ Debye length [3]). The above expressions are, however, still important for the concept of a refractive index for electromagnetic waves. In matter, Maxwell's equations can be written as [4]:

$$\nabla \cdot \vec{D} = \rho_{ext} \qquad \nabla \times \vec{E} + \frac{\partial}{\partial t}\vec{B} = 0 \tag{2.8}$$

$$\nabla \times \vec{H} - \frac{\partial}{\partial t}\vec{D} = \vec{j}_{ext} \qquad \nabla \cdot \vec{B} = 0 \tag{2.9}$$

2.2 The Refractive Index

Applying the $\nabla\times$ operator to Faraday's law and assuming charge neutrality, $\rho_{ext} = 0$, gives the equation for a damped wave:

$$-\Delta\vec{E} + \mu\mu_0\epsilon\epsilon_0\frac{\partial^2}{\partial t^2}\vec{E} = -\frac{\partial}{\partial t}(\mu\mu_0\vec{j}_{ext}) \tag{2.10}$$

$$-\Delta\vec{E} + \mu\left(\frac{1}{c^2}\frac{\partial^2}{\partial t^2}\vec{E} + \frac{1}{\epsilon_0 c^2}\frac{\partial^2}{\partial t^2}\vec{P}\right) = -\frac{\partial}{\partial t}(\mu\mu_0\vec{j}_{ext}) \tag{2.11}$$

$$= \underbrace{-\mu\mu_0\sigma\frac{\partial}{\partial t}\vec{E}_{ext}}_{\text{damping term}} \tag{2.12}$$

where Ohm's law $\vec{j} = \sigma\vec{E}$ was applied with the conductivity σ.
Assuming no externally induced currents, $\vec{j}_{ext} = 0$, one can deduce the dispersion relation in Fourier space:

$$k^2 = \mu\mu_0\epsilon\epsilon_0\omega^2 \tag{2.13}$$

$$\Rightarrow\ v_p \equiv \frac{\omega}{k} = \sqrt{\frac{1}{\mu\epsilon}\frac{1}{\mu_0\epsilon_0}} = \frac{1}{\sqrt{\mu\epsilon}}\frac{\omega}{k_0} = \frac{c}{\eta} \tag{2.14}$$

with the (complex) refractive index $\eta = \sqrt{\epsilon\mu}$. For weakly magnetic materials, $\mu \approx 1$, the undamped wave equation describes the vacuum wave $\vec{E}$ propagating with phase velocity c with a superimposed induced wave, due to $\vec{P}$.

In a linear model, the polarization is proportional to the applied field

$$\vec{P} = n\alpha\vec{E} \tag{2.15}$$

where n is the particle number density, and α the polarizability. Inserting this into equation 2.12 and solving in Fourier space (see Appendix B) results in:

$$k^2\vec{E} + \mu\left(\frac{1}{c^2}(-\omega^2)\vec{E} + \frac{1}{\epsilon_0 c^2}(-n\alpha\omega^2)\vec{E}\right) = 0 \tag{2.16}$$

$$k^2 - \mu\left(\frac{\omega^2}{c^2} + \frac{n\alpha\omega^2}{\epsilon_0 c^2}\right) = 0 \tag{2.17}$$

$$\Rightarrow\ k^2 = \frac{\omega^2}{c^2}\mu\left[1 + \frac{n\alpha}{\epsilon_0}\right] \tag{2.18}$$

$$= k_0^2\eta^2 \tag{2.19}$$

where:

$$\eta^2 = \mu\left[1 + \frac{n\alpha}{\epsilon_0}\right] \tag{2.20}$$

From the Lorentz model:

$$\vec{F} = e\vec{E} = m\,\ddot{\vec{r}} + m\Gamma\,\dot{\vec{r}} + m\omega_0^2\vec{r} \tag{2.21}$$

we obtain an equation for a single electron dipole moment oscillating in the driving field $\vec{E}$ with the damping Γ:

$$\vec{p} = -e\vec{r} \tag{2.22}$$

$$= \frac{e^2\vec{E}}{m(\omega_0^2 - \omega^2 + i\Gamma\omega)} = \alpha\vec{E} \tag{2.23}$$

Thus, the refractive index can be written as:

$$\eta^2 = \mu\left[1 + \frac{ne^2}{\epsilon_0 m(\omega_0^2 - \omega^2 + i\Gamma\omega)}\right] \tag{2.24}$$

In a plasma, electrons are not bound, thus ω_0 vanishes and, with the definition of the plasma frequency:

$$\omega_p \equiv \sqrt{\frac{ne^2}{\epsilon_0 m}} = \sqrt{\frac{ne^2}{\epsilon_0\gamma m_e}} \tag{2.25}$$

this becomes:

$$\eta^2 = \mu\left[1 - \frac{\omega_p^2}{\omega^2 - i\Gamma\omega}\right] \tag{2.26}$$

For sufficiently large frequencies $\omega \gg 1$ usually implying that $\Gamma\omega \ll \omega^2$ and $\mu \approx 1$, we obtain:

$$\eta = \sqrt{1 - \left(\frac{\omega_p}{\omega}\right)^2} \tag{2.27}$$

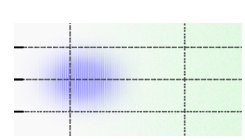

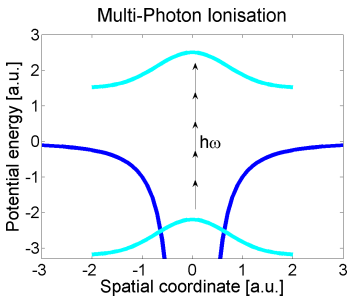

Figure 2.1. *Multi-photon ionization allows the energy of an electron in a bound state to leave the potential. In this model it is assumed that the laser field does not disturb the potential.*

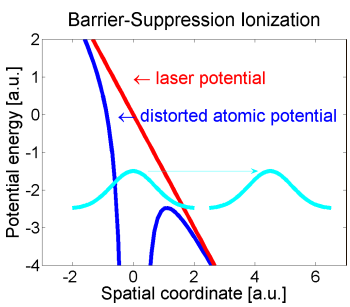

Figure 2.2. *Distortion of the intra atomic field allows the electron to escape. Here the laser field becomes of comparable strength as the intra atomic field.*

Generally, $\eta \in \mathbb{C}$ and $\vec{k} = \vec{k}_0\eta$. Depending on the ratio ω_p/ω, a wave might not be able to propagate inside the plasma.

$\omega < \omega_p \quad \Leftrightarrow \quad \eta \in \mathbb{C}\backslash\mathbb{R}$ Overdense plasma (evanescent wave)
$\omega > \omega_p \quad \Leftrightarrow \quad \eta \in \mathbb{C}$ Underdense (transparent) plasma

Equation (2.27) can be rewritten giving

$$\eta = \sqrt{1 - \frac{n}{n_c}} \tag{2.28}$$

where the critical density, n_c, is given by

$$n_c = \omega^2 \frac{m\epsilon_0}{e^2} = \frac{4\pi^2 c^2 m\epsilon_0}{\lambda^2 e^2} \tag{2.29}$$

above which light propagation is inhibited. For non-relativistic electrons and the visible wavenlength range, critical densities are $\sim 10^{21}\,\mathrm{cm}^{-3}$.

Equation (2.26) shows the dependence of the refractive index on the relative magnetic permeability, μ. Furthermore, the Lorentz model, with linear one dimensional displacement, is not sufficient to incorporate magnetic forces, which are of the same order as those produced by electric fields.

Given the limitations of Equation (2.26) this model still describes some interesting phenomena observable when focusing a high-power laser pulse into a plasma. The focused pulse will normally diffract after reaching the smallest obtainable spot size defined by the numerical aperture of the focusing set-up. This limits the effective range over which laser-plasma interaction can take place at the highest intensities. Equation (2.27) states that the radial refractive index profile depends on the density of free electrons. The laser ionizes the gas according to its radial intensity profile. Various mechanisms, such as multi-photon ionization (MPI) (see Figure 2.1) or barrier suppression ionization BSI (see Figure 2.2) are responsible for the production of free charge carriers. Typical intensities are given in Table 2.1. Unfortunately, this has a defocusing effect, leading to a lower refractive index, with increasing intensity and carrier density closer to the optical axis. However, if the interaction is highly relativistic, the relativistic mass increase of the electrons executing quiver motions in the electric field overcompensates for ionization defocusing, leading to an increase in the refractive index closer to the axis (see Figure 2.3). This relativistic self-focusing (see Chapter 5) enables laser guiding over several Rayleigh lengths [5].

2.3 Focusing a Gaussian laser pulse

Satisfying Gauss's law has implications on the required transversality of the electric field, especially in tight focusing conditions in vacuum. Assume a linearly polarized laser field of the form

$\vec{E}(\vec{r},t) = \vec{E}_\perp(\vec{r},t) + \vec{E}_\parallel(\vec{r},t)$, where the parallel component is the mandatory nontransversal contribution. Its propagation is described by a factor $e^{i(\omega t - k_z z)}$. It follows:

$$\begin{aligned} \nabla \cdot \vec{E} &= \nabla_\perp \cdot \vec{E}_\perp + \nabla_\parallel \cdot \vec{E}_\parallel && (2.30)\\ &= 0 && (2.31)\\ \Rightarrow -\nabla_\parallel \cdot \vec{E}_\parallel &= \nabla_\perp \cdot \vec{E}_\perp && (2.32)\\ & && (2.33) \end{aligned}$$

where the following substitutions can be made [7]:

$$\begin{aligned} \nabla_\perp \cdot \vec{E}_\perp &\approx \tfrac{|\vec{E}_\perp|_{max}}{r(z)} && (2.34)\\ \nabla_\parallel \cdot \vec{E}_\parallel &\approx -i\vec{k}\vec{E}_\parallel && (2.35) \end{aligned}$$

Here, the radial component has been approximated utilizing the beam diameter $r(z)$. It follows:

$$|\vec{E}_\parallel| \approx \frac{1}{|\vec{k}|r(z)}|\vec{E}_\perp| \qquad (2.36)$$

Note that equivalent results can be obtained from the Gauss's law of magnetism, leading to a longitudinal magnetic field component in accordance to the equations above.

A Gaussian beam with diameter D at $I_0 e^{-2}$ can be focused down to the diffraction limited spot size [8]

$$r_0 = \frac{f\lambda}{\pi r_{beam}} \qquad r_{beam} = \frac{1}{2}D \qquad (2.37)$$

The equation for light propagation around the beam waist:

$$r(z) = r_0\sqrt{1 + \left(\frac{\lambda z}{\pi r_{focus}^2}\right)^2} \qquad (2.38)$$

provides the expression for the Rayleigh length:

$$Z_R = \frac{f^2\lambda}{\pi r_{beam}^2} \qquad (2.39)$$

An Example

An $f/3$ optics with a focal length $f = 15\,\text{cm}$, a laser beam with a diameter $D = 3.5\,\text{cm}$ $(I_0 e^{-2})$, not using the full aperture of the focusing optics, and a wavelength of 800 nm lead to a diffraction-limited focal spot with radius $r_0 = 2.2\,\mu\text{m}$. This yields $|\vec{E}_\parallel|/|\vec{E}_\perp| = 0.058$, i.e., almost 6%.

A typical intensity that can be reached at the Lund High-Power Laser facility can be calculated from measured quantities such as

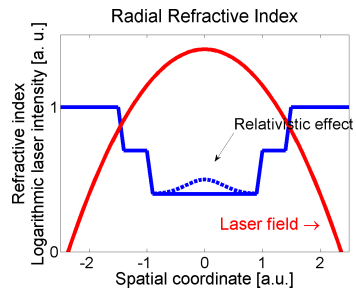

Figure 2.3. *Schematic of $\eta(r)$ (blue) decreasing in steps whenever laser intensity (red, logarithmic) exceeds a threshold level and a new atomic shell can be ionized. In a highly relativistic plasma response, the electrons however create a guiding channel on the axis.*

Table 2.1. *Apperance Intensities for ionized states of typcial target gases calculated with the barrier suppression ionization model [6]*

Ion	I [W/cm^2]
H^+	1.4×10^{14}
He^+	1.4×10^{15}
He^{2+}	8.8×10^{15}

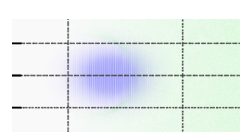

the total pulse energy, E, its duration (FWHM) τ_l, wavelength, λ and numerical aperture. The maximum on-axis intensity, I_{max}, is given by:

$$I_{max} = \frac{2E}{<\tau> \pi r_o^2} \qquad \begin{aligned} r_0 &= \frac{f\lambda}{\pi r_{beam}} \\ <\tau> &= \tau_l \sqrt{\frac{\pi}{4\ln 2}} \end{aligned} \tag{2.40}$$

The expressions on the right are valid for a Gaussian pulse in the time and space domains and apply to the measured pulse length and focal spot size. They are derived in Appendix C. With the well known relation between average intensity and electric field amplitude:

$$I = \frac{1}{2}\epsilon_0 c E_0^2 \tag{2.41}$$

a test particle (or a reasonably low plasma density n) would experience a longitudinal field of 2.8 TV/m. In this case it was assumed that a 1 J pulse hits the target within $\tau_l = 42$ fs.

Note that in this example the laser beam at the Lund high-power facility is modelled by a transverse Gaussian profile. This is only an approximation as the beam has a supergaussian lateral intensity profile. Nevertheless, $D = 3.5$ cm provides reasonable values with regard to obtainable spot size, field strenghts and intensities.

2.4 The Vector Potential

In laser-plasma interactions one commonly introduces the normalized vector potential:

$$\vec{a}(\vec{r},t) \equiv \frac{e}{m_e c}\vec{A}(\vec{r},t) \tag{2.42}$$

in such a way that for a given modulus of $\vec{a}$ we stimulate a

$|a(\vec{r},t)| \ll 1$ linear plasma response

$|a(\vec{r},t)| \gtrapprox 1$ nonlinear plasma response

$\vec{A}(\vec{r},t)$ is related to the electric and magnetic fields in the Lorentz gauge via

$$\vec{E}(\vec{r},t) = -\frac{\partial}{\partial t}\vec{A}(\vec{r},t) \qquad \vec{B}(\vec{r},t) = \nabla \times \vec{A}(\vec{r},t) \tag{2.43}$$

and is derived in Appendix A.

The energy flow out of a volume element is given by the Poynting vector $\vec{S}$, defined by:

$$\vec{S} \equiv \vec{E} \times \vec{H} \tag{2.44}$$

which, in vacuum ($\mu = 1$), can be rewritten as:

$$\vec{S} = \frac{1}{\mu_0}\vec{E} \times \vec{B} \tag{2.45}$$

The intensity, I, is the modulus of the time average of the real part of the Poynting vector:

$$I = | < \Re(\vec{S}) > | \tag{2.46}$$

$$= \frac{1}{\mu_0} | < \Re(\vec{E}) \times \Re(\vec{B}) > | \tag{2.47}$$

which, applying the expressions from Equation (2.43) and solving in Fourier space (see Appendix B), leads to:

$$I = \frac{1}{\mu_0} | < \Re(\partial_t \vec{A}) \times \Re(\nabla \times \vec{A}) > | \tag{2.48}$$

$$I = \frac{1}{\mu_0} | < \Re(-i\omega \vec{A}) \times \Re(i\vec{k} \times \vec{A}) > | \tag{2.49}$$

Calculating the time average (see Appendix D) yields

$$I = \frac{1}{2\mu_0} \left| \Re\left[(-i\omega \vec{A_0}) \times (i\vec{k} \times \vec{A_0})^* \right] \right| \tag{2.50}$$

$$= \frac{\omega}{2\mu_0} \left| \Re\left[(\vec{A_0}) \times (\vec{k} \times \vec{A_0})^* \right] \right| \tag{2.51}$$

$$= \frac{\omega}{2\mu_0} |\vec{k}| (\vec{A_0}\vec{A_0}^*) \tag{2.52}$$

$$= \frac{\omega}{2\mu_0} |\vec{k}| |\vec{A_0}|^2 \tag{2.53}$$

The time-averaged vector potential, $\vec{A}$, can be replaced by half its amplitude $|\vec{A_0}|$. Finally, using the vacuum dispersion relation, $\omega = c|\vec{k}|$, and Equation (2.42), we arrive at:

$$\Rightarrow a_0 = \sqrt{I} \frac{e}{m_e \omega} \sqrt{\frac{2\mu_0}{c}} \tag{2.54}$$

An Example

In a typical electron acceleration experiment $f/9$ focusing optics or larger is used to provide a sufficient Rayleigh length (see Section 2.3). Thus, with the $f/9$ focusing optics at the Lund High-Power Laser facility, with $f = 45\,\text{cm}$, a laser beam with a diameter $D = 3.5\,\text{cm}$ ($I_0 e^{-2}$), not using the full aperture of the focusing optics, $E = 1\,\text{J}$ and $\tau_l = 42\,\text{fs}$, the maximum intensity is:

$$\begin{aligned} I_{max} &= 3.3 \times 10^{19}\,\text{W/cm}^2 \\ a_0 &= 3.9 \end{aligned}$$

thus stimulating a nonlinear relativistic plasma response.

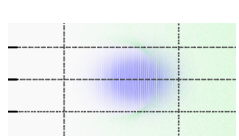

If we consider the complete expression for a_0:

$$a_0 = \frac{\sqrt{E} r_{beam}}{\sqrt{\tau_l} f} \frac{(\ln 2)^{1/4}}{\pi^{3/4}} \frac{e\sqrt{2\mu_0}}{mc^{3/2}} \tag{2.55}$$

we see that a_0 is not influenced by the choice of laser frequency. However, frequency doubling will improve laser contrast (see Section 3.3 on high power laser systems), as a second order effect, and double the electric laser fields present in the plasma.

Maxwell's equations together with the continuity equation:

$$\frac{\partial}{\partial t}\rho + \nabla \cdot \vec{j} = 0 \tag{2.56}$$

the energy equation:

$$\frac{d}{dt}(\gamma m_e c^2) = q(\vec{v}\vec{E}) \tag{2.57}$$

and the equation of motion for particles of charge q (Lorentz force):

$$\vec{F} = q(\vec{E} + \vec{v} \times \vec{B}) \tag{2.58}$$

provide a full mathematical description for laser-plasma interactions. While special cases can be solved algebraically, the investigation of especially nonlinear behaviour and higher dimensional effects relies strongly on computer simulations. However, one-dimensional idealizations can provide important insight into certain features of the laser-plasma interaction, which is why in the following some 1D results are discussed.

2.5 Linear Plasma Waves

Solving Gauss's law in a 1D linear case [9] for a plasma wave, $E_z = E_{max} \sin[\omega_p(z/v_p - t)]$, and $v_p \approx c$, under the assumption that all electrons oscillate with the wave number $k_p = \omega_p/c$, yields an estimate of field strengths attainable in plasmas:

$$k_p E_{max} = \frac{\rho}{\epsilon_0} \tag{2.59}$$

$$\Rightarrow \; E_{max} = \frac{cne}{\omega_p \epsilon_0} \propto \sqrt{n} \tag{2.60}$$

where n refers to the undisturbed electron density.

Trapped electrons may outrun the accelerating phase of the plasma wave, which propagates approximately with the group velocity of the laser pulse ($v_{p\ \mathrm{plasma}} \approx v_{g\ \mathrm{laser}}$). Thus, after a given

dephasing time, τ_D, electrons that are propagating with a velocity $\approx c \geq v_p$ will be decelerated again. This happens when their difference in velocity enables a propagation offset between the plasma phase and their own propagation by half the plasma wavelength, $\lambda_p/2$:

$$(c - v_p)\tau_D = (c - v_p)\frac{L_D}{c} = (1 - \frac{v_p}{c})L_D = \frac{\lambda_p}{2} \tag{2.61}$$

$$\Rightarrow \; L_D = \frac{\lambda_p}{2(1 - \beta_p)} \tag{2.62}$$

$$\approx \gamma_p^2 \lambda_p \; (\Leftrightarrow \; \beta_p \approx 1) \tag{2.63}$$

using that

$$1 - \beta_p^2 = (1 + \beta_p)(1 - \beta_p) \approx 2(1 - \beta_p) \tag{2.64}$$

Comparison with Equation (2.27) yields:

$$\gamma_p^2 = \frac{1}{1 - \beta_p^2} = \frac{1}{1 - \eta^2} = \left(\frac{\omega}{\omega_p}\right)^2 \tag{2.65}$$

so that

$$L_D \approx \left(\frac{\omega}{\omega_p}\right)^2 \lambda_p \approx \left(\frac{\omega}{\omega_p}\right)^2 \frac{2\pi c}{\omega_p} \; \propto n^{-3/2} \tag{2.66}$$

Thus, the maximum energy gain $W \propto E_{max} L_D \propto n^{-1}$. Means to maintain the laser well collimated at densities too low for relativistic self-focusing to counteract diffraction have been investigated and are described in Paper **IX**, where a linear or moderately nonlinear plasma wave is driven by a laser over a distance of $\approx 8\,\mathrm{cm}$ at plasma densities $\lesssim 10^{18}\,\mathrm{cm}^{-3}$.

An Example

A typical laser pulse at LLC is centred at $\lambda_l = 800\,\mathrm{nm}$ and has a duration of $\tau_l = 42\,\mathrm{fs}$ ($\Rightarrow l_l = \tau_l c = 13\,\mu\mathrm{m}$). This pulse resonantly drives a plasma wave with $\lambda_p = 25\,\mu\mathrm{m}$ at a plasma density of $n = 1.8 \times 10^{18}\,\mathrm{cm}^{-3}$, yielding a plasma frequency $\omega_p = 7.5 \times 10^{13}\,\mathrm{s}^{-1}$. This results in acceleration fields of the order of $E_{max} = 130$ GV/m and a dephasing length around $L_D = 25\,\mathrm{mm}$. Thus, electrons can be boosted to $W = 3.2\,\mathrm{GeV}$.

However, if a Gaussian beam with size of $D = 3.5\,\mathrm{cm}$ (at $I_0 e^{-2}$) is focused by optics with a focal length of $f = 1.5\,\mathrm{m}$, the diffraction-limited spot size $2r_0 = 44\,\mu\mathrm{m}$ can be achieved (see Section 2.3). In this example, the Rayleigh length is $Z_R = 1.9\,\mathrm{mm}$. If we replace L_D by $2Z_R$ the gain will be limited to $W = 490\,\mathrm{MeV}$. Here, electron injection into the accelerating phase of the plasma wave was not considered but will tend to limit this value further.

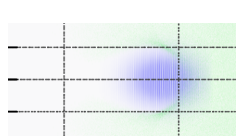

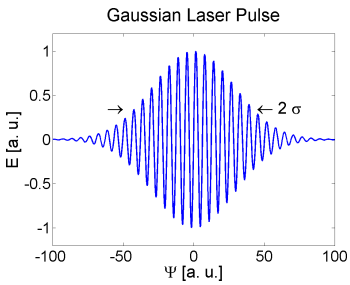

Figure 2.4. *Gaussian laser pulse with characteristic length σ.*

2.6 Self-Phase Modulation (SPM)

Usually self-phase modulation describes the generation of new frequency components in a laser pulse propagating through matter due to the dependence of the refractive index on the intensity, $\eta = \eta_1 + \eta_2 I$. In a plasma, the refractive index is modulated indirectly through modulations of the electron density as a result of the intensity dependent ponderomotive force, which expells electrons from regions of high intensity. Mathematically both effects can be described in a similar way.

A laser pulse such as the one depicted in Figure 2.4 with a characteristic length σ propagating in a medium can be described by

$$\vec{E} = \vec{E}_0 e^{i(\omega t - \vec{k}\vec{r})} e^{-\frac{\Psi^2}{\sigma^2}} \tag{2.67}$$

where $\vec{k} = \eta \vec{k}_0$, the phase $\Psi = \omega t - \vec{k}\vec{r}$ and the width $\sigma = \sqrt{2}\omega t_0$. The refractive index can be rewritten:

$$\eta = \sqrt{1 - \left(\frac{\omega_p}{\omega}\right)^2} \tag{2.68}$$

$$= \sqrt{1 - \left(\frac{\lambda_l e\sqrt{n}}{2\pi c\sqrt{\epsilon_0 m}}\right)^2} \tag{2.69}$$

$$= \sqrt{1 - \left(\frac{\lambda_l e}{2\pi c}\right)^2 \frac{1}{\epsilon_0 m} n} \equiv \sqrt{1 - \varphi n} \tag{2.70}$$

and the momentary effective frequency, ω_{eff}, can be extracted from the phase, Ψ, using the relation:

$$\omega_{eff} = \frac{\partial \Psi}{\partial t} = \frac{\partial}{\partial t}(\omega t - \vec{k}\vec{r}) \tag{2.71}$$

$$\approx \omega + \vec{k}_0 \vec{r} \frac{\varphi}{2} \frac{\partial n}{\partial t} \tag{2.72}$$

assuming that $\lambda_l = 800\,\text{nm}$ and $n = 10^{18}\,\text{cm}^{-3}$, thus $(\varphi n) \ll 1$. Hence, higher frequencies will be created at the pulse front, where the electron density is increasing. This is called ionization blue shift [10, 11]. However, at the front of the the electron-evacuated bubble in the blow-out regime (see Chapter 5) the decrease in electron density creates a rather strong red shift. This was calculated in detail in Paper **X** and observed experimentally in Paper **IX**.

2.7 The Ponderomotive Force

The ponderomotive force is the negative gradient of the ponderomotive energy (in literature often misleadingly referred to as ponderomotive potential). This in turn describes the time-averaged

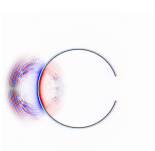

quiver energy of an electron exposed to an inhomogeneous oscillating electric field such as that provided by a tightly focused laser pulse. Here, strong intensity gradients give rise to an average force "pushing" charged particles away from the high-intensity regions. In a nonrelativistic treatment [6] the equation of motion for a free electron in an electric field can be written:

$$m_e \frac{\partial \vec{r}(t)}{\partial t} = -e\vec{E}_0(\vec{r}) \cos(\Psi), \text{ with } \Psi = \vec{k}\vec{r} - \omega t \tag{2.73}$$

If we assume a radially decreasing electric field amplitude $\vec{E}_0(r)$ around $r = 0$, motivated by experiment, we can Taylor approximate the field distribution and introduce a perturbation factor, λ, which yields:

$$\vec{E}_0(\vec{r}) \approx \vec{E}_0|_{r=0,z} + \lambda(\vec{r} \cdot \nabla)\, \vec{E}_0|_{r=0,z} + O(\vec{E}_0^2) \tag{2.74}$$

and with the perturbation ansatz: $\vec{r} = \vec{r}^{(0)} + \lambda^1 \vec{r}^{(1)} + \lambda^2 \vec{r}^{(2)} + ..$ the equation to be solved becomes:

$$\begin{aligned} &\frac{\partial^2}{\partial t^2}(\vec{r}^{(0)} + \lambda \vec{r}^{(1)} + ..) = \\ &-\frac{e}{m_e}\left[\vec{E}_0|_{r=0,z} + \lambda((\vec{r}^{(0)} + \lambda \vec{r}^{(1)} + ..) \cdot \nabla)\, \vec{E}_0|_{r=0,z} + ..\right] \cos(\Phi) \end{aligned} \tag{2.75}$$

To zeroth order (λ^0) this becomes:

$$\frac{\partial^2}{\partial t^2}\vec{r}^{(0)} = -\frac{e}{m_e}\vec{E}_0|_{r=0,z} \cos(\Psi) \tag{2.76}$$

Integration leads to:

$$\frac{\partial}{\partial t}\vec{r}^{(0)} = -\frac{e}{m_e \omega}\vec{E}_0|_{r=0,z} \sin(\Psi) + c_1 \tag{2.77}$$

$$\vec{r}^{(0)} = \frac{e}{m_e \omega^2}\vec{E}_0|_{r=0,z} \cos(\Psi) + c_2(t) \tag{2.78}$$

The first-order perturbation in (λ^1) is:

$$\frac{\partial^2}{\partial t^2}\vec{r}^{(1)} = -\frac{e}{m_e}\left[(\vec{r}^{(0)} \cdot \nabla)\, \vec{E}_0|_{r=0,z}\right] \cos(\Psi) \tag{2.79}$$

Inserting $\vec{r}^{(0)}$ from Equation (2.78) gives:

$$\frac{\partial^2}{\partial t^2}\vec{r}^{(1)} = -\frac{e^2}{m_e^2 \omega^2}\left[(\vec{E}_0 \cdot \nabla)\, \vec{E}_0\right]_{r=0,z} \cos^2(\Psi) \tag{2.80}$$

The time average over the first-order perturbation and a linear polarization

$$\vec{F}_{pond} = m_e \left\langle \frac{\partial^2}{\partial t^2}\vec{r}^{(1)} \right\rangle = -(\hat{e}_{\vec{E}_0} \cdot \nabla)\left[\frac{e^2}{4m_e \omega^2}\vec{E}_0^2\right] \cdot \hat{e}_{\vec{E}_0} \tag{2.81}$$

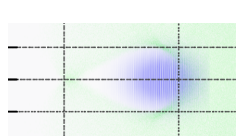

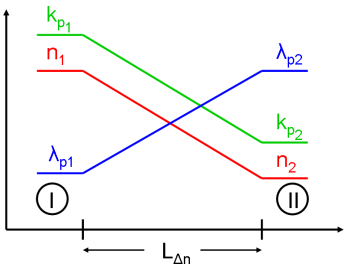

Figure 2.5. *A schematic illustrating gradients over the scale length $L_{\Delta n}$*

will cause the electron to drift on average along the negative gradient of the field amplitude into the direction of the polarization of the electric field. This direction is denoted by the unity vector:

$$\hat{e}_{\vec{E}_0} = \frac{\vec{E}_0}{|\vec{E}_0|} \tag{2.82}$$

thus the field forces electrons away from regions of high intensity. This is called the ponderomotive force, $\vec{F}_{pond}$, with the non-relativistic ponderomotive potential $\Phi_{pond} = \frac{e^2 \vec{E}_0^2}{4 m_e \omega^2}$.

In the relativistic case, magnetic fields, $\vec{B}$, and the average relativistic mass increase, $< \gamma >$, become important. In a real experiment with $a_0 \gg 1$, the $\vec{v} \times \vec{B}$ force and longitudinal electric field components (see Section 2.3) lead to a radially symmetric displacement of the electrons, away from the optical axis without trace of a preferential axis due to the laser field polarization vector.

2.8 Density Gradient Injection

To capture and accelerate electrons in a plasma wave, such as the one described in Section 2.5, they must be injected into the correct phase. Here, a mathematical formalism for electron injection using density gradients [12–14] is presented, while a more thorough discussion of gradients, electron injection and acceleration is given in Chapter 5.

Assume a plasma density gradient from density n_1 to n_2 over a scale length $L_{\Delta n}$ and define regions I and II as those regions along the laser interaction (z-axis), where the densities n_1 and n_2 are encountered (see Figure 2.5). This yields the following changes in the plasma channel:

$n_1 > n_2$	densities
$k_{p1} > k_{p2}$	k vectors
$\lambda_{p1} < \lambda_{p2}$	plasma wavelengths

Under the assumption for the group velocity of the laser pulse being close to the speed of light, i.e. $v_g = v_p \approx c$, the local phase of the wake, Ψ, can be written as $\Psi = k_p(z)\xi$, where $\xi > 0$ designates the leading and $\xi < 0$ the trailing parts of the oscillation. From this, a local phase velocity can be calculated via $v_p = \frac{\omega_{eff}}{k_{eff}}$, where $\omega_{eff} = -\frac{\partial \Psi}{\partial t}$ and $k_{eff} = \frac{\partial \Psi}{\partial z}$, yielding:

$$\beta_p = \frac{v_g}{c} = \frac{1}{1 + \frac{\xi}{k_p}\frac{\partial k_p}{\partial z}} \tag{2.83}$$

where expression $\frac{1}{k_p}\frac{\partial k_p}{\partial z}$ can be expressed in terms of densities: $\frac{1}{2n}\frac{\partial n}{\partial z}$.

Trapping can occur if the phase velocity of the wake becomes comparable to the fluid velocity of the electrons $v_p = v_e$, i.e., $\beta_p =$

β_e. It can be seen from Equation (2.83) that for a fixed position in the negative density gradient, v_p will decrease for decreasing ξ, i.e. later times. Thus, we can calculate $\xi(v_e) = \xi_e$ for any given value of v_e so that trapping occurs for those electrons.

$$\beta_p \stackrel{!}{=} \beta_e \equiv \frac{v_e}{c} = \frac{1}{1 + \frac{\xi_e}{2n}\frac{\partial n}{\partial z}} \tag{2.84}$$

The density gradient resulting in a change in the plasma wavelength over its characteristic length, $(\lambda_{p1} - \lambda_{p2})/L_{\Delta n} \approx \frac{\partial \lambda_p}{\partial z} = -\frac{\lambda_p}{2n}\frac{\partial n}{\partial z}$, enables a rigorous substitution into Equation (2.84):

$$\beta_e = \frac{1}{1 + \frac{\xi_e}{2n}\frac{\partial n}{\partial z}} \tag{2.85}$$

$$\approx \frac{1}{1 - \frac{\xi_e}{2L_{\Delta n}}} \tag{2.86}$$

$$\Rightarrow -2L_{\Delta n}\left(\frac{1}{\beta_e} - 1\right) = \xi_e \tag{2.87}$$

Physically, this means that due to the increase in plasma wavelength λ_p behind the laser pulse at a density down ramp, the distance between phase fronts increases, which locally lowers v_p. This reduces the required initial speed, v_e, for electrons to be captured in the plasma wave at the gradient. An estimation, calculated for specific experimental parameters can be found in Section 5.2.

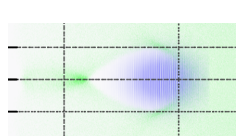

Chapter 3

High-Power Laser Systems

Two high-power laser systems, each representative of an entire class of laser systems, were used to irradiate targets at intensities that lead to plasma formation and to drive nonlinear or highly relativistic interactions. Much of the work was carried out using the Lund multi-TW laser at the LLC in Sweden, while the Vulcan Glass laser at the Rutherford Appleton Laboratory in the UK was used for studies at higher pulse energies and longer ($\sim$ ps) pulse durations. Both systems are presented in this chapter with special focus on laser contrast.

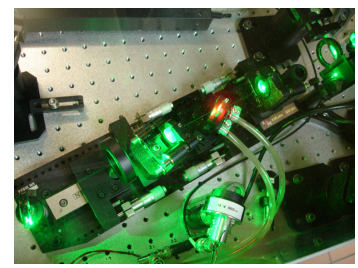

Figure 3.1. *80 MHz oscillator utilizing Kerr lens mode locking [16], pumped by a 5 W Millennia DPSS at 532 nm at a power of 3.8 W*

3.1 The Lund Multi-Terawatt Laser

The Lund multi-TW laser is a Ti:Sapphire femtosecond laser system, using chirped pulse amplification (CPA) [15]. At the beginning of the laser chain, an 80 MHz Ti:Sapphire oscillator produces pulses with $\sim$ 50 nm bandwidth (FWHM) and nJ energy via Kerr Lens Mode Locking. It is pumped by a 5 W Millennia diode-pumped solid state (DPSS) laser with a power of $\approx$ 3.8 W cw at a wavelength of 532 nm, where the transverse spatial pump profile on the crystal and stability properties of the laser cavity encourage mode locking. Mirror leakage of the circulating pulse triggers a master clock for the entire laser chain; part of it being forwarded to a spectrometer.

From the emitted 80 MHz pulse train, a pulse picker selects single pulses with a 10 Hz repetition rate. If high contrast is required, the pulses can be forwarded through a 4-pass "butterfly" preamplifier. The pulses are then passed through a saturable absorber to remove low-intensity noise that may otherwise seed laser amplification prior to the main pulse. The preamplifier is powered by a pulsed, 10 Hz Q-switched flash-lamp-pumped Nd:YAG laser, emitting 0.2 J pulses at 532 nm. If high contrast is

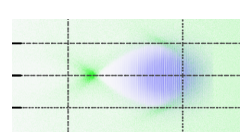

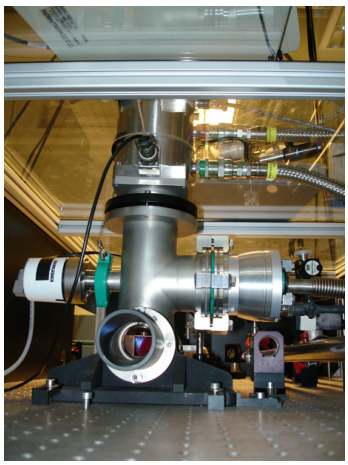

Figure 3.2. *Cryogenically cooled $25 \times 25 \times 20\,mm^3$ Ti:Sapphire crystal, pumped with 7 J at 532 nm. Transverse lasing is inhibited by absorbing carbon sheets surrounding the amplifying medium.*

not crucial for the application, the pulses bypass the preamplifier and saturable absorber and are directly forwarded to an acousto-optic programmable dispersive filter (Dazzler), where different frequency components can be delayed relative to each other. In this way, third- and fourth-order phases can be precompensated for, as grating compressors can only easily correct for the second-order phase.
After the dazzler, the pulses enter a stretcher (Öffner design [17]) where they are dispersed by 9 ps/nm. After matching the transverse laser mode to the proceeding regenerative amplifier cavity, they make 9 to 12 round trips before extraction, reaching energies of several mJ.
A pair of cleaning Pockels cells effectively eliminates prepulses after the regenerative amplifier, and is followed by a beam expander and further amplification in a 5-pass butterfly amplifier reaching $\approx$ 300mJ, of which $\approx$ 100 mJ is used to seed the cryogenically cooled power amplifier. Before entering the final phase of amplification, a spatial filter and a third Pockels cell "clean" the pulses in the space and time domains. This is done to reduce the risk of burning crystals and optics due to "bad" laser modes being amplified, and to block reflections from the experiment, which may otherwise seed amplification backwards through the laser chain.
In the final 4-pass butterfly amplifier, which is pumped by 5 frequency-doubled, ns, flash-lamp-pumped and Q-switched Nd:YAG lasers, that provide up to 7 J of green pump energy at a 10 Hz repetition rate, the pulse energy can be increased to 2 J before compression. From there, approximately 60% will reach the target after passing through a grating compressor. A deformable mirror (DM) [18] with 32 actuators, placed after the grating compressor, in combination with a phase front detector at the target site, effectively corrects phase abberrations to obtain a focal spot with a Strehl ratio of typically 99%. A schematic illustration of the laser system can be seen in Figure 3.3

A small fraction of each pulse ($\lessapprox$ 20 mJ) can be extracted and diverted from the multi-pass power amplifier to be utilized as an additional uncompressed or compressed IR or frequency-doubled 400 nm compressed pulse for experiments that require a probe beam (e.g. plasma interferometry).

As highlighted in Paper **VIII**, a recently developed beam pointing stabilization system locks the beam in the focal plane on the optical axis with an RMS spread of only $\sim 2\,\mu$rad.

Various beam diagnostics are available in the target area, such as a second-order autocorrelator, a third-order autocorrelator for measurements of the ps contrast, a frequency-resolved optical gating (FROG) [19] and a beam profiler. The round target chamber, probe pulse preparation table, vacuum compressor chamber and auxiliary diagnostics table can be seen in Figure 3.4.

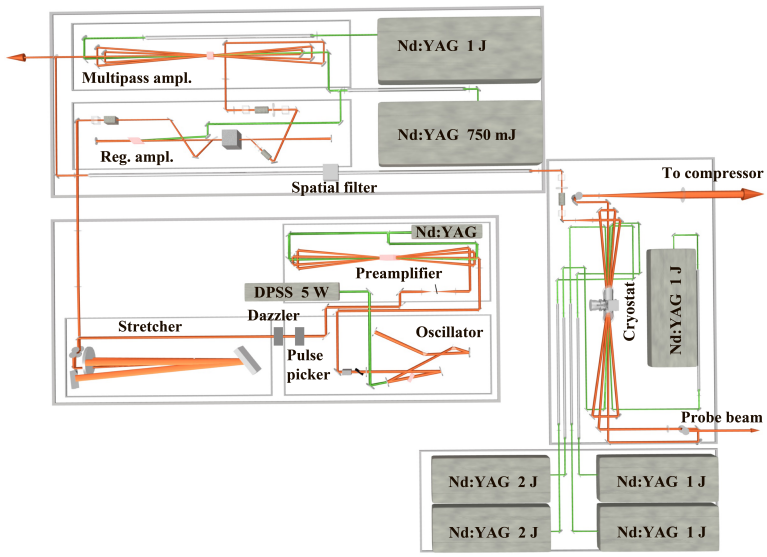

Figure 3.3. *Laser amplification chain of the Lund multi-TW CPA Ti:Sapphire system, currently providing* $\gtrsim 1\,J$ *on target during* 42 *fs at a wavelength of* 800 *nm.*

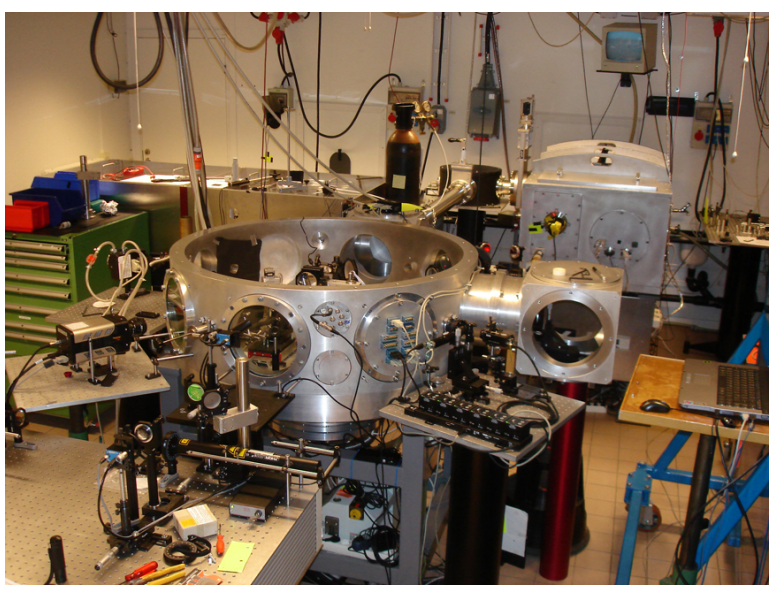

Figure 3.4. *Target area of the Lund multi-TW laser. The vacuum compressor (the square chamber at the back on the right), the round target chamber (front), the probe pulse table (back left) and other diagnostic equipment can also be seen.*

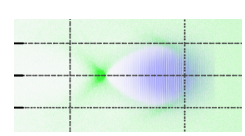

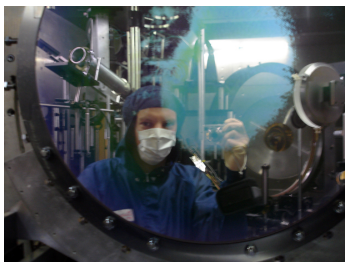

Figure 3.6. *Primary focusing optics: the 1 m diameter $f/3$ off-axis parabolic mirror at the target area Petawatt of the Vulcan Glass laser*

3.2 The Vulcan Glass Laser at Rutherford Appleton Laboratory

The Vulcan Glass laser is an optical parametric chirped-pulse amplification (OPCPA) [20, 21] seeded Nd:Glass amplifier, operating at 1053 nm. Due to its tremendous power, delivering up to 500 J during 500 fs, only eight shots per day are available at each of the two target areas. The author has worked at both target areas: the target area Petawatt (TAP), with results presented in Papers **II** and **III**, and the target area West (TAW), where the results are still analysed. As the system is managed by technical staff, only the user-relevant pulse specifications are given in Table 3.1.

Table 3.1: Laser comparison (ASE: amplified spontaneous emission, see Section 3.3. Beam diameter: Required aperture to avoid clipping of the beam.)

	Lund multi-TW laser	**Vulcan Glass laser (TAP)**
Laser material	Ti:Sa	Nd:Glass
Amplification	CPA	OPCPA front-end/ CPA
λ_{centre} [nm]	800	1053
Repetition rate [Hz]	10	3×10^{-4}
τ_l [fs]	35	500
E_{max} [J]	1.5	500
ASE contrast	10^9	10^9
Focusing optics	$f/30 - f/3$	$f/3$
Beam diameter [cm]	5	60
Auxiliary beams	1	2
Target chamber [m^3]	0.5	16

3.3 Plasma Mirrors - Enhancing Contrast on a ps Time Scale

In experiments on laser-matter interaction the contrast of the laser system is crucial for the interaction taking place. By contrast, one usually means the ratio of the peak intensity of the laser pulse on the target during laser interaction to the intensity passing downstream the laser chain and irradiating the target some tens of picoseconds earlier. The radiation reaching the target before the main peak may be intense enough to form an expanding preplasma. This is characterized by its scale length, which is the length over which the plasma density decreases to the fraction e^{-1} away from the target. Preplasma formation influences laser absorption, as shown by Glinec *et al.* and McKenna *et al.* [22, 23].

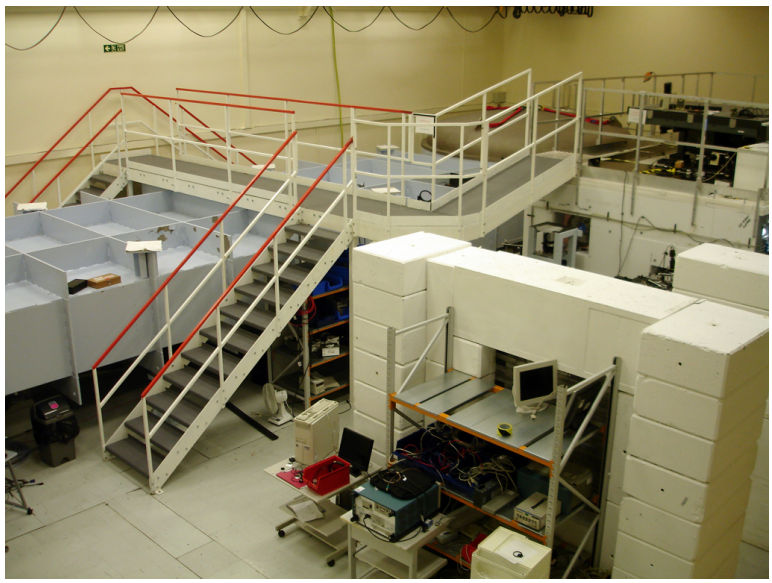

Figure 3.5. *Target area Petawatt of the Vulcan Glass laser at the Rutherford Appleton Laboratory. Part of the compressor can be seen on the left (pale blue) as well as the shielding for the large target vacuum chamber on the right.*

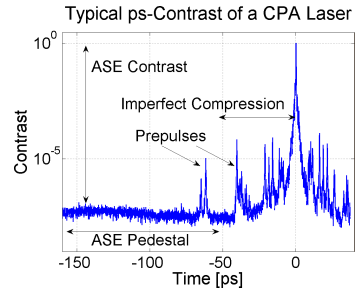

Figure 3.7. *Typical third-order contrast measurement at the Lund multi-TW laser (without preamplifier to boost contrast)*

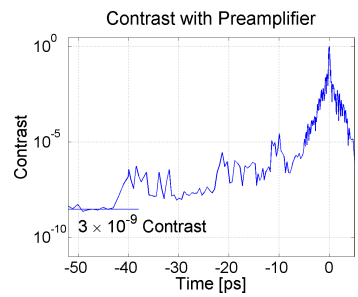

Figure 3.8. *Picosecond ASE contrast reaching $\sim 10^9$, 50 ps prior to the main pulse. The intensity increase especially around minus 8 ps is mostly due to non-perfect compression in the CPA system.*

Two important features that are inherent in CPA systems are amplified spontaneous emission (ASE) and imperfect compression. While the first produces a so-called pedestal, i.e. an area of nearly constant intensity up to some hundreds of picoseconds prior to the main pulse, the latter may also produce premature intensity spikes, especially if the spectrum is clipped. Figure 3.7 shows a typical third-order contrast measurement, conducted with a Sequoia third-order autocorrelator. It should be pointed out that ASE build-up can be reduced by lowering the pump energy in the cavity of the regenerative amplifier, and by prior pulse cleaning using a saturable absorbers or cross-polarized wave (XPW) generation [24] [25]. Preamplification in combination with a reduced number of round trips and slightly reduced pump power results in one order of magnitude increased ASE contrast with the Lund multi-TW laser. This is exemplified in Figure 3.8.

If contrast improvements in the amplification chain are not sufficient, a fast optical switch may provide a solution. Such a switch must react quickly enough to suppress laser radiation up to some ps prior to the arrival of the main pulse, until the intensity exceeds a critical threshold. A simple glass plate can fulfil this requirement as it will transmit laser radiation according to the

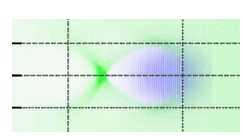

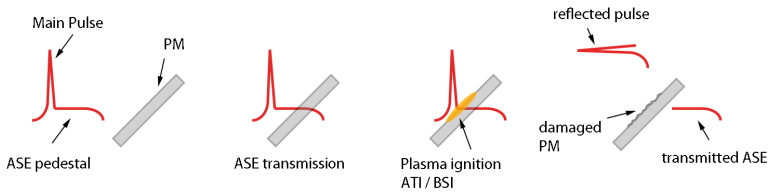

Figure 3.9. *The laser arrives from the left. As long as the intensities are matched correctly, most of the ASE will be transmitted by the glass plate, according to the Fresnel coefficients. An increase in intensity will lead to plasma formation, which leads to reflection of the laser pulse at the critical density surface. The glass plate has thus become a plasma mirror. The improvement in contrast is mainly governed by the maximum transmission achievable at the low ASE intensities.*

Fresnel coefficients [4], until the impinging intensity has increased sufficiently to form a plasma on its surface, a process that starts at around $\geq 10^{13}\,\mathrm{W/cm^2}$. From that moment on, the laser beam will be reflected at the critical density surface of the plasma (see Figure 3.9), where the plasma frequency is equal to the laser frequency ($\omega_p \approx \omega$) and the refractive index (see Equation (2.27)) becomes imaginary. Thus only the main pulse will be reflected onto the target.

Such so-called plasma mirrors (PMs) are implemented at many high-power laser facilities around the world, and have been investigated by many groups (see e.g. Dromey *et al.* [26] and Doumy *et al.* [27]). The PM assembly used in the experiment described in Paper **I** is depicted in Figure 3.10. The increase in contrast in the Lund multi-TW laser system when using this PM, located 3 mm in front of the primary focus, and exposed to intensities up to $\approx 5 \times 10^{15}\,\mathrm{W/cm^2}$, was estimated using ray tracing simulations with the software FRED (Photon Engineering). A simulated experimental set-up can be seen in Figure 3.11. It was assumed that a linearly polarized beam with a 22 nm Gaussian spectrum (FWHM) was focused by an $f/3$ OAP and impinged on an uncoated glass plate (Schott BK7) 3 mm in front of the focus in such a way that the central wavelength at the center of the beam encounters the surface at the Brewster angle. In this case, only $\approx 0.5\%$ of the laser radiation is reflected and reaches the target. Assuming that $\approx 50\%$ of the laser pulse energy is reflected (due to absorption in the forming plasma), a contrast gain on the target of the order of 100 can be achieved on a ≤ 1 ps time scale with this simple arrangement. However, suitable anti-reflection coatings on the PM to further reduce the reflectivity prior to the pulse arrival would further increase the performance. With these implementations a contrast of the order 10^{11}, ~ 50 ps prior to the pulse could be

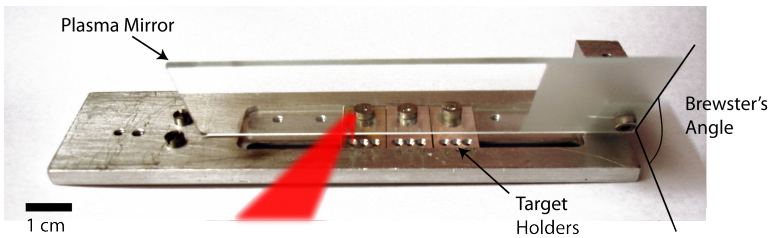

Figure 3.10. *Combined plasma mirror and target holder assembly used in the experiments presented in Paper **I**. The laser impinges on the glass plate at Brewster's angle, allowing most of the ASE to be transmitted until the intensity becomes high enough to ionize the glass surface and form an overdense plasma, which homogeneously reflects the impinging laser light. At the LLC an overall ps contrast of the order of 10^{11} was achieved. This restricts experiments to ultra-thin targets or layers only tens of nm thick*

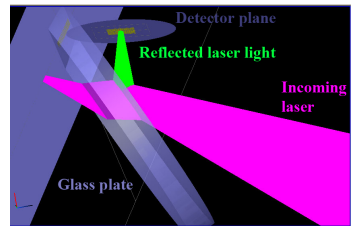

Figure 3.11. *FRED ray tracing simulation. The laser beam (magenta) enters from the right, and impinges on a BK7 glass plate at Brewster's angle. A detection zone is defined in reflection giving an estimate of the reflection of a convergent p-polarized 800 nm beam, 3 mm prior to reaching the focus.*

accomplished during experiments presented in Paper **I**.

However, it must be borne in mind that plasma instabilities will degrade the surface of the PM shortly after plasma formation ($\gtrapprox$ 2 ps). A non-uniform lateral laser intensity will cause the plasma to be formed at different times at different locations. Both effects may alter the quality of the focal spot and it is highly recommended that investigations on PM behaviour be carried out using a fast optical probe, e.g. plasma interferometry (see Section 4.2.1).

A limitation of PMs is that they are single-shot optical elements, and may thus constitute a bottleneck in high-repetition rate high-contrast experiments. Furthermore, means for active control or feedback are limited. It may, therefore, be necessary to consider different laser schemes than CPA, such as OPCPA, second harmonic generation (SHG) or XPW, which provide higher contrast while circumventing the necessity for a PM.

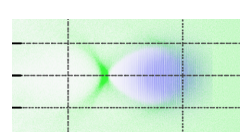

Chapter 4

Optical Diagnostics

High-intensity laser-plasma experiments require a wide arsenal of diagnostics to shed light on the interaction. Generally, detectors can be divided in particle- and light-sensitive detectors. While the first group includes detectors such as nuclear track detectors [28] and radiochromatic film (RCF) [29] for the detection of protons, or a fluorescent Lanex screen sensitive to electrons, the latter group comprises mostly CCD-based imaging devices and, in rare cases, imaging plates. Because of their significance for this thesis, this chapter focuses on CCD-based imaging devices. The emphasis is placed on phase imaging for applications that allow for target characterization to achieve a suitable or *smart target design* and plasma expansion studies.

4.1 Intensity Imaging

Imaging of the target during the interaction has been proven useful as it can provide valuable information leading to a better understanding of the interaction and thus improved performance. A rather straightforward example is the use of a top-view camera (Papers **V** and **XII**), looking at a gas jet target from above. During the interaction, Thomson-scattered [30] laser light is recorded. Orthogonal to the optical laser axis the scattering intensity [31] can be written as

$$I_{Th}(x,z) \propto \int_x^\infty n(r,z) \left| \frac{a_0(r,z)}{\gamma(r,z)} \right|^2 \frac{r}{\sqrt{r^2-x^2}} dr \qquad (4.1)$$

and being proportional to nI/γ^2. An example can be seen in Figure 4.1. The nozzle is photographed in continuous light to provide length calibration, while the plasma channel is typically recorded with an (800 ± 50) nm bandpass filter to suppress plasma self-emission. The laser polarization is horizontal.

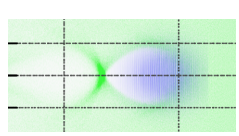

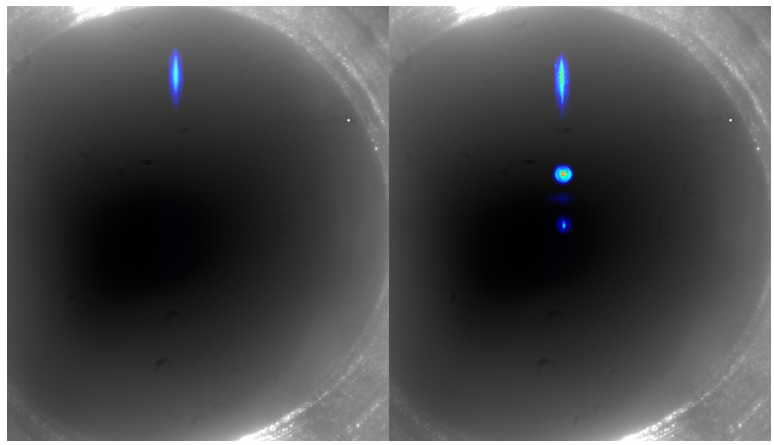

Figure 4.1. *Top-view of the 3 mm orifice of a pulsed gas nozzle (grayscale) with Thomson scattering superimposed (false colour) during laser-plasma interaction in a free-flow gas jet (left) and a density-modulated flow (right), producing two additional emissions separated by $\sim 350\,\mu$m; the laser pulse enters from above.*

In the first phase of laser-matter interactions in the underdense regime, the laser pulse undergoes self-modulation and compression in the longitudinal direction as well as relativistic self-focusing in the transverse direction (see Chapter 5 for a more detailed description). As a result, the amplitude of the normalized vector potential, a_0, increases, leading to a highly nonlinear plasma response. This may result in the ponderomotive force (see Section 2.7) displacing all electrons away from the high-intensity region of the laser pulse. As a result, a plasma cavity, called a bubble (see Chapter 5), may form around the laser pulse and moving with its group velocity v_g. As Thomson scattering is dependent on the product of the laser intensity, I and the plasma density, n, reaching the bubble regime will reduce the probability of Thomson scattering. From Figure 4.1 it can be estimated that a bubble has formed after $\approx 800\,\mu$m in a hydrogen plasma with $n = 5 \times 10^{18}\,\mathrm{cm}^{-3}$, using a 1 J laser pulse with $\tau_l = 42\,$fs, .

4.2 Phase Imaging

Interferometry is a common tool in both laser-gas and laser-solid interactions. It has been widely applied throughout the work of the thesis (Papers **II**, **III**, **V**, **VII** and **VI**). However, full tomography of the target is often unsuitable due to spatial restrictions in the experimental set-up. Usually interferometry is carried out along one predefined axis. The assumptions made regarding symmetry

when calculating the prevailing plasma densities must therefore be justified.

LWFA experiments usually employ a gas jet (see e.g. Papers **V** - **VII**), a gas cell [32, 33] or capillaries (see e.g. Papers **IX** - **XII**) to contain the target gas prior to the interaction. Gases typically used for plasma experiments are hydrogen, helium or argon, and these may be probed with both continous wave (cw) and pulsed laser beams. If plasma densities cannot be derived from the prevailing gas density or if high temporal resolution is required, pulsed probe beams may be used [34]. This is especially true for laser-solid experiments where plasma expansion is recorded. The probe beam is usually split directly from the main beam, thus jitter is low.

Low phase shifts, especially when working with gas jet targets at densities $\lesssim 5 \times 10^{18}\,\mathrm{cm}^{-3}$, pose a considerable experimental challenge. Table 4.1 summarizes the refractive indices of typical target gases.

Table 4.1. *Refractive indices for some gases at $\lambda_{probe} = 633\,nm$ wavelength under standard conditions, i.e. $p_0 = 101325\,Pa$, $T_0 = 273.15\,K$, from [35]*

Gas	$\eta - 1$
H_2	1.3888×10^{-4}
He	3.4879×10^{-5}
Ar	2.8106×10^{-4}

From Equation (2.20) and table Table 4.1, α_{He} can be approximated by:

$$\alpha_{He} \approx 2\epsilon_0(\eta - 1)\frac{kT_0}{p_0} = 2.2989 \times 10^{-41}\frac{\mathrm{A^2s^4}}{\mathrm{kg}} \tag{4.2}$$

where $p_0 = 101325\,\mathrm{Pa}$ and $T_0 = 273.15\,\mathrm{K}$ and k is the Boltzmann constant, which when put back into eqation 2.20 provides a typical value of

$$\eta(n = 5 \times 10^{18}\,\mathrm{cm}^{-3}) - 1 = 6.4908 \times 10^{-6} \tag{4.3}$$

and the phase shift of the probe beam experienced during $\Delta z = 1\,\mathrm{mm}$ is only:

$$\Delta\varphi = (\eta - 1)\,\vec{k}\hat{e}_z\,\Delta z = 0.0644 \tag{4.4}$$

for a probe wavelength of $\lambda_{probe} = 633\,\mathrm{nm}$. Evidently this places high demands on optical design and quality. However, the larger refractive indices of most other gases at common laser wavelengths alleviates this situation slightly. In Figure 4.2 the gas flow of argon, hydrogen and helium around a round obstacle (a $50\,\mu\mathrm{m}$ diameter steel wire) in a supersonic gas flow is compared. It can be seen that there are some qualitative differences in the fluid characteristics of these gases, regarding the gradients and the densities directly above the obstacle. Care must therefore be exercised when drawing conclusions from measurements of densities in gases with high values of $\eta - 1$ to predict the gas flow of an optically thinner gas.

4.2.1 The Normarski Interferometer

The type of interferometer preferably used by the author was a Normarski interferometer [36]. An illustration can be seen in Figure 4.3. A linearly polarized probe beam back-illuminates the

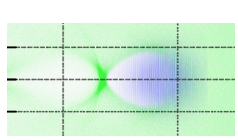

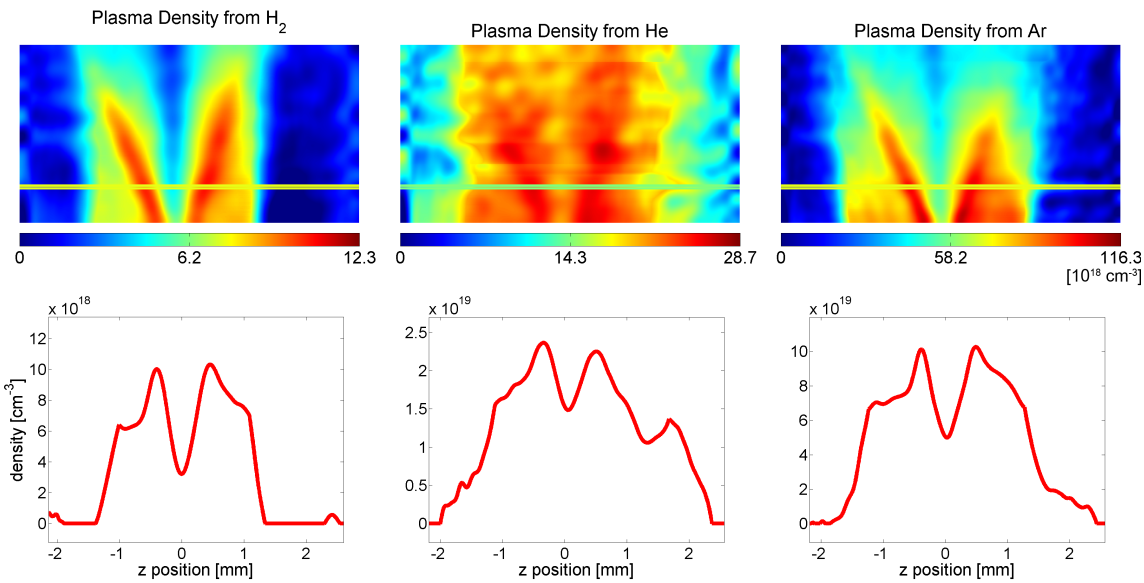

Figure 4.2. *Qualitative comparison of plasma densities obtainable with H_2, He and Ar flowing around a 50 μm diameter wire. The gas is released through a 3 mm supersonic nozzle with 10 bar backing pressure: Top: Density maps with diverging compression waves, caused by the wire. The plasma densities are for a fully ionised gas. Bottom: Lineout of plasma densities at laser interaction height. One can distinguish different fluid characteristics of the gases around the obstacle, leading to a variation in the relative depth of the density depletion centrally above the obstacle.*

target plane and while part of it traverses the phase object, and is thus refracted and delayed (see equation 4.4), the undisturbed part serves as a reference wave to produce the interferogram. It is thus desirable to place the phase object off-centre relative to the back-lighter. A lens system images the object plane onto a CCD.

However, prior to reaching the image plane, the probe light passes through a Wollaston prism [37]. The Wollaston prism (see Figure 4.5), consists of two birefringent crystals of the same material, which are oriented in such a way that the ordinary and extraordinary beam copropagate, but change role halfway through the prism at a diagonal interface. The change in refractive indices, from η_o to η_e and vice versa, deviates both beams with typical angles between 1^o and 5^o. This design provides symmetric splitting of the beams relative to the central optical axis . The spatial orientation of the index ellipsoid of the birefringent crystal and the orientation of the interface layer determine the fringe orientation, and together with the incoming polarization, the relative intensity between the reference and object waves. This is impor-

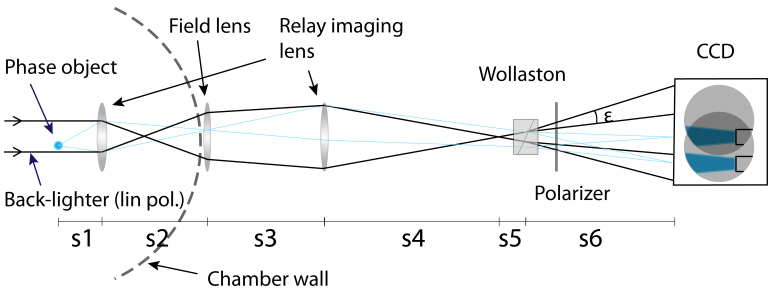

Figure 4.3. *Illustration of the Normarski interferometer used during the wire experiment (Paper* **V***), utilizing a calcite Wollaston prism with $\epsilon = 5^o$ splitting angle and 15×15 mm cross section. The fringe pattern occurs in the overlapping area on the CCD, while at the same time a shadowgraphic image can be obtained.*

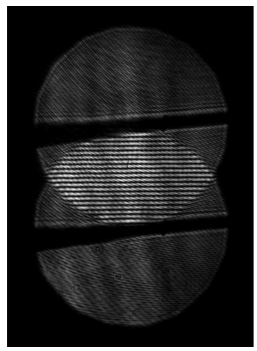

Figure 4.4. *The Wollaston prism produces two images of the same object, here a horizontal wire, which are orthogonally polarized relative to each other. The final polarizer (see Figure 4.3) projects the field onto the same polarization axis and interference fringes thus emerge in the overlapping region.*

tant to ensure good contrast, $\tilde{c} = \frac{I_{max}-I_{min}}{I_{max}+I_{min}}$, in the interferogram (the overlapping region in figure Figure 4.3). The transverse image separation, Δs, on the CCD is given by the divergence angle, ϵ, via [36]

$$\Delta s = 2 s_6 \tan \frac{\epsilon}{2} \tag{4.5}$$

The fraction of the image containing the phase object is superimposed on a spatially separated reference wave from the object plane having orthogonal polarization. A polarizer projects the object and reference waves onto the same polarization to produce the interferogram (see Figure 4.4). The fringe separation, δ, can be estimated by [36]

$$\delta \approx \frac{\lambda_{probe}\, s_6}{\epsilon\, s_5} \tag{4.6}$$

and should be well sampled by the pixel size ($\gtrsim 9$ pixels per fringe).

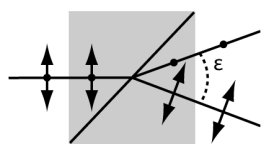

Figure 4.5. *Polarization-dependent beam path through a Wollaston prism.*

Given the interdependencies described above, interferometer design should provide a good compromise between factors such as the magnification and resolution of the imaging lens system, as well as the image separation and fringe separation produced by the Wollaston prism. This usually involves a trade-off between spatial and phase resolution. Low but noisy phase shifts, such as those produced by helium jets, may be made visible by lateral averaging, simultaneously reducing spatial resolution. However, phase maps may be averaged later in the evaluation process if the target remains stationary over several exposures, reducing noise and increasing phase sensitivity, while maintaining spatial resolution.

Pulsed interferometry requires adequate background suppression, as phase image acquisition takes place simultaneously with the main laser pulse interacting with the target. This is eas-

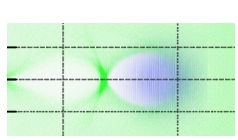

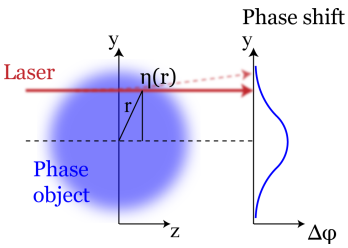

Figure 4.6. *A laser beam (red) probing the phase object (blue) from the left and being phase shifted. Given radial symmetry, radial information about the refractive index, $\eta(r)$, and plasma density, $n(r)$, can be retrieved via an Abel inversion.*

ily accomplished by laser line interference filters for the probe beam wavelength, which suppress the main pulse and plasma self-emission as long as $\lambda_{probe} \neq \lambda_{laser}$. Generally, this approach is rather sensitive to non-uniformities in the laser mode of the backlighter, but rather robust with regard to temporal overlap given sub-picosecond probe pulses.

A practical disadvantage of the Normarski interferometer is that only integrated phase shifts are obtained (see Figure 4.6). Tomography is often not an option as plasma densities are usually measured *in situ* and space is restricted in ongoing experiments. Furthermore, large-aperture Wollaston prisms are quite expensive, and placed close to the beam waist of the backlighter (see Figure 4.3) which gives risk for exceeding its damage threshold.

As laser beams are best described as spherical waves, different lateral positions of curved surfaces are superimposed in the image plane. The Normarski interferometer is not an autointerferometer, such as e.g. Mach Zehnder or Michelson interferometers [38], and may produce a systematic error in gas density measurements. This may be understood from the following. For part of the wave to be delayed, the phase fronts have to get curved, which inevitably alters the light propagation downstream through the optics. If the optics suffer from spatial inhomogenities they cause an additional phaseshift, encountered by the altered phase front only. This superimposes a systematic error on the measured total phase shift, which is now not only the phase shift of the phase object but also contains a contribution from non-perfectly formed lenses and windows. This is probably the cause of the inclined density plateau in the free-flow plasma density measurement depicted in Figure 5.3 in Chapter 5.

Abel Inversion

Given a density distribution such as that depicted in Figure 4.6, the integral phase shift, $\Delta\varphi$, can be calculated from

$$\Delta\varphi(y) = \int_s \vec{k}[\eta(\vec{r}) - 1]\, d\vec{s}, \text{ integrated along the path, s.} \quad (4.7)$$

Neglecting refraction of the probe beam (dashed red line in Figure 4.6) and assuming radial symmetry, i.e. $\eta(\vec{r}) = \eta(r = \sqrt{z^2 + y^2})$, gives

$$\Delta\varphi(y) = \int_{-\infty}^{\infty} k_z[\eta\left(\sqrt{z^2 + y^2}\right) - 1]\, dz \quad (4.8)$$

$$= 2\int_{y}^{\infty} k_z[\eta(r) - 1]\frac{dz}{dr}dr \quad (4.9)$$

$$\overset{P.I.}{=} \int_{y}^{\infty} k_z[\eta'(r)]\sqrt{r^2 - y^2}\, dr \quad (4.10)$$

or

$$\frac{d}{dy}\left[\Delta\varphi(y)\right] = \Delta\varphi'(y) = -y\int_y^\infty \frac{k_z\eta'(r)}{\sqrt{r^2-y^2}}\,dr \tag{4.11}$$

The inverse Abel transform is given by

$$\eta(r) - 1 = -\frac{1}{\pi}\int_r^\infty \Delta\varphi'(y)\frac{1}{\sqrt{y^2-r^2}}\,dy \tag{4.12}$$

$$= \int_r^\infty\int_y^\infty \frac{yk_z\eta'(\tilde{r})}{\pi\sqrt{\tilde{r}^2-y^2}\sqrt{y^2-r^2}}\,d\tilde{r}dy \tag{4.13}$$

The mathematical proof involves Fubini's theorem for integrals.

Knowing $\eta(r)$, the radial plasma density $n(r)$ can be deduced from Equation (2.27). This is a valid approach if cylindrical symmetry is applicable. However, in the special case of a linear obstacle introduced into the supersonic gas flow, an Abel inversion may not be applied as this destroys the symmetry. Instead, reasonable assumptions about the optical path length and gas density distribution provide the basis for a qualified estimate of the plasma densities. This was done in the study reported in Paper **V** and illustrated in Figure 4.2, where a wire disturbs the gas flow from a supersonic nozzle.

The Normarski Interferometer and its Potential, an Outlook

In one study, magnetic fields in the wake of the laser pulse inside a plasma were investigated by means of a femtosecond backlighter, subjected to Faraday rotation and the Cotton-Mouton effect [39, 40]. This was done using polarimetry (Section 4.3). In this approach only the Faraday effect and two Stokes parameters were taken into account to provide an educated guess concerning the encountered field strength, B, as the rotation angle, θ, is proportional to the propagation length, $\int_s ds$, the field $\vec{B}$, and the plasma density n; with the last two being unknown:

$$\theta \propto \int_s n\vec{B}ds \text{ , along the beam path, s} \tag{4.14}$$

The goal must thus be to measure magnetic fields and density at the same time. Potentially, the Normarski interferometer allows this to be done in a single exposure.

Generally, a Normarski interferometer is utilized to interferometrically infer densities, $n(\vec{r})$. This information is extracted from the fringe pattern alone and the raw data are usually preprocessed by a low-pass Fourier filter in such a way that most intensity modulations, except of course the fringe pattern, are eliminated prior to unwrapping the phase. Unfortunately, this also eliminates information about how well the polarization of the back-lighter could be

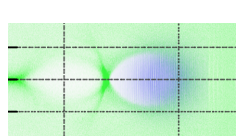

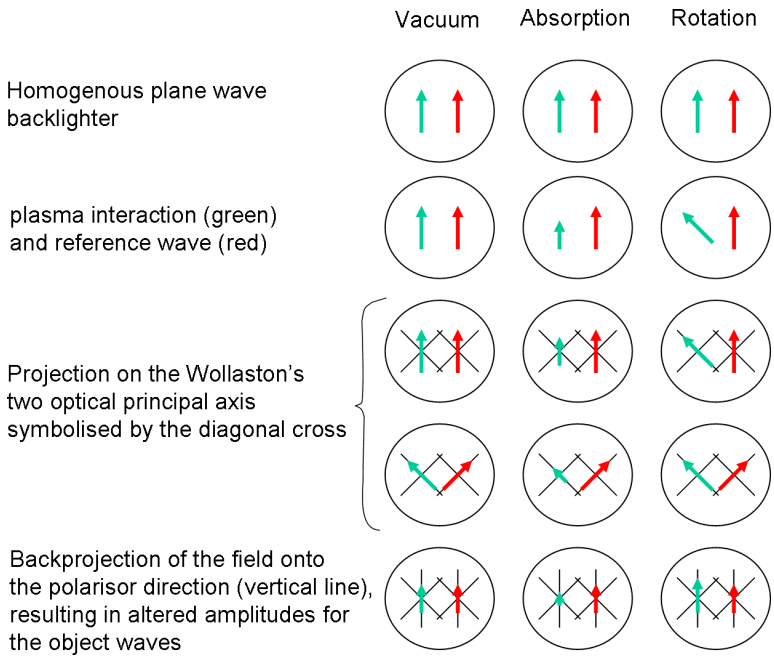

Figure 4.7. *Illustration of how absorption and Faraday rotation will affect contrast: red arrows depict the polarization and amplitude of the reference wave, while green arrows represent the object wave. Both absorption and Faraday rotation decrease the contrast in the interferogram as the amplitudes of the object wave are no longer equal to those of the reference wave.*

maintained while traversing the plasma. This can be understood in the following way. The Wollaston prism projects the incoming polarization onto its two principal axes, which are then superimposed and projected onto the final polarizer axis. Assume now that the reference wave, originating from a spatially different position in the object plane, always arrives with the same amplitude. The contrast, $\tilde{c}$, of the interferogram will be at its best if both waves experience a relative delay only, and the object wave does not experience any absorption. If the object wave suffers from absorption, the contrast will be decreased. However, the same is true if its polarization is rotated. This is illustrated and compared in Figure 4.7. Assuming a pure phase object with negligible absorption, which is commonly the case for low-density plasmas, information on the magnetic field is concealed in the contrast of the interferogram.

A Normarski-based plasma interferometer with high spatial resolution and a very homogeneous pulsed back-lighter can be used to obtain an interferogram containing information about both the

density, n, which will reveal itself as a fringe shift, and the Faraday rotation, which will affect the contrast, $\tilde{c}$. A rectangular homogeneous gas nozzle that covers the entire probe beam, and high spatial resolution in combination with an Abel inversion, may in the case of cylindrical symmetry for the produced plasma, have the potential to simultaneously provide information about n, B and l with high temporal resolution, and thus provide a more accurate measurement of magnetic fields such as those encountered in the wake of a laser pulse.

Conducting measurements on both fringe shift and contrast will require very flat phase fronts. Inserting spatial filters for the probe beam in vacuum, shortly before the target, and polarizers prior to the interaction point, together with a relatively small field of view, may help produce the required homogeneous back-lighter, making such an experiment feasible.

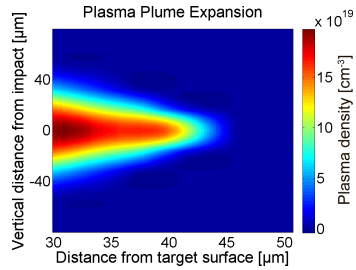

Figure 4.10. *Abel-reconstructed plasma density in the expanding plasma plume. The two-dimensional map shows a plane through the axis on which the laser impinged on the target.*

Plasma Expansion on Solid Surfaces

During a study of electron transport through various allotropes of carbon, presented in Paper **II**, Normarski interferometers were used to study plasma expansion at the front of the target. Besides employing mode cleaning of the back-lighter and double interference filters (Figure 4.9), care had to be taken not to exceed the destruction threshold of the Wollaston prism. Cylindrical symmetry allows for a density reconstruction by an Abel inversion, shown in Figures 4.10 and 4.11. A typical interferogram from a laser-solid interaction obtained during this experimental campaign is shown in Figure 4.8.

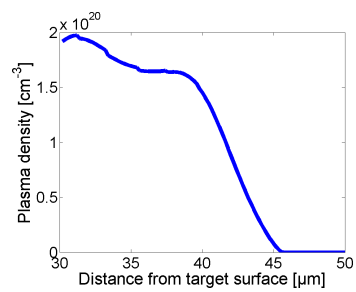

Figure 4.11. *Lineout from Figure 4.10 on the optical axis.*

4.3 Polarimetry

In an ultra-intense laser-solid interaction, extremely high magnetic fields are produced in the coronal plasma at the front of as well as inside the target. (The term coronal plasma is a synonym for the previously mentioned expanding plasma plume on the laser-irradiated side and depicted in Figure 4.8.) These magnetic fields have a major influence on electron transport through the target and affect electron dynamics on the target surface. An understanding of the surface fields may prove important for the development of *smart target designs*. Experimentally, it enables astrophysical conditions to be created and studied in a laboratory system as the fields produced reach $\sim 10\,\mathrm{kT}$, which is comparable to field strengths prevailing on white dwarfs [41].
To probe these fields, self-generated, high-order harmonics can be used. These are produced at the critical density surface, where the pump laser pulse is reflected ($n_c \approx 2 \times 10^{21}\,\mathrm{cm}^{-3}$ for $\lambda_l = 800\,\mathrm{nm}$). Their initial polarization is equal to that of the driving pulse in the case of p-polarised incident light. For

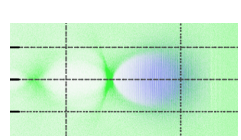

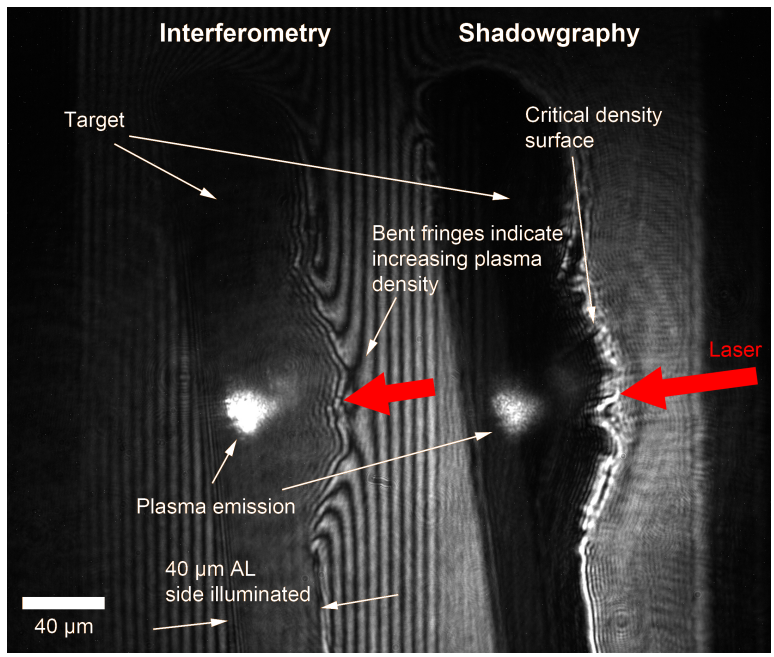

Figure 4.8. *Combined interferometry (left) and shadowgraphy (right) achieved using an off-centred path of the probe beam over the target, as depicted in Figure 4.3, obtained at the Rutherford Appleton Laboratory. A frequency-doubled 527 nm back-lighter was used. Vertical apertures and a large CCD detector allowed simultaneous acquisition of an interferometry (left) and shadowgraphy (right) image of the same object, which is a small, only 40 µm thick Al foil, which served as the target. The probe laser traverses parallel to the target surface at a given delay after the main interaction, hence a plasma has been formed on the front of the laser-irradiated target (right side), which expands into vacuum. In the interferometry region, bent fringes indicate increasing plasma density when approaching the target surface from the right. However, at increasingly higher densities left of the critical density surface, n_c, where the refractive index of the plasma becomes imaginary, light cannot penetrate the plasma plume. This border can be seen more clearly in the shadowgraphic image on the right.*

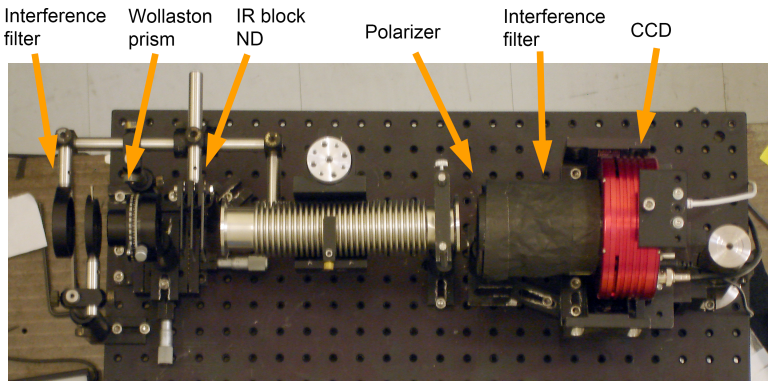

Figure 4.9. *Interferometry set-up used to aquire the interferogram and shadowgraphic image depicted in Figure 4.10. IR: infra-red, ND: neutral density.*

s-polarization, p-polarized (even) and s-polarized (odd) harmonics are generated [42]. As mentioned in Section 2.2 the refractive index, η, is influenced by magnetic fields via μ and the $\vec{v} \times \vec{B}$ force. This causes a change in the polarization state of light traversing a magnetized plasma.

Magnetic field strengths in the underdense regime of a LWFA, at plasma densities of $\sim 5 \times 10^{18}\,\mathrm{cm}^{-3}$, have been estimated by Kaluza *et al.* [43], who assessed magnetic field strengths around the injected electron bunch inside a plasma bubble (see Chapter 5). Their experiment was reconstructed at the LLC, and fields of the order 100 T were estimated. As described by Equation (4.14), the Faraday effect is more easily observed when working close to the overdense regime, where higher plasma densities give rise to large changes in polarization over short ranges. The experiment presented in Paper **IV** was conducted at densities $\approx 10^{21}\,\mathrm{cm}^{-3}$, i.e., ≈ 3 orders of magnitude higher than those in the underdense LWFA regime. The refractive index of a magnetized plasma may even inhibit the escape of a harmonic when a certain threshold field strength is exceeded, seen as cut-off in the experiment.

The light intensity and its polarization are well defined by a set of four parameters, contained in the Stokes vector, $\vec{S}$ [44].

$$\vec{S} = J \begin{pmatrix} 1 \\ s_1 \\ s_2 \\ s_3 \end{pmatrix} \begin{matrix} \text{lin. pol. in x} \\ \text{lin. pol. } 45^o \\ \text{circ. pol.} \end{matrix} = J \begin{pmatrix} 1 \\ \cos(2\chi)\cos(2\theta) \\ \cos(2\chi)\sin(2\theta) \\ \sin(2\chi) \end{pmatrix} \quad (4.15)$$

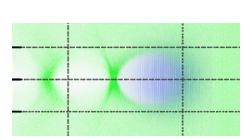

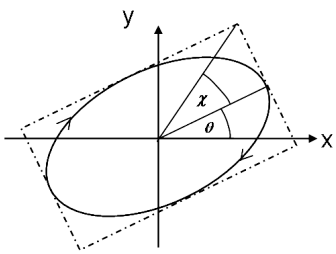

Figure 4.12. *Definition of χ and θ in the plane of polarization orthogonal to the direction of laser propagation*

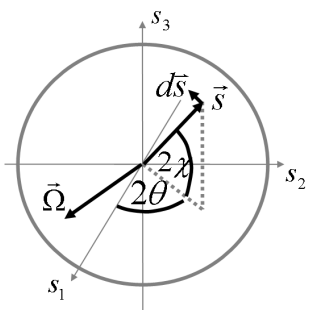

Figure 4.13. *Poincaré sphere with normalized vector $\vec{s}$ indicating the light's polarization state. Principal axis $\vec{\Omega}$ around which the vector $\vec{s}$ is moving in the direction of $d\vec{s}$*

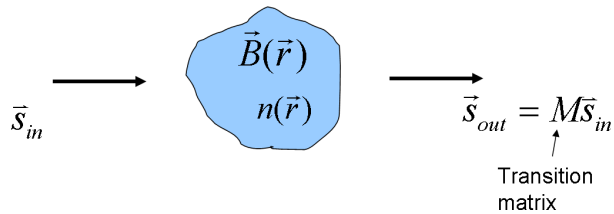

Figure 4.14. *While traversing a plasma, the polarization state of the probe light is changed. Mathematically this is described by the transition matrix $\boldsymbol{M}$.*

The angles are defined in Figure 4.13 where x and y are axes orthogonal to the probe light propagation direction along z. However, in the experiment, only the normalized reduced Stokes vector, $\vec{s}$, is of interest.

$$\vec{S} = J \begin{pmatrix} 1 \\ \vec{s} \end{pmatrix} \quad \text{reduced Stokes vector} \tag{4.16}$$

$$\vec{s} = s_1^2 + s_2^2 + s_3^2 = 1 \tag{4.17}$$

When light travels through a magnetized plasma, the change in polarization can be described as the rotation of its polarization vector around a principal axis, $\Omega(\vec{r})$, on the Poincaré sphere (see Figure 4.13), following the equation of motion [45]:

$$\frac{d\vec{s}(z)}{dz} = \vec{\Omega}(z) \times \vec{s}(z) \text{ with z: propagation axis of light} \tag{4.18}$$

$$\vec{\Omega} = \frac{\omega_p^2}{2c\omega^3(1-\frac{\omega_c^2}{\omega^2})} \begin{pmatrix} \left(\frac{e}{m}\right)^2 (B_x^2 - B_y^2) \\ \left(\frac{e}{m}\right)^2 2B_x B_y \\ 2\omega \frac{e}{m} B_z \end{pmatrix} \tag{4.19}$$

where the cyclotron frequency is $\omega_c = \frac{e}{m}|\vec{B}|$, ω is the frequency of the probing wavelength and ω_p is the plasma frequency defined in Equation (2.25). When starting out with horizontally polarized light, i.e. $\vec{s} = (1\,0\,0)$, the Faraday effect gives rise to a movement of $\vec{s}$ around the s_3, axis while the Cotton-Mouton effect causes a movement around s_2.

$\Omega(\vec{r})$ depends on the local magnetic fields and on the plasma density n through the local plasma frequency $\omega_p(\vec{r})$. Having a good idea about the coronal plasma density distribution, and knowledge of the initial and final polarization states, $\vec{s}_{in}$ and $\vec{s}_{out} = \mathbf{M}\vec{s}_{in}$, allows for a qualified guess regarding the transition matrix, $\mathbf{M}$ (see Figure 4.14), taking field structure, strength and scale lengths into

account. **M** may have to be modified iteratively until observations of $\vec{s}_{out}$ match the physical picture for given $\vec{s}_{in}$ and n.

Various effects taking place during laser-solid interactions, in particular temperature and density gradients, the fast electron current produced and radiation pressure, give rise to cylindrical and azimuthal fields. Coronal cylindrical magnetic fields were investigated (Paper **IV**) by measuring Stokes parameters temporally and spatially integrated for individual higher harmonics emitted along a narrow acceptance angle for the polarimetry set-up. Higher harmonics were observed, escaping in the direction of specular reflection of the incoming laser pulse. Shadowgraphy and interferometry provide density information. Using this information, a qualified estimate regarding the magnetic fields can be made, to suggest a transition matrix, when traversing the coronal plasma.

A drawback of this technique is the small collection angle of the polarimeter. Imaging a larger spatial angle into different channels of the polarimeter, may potentially provide a more accurate picture of the prevailing magnetic fields.

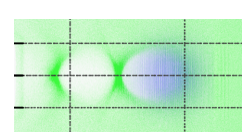

Chapter 5

Electron Acceleration

Laser-driven electron accelerators make use of the extremely strong oscillating electric fields, $\sim 10\,\mathrm{TV/m}$, attainable at the focus of a high-power femtosecond laser system (see Sections 2.3 and 2.4). These are transformed into longitudinal quasistatic fields that can effectively accelerate electrons. They should be quasistatic in a comoving reference frame for the accelerated particles and ideally be accompanied by focusing fields that counteract the Coulomb explosion of a bunch of accelerating electrons. This field rectification can be achieved when focusing the laser pulse into a gas medium, such as hydrogen or helium. The rising intensity prior to the main pulse (see Section 3.3) quickly ionizes the target and forms a plasma of low enough density, typically $\sim 10^{18}\,\mathrm{cm}^{-3}$, that its refractive index is predominantly real for a typical laser wavelength, $\sim 1\,\mu\mathrm{m}$, allowing the pulse to propagate.

In combination with the remaining charge background of the much heavier ions, which are almost unaffected by the ponderomotive force, the blow-out of electrons sets up space-charge fields that force the electrons into orbits and start a plasma oscillations in the wake of the pulse. In a constant-density plasma, this density wave propagates with a phase velocity, v_p, equal to the group velocity of the laser pulse, $v_p = v_g \lessapprox c$, close to the speed of light in vacuum, and contains phases with both accelerating and focusing fields. This provides the accelerating structure for electrons in a plasma, known as laser wakefield acceleration (LWFA). An illustration of this plasma oscillation driven by a high-intensity laser pulse, $a_0 \approx 1$, obtained from a three-dimensional particle in cell (PIC) simulation [46] is given in Figure 5.1. Extreme field strengths, $\sim 100\,\mathrm{GV/m}$, are reached in the wake oscillation, several orders of magnitude higher than those attainable with metallic structures in vacuum, which suffer from electric breakdown when exposed to fields $\gtrsim 100\,\mathrm{MV/m}$. This gives laser wakefield accel-

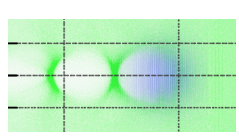

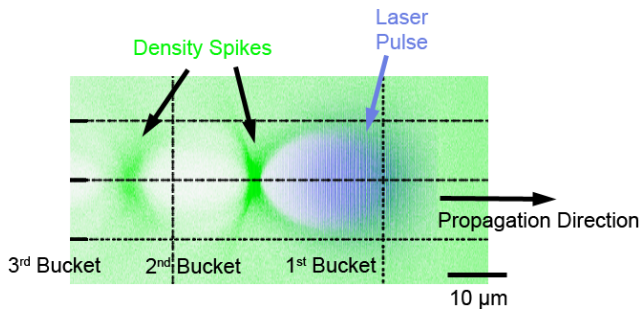

Figure 5.1. *Wake oscillation trailing the driving pulse. Blue shading indictates the electric field of the laser pulse driving the trailing plasma wave, while different shades of green visualize the electron plasma density. The entire structure moves from left to right at a speed close to the speed of light. Radial electric fields have both a focusing and accelerating effect on a test particle placed in a bucket.*

erators an advantage over conventional accelerators that employ radio-frequency cavities.

To actually accelerate electrons, they must be relocated or created in phase space, so that they end up in the accelerating and focusing phase of the wake oscillation and gain energy. When driving a highly nonlinear plasma wave, electron densities may increase to such a degree that the plasma wave becomes nonlinear and breaks, which injects a charge of $1 - 100\,\mathrm{pC}$ into the accelerating phase. This is called self-injection, and is the simplest experimental approach as it does not require any additional equipment apart from the driving laser pulse and the target gas to trigger injection. The resulting electron spectra are usually broadband, with an almost thermal distribution.

A very interesting regime in this context is the bubble regime [47]. Here, a high-intensity laser pulse resonantly drives a highly nonlinear plasma wave, i.e. $\lambda_p \approx 2c\tau_l$ and $a_0 \gtrsim 1$. This can totally evacuate an almost spherical region behind the laser pulse front of electrons. A density structure emerges, called a bubble. Electron injection via self-injection at densities just above the threshold density was used to produce the first monoenergetic spectra in 2004 [48–50].

The electron injection mechanism is crucial for the quality of laser-accelerated electron beams, regarding brightness, divergence and emittance. Various techniques have been proposed and investigated over the years to control this process externally, leading to superior performance of LWFA, but with increased complexity. The most important examples are colliding pulse techniques [51–54], the use of density gradients [55, 56], and ionization injection [57, 58]. These techniques can provide tunable quasi-

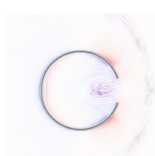

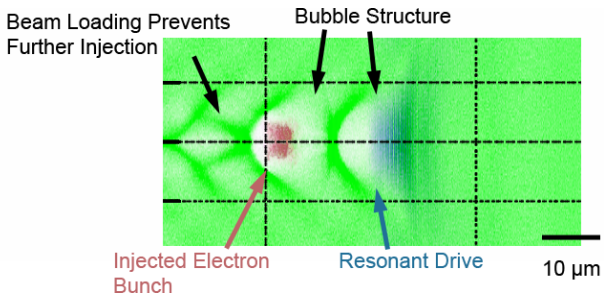

Figure 5.2. *Plasma wake oscillation with colours as in Figure 5.1. Here, electrons have been injected into the second bucket, and the laser pulse drives the plasma wave resonantly.*

monoenergetic spectra, with spreads $\Delta E/E \lesssim 4\,\%$ and divergences $\lesssim 4\,\mathrm{mrad}$. An example from simulations is given in Figure 5.2, with the bubble structure clearly visible. Due to the electron momentum, several cavities will form behind the first bubble, called buckets. In this figure, an electron bunch has been injected into the second bucket using the density gradient technique (Paper **V**).

5.1 Laser Propagation in an Underdense Plasma

Ionization at the rising edge of the laser pulse leads to the formation of new frequency components in the spectrum, comprising the laser pulse. This is called ionization blue shift and was discussed in Section 2.6. With ultra-intense lasers, producing intensities on the target of $\sim 10^{19}\,\mathrm{W/cm^2}$ (Section 2.4), the ponderomotive force, $\vec{F}_{pond}$ (Section 2.7), drives electrons away from the region of highest intensity. The resulting decrease in plasma density, n, close to the maximum intensity of the laser pulse produces red frequency components in accordance with Equation (2.72). In addition, as the back of the pulse effectively propagates in vacuum, while the front travels with at v_g, which is slightly less than c, this allows self-compression of the laser pulse in the time domain down to its Fourier limit, which, after spectral broadening, can be shorter than that upon entering the plasma.

The laser pulse from the CPA chain is usually compressed to its Fourier limit, which gives the shortest pulses in vacuum. However, there are qualitative differences in the laser-plasma interaction if a minor chirp is imposed on the laser pulse. In the case of an up-chirped pulse, i.e. red frequency components at the leading edge of the pulse, the red shift, which occurs at higher laser in-

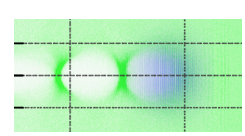

tensities than the ionization blue shift, may produce new, strong frequency components outside the pulse spectrum. In contrast, a down-chirped pulse, whose blue components at the front produce red-shifted frequencies may still lie within the overall pulse spectral envelope and lead to interference. Thus, a positively chirped pulse may lead to an enhanced self-compression. The resulting lowered threshold pulse energy for electron injection was observed experimentally, as discussed in Paper **VII**.

Due to the high electric field strengths of the laser pulse, the electrons' response is ultra-relativistic, i.e. they perform orbits with $\gamma \gg 1$. This enables relativistic guiding over several Rayleigh lengths of the focusing optics being used. However, after a certain distance, continuous energy transfer to the plasma wave and diffraction losses (erosion) at the pulse front deplete the laser energy so that diffraction sets in after the depletion length, L_{dpl}. As the plasma wave propagates with a velocity $v_p \lesssim c$, ultra-relativistic electrons outrun the accelerating phase of the plasma wave after the dephasing length, L_d (Section 2.5), where they are decelerated again. Both, L_d and L_{dpl} thus set an upper limit on the acceleration length and maximum electron energy that can be achieved using LWFA.

The efficiency of energy transfer from the laser to the wake oscillation can be improved by guiding the laser externally, and recollecting diffracted laser energy in the wings of the laser pulse, where the intensity is insufficient to lead to relativistic self-focusing, as the critical power for relativistic self-focusing depends on the plasma density, $P_c \propto 1/n$ [5, 59]. External guiding and a lower density can enable acceleration to higher peak electron energies, as discussed in Section 2.5. This can be accomplished either by the use of a plasma discharge capillary [60–62], which after discharge and hydrodynamic expansion creates a guiding index structure, or by means of a gas-filled dielectric glass capillary, where the pulse is coupled to the hollow core and guided by internal Fresnel reflection over several centimetres Papers **IX** - **XII**.

5.2 Shock-Wave Density-Modulated Gas Jets

A novel approach to electron injection and acceleration, as an alternative to wavebreaking and self-injection in a nonlinear plasma wave, is described in Paper **V**. This utilizes a wire, which is introduced into the flow of a supersonic gas jet. This produces shock and expansion waves originating from the flow around the obstacle, modulating plasma densities and producing sharp density gradients. For this novel acceleration scheme to work, the densities along the optical axis must be tailored to promote the physical mechanisms described in the paper, thus transforming the free-flow constant density plateau of a gas jet into a *smart target de-*

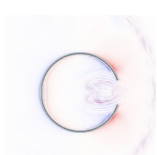

sign. As densities and distances can be adjusted to the experimental needs, this increases stability and control over the entire accelerating mechanism compared to self-injection.

Plasma density profiles were inferred interferometrically using hydrogen as target gas (see Figure 5.4) with a 3 mm supersonic nozzle. Examples are given in Figure 5.3. These measurements reveal downward density gradients over $\lesssim 0.3$ mm from region I to region II and a relatively short (~ 0.1 mm) density-diluted area (region II) centrally above the wire. The density lineouts were collected on the optical axis, 500 μm above the wire. However, the modelled plasma densities in b) - d) are qualified guesses, obtained by extrapolating two-dimensional simulation results [63]. Note that the 3 mm gas jet used in the experiments presented in Paper **V**, has a much lower temperature

$$T_{jet} = \left(\frac{n_I}{n_{backing}}\right)^{2/f} T_{backing} \tag{5.1}$$

than the simulations. f denotes the degree of freedom of the gas species, which in turn depends on the temperature, and n_I and $n_{backing}$ are the *gas* densities in region I and for the backing pressure, respectively. The speed of sound in a gas is given by:

$$c = \sqrt{(1+2/f)\frac{p}{\varrho}} \tag{5.2}$$

where p denotes pressure and the mass density is given by $\varrho = 2M_p n_{gas}$ [64]. Using the equation for an ideal gas, $p = n_{gas}kT$, results in:

$$c = \sqrt{(1+2/f)\frac{kT}{2M_p}} \tag{5.3}$$

The average molecular speed in hydrogen gas is given by:

$$\overline{v} = \sqrt{\frac{8kT}{\pi 2M_p}} \tag{5.4}$$

The vertical jet speed, estimated from the cone angle with a 25 μm diameter wire in the gas flow, and the transverse expansion $\sim \overline{v}$ are given in Table 5.1 below. The values in Table 5.1 indicate that the expansion wave should quickly fill the region above the wire, allowing mainly the the outwards shock fronts to be encountered on the optical axis. Distances in the real world experiment exceed the simulation box, but the ~ 10 times lower temperatures might preserve the sharp density transitions to be encountered by the laser even $\approx 500\,\mu$m above the obstacle.

Experimentally it was found that shock wave divergence angle and density ramps were symmetric as long as the wire was

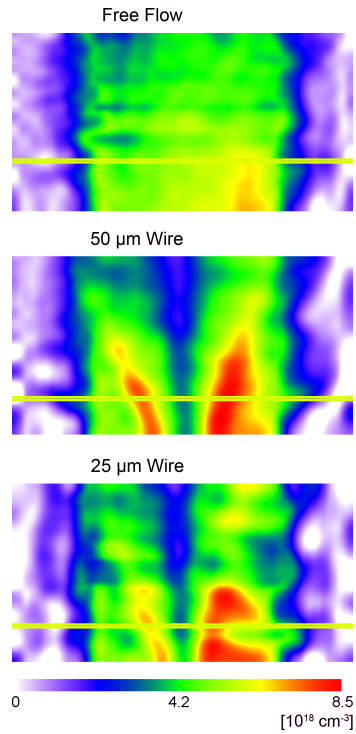

Figure 5.4. *Hydrogen flow from a 3 mm supersonic nozzle at 9 bar backing pressure in free flow (top) and around wires with different diameters (middle, bottom). The horizontal line represents the optical axis of the laser interaction with the densities plotted in Figure 5.3.*

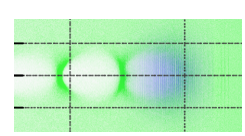

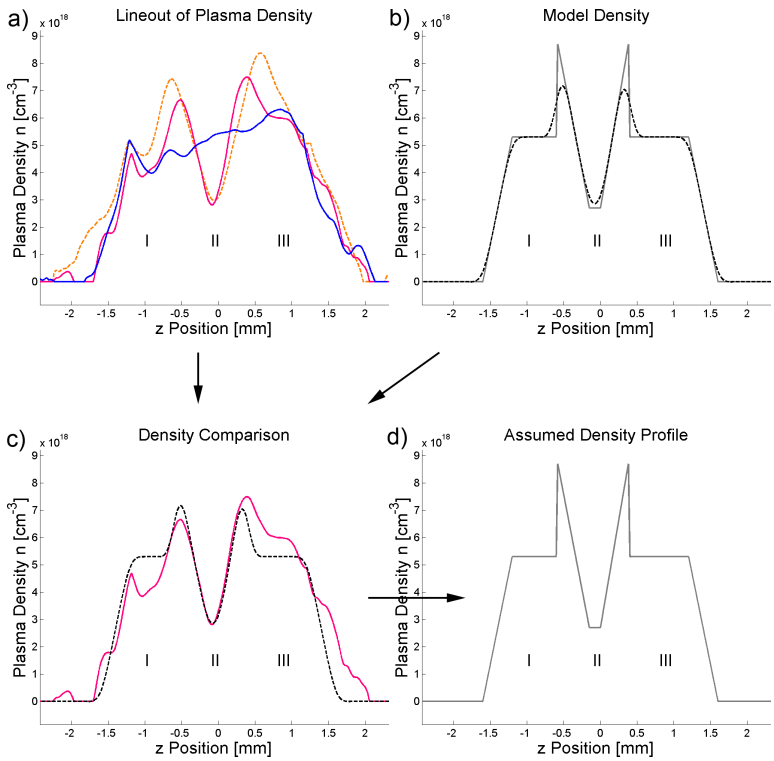

Figure 5.3. *a) Measured plasma densities along the laser axis of the undisturbed jet (blue line), after the introduction of a 50 μm diameter wire (dashed amber line) and a 25 μm wire (solid magenta line), $\approx$ 500 μm below the axis. Note the decreased length at FWHM of the density-diluted region II, which is $\approx$ 440 μm with the 25 μm wire and $\approx$ 610 μm with the 50 μm wire. All interferograms were recorded using H_2 at 9 bar backing pressure and a 3 mm supersonic nozzle. b) Broken line model density (grey solid line), motivated by simulations [63]. Subjecting this theoretical density distribution to a blur corresponding to the experimental resolution limitations in the measurements, provides an apparent density as depicted by the black dashed curve. c) Comparison between blurred model density and measured density for the 25 μm wire. d) shows the density used as input data for the PIC simulations, presented in Paper* **V**.

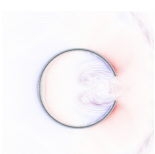

Table 5.1: Flow speed and average relative particle speed in a Mach 3 hydrogen gas jet assuming $n_I = 0.5 \times 5.3 \times 10^{18}\,\mathrm{cm}^{-3}$ and $T_{backing} = 300\,\mathrm{K}$.

	T_{jet}	$3 \times c$ [m/s]	$\overline{v}$ [m/s]	ratio $3c/\overline{v}$
$f = 3$	13	901	371	2.4
$f = 5$	46	1544	694	2.2

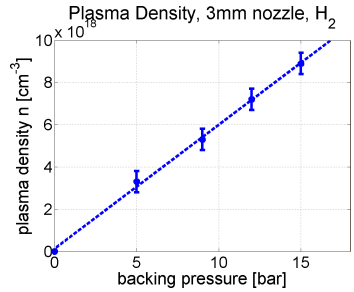

Figure 5.5. *Plasma density n as a function of backing pressure. The measurement is valid for a free-flow jet or plateau regions I and III with a $\leqq 50\,\mu$m diameter wire in place.*

$\leqq 0.5\,$mm off the nozzle centre. Wire thickness affects the amount of gas that is redirected, and alters the divergence angle of the shock fronts, even if the Mach number is kept constant. The distance between the wire and optical axis affects the density ratio between region I and II, and the steepness of the gradients, which tend to become less steep with increasing distance. Due to the diverging shock cone, the intersection point of the shock with the laser axis is also affected. This further changes the length of the density-diluted region II, that has to be traversed by the laser, possibly promoting diffraction, which cannot be counteracted by relativistic self-focusing. The density on the optical axis scales linearly with packing pressure (see Figure 5.5) and has a smaller impact on cone angle, and thus on the length of region II. Plasma density also affects the nonlinear pulse evolution prior to reaching the shock fronts, as well as the intersection point between the shock wave and plasma channel.

The spatial resolution in Figures 5.4 is limited to $\sim 110\,\mu$m, and the measured density gradients may therefore be underestimated. The low spatial resolution may be due to low phase shifts, a short depth of focus of the imaging set-up and phase distortions due to low-quality chamber windows, which together smear out the phase information.

From Figure 5.3, densities of $n_1 = 5.3 \times 10^{18}\,\mathrm{cm}^{-3}$ for the plateau regions I and III and $n_2 = 2.8 \times 10^{18}\,\mathrm{cm}^{-3}$ decreasing over $L_{\Delta n} = 190\,\mu$m were estimated. The densities were calculated from the refractive index using Equation (2.20) with $\alpha = 1.01 \times 10^{-40}\,\frac{\mathrm{A}^2\mathrm{s}^4}{\mathrm{kg}}$ (see Section 4.2).

The kinetic energy of the electrons can be estimated integrating the ponderomotive force $\vec{F}_{pond}$ (Equation (2.81)) of the laser over the spot size r_0 (Equation (2.37)) at the focus.

Substituting the field with the intensity, gives the ponderomotive force as:

$$|\vec{F}_{pond}| \approx \frac{e^2}{2m\omega_{laser}^2} \frac{I_{max}}{r_0 c \epsilon_0} \tag{5.5}$$

Together with a known intensity, $I_{max} = 1.4 \times 10^{19}\,\mathrm{W/cm}^2$ ($f/20$ numerical aperture, $E = 1\,$J, $\tau_l = 42\,$fs), an electron fluid energy can be calculated via $E_{kin} = \int_s \vec{F}_{pond}(\vec{r})ds \approx |\vec{F}_{pond}|r_0 = 820\,$keV,

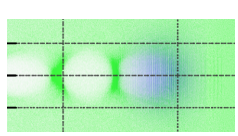

which gives

$$\beta_e = \sqrt{1 - \frac{1}{\left(\frac{E_{kin}}{E_0} + 1\right)^2}} \tag{5.6}$$

$\Rightarrow \beta_e = 0.92$ and $\gamma = 2.6$, which in turn leads to a plasma wavelength $\lambda_p = 2\pi \frac{v_g}{\omega_p} \approx \frac{2\pi c}{\omega_p} = 32\,\mu$m in region II, where trapping occurs. Inserting this into Equation (2.85) gives:

$$\xi_e = \frac{2n_2 L_{\Delta n}}{n_1 - n_2}\left(1 - \frac{1}{\beta_e}\right) \tag{5.7}$$

$$= -1.1\,\lambda_p \tag{5.8}$$

The above calculations indicate that, with the 25 μm diameter wire, injection could occur in the second bucket. However, transitions $< 170\,\mu$m, or a higher intensity due to relativistic self-focusing and compression inside the plasma should facilitate earlier injection.

To ensure that ionization injection due to laser ablation from the wire is not responsible for the observed electron injection and resulting beams, investigations were performed with the wire positioned at the optimum working distance but above the plasma channel (PC). No electron beams were seen above 29 MeV, which is the lowest energy detectable by of the spectrometer used. Table 5.2 summarizes the parameter scan conducted for Paper **V**.

Table 5.2: Scanned parameter space ($h = 0$ mm corresponds to plasma channel (PC) height and $z = 0$ mm coincides with the centre of the nozzle.)

Scan	**Const. parameters**
$300\,\mu\text{m} \geq d \geq 25\,\mu\text{m}$	*None*
$-0.65\,\text{mm} \leq h \leq -0.32\,\text{mm}$ $h = 0.50\,\text{mm}$ (above PC)	z_{opt}, bp_{opt}, $d = 25\,\mu$m
$-0.16\,\text{mm} \leq z \leq 0.39\,\text{mm}$	h_{opt}, bp_{opt}, $d = 25\,\mu$m
$8\,\text{bar} \leq p_{backing} \leq 12\,\text{bar}$	z_{opt}, h_{opt}, $d = 25\,\mu$m

Scanning along the optical axis (z-axis) reveals that the production of electron beams is in an $\approx 200\,\mu$m wide window, and is highly sensitive to the position of the wire (see Figure 5.6a). The optimum working position of the wire along the axis is influenced by laser performance. An injection probability over 95 % was obtained after fine-tuning of experimental parameters such as the vertical wire position (0.5 mm below the optical axis), backing pressure ($p_{backing\ opt} \approx 9$ bar) and wire diameter $d_{opt} = 25\,\mu$m). Figure 5.6b shows typical spectra obtained at different wire z-positions. Spectra at higher energies correspond to earlier injection and lower values of z.

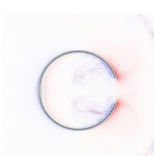

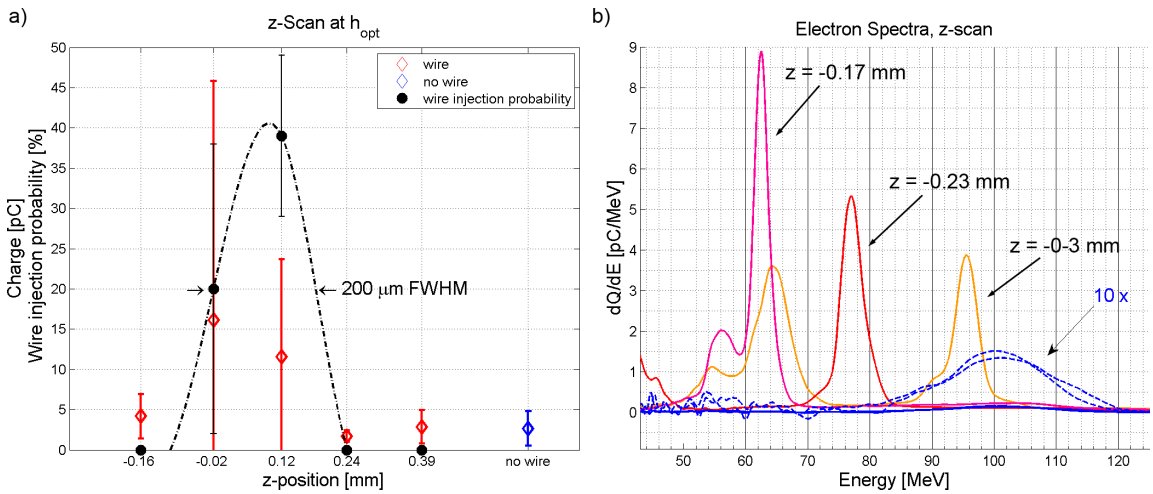

Figure 5.6. *a) Integrated charge (diamonds) and probability of wire-triggered injection (black dots) during a scan of wire position along the z-direction. Error bars indicate the standard deviation. b) Electron spectra as a function of z-position of the wire (magenta, red, amber) and without the wire (blue). Note the relative spread of only* $\Delta E/E \approx 4\,\%$*. However, spectromerter dispersion convoluted with an electron beam divergence of* ≈ 4 *mrad alone produces an apparent spread of* $\Delta E/E \approx 4\,\%$*, thus it is resonable to expect the real spread to be* $\Delta E/E \lesssim 1\,\%$*.*

5.2.1 Simulations

To study the effect of double density ramps on laser evolution, electron injection and acceleration, three-dimensional PIC simulations were carried out by colleagues at Umeå University. They predicted that in region I, no longitudinal or transverse wavebreaking would occur at the densities in question and that the injection scheme would not be particularly sensitive to the actual position along the z-axis as long as the wire is placed after the pulse has self-focused and self-compressed. However, in a real experiment imperfections in the nozzle and irregularities in the gas flow, as well as target gas impurities may still lead to electron injection. This may explain the narrow window seen in Figure 5.6a.

This thesis features two flip book movies. Frames from the simulation representing different times, are printed in the lower right corner of odd pages in this thesis, next to the page number. As in Figure 5.1, various shades of green represent the plasma density and blue represents the laser field driving the plasma wave. The laser pulse, which enters from the left and moves towards the right, is observed in a comoving reference frame once positioned in the middle of the simulation box. Quickly flipping through the pages while observing the small inset gives an intuitive picture

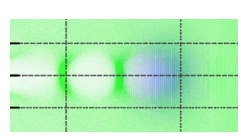

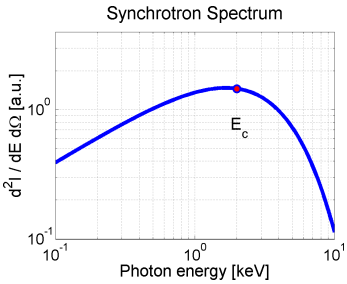

Figure 5.7. *Synchrotron spectrum with a critical energy $E_c = 2\,keV$.*

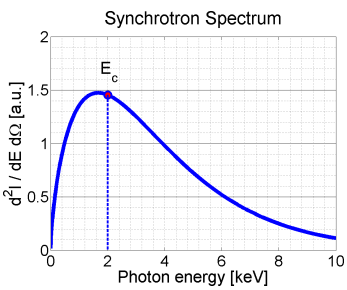

Figure 5.8. *Spectrum as in Figure 5.7 but on a linear scale.*

of the plasma wake oscillation in the case of a highly nonlinear ($a_0 > 1$), relativistic interaction.
The formation of a bubble behind the laser pulse can be seen. It is a region where electrons are evacuated by the strong ponderomotive force (see Section 2.7) of the driving pulse at these intensities. This leads to electron orbits around the laser field, curved towards the positively charged ion cavity thus created. At the rear of the bubble, the electron density becomes very high, which may result in wave-breaking and the injection of electrons into the bubble.

5.3 X-ray Emission

During LWFA in the bubble regime, the electron trajectories in radially focusing fields of the wake can result in the emission of very bright, short x-ray bursts. The betatron strength parameter, $K = \gamma \frac{\omega_\beta}{c} r_\beta$, describes the type of oscillation and depends on the betatron frequency, ω_β, and the oscillation amplitude, r_β. In the wiggler regime, i.e. $K > 1$, the spectrum emitted close to the optical axis is synchrotron-like. Example spectra are shown in Figures 5.7 and 5.8. The spectra are of the following form:

$$\frac{d^2I}{dEd\Omega} \propto \gamma_z^2 \left(\frac{E}{E_c}\right)^2 \kappa_{2/3}^2 \left(\frac{E}{2E_c}\right) \tag{5.9}$$

where

$$E_c = \frac{3}{4}\hbar\gamma^2\omega_p^2 r_\beta / c \tag{5.10}$$

$$\kappa_{2/3}(\rho) = \frac{1}{3}\int_0^\infty \frac{3+2x^2}{\sqrt{1+x^2/3}} \exp\left[-\rho\left(1+\frac{4x^2}{3}\sqrt{1+\frac{x^2}{3}}\right)\right] dx \tag{5.11}$$

and the critical energy E_c is the only parameter. This, in turn, is influenced by the oscillation amplitude of the electrons, r_β, which is limited by the bubble radius $\approx \lambda_p/2$. However, at the focus of an aberration-free laser, r_β is usually much smaller than $\lambda_p/2$ for injected electrons, but can be increased by promoting asymmetry during injection. This can be done by introducing a coma into the laser focus. This may increase r_β to its limit $\approx \lambda_p/2$ and enhance the brightness at higher x-ray energies. In gas densities around $1.5 \times 10^19\,\mathrm{cm}^{-3}$, E_c could be increased from 1.5 keV with a flat wavefront to 4 keV with coma, as demonstrated in Paper **VI**.

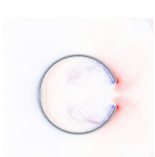

Chapter 6

Proton Acceleration

Laser-produced beams of protons and ions have numerous applications, ranging from use as diagnostic tools in diffraction and shadowgraphy of dense targets, to selective energy deposition in materials, including isochoric heating and cancer proton therapy. A short survey of applications can be found in the introduction of Paper **I**. Due to their importance and potential future applications, target design and materials have been investigated by the author in the work described in this thesis.

6.1 Target Normal Sheath Acceleration

As with electron acceleration experiments in the underdense regime, the strong and oscillating laser field, which is $\gtrsim 10\,\mathrm{TV/m}$ must be converted into a quasistatic directed field, which then accelerates protons or heavier ions. One typical acceleration mechanism normally utilized in the $(10^{18}-10^{20})\,\mathrm{W/cm^2}$ intensity regime is called target normal sheath acceleration (TNSA) [65]. Here, the laser pulse interacts with an overdense plasma (see Figure 6.1). In practice, this means that the laser strikes a solid target, e.g. a thin foil, up to $\sim 300\,\mu$m thick. During this interaction, a population of free hot electrons is produced at the laser-irradiated side by various heating processes (stochastic [66], ponderomotive [67, 68], resonant [69], Brunel [70], etc.). Some of the hot electrons traverse the bulk of the target as a collimated beam of electrons. Upon reaching the back of the target they leave the surface and create huge, $\sim$TV/m, but short-lived electrostatic sheath field. This ionizes surface contaminants such as hydrocarbons, which adhere to the target surface as a result of impurities such as water vapour or hydrocarbon fumes from the pumps at typical vacuum conditions $\sim 10^{-4}\,$mbar. The freed protons are now accelerated in the sheath field and leave along the target normal in a collimated $30^o - 60^o$

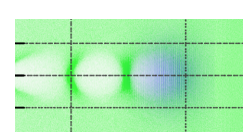

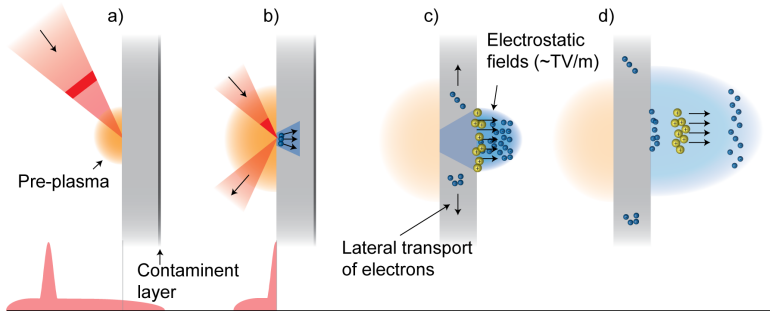

Figure 6.1. *Visualisation of the TNSA process: a) The rising laser intensity forms a preplasma on the target surface. b) During arrival of the pulse peak, electrons are heated. c) Some traverse the bulk of the target towards the rear surface, where they set up a sheath field. d) This ionises and accelerates surface contaminants. Courtesy G. Genoud*

divergent beam which, in the case of a simple foil target, is composed of particles with a thermal spectrum and a cut-off energy above which no particles are accelerated.

TNSA is not very efficient in converting laser energy into kinetic ion energy. Only part of the laser energy is converted to fast electrons ($\approx 30\%$), of which only a fraction traverses the target to contribute to the sheath field. Some electrons escape immediately and leave behind a positively charged target. Some spread laterally but are confined to the charged target surface [71], propagating towards the target edge where they can create a charge separation field and accelerate surface contaminants [72]. Here they are reflected back, and depending on the laser pulse length, τ_l, and the lateral dimensions of the target, they may be reheated if the laser is still irradiating the target upon their return. This is called transverse refluxing [73]. Unfortunately, this current does not contribute to the sheath field at the rear of the target and thus represents a loss of conversion efficiency.

To produce a very homogeneous beam of protons through TNSA, a cold return current inside the target may prevent the beam of hot electrons from breaking up and filamenting. This requires that sufficient free carrier charges are available inside the target material once it has been heated to the warm dense matter state during which electron transport occurs (see Paper **II**). This is especially important for thicker targets ($\gtrsim 10\,\mu$m), where instabilities may have sufficient time to grow. A $2\,\omega$ microbunching of this electron beam arises due to the primary interaction with the driving laser field. Continuity requirements of $\vec{D}$ and $\vec{B}$ for electrons traversing a dielectric interface lead to the emission of optical transition radiation (OTR) [74], at the rear of the target

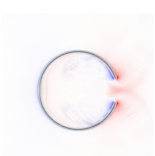

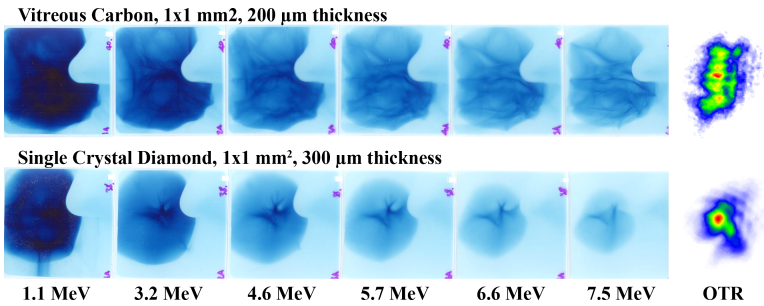

Figure 6.2. *Layers of RCF show qualitative differences in the degree of uniformity in the proton beam depending on the regularity of the target bulk. OTR emission, shown in the right images, confirms these findings. It can be seen that the regular crystal structure in diamond is beneficial for electron transport to the rear of the target, producing smoother TNSA beams.*

[75]. This provides information on lateral size or beam break-up inside the bulk, and may help in the development of a *smart target design* to efficiently guide the electron beam through the target, and to produce smooth beams of protons.

Knowledge of the electron spectrum inside the bulk is of major importance in modelling target dynamics. This electron transport through various allotropes of carbon, which exhibit various degrees of short- and long-range order in their bulk structure has been investigated by the author (Paper **II**). In this experiment, stacks of RCF, where each layer corresponds to a certain proton energy range, serve as a particle spectrometer with angular resolution (see Figure 6.2). Evaluating the smoothness of the proton beam allows conclusions to be drawn regarding the accelerating sheath field and thus the lateral charge distribution of the electron bunch arriving at back of the target. However, OTR may serve the same purpose by directly measuring the electron current reaching the back of the target. A comparison between OTR and RCF is shown in Figure 6.2.

6.2 General TNSA Proton Beam Considerations

If we calculate the stopping power of protons in a dense material such as water (see Figure 6.3) [76], we see that $\sim 100\,\mathrm{MeV}$ protons are needed to penetrate some centimetres into the material[1]. Assume a thermal spectrum and a constant particle number N, such

[1]Note that this refers to kinetic energy only. The proton rest mass is 938 MeV and these protons are still non-relativistic.

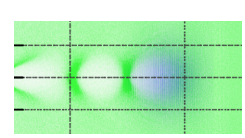

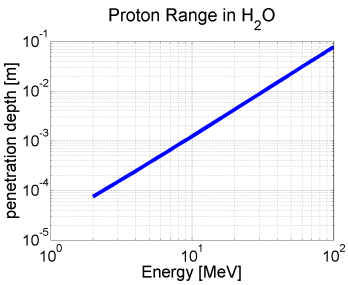

Figure 6.3. *Stopping Power for protons in water*

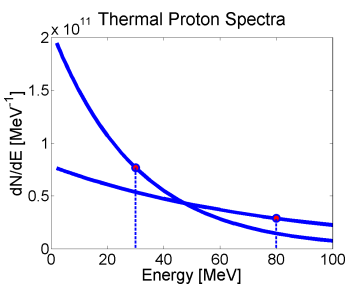

Figure 6.4. *Thermal proton spectra at temperatures $kT = 30\,MeV$ and $80\,MeV$ and constant particle number*

as in the example spectra depicted in Figure 6.4. The spectral distribution dN/dE can be written as:

$$\frac{dN}{dE} = Nf(E,T) \tag{6.1}$$

with the distribution function:

$$f(E,T) = \frac{e^{-\frac{E}{kT}}}{\int_0^\infty e^{-\frac{\tilde{E}}{kT}} d\tilde{E}} \tag{6.2}$$

$$\Leftrightarrow \int_0^\infty f(E,T)dE = 1 \tag{6.3}$$

To obtain as many particles as possible in the infinitesimal interval between E_0 and $E_0 + dE$ it is necessary to adjust the temperature, T. Mathematically this can be found by:

$$\frac{d}{dT}\left[\frac{Ne^{-\frac{E}{kT}}}{\int_0^\infty e^{-\frac{\tilde{E}}{kT}} d\tilde{E}}\right]_{E=E_0} = 0 \tag{6.4}$$

Solving this equation gives $E_0 = kT \equiv kT_0$. The energy of the entire beam, E_{tot}, with a temperature T_0 is thus given by:

$$E_{tot} = \int_0^\infty NEf(E,T)dE = NE_0 \tag{6.5}$$

and can be seen to increases linearly with the temperature.

In the experiment presented in Paper **I**, a 1 J laser pulse on target, delivered in ≈ 45 fs, was used to obtain a proton temperature of $kT \approx 1$ MeV. This energy is not sufficient for the protons to be used as a diagnostic to probe a solid or liquid sample, as their penetration depth is limited $\lesssim 100\,\mu$m. One way of improving performance is to increase the laser energy in order to increase the proton beam temperature. This would give deeper penetration and deposition the proton energy continuously with depth, resulting in homogeneous heating of the sample. This was done by the author to study effects of thermal degradation of a lattice structure on electron transport in a TNSA experiment by isochoric preheating of the TNSA target with proton beams created in a second TNSA set-up. For example, the depth-dependent energy deposition in water of a thermal proton beam with an energy of $kT_p = 80$ MeV is shown by the blue line in Figure 6.5.

However, some applications, such as proton therapy for cancer treatment [77, 78], require a shaped spectrum to delineate energy deposition and avoid exposing healthy tissue. The current method of treatment employs x-rays, and the depth-dependent energy deposition of an x-ray beam from a 50 kV x-ray tube is depicted by the red line in Figure 6.6. The corresponding x-ray spectrum is shown in Figure 6.7. This beam is absorbed exponentially. In

contrast, monochromatic beams of protons are characterized by a well defined depth at which almost all of their energy is deposited, the so-called Bragg peak. No energy is deposited at deeper levels, while energy transfer prior to the Bragg peak is negligible, as depicted by the blue line in Figure 6.6. This gives proton beams with shaped spectra an advantage over x-rays in the controlled destruction of tissue at a given depth, and has inspired many groups to investigate the potential of TNSA in the production of proton beams for cancer treatment.

Although TNSA proton spectra from foil targets are usually thermal with a maximum cut-off energy, during the past decade several groups have succeeded in shaping TNSA spectra [79–82], making them non-thermal, even quasi-monoenergetic, and increased the efficiency in converting laser energy to desired proton energy. Most of the beam shaping strategies employed could be described as *smart target design*, and a short survey of these developments can be found in the introduction of Paper **I**. Shaping proton beams through *smart target designs* requires studies on target material and composition, as presented in Paper **II**, as well as geometry and function, as in the experiment described in Paper **I**. Laser irradiance properties and their effect on the resulting proton energy have been examined and are summarized in Paper **III**. Laser power, intensity, time envelope and contrast all play a crucial role in these studies.

The experiment conducted by the author, and published in Paper **I**, is one example of an enhanced laser to desired proton energy coupling, utilizing a *smart target design*, which is here called a hollow *microsphere*, described in detail in the following section.

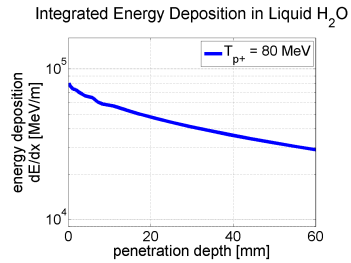

Figure 6.5. *Integrated depth-dependet energy deposition in water for a thermal proton beam with a temperature of* $kT_p = 80\,MeV$

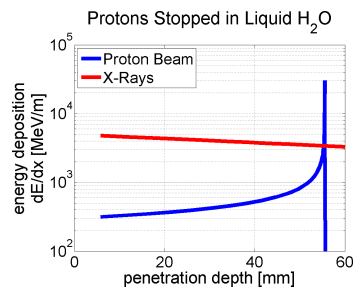

Figure 6.6. *Depth-dependet energy deposition for a monoenergetic proton beam (80 MeV) and x-rays from a 50 keV tube, whose spectral emission can be seen in Figure 6.7*

6.3 Hollow Glass *Microspheres*

The use of a hollow *microsphere* is an example of a novel and *smart target design*. It enables TNSA to take place at an increased and constant potential in the interior of the sphere, which acts as a Faraday cage. At the same time, a second acceleration stage boosts the energy of protons close to the opening, where laterally spreading surface currents that do not contribute to TNSA inside the sphere are refocused. Their charge separation field when reaching the opening boosts the energy of protons that traverse this region at the correct time. Hence, the laser-to-proton energy efficiency is increased with this target design.

The physics of oscillating surface currents around the *microsphere* is described in detail in Paper **I**, and this section will provide some background information on the target, its preparation and the performance of the experiment.

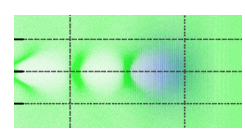

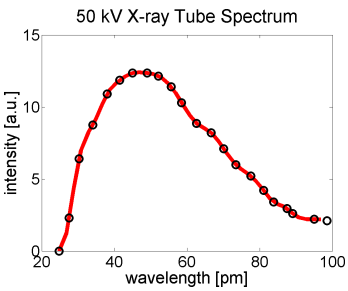

Figure 6.7. *X-ray spectrum of a typical x-ray tube with 50 kV acceleration voltage*

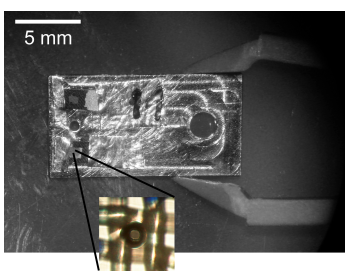

Figure 6.8. *Target holder plate showing the mesh and an isolated microsphere between the fibres. The plate is then mounted on the target holder / PM assembly shown in Figure 3.10.*

6.3.1 Target Fabrication and Laser Micromachining

The hollow *microspheres* used for the experiment described in Paper **I** are glass bubbles of $50\,\mu$m diameter with a $\lesssim 1\,\mu$m thick wall and are mass produced for applications such as thermal insulation and low-weight filling material, hence the cost is fairly low. An $\approx 50\,$nm thick silver coating was applied to the outside by the manufacturer. This was done to guide the previously mentioned lateral surface current as this is a key feature of this target. With these commercially available raw targets, the experimental challenges comprised single target isolation, fixation, and micromachining, as well as target positioning and alignment for a high-power laser shot.

These ultralight targets, which are extremely sensitive to electrostatic charge, have a tendency to form clusters and show Brownian motion [83]. They are also very fragile. Any direct mechanical contact will destroy the ultrathin coating or the entire sphere, requiring the target fixation process to be a self-organising and result in isolated targets. Individual targets could be isolated by dispensing them in methane at rather low concentration, and spraying them at high velocity through a pipette onto a nylon cloth. By chance, some spheres end up at the centre of the nylon grid, as depicted in Figure 1.2, where they are accessible from both sides. These areas can be cut out ($\approx 2 \times 2\,$mm^2) and glued onto a target holder plate such as that depicted in Figure 6.8.

The next step in target preparation is the production of the opening. The function of this hole is twofold. Firstly, it enables contaminants to enter the sphere so that TNSA may take place on the inner surface of the sphere, and secondly it provides the second accelerating structure as the laterally spreading surface currents from the TNSA interaction refocus at the opening, creating a charge separation field, which, if timed correctly, coincides with traversing protons post-accelerating them. Considering the fragility of the target, laser micromachining with femtosecond pulses seemed to be a suitable choice for hole production. The set-up is depicted in Figure 6.9. The same laser system, i.e. the Lund multi-TW laser (see Section 3.1), used to make the high-power shots on the target, was used for micromachining. A low-power, 800 nm 10 Hz beam is split from the amplification chain, compressed, attenuated and mode cleaned before being superimposed with a HeNe alignment beam, which serves as a target marker in the micromachining process. Micromachining was carried out with the help of a modified inverted confocal microscope (Nikon Diaphot 300) due to its variety in optical beam paths that can be used simultaneously. This enables a live view of the *microsphere* during micromachining of the target in the nylon mesh, glued onto

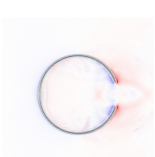

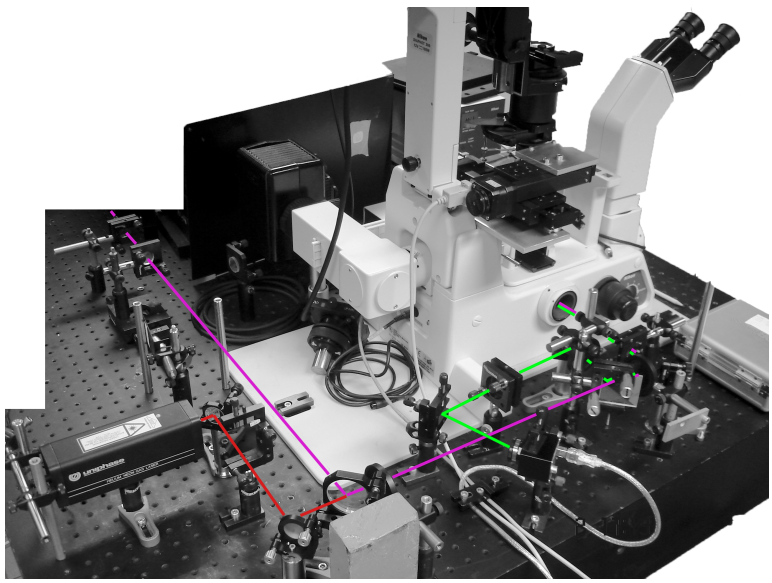

Figure 6.9. *Laser micromachining set-up with the confocal microscope equipped with visual target observation, confocal imaging, HeNe laser target alignment and motorized target holder. A HeNe laser (red) for alignment in the x-, y- and z directions is superimposed on the machining beam (magenta). The confocal reflection beam (green) is directed to a spectrometer, and a view on the microsphere can be provided during machining.*

the target holder plate. The red spot from the HeNe laser serves as a highly accurate indication of where the infrared pulse will ablate material. A specially designed x-y motorized target holder enabled computer-controlled lateral positioning of the target. The target is moved in a spiral, steered by a Labview program, to ablate material and to create the desired opening. Various shapes of the opening were possible, as shown in Figure 6.10. .

It was found experimentally that with $\sim 40\,\mathrm{fs}$ long laser pulses the energy range for micromachining was very narrow. An energy slightly higher ($\sim 10\,\%$) than that necessary to produce a plasma and to ablate material disrupted the sphere immediately. Therefore, a spectrometer analysing light from the microscope's confocal reflection provided important information on the onset of plasma formation. The corners of the opening were smoothest when ablation was conducted in a two-step process. First, the silver coating was ablated, followed by removal of the glass substrate. The numerical aperture (NA) of the microscope objective affects the depth selectivity during machining. Too low a value of NA results in damage to the inner surface on the opposite side of the

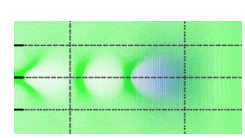

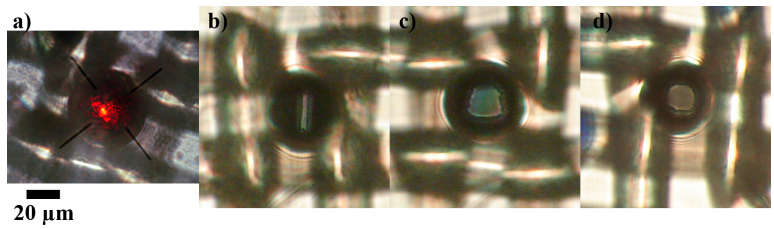

Figure 6.10. *Laser micromachining: a) Premachined sphere showing the red confocal alignment laser reflection. Openings of different shapes are possible, b) slit, c) square and d) round, demonstrating the resolution and accuracy of the home-built laser micromachining set-up*

sphere, where TNSA is supposed to take place. A large value of NA makes drilling difficult as the sphere moves out of focus when moved laterally. A 20× APO planar microscope objective was found to be a suitable choice.

After successful micromachining, the target was mounted on the target holder and PM assembly shown in Figure 3.10, which was then mounted in the target chamber.

6.3.2 Target Alignment

The small target dimensions require accurate alignment to ensure that the laser beam hits the sphere. It is essential to be able to distinguish and control whether the beam hits the nylon mesh or the target. This was achieved and proton beam imprints on CR39 originating from a controlled shot onto the mesh and a *microsphere* are depicted in Figure 6.11. To achieve this accuracy, a HeNe beam was superimposed on the high-intensity IR pulsed beam. The HeNe is integrated as a confocal microscope, using the off-axis parabolic mirror (OAP) as an objective. In this way, once roughly aligned, the *microsphere* target positioning can be fine-adjusted with the help of the confocal HeNe reflection. However, accurate overlap of the IR and HeNe beams is critical, and small drifts required realignment prior to every shot. The focal spot size is $\approx 4\,\mu$m. Due to the curvature of the target a strongly asymmetric off-centre proton beam will be produced if the IR beam is displaced by only one focal spot diameter. Therefore, a flip mirror system mounted close to the target was used to redirect both the IR and the HeNe beams onto an in-chamber CCD microscope. Equipped with a Schwarzschild objective, wavelength-independent, high-resolution superposition becomes possible prior to every shot. Rough alignment is accomplished using a low-magnification, long-working-distance microscope to identify metallic reflections of the HeNe beam in order to find the sphere.

The failure rate from target fixation to a successful shot was rather high. Only $\sim 5\,\%$ of the *microspheres* end up as an isolated sphere at a suitable position on the nylon mesh, and about $80\,\%$ of them suffered defects during the micromachining, making them unusable. Of the final targets, only half of them were sufficiently uniform and smooth to be utilized in a TNSA experiment. After optimization of the target fabrication, ≈ 4 targets could be prepared in one day and mounted and aligned in the target chamber on the following day. A miss rate of $\sim 50\,\%$ gives on average one successful shot per day.

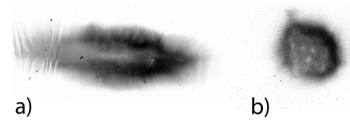

Figure 6.11. *CR39 imprints of proton beams, shown on the same greyscale: a) controlled shot into a vertical fibre of the nylon mesh, and b) a shot on a* microsphere. *Both beams have a vertical full divergence angle of* $\approx 30^o$.

6.3.3 Simulations

To study the laser-matter interaction in hollow *microspheres* in a computer model, PIC simulations were carried out with a supercomputer in collaboration with colleagues at Umeaå University. This resulted in several movies, describing the evolution of electric fields, hot and cold surface currents and proton acceleration. Some frames are shown and explained in Figure 6.12. This thesis features two flip book movies. In the lower left corner of even pages the evolution of fields and proton expansion can be followed in a two-dimensional simulation of microsphere dynamics by quickly flipping through the pages while observing the small inset. This gives an intuitive understanding of the dynamics encountered in the experiment.

6.3.4 Outlook

In Paper **I** the possibility of adjusting the timing between the arrival of the TNSA protons and the charge wave at the opening by oblates or dielectric coatings is discussed. In this way, proton energies could already be boosted during the first cycle of the oscillating electron surface current. Simulations were carried out and the results are depicted in Figures 6.13 and 6.14 for on oblate and a sphere with a thick "belly" coating, respectively. An increase in proton energy enhancement was seen in both cases.

Oblates are difficult to produce, and spheres with a silver coating were used in the experiments due to their availability and easier handling. As spheres are created by an expanding gas inside a liquid glass bubble, which after expansion and cooling naturally produces the spherical shape, the absence of any preferred symmetry axis makes them easy to machine and align. The application of localized dielectric surface coatings is currently beyond the target fabrication capabilities in Lund.

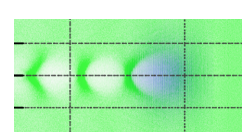

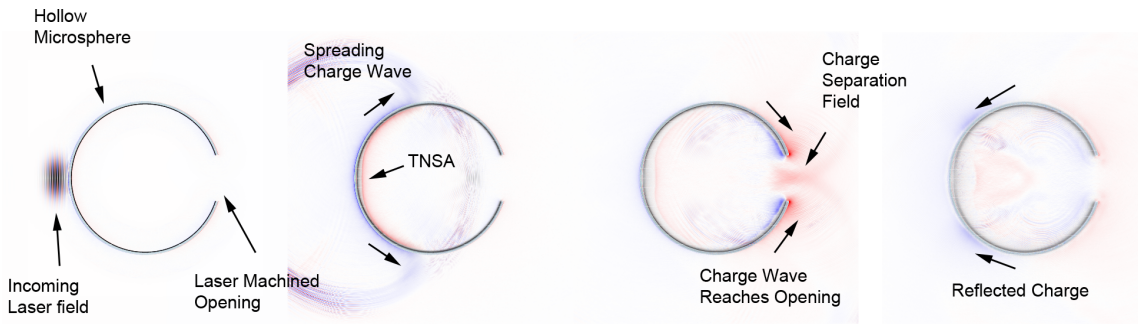

Figure 6.12. *Summary of 2D simulations of a laser pulse interacting with a hollow microsphere. Starting from the left, a linearly polarized Gaussian laser pulse with a spot size of $2r_0 = 10\,\mu m$ impinges on a 2D hollow microsphere, consisting of a neutral plasma of fully ionized gold ions and electrons and a contaminant layer of protons on the inside wall of the sphere, where TNSA takes place. Red and blue depict the accelerating and decelerating electric fields as experienced by the protons, while the protons are shown in black. After interaction, TNSA takes place at the inner surface of the sphere, while a charge wave spreads out laterally from the laser focus with a velocity of $\approx 0.7\,c$, guided by the sphere surface. After some time this wave reaches the opening and sets up a proton-accelerating charge-separation field. At this point, the charge wave is reflected back towards the laser focus, oscillating several times around the sphere. This oscillation decays over ≈ 5 cycles. In this experiment, the third occurance of the charge separation field at the opening was expected to coincide with traversing protons of $\approx 6\,MeV$, which are moving with a velocity of $\approx 0.1\,c$. The energy of these protons can be boosted.*

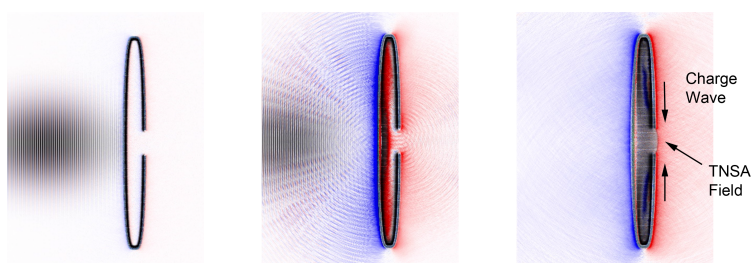

Figure 6.13. *Simulation of a hollow oblate. The simulation parameters and colour codes are the same as in Figure 6.12. The laser arrives from the left and launches a charge wave with a similar velocity to that of the sphere ($\approx 0.7\,c$), but in this geometry it arrives at the opening at approximately the same time as the non-relativisitc protons originating from TNSA within the oblate. Interacting during its first half oscillation cycle, the charge wave has not been decaying so much as in the case with the sphere, and the resulting charge separation field gives rise to a stronger boost of the traversing protons.*

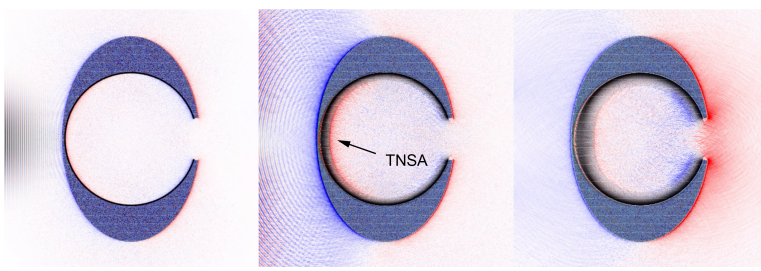

Figure 6.14. *Simulation of a hollow microsphere with a thick "belly" coating: Simulation parameters and colour codes are the same as in Figure 6.12. The laser arrives from the left and launches a charge wave, which spreads laterally from the laser focus. As in the case of the oblate, the arrival of the charge wave at the opening coincides with the passage of non-relativistic TNSA protons from within the sphere.*

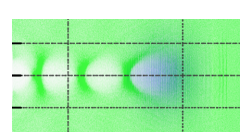

Appendix A

Vector Potential and Gauges

Potentials Φ and $\vec{A}$ can be introduced together with an appropriate gauge transformation to simplify the description of radiation transport.
In vacuum, for the Gauss's law of magnetism, Equation (2.4), we can introduce a vector potential $\vec{A}$, so that $\vec{B}(\vec{r},t) = \nabla \times \vec{A}(\vec{r},t)$. Inserting $\vec{A}$ into Maxwell-Ampère's law Equation (2.3) gives:

$$\frac{\partial}{\partial t}\nabla \times \vec{A}(\vec{r},t) + \nabla \times \vec{E}(\vec{r},t) = 0 \tag{A.1}$$

$$\nabla \times \left(\frac{\partial}{\partial t}\vec{A}(\vec{r},t) + \vec{E}(\vec{r},t)\right) = 0 \tag{A.2}$$

Introducing a scalar potential Φ yields:

$$\nabla \times (-\nabla\Phi(\vec{r},t)) = 0 \tag{A.3}$$

$$\iff \vec{E}(\vec{r},t) = -\nabla\Phi(\vec{r},t) - \frac{\partial}{\partial t}\vec{A}(\vec{r},t) \tag{A.4}$$

Expressing Maxwell-Ampère's law (Equation (2.4), left) in terms of potentials yields:

$$\nabla \times \nabla \times \vec{A}(\vec{r},t) - \frac{1}{c^2}\frac{\partial}{\partial t}\left(-\nabla\Phi(\vec{r},t) - \frac{\partial}{\partial t}\vec{A}(\vec{r},t)\right) = \mu_0\vec{j}(\vec{r},t) \tag{A.5}$$

$$\nabla\nabla \cdot \vec{A}(\vec{r},t) - \Delta\vec{A}(\vec{r},t) - \frac{1}{c^2}\frac{\partial}{\partial t}\left(-\nabla\Phi(\vec{r},t) - \frac{\partial}{\partial t}\vec{A}(\vec{r},t)\right) = \mu_0\vec{j}(\vec{r},t) \tag{A.6}$$

$$\left(-\Delta + \frac{1}{c^2}\frac{\partial^2}{\partial t^2}\right)\vec{A}(\vec{r},t) + \nabla\underbrace{\left(\frac{1}{c^2}\frac{\partial}{\partial t}\Phi(\vec{r},t) + \nabla \cdot \vec{A}(\vec{r},t)\right)}_{=f(\vec{r},t)} = \mu_0\vec{j}(\vec{r},t) \tag{A.7}$$

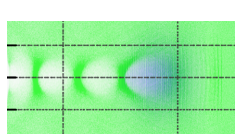

Hitherto $\vec{A}$ is not uniquely defined. A gauge transformation

$$\widetilde{B}(\vec{r},t) = \nabla \times \widetilde{A}(\vec{r},t) \tag{A.8}$$

$$= \nabla \times \left(\vec{A}(\vec{r},t) + \nabla\lambda(\vec{r},t)\right) \tag{A.9}$$

$$= \nabla \times \left(\vec{A}(\vec{r},t)\right) \tag{A.10}$$

$$= \vec{B}(\vec{r},t) \tag{A.11}$$

requiring

$$\widetilde{E}(\vec{r},t) = -\nabla\widetilde{\Phi}(\vec{r},t) - \frac{\partial}{\partial t}\widetilde{A}(\vec{r},t) \tag{A.12}$$

$$= -\nabla\widetilde{\Phi}(\vec{r},t) - \frac{\partial}{\partial t}\left(\vec{A}(\vec{r},t) + \nabla\lambda(\vec{r},t)\right) \tag{A.13}$$

$$= -\nabla\left(\widetilde{\Phi}(\vec{r},t) + \frac{\partial}{\partial t}\lambda(\vec{r},t)\right) - \frac{\partial}{\partial t}\vec{A}(\vec{r},t) \tag{A.14}$$

$$= \vec{E}(\vec{r},t) \;\Leftrightarrow\; \widetilde{\Phi}(\vec{r},t) = \Phi(\vec{r},t) - \frac{\partial}{\partial t}\lambda(\vec{r},t) \tag{A.15}$$

leaves the fields unchanged can be applied in such a way that the gradient in Equation (A.7) expressed in the new potentials vanishes:

$$\frac{1}{c^2}\frac{\partial}{\partial t}\widetilde{\Phi}(\vec{r},t) + \nabla\cdot\widetilde{A}(\vec{r},t) = \frac{1}{c^2}\frac{\partial}{\partial t}\left(\Phi(\vec{r},t) - \frac{\partial}{\partial t}\lambda(\vec{r},t)\right) + \nabla\cdot\left(\vec{A}(\vec{r},t) + \nabla\lambda(\vec{r},t)\right) \tag{A.16}$$

$$= \frac{1}{c^2}\frac{\partial}{\partial t}\Phi(\vec{r},t) + \nabla\cdot\vec{A}(\vec{r},t) - \left(\left(\frac{1}{c^2}\frac{\partial^2}{\partial t^2} - \Delta\right)\lambda(\vec{r},t)\right) \tag{A.17}$$

$$= 0 \;\Leftrightarrow\; \left(\frac{1}{c^2}\frac{\partial^2}{\partial t^2} - \Delta\right)\lambda(\vec{r},t) = f(\vec{r},t) \tag{A.18}$$

The general solution for λ consists of both a particular and a homogeneous solution

$$\lambda(\vec{r},t) = \lambda_{part}(\vec{r},t) + \lambda_{hom}(\vec{r},t) \tag{A.19}$$

of which only $\lambda_{part}(\vec{r},t)$ is needed to satisfy Equation (A.18). $\lambda_{hom}(\vec{r},t)$ can be chosen in such a way that $\nabla\cdot\widetilde{A}(\vec{r},t) = 0$ leaving only

$$\left(\Delta - \frac{1}{c^2}\frac{\partial^2}{\partial t^2}\right)\widetilde{A}(\vec{r},t) = -\mu_0\vec{j}(\vec{r},t) \tag{A.20}$$

.

Choosing $\vec{A}$ and Φ from the beginning in such a way that the above simplifications apply (Lorentz gauge), E and B in vacuum are simply given by:

$$\vec{E}(\vec{r},t) = -\frac{\partial}{\partial t}\vec{A}(\vec{r},t) \qquad \vec{B}(\vec{r},t) = \nabla\times\vec{A}(\vec{r},t) \tag{A.21}$$

Appendix B

Fourier Transformation and Differential Equations

To solve a set of differential equations such as Maxwell's equations in Chapter 2, they are usually rewritten in Fourier space and solved for one Fourier component only.

The Fourier transformation $f(\omega) = \mathfrak{F}[f(t)] = [f(t)]^\wedge$ of a function $f(t)$ is defined as:

$$f(\omega) = [f(t)]^\wedge = \frac{1}{\sqrt{2\pi}} \int f(t) e^{-i\omega t} dt \tag{B.1}$$

$$f(t) = [f(\omega)]^\vee = \frac{1}{\sqrt{2\pi}} \int f(\omega) e^{i\omega t} d\omega \tag{B.2}$$

requiring

$$f(t) = [[f(t)]^\wedge]^\vee \tag{B.3}$$

$$= \frac{1}{2\pi} \int \left(\int f(\tilde{t}) e^{-i\omega\tilde{t}} d\tilde{t} \right) e^{i\omega t} \, d\omega \tag{B.4}$$

$$= \int \left(\frac{1}{2\pi} \int e^{i\omega(t-\tilde{t})} d\omega \right) f(\tilde{t}) \, d\tilde{t} \tag{B.5}$$

$$= \int \delta(t-\tilde{t}) f(\tilde{t}) d\tilde{t} \tag{B.6}$$

and comparison yields the definition of the delta function $\delta(t-\tilde{t})$ as:

$$\delta(t-\tilde{t}) = \frac{1}{2\pi} \int e^{i\omega(t-\tilde{t})} d\omega \tag{B.7}$$

Thus a derivative can be rewritten as a simple multiplier in

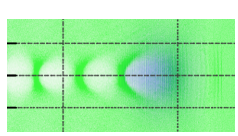

Fourier space using:

$$\frac{\partial}{\partial t} f(t) = \frac{1}{\sqrt{2\pi}} \frac{\partial}{\partial t} \int f(\omega) e^{i\omega t} d\omega \quad \text{(B.8)}$$

$$= \frac{1}{\sqrt{2\pi}} \int i\omega f(\omega) e^{i\omega t} d\omega \quad \text{(B.9)}$$

$$\partial_t f(t) = [i\omega f(\omega)]^{\vee} \quad \text{(B.10)}$$

$$\text{transforming back } \Rightarrow [\partial_t f(t)]^{\wedge} = i\omega f(\omega) \quad \text{(B.11)}$$

This enables us to rewrite complex differential equations in Fourier space substituting:

$$[\partial_t f(t)]^{\wedge} = i\omega f(\omega) \quad \text{(B.12)}$$

$$\text{or } \left[\nabla \times \vec{A}(\vec{r})\right]^{\wedge} = i\vec{k} \times \vec{A}(\vec{k}) \quad \text{(B.13)}$$

and solving for one Fourier component only. The solution to the original differential equation is then an integral over the entire spectrum in k-space or ω, respectively, i.e. the quantities are transformed back to real space.

Appendix C

Gaussian Pulses, Time and Space Considerations

C.1 Integrals over Gauss Functions

C.1.1 1D Case

While the integral over the Gauss function

$$\int_{-\infty}^{\infty} e^{-ax^2}\,dx \tag{C.1}$$

is difficult to solve, its square

$$\left(\int_{-\infty}^{\infty} e^{-ax^2}\,dx\right)^2 = \int_{-\infty}^{\infty} e^{-ax^2}\,dx \int_{-\infty}^{\infty} e^{-ay^2}\,dy \tag{C.2}$$

$$= \int_{-\infty}^{\infty}\int_{-\infty}^{\infty} e^{-a(x^2+y^2)}\,dx\,dy \tag{C.3}$$

can be rewritten in spherical coordinates, leading to

$$\int_{-\infty}^{\infty}\int_{-\infty}^{\infty} e^{-a(x^2+y^2)}\,dx\,dy = \int_0^{2\pi}\int_0^{\infty} e^{-ar^2} r\,d\varphi\,dr \tag{C.4}$$

$$= 2\pi\int_0^{\infty} e^{-ar^2} r\,dr \tag{C.5}$$

$$= 2\pi\left[-\frac{1}{2a}e^{-ar^2}\right]_0^{\infty} \tag{C.6}$$

$$= \frac{\pi}{a} \tag{C.7}$$

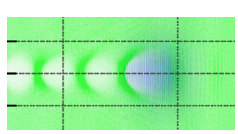

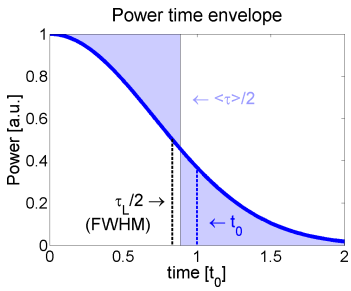

Figure C.1. *Gaussian pulse time envelope of power or intensity. The graph shows the relations between $\tau_l, <\tau>$ and t_0*

resulting in:

$$\int_{-\infty}^{\infty} e^{-ax^2} dx = \sqrt{\frac{\pi}{a}} \tag{C.8}$$

and

$$\int_{0}^{\infty} e^{-ax^2} dx = \frac{1}{2}\sqrt{\frac{\pi}{a}} \tag{C.9}$$

C.1.2 2D Case

Assume a radial Gaussian function. Its integral over the entire space is

$$\int_0^{2\pi}\int_0^{\infty} e^{-ar^2} r\, d\varphi\, dr = 2\pi \int_0^{\infty} r e^{-ar^2} dr \tag{C.10}$$

$$= 2\pi \left[-\frac{1}{2a} e^{-ar^2}\right]_0^{\infty} \tag{C.11}$$

$$= \frac{\pi}{a} \tag{C.12}$$

C.2 Time Domain (τ_l, $<\tau>$ and t_0)

Assume a Gaussian pulse (see Figure C.1) in the time domain, delivering a power P of the form: .

$$P(t) = P_0 e^{-\frac{t^2}{t_0^2}} \tag{C.13}$$

In this section the correlations between the decay time, t_0, the pulse length at FWHM, τ_l, and an average energy delivery time $<\tau>$ are derived.

The delivered energy E can be written as the time integral over the power:

$$\Rightarrow E = \int_{-\infty}^{\infty} P(t) dt \tag{C.14}$$

$$= 2P_0 \int_0^{\infty} e^{-\frac{t^2}{t_0^2}} dt = P_0 <\tau> \tag{C.15}$$

From Equation (C.9) the integral can be solved yielding:

$$E = 2P_0 \frac{1}{2} t_0 \sqrt{\pi} = P_0 <\tau> \tag{C.16}$$

$$\Rightarrow t_0 \sqrt{\pi} = <\tau> \tag{C.17}$$

The laser pulse length, τ_l, at FWHM is related to t_0 by:

$$\tau_l = 2t_0\sqrt{\ln 2} \tag{C.18}$$

Combining everything, gives the equations for the peak power:

$$P_0 = \frac{E}{<\tau>} = \frac{E}{t_0\sqrt{\pi}} = \frac{E}{\tau_l\sqrt{\frac{\pi}{4\ln 2}}} \tag{C.19}$$

Note that usually τ_l is measured, and when using an average time this should be corrected according to Equation (C.19) above.

C.3 Space Domain (r_0)

As the intensity, $I = dP/dA$, depends on the radial energy distribution it is interesting to investigate the peak intensity obtained on axis.

Assume a 2D radial Gaussian intensity or power distribution of the form

$$f(r) = f_0 e^{-2\frac{r^2}{r_0^2}} \qquad \text{with } f_0 = \frac{2}{r_0^2\pi} \tag{C.20}$$

(see Section C.1.2) so that

$$\int_0^{2\pi}\int_0^{\infty} f(r)\, r\, d\varphi\, dr = 1 \tag{C.21}$$

The question is, can we define a radius, $\tilde{r}$, within which the fraction of the power, δ, is delivered? This leads to the following equation:

$$\delta = \int_0^{2\pi}\int_0^{\tilde{r}} \frac{2}{r_o^2\pi} e^{-2\frac{r^2}{r_o^2}}\, r\, d\varphi\, dr \tag{C.22}$$

$$= \frac{4}{r_0^2}\int_0^{\tilde{r}} r e^{-2\frac{r^2}{r_o^2}} dr \tag{C.23}$$

$$= \frac{4}{r_0^2}\left[-\frac{r_0^2}{4} e^{-\frac{r^2}{r_o^2}}\right]_0^{\tilde{r}} \tag{C.24}$$

$$\Rightarrow \delta = 1 - e^{-2\frac{\tilde{r}^2}{r_o^2}} \tag{C.25}$$

or

$$\tilde{r}(\delta) = \frac{r_0}{\sqrt{2}}\sqrt{-\ln(1-\delta)} \tag{C.26}$$

The average intensity, I, depends on the fraction of the central beam considered:

$$I = \frac{\delta E}{<\tau>\pi\tilde{r}^2(\delta)} = \frac{2E}{<\tau>\pi r_0^2}\frac{\delta}{-\ln(1-\delta)} \tag{C.27}$$

Considering only on-axis contributions, i.e. $\delta \to 0$ and using L'Hôpital's rule

$$\lim_{\delta\to 0}\frac{\delta}{-\ln(1-\delta)} = \lim_{\delta\to 0}\frac{1}{\frac{1}{1-\delta}} = 1 \tag{C.28}$$

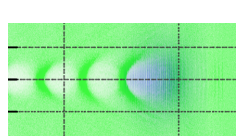

leads to an expression for the peak intensity.

$$I_{max} = \frac{2E}{<\tau> \pi r_0^2} = \frac{E}{\tau_l \pi r_0^2} \sqrt{\frac{16 \ln 2}{\pi}} \tag{C.29}$$

$$= \frac{2P_0}{\pi r_0^2} \tag{C.30}$$

Appendix D

Time Average over Complex Vector

Assume two complex vectors of the from $\vec{a} = \vec{a}_0 e^{-i\omega t}$ and $\vec{b} = \vec{b}_0 e^{-i(\omega t)}$, where $\vec{a}_0 = \vec{a}_{0re} + i\vec{a}_{0im}, \vec{b}_0 = \vec{b}_{0re} + i\vec{b}_{0im} \subseteq \mathbb{C}$. Their time average over the real part can be written as

$$< \Re(\vec{c}) >= \frac{1}{T}\int_0^T \Re(\vec{a}) \times \Re(\vec{b}) dt = \frac{1}{2}\Re\left[\vec{a}_0 \times \vec{b}_0^*\right] \tag{D.1}$$

This can be derived in the following way.

$$< \Re(\vec{c}) > = \frac{1}{T}\int_0^T \frac{1}{2}\left[\vec{a}_0 e^{-i\omega t} + \vec{a}_0^* e^{i\omega t}\right] \times ... dt \tag{D.2}$$

$$= \frac{1}{T}\int_0^T \frac{1}{2}\left[(\vec{a}_{0re} + i\vec{a}_{0im})e^{-i\omega t} + (\vec{a}_{0re} - i\vec{a}_{0im})e^{i\omega t}\right] \times ... dt \tag{D.3}$$

$$= \frac{1}{T}\int_0^T \frac{1}{2}\left[\vec{a}_{0re}(e^{-i\omega t} + e^{i\omega t}) + i\vec{a}_{0im}(e^{-i\omega t} - e^{i\omega t})\right] \times ... dt \tag{D.4}$$

$$= \frac{1}{T}\int_0^T \frac{1}{2}\left[\vec{a}_{0re}(2\cos(\omega t)) + i\vec{a}_{0im}(-2i\sin(\omega t))\right] \times ... dt \tag{D.5}$$

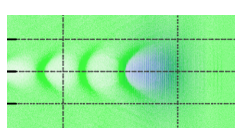

$$= \frac{1}{T}\int_0^T \left[\vec{a}_{0re}\cos(\omega t) + \vec{a}_{0im}\sin(\omega t)\right] \times \left[\vec{b}_{0re}\cos(\omega t) + \vec{a}_{0im}\sin(\omega t)\right] dt \tag{D.6}$$

$$= \frac{1}{T}\int_0^T \left[(\vec{a}_{0re}\times\vec{b}_{0re})\cos^2(\omega t) + (\vec{a}_{0im}\times\vec{b}_{0im})\sin^2(\omega t)\right] \times ...dt \tag{D.7}$$

$$= \frac{1}{2}\left[\vec{a}_{0re}\times\vec{b}_{0re} + \vec{a}_{0im}\times\vec{b}_{0im}\right] \tag{D.8}$$

$$= \frac{1}{2}\Re\left[(\vec{a}_{0re} + i\vec{a}_{0im})\times(\vec{b}_{0re} - i\vec{b}_{0im})\right] \tag{D.9}$$

$$= \frac{1}{2}\Re\left[\vec{a}_0\times\vec{b}_0^*\right] \tag{D.10}$$

Role of the Author

The papers included in this thesis can be divided into three groups:

(i) Papers **I-IV** describe experiments in the overdense plasma regime, where the laser pulse interacts with a solid target. While the first three papers focus on TNSA, the fourth is devoted to magnetic field measurements in short pulse laser-matter interactions.

(ii) Papers **V-VII** describe experiments in which the laser interacts with a gas jet in a low-density plasma. Beams of electrons and soft x-rays are produced.

(iii) Papers **VIII-XII** focus on the use of capillaries as targets. In this context Paper **VIII** describes a technical improvement, necessary to enable the experiments described in the proceeding papers.

I **Hollow microspheres as targets for staged laser-driven proton acceleration**
M. Burza, A. Gonoskov, G. Genoud, A. Persson, K. Svensson, M. Quinn, P. McKenna, M. Marklund and C.-G. Wahlström
This paper describes a proton acceleration experiment in the TNSA regime. A *smart target design* utilizes laser energy that is deposited in laterally spreading electron currents in the target not normally contributing to proton acceleration. However, in this particular target geometry, a hollow microsphere allows these electrons to be guided towards a secondary interaction point, where they can boost some of the traversing protons, thus exploiting laser energy more efficiently. As main investigator, the author played a major role in all experimental stages including administrative tasks such as planning and organisation. It should be considered the author's major contribution to the field of proton acceleration.
While the spheres were manufactured and coated by industrial means, the author developed techniques of mechanically fixing

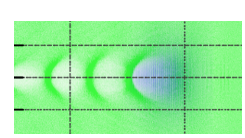

these micron-scale targets in the desired geometry, so that they became accessible to a high-power laser pulse. As the experiment requires a micro-structured target, the author built a confocal micromachining set-up and investigated laser specifications for material ablation of compound targets by ultrashort pulses on the micron scale. For the micromachining itself, he developed a *Labview* program to integrate stepping motors into the set-up, built a motorized microscope object holder assembly and machined all of the targets.

As laser-matter interactions with ultra-thin targets require high laser contrast on the ps time scale prior to the main pulse, he devoted considerable effort to adjusting and tuning laser parameters. In connection with high contrast requirements, the author constructed a Brewster angle plasma mirror set-up and manufactured most of the plasma mirrors, involving glass machining. Target holders were designed by the author.

The experimental set-up inside the target chamber was built under the supervision of and contributions by the author, while the set-up for confocal targeting alignment was built by the author alone, who played an essential role in targeting and hitting the spheres.

The evaluation of experimental data and most of the article writing was also done by the author.

II **Effect of lattice structure on energetic electron transport in solids irradiated by ultraintense laser pulses**

P. McKenna, A. P. L. Robinson, D. Neely, M. P. Desjarlais, D. C. Carroll, M. N. Quinn, X. H. Yuan, C. M. Brenner, M. Burza, M. Coury, P. Gallegos, R. J. Gray, K. L. Lancaster, Y. T. Li, X. X. Lin, O. Tresca and C.-G. Wahlström

The author was part of the experimental team, conducting a systematic study on energy transfer relevant to TNSA at the Rutherford Appleton Laboratory, UK. Some of the experimental findings resulted in this paper. A large range of complementary diagnostic methods was used to analyse laser energy to electron coupling at the target front, electron-to-proton coupling at its rear, and electron transport and pinching effects inside the target.

The author was assigned the task of constructing part of the in-chamber set-up and contributed to the arrangement and alignment of a variety of diagnostics involved. In particular, he built a fast optical probe, providing interferometric and shadowgraphic images of the target and of the expanding plasma.

III **Influence of laser irradiated spot size on energetic electron injection and proton acceleration in foil targets**

M. Coury, D. C. Carroll, A.P.L. Robinson, X. H. Yuan, C. M. Brenner, M. Burza, R. J. Gray, M. N. Quinn, K. L. Lancaster, Y. T. Li, X. X. Lin, O. Tresca, C.-G. Wahlström, D. Neely and P. McKenna

The role of the author is identical to that described for Paper **II** above as this article is the result of the same experimental campaign.

IV **Megagauss magnetic field generation at relativistic intensities using 35 femtosecond laser pulses**

A. Gopal, S. Minardi, M. Burza, G. Genoud, I. Tzianaki, A. Karmakar, P. Gibbon, M. Tatarakis, A. Persson and C.-G. Wahlström

The author was involved in the planning and preparation of this experiment, and made substantial contributions in the experimental phase from set-up to data acquisition. He was also involved in data interpretation.

V **Staged laser wakefield acceleration using double density ramps**

M. Burza, K. Svensson, A. Gonoskov, F. Wojda, A. Persson, O. Lundh, M. Marklund and C.-G. Wahlström

The wire experiment is based on an idea by the author, inspired by his aviation background and insight into supersonic flight to exploit shock waves in a supersonic gas flow to improve electron beam characteristics in LWFA by controlling injection through density gradients. This should be regarded as the author's main contribution in the field of electron acceleration.

As main investigator, the author did extensive background research and preliminary calculations, demonstrating the feasibility of the experiment. In the laboratory, he set up a Normarski interferometer to investigate density gradients and shock waves in a wire disturbed gas flow under typical experimental conditions, tailoring densities and gradients and characterizing the gas flow. During the experimental phase he integrated the wire into the already existing LWFA set-up in the target chamber. He took a major part in the evaluation of the experimental data and collaborated with the theoreticians providing the simulation results.

VI **Controlling the spectrum of x-rays generated in a laser-plasma accelerator by tailoring the laser wavefront**

S. P. D. Mangles, G. Genoud, S. Kneip, M. Burza, K. Cassou, B. Cros, N. P. Dover, C. Kamperidis, Z. Najmudin, A. Persson, J. Schreiber, F. Wojda and C.-G. Wahlström

As part of the experimental team, the author contributed to the experiment, and was involved in the critical revision of the manuscript.

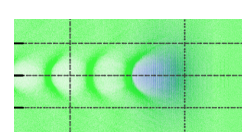

VII **Self-injection threshold in self-guided laser wakefield accelerators**

S. P. D. Mangles, G. Genoud, M. S. Bloom, M. Burza, Z. Najmudin, A. Persson, K. Svensson, A. G. R. Thomas and C.-G. Wahlström

As part of the experimental team, the author contributed to this paper through planning and conducting the experiment, and was involved in critical revision of the manuscript.

VIII **Active control of the pointing of a multi-terawatt laser**

G. Genoud, F. Wojda, M. Burza, A. Persson and C.-G. Wahlström

This paper describes in-house laser development to attain the pointing accuracy required to enable efficient coupling of the laser energy from a 30 TW class laser to the core of a glass capillary, minimizing pointing fluctuations to prevent the residual energy in the wings of the focal spot from destroying the target. This was a critical achievement for the experiments described in Papers **XII**, **XI**, **X** and **IX**.

The author performed first measurements on the resolution and sensitivity of the position-sensitive detectors and built the first detector module prototype incorporated into the experiment. It was the author's idea to use the non-amplified remainder of the 80 MHz oscillator pulse train as a quasi-cw beam providing a pointing reference.

IX **Laser-driven plasma waves in capillary tubes**

F. Wojda, K. Cassou, G. Genoud, M. Burza, Y. Glinec, O. Lundh, A. Persson, G. Vieux, E. Brunetti, R. P. Shanks, D. Jaroszynski, N. E. Andreev, C.-G. Wahlström and B. Cros

As part of the experimental team, the author contributed to the experiment and was involved in the critical revision of the manuscript. In particular, he worked with the laser and helped with the alignment of some diagnostics.

X **Analysis of laser wakefield dynamics in capillary tubes**

N. E. Andreev, K. Cassou, F. Wojda, G. Genoud, M. Burza, O. Lundh, A. Persson, B. Cros, V. E. Fortov and C.-G. Wahlström

The author participated in the experiment that laid the foundation and provided reference data for comparison with the theoretical model and calculations presented in this paper (see Paper **IX**).

XI **Laser-plasma electron acceleration in dielectric capillary tubes**

G. Genoud, K. Cassou, F. Wojda, H. E. Ferrari, C. Kamperidis, M. Burza, A. Persson, J. Uhlig, S. Kneip, S. P. D. Mangles, A.

Lifschitz, B. Cros and C.-G. Wahlström
As part of the experimental team, the author was involved in planning and performing the experiment, and was involved in the critical revision of the manuscript. In particular, he managed the laser system and helped with the use of the x-ray camera.

XII **Enhancement of x-rays generated by a guided laser wakefield accelerator inside capillary tubes**
J. Ju, K. Svensson, A. Döpp, H. E. Ferrari, K. Cassou, O. Neveu, G. Genoud, F. Wojda, M. Burza, A. Persson, O. Lundh, C.-G. Wahlström and B. Cros
As part of the experimental team, the author was involved in the experiment and the critical revision of the manuscript. In particular he shared the responsibility for the x-ray camera, filter array and laser operation.

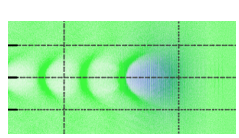

Acknowledgements

I would like to express my sincere thanks to my supervisor, Prof. Claes-Göran Wahlström. In fact, I could hardly imagine any better, more friendly or experienced tutor, who even if seemingly drowning in work always made me feel welcome in his office, no matter how high the piles of paperwork on his desk. Thanks as well to my co-supervisor Prof. Sune Svanberg. Special thanks also to my dear colleagues, Franck Wojda, Olle Lundh and Martin Hansson, with whom I had the pleasure of sharing an office. Thank you for plenty of inspiring discussions! Thanks also to Anders Persson. I learned so much about lasers and optics just by looking over your shoulders for a year. Interestingly, you always seemed to have the right gadget somewhere lying in your office if I needed some particular kind of equipment to get some diagnostics running. Thanks to Kristoffer Svensson, Lovisa Senje and in particular to Guillaume Genoud for the very professional and effective way we worked together in the laboratory. Many thanks as well to all my collaborators in Umeå, Oxford, London, Glasgow, Nizhny Novgorod and Orsay for the exciting times and physics we did. It was amazing! In particular I'd like to thank Prof. Paul McKenna for inviting me to two experiments at the Vulcan laser. These have been exciting times for me!

Grosser Dank geht natürlich auch an meine Familie, die mich auf all meinen Lebenswegen immer unterstützt hat und mir immer das Gefühl von Sicherheit und Geborgenheit gab.

Till slut vill jag gärna tacka mina trognaste vänner som alltid var där för mig med råd och tröst i fall det skulle behövas, såsom för att dela glada stunder med mig. Särskilda kramar för många glada timmar och spännande diskussioner om allt möjligt går till Anja Hoppe, Markus Nilsson och Anja Ödman.

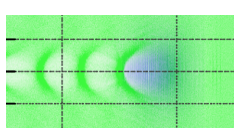

References

[1]. John David Jackson. *Klassische Elektrodynamik*. Walter de Gruyter 3 edition (2002).

[2]. Wolfgang Demtröder. *Experimentalphysik 2* vol. 2. Springer 2 edition (1999).

[3]. Fernando Haas. *Quantum Plasmas - An Hydrodynamic Approach* vol. 65. Springer Series on Atomic, Optical, and Plasma Physics (2011).

[4]. Torsten Fliebach. *Elektrodynamik, Lehrbuch zur Theoretischen Physik II* vol. 2. Spektrum Akademischer Verlag 3 edition (2000).

[5]. P. Sprangle, Cha-Mei Tang and E. Esarey. *Relativistic Self-Focusing of Short-Pulse Radiation Beams in Plasmas*. Plasma Science, IEEE Transactions **15**, 145 –153 (1987).

[6]. Paul Gibbon. *Short Pulse Laser Interactions with Matter*. Imperial College Press (2005).

[7]. H. Fouckhardt. *Photonik*. Teubner Studienbuecher (1994).

[8]. Wolfgang Demtröder. *Laser Spectroscopy*. Springer 3 edition (1981).

[9]. E. Esarey, C. B. Schroeder and W. P. Leemans. *Physics of laser-driven plasma-based electron accelerators*. Reviews of Modern Physics **81**, 1229–1285 (2009).

[10]. E. Yablonovitch. *Energy conservation in the picosecond and subpicosecond photoelectric effect*. Physical Review Letters **60**, 795–796 (1988).

[11]. W.M. Wood, C.W. Siders and M.C. Downer. *Femtosecond growth dynamics of an underdense ionization front measured by spectral blueshifting*. Plasma Science, IEEE Transactions **21**, 20 –33 (1993).

[12]. S. Bulanov, N. Naumova, F. Pegoraro and J. Sakai. *Particle injection into the wave acceleration phase due to nonlinear wake wave breaking*. Physical Review E **58**, R5257–R5260 (1998).

[13]. H. Suk, N. Barov, J. B. Rosenzweig and E. Esarey. *Plasma Electron Trapping and Acceleration in a Plasma Wake Field Using a Density Transition*. Physical Review Letters **86**, 1011–1014 (2001).

[14]. C. G. R. Geddes, K. Nakamura, G. R. Plateau, Cs. Toth, E. Cormier-Michel, E. Esarey, C. B. Schroeder, J. R. Cary and W. P. Leemans. *Plasma-Density-Gradient Injection of Low Absolute-Momentum-Spread Electron Bunches*. Physical Review Letters **100**, 215004 (2008).

[15]. Donna Strickland and Gerard Mourou. *Compression of amplified chirped optical pulses*. Optics Communications **55**, 447 – 449 (1985).

[16]. D. E. Spence, P. N. Kean and W. Sibbett. *60-fsec pulse generation from a self-mode-locked Ti:sapphire laser*. Optics Letters **16**, 42–44 (1991).

[17]. G. Cheriaux, P. Rousseau, F. Salin, J. P. Chambaret, Barry Walker and L. F. Dimauro. *Aberration-free stretcher design for ultrashort-pulse amplification*. Optics Letters **21**, 414–416 (1996).

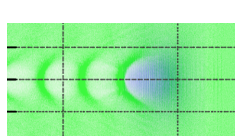

[18]. Frédéric Druon, Gilles Chériaux, Jérôme Faure, John Nees, Marc Nantel, Anatoly Maksimchuk, Gérard Mourou, Jean Christophe Chanteloup and Gleb Vdovin. *Wave-front correction of femtosecond terawatt lasers by deformable mirrors.* Optics Letters **23**, 1043–1045 (1998).

[19]. Daniel J. Kane and Rick Trebino. *Single-shot measurement of the intensity and phase of an arbitrary ultrashort pulse by using frequency-resolved optical gating.* Optics Letters **18**, 823–825 (1993).

[20]. A. Dubietis, G. Jonuauskas and A. Piskarskas. *Powerful femtosecond pulse generation by chirped and stretched pulse parametric amplification in BBO crystal.* Optics Communications **88**, 437 – 440 (1992).

[21]. Ian N. Ross, John L. Collier, Pavel Matousek, Colin N. Danson, David Neely, Ric M. Allott, Dave A. Pepler, Cristina Hernandez-Gomez and Karoly Osvay. *Generation of terawatt pulses by use of optical parametric chirped pulse amplification.* Applied Optics **39**, 2422–2427 (2000).

[22]. Y. Glinec, G. Genoud, O. Lundh, A. Persson and C.-G. Wahlström. *Evolution of energy spectrum from laser-accelerated protons witha 100 fs intense prepulse.* Applied Physics B: Lasers and Optics **93**, 317–321 (2008).

[23]. P. McKenna, D.C. Carroll, O. Lundh, F. Nrnberg, K. Markey, S. Bandyopadhyay, D. Batani, R.G. Evans, R. Jafer, S. Kar, D. Neely, D. Pepler, M.N. Quinn, R. Redaelli, M. Roth, C.-G. Wahlstrm, X.H. Yuan and M. Zepf. *Effects of front surface plasma expansion on proton acceleration in ultraintense laser irradiation of foil targets.* Laser and Particle Beams **26**, 591–596 (2008).

[24]. N. Minkovski, G. I. Petrov, S. M. Saltiel, O. Albert and J. Etchepare. *Nonlinear polarization rotation and orthogonal polarization generation experienced in a single-beam configuration.* Journal of the Optical Society of America B **21**, 1659–1664 (2004).

[25]. Aurélie Jullien, Olivier Albert, Frédéric Burgy, Guy Hamoniaux, Jean-Philippe Rousseau, Jean-Paul Chambaret, Frédérika Augé-Rochereau, Gilles Chériaux, Jean Etchepare, Nikolay Minkovski and Solomon M. Saltiel. 10^{-10} *temporal contrast for femtosecond ultraintense lasers by cross-polarized wave generation.* Optics Letters **30**, 920–922 (2005).

[26]. B. Dromey, S. Kar, M. Zepf and P. Foster. *The plasma mirror—A subpicosecond optical switch for ultrahigh power lasers.* Review of Scientific Instruments **75**, 645–649 (2004).

[27]. G. Doumy, F. Quéré, O. Gobert, M. Perdrix, Ph. Martin, P. Audebert, J. C. Gauthier, J.-P. Geindre and T. Wittmann. *Complete characterization of a plasma mirror for the production of high-contrast ultraintense laser pulses.* Physical Review E **69**, 026402 (2004).

[28]. B.G. Cartwright, E.K. Shirk and P.B. Price. *A nuclear-track-recording polymer of unique sensitivity and resolution.* Nuclear Instruments and Methods **153**, 457 – 460 (1978).

[29]. Christopher G. Soares. *Radiochromic film dosimetry.* Radiation Measurements **41**, S100 – S116 (2006). The 2nd Summer School on Solid State Dosimetry: Concepts and Trends in Medical Dosimetry.

[30]. D E Evans and J Katzenstein. *Laser light scattering in laboratory plasmas.* Reports on Progress in Physics **32**, 207 (1969).

[31]. P. Gibbon, P. Monot, T. Auguste and G. Mainfray. *Measurable signatures of relativistic self-focusing in underdense plasmas.* Physics of Plasmas **2**, 1305–1310 (1995).

[32]. J. Osterhoff, A. Popp, Zs. Major, B. Marx, T. P. Rowlands-Rees, M. Fuchs, M. Geissler, R. Hörlein, B. Hidding, S. Becker, E. A. Peralta, U. Schramm, F. Grüner, D. Habs, F. Krausz, S. M. Hooker and S. Karsch. *Generation of Stable, Low-Divergence Electron Beams by*

Laser-Wakefield Acceleration in a Steady-State-Flow Gas Cell. Physical Review Letters **101**, 085002 (2008).

[33]. C. E. Clayton, J. E. Ralph, F. Albert, R. A. Fonseca, S. H. Glenzer, C. Joshi, W. Lu, K. A. Marsh, S. F. Martins, W. B. Mori, A. Pak, F. S. Tsung, B. B. Pollock, J. S. Ross, L. O. Silva and D. H. Froula. *Self-Guided Laser Wakefield Acceleration beyond 1 GeV Using Ionization-Induced Injection*. Physical Review Letters **105**, 105003 (2010).

[34]. T. R. Clark and H. M. Milchberg. *Time- and Space-Resolved Density Evolution of the Plasma Waveguide*. Physical Review Letters **78**, 2373–2376 (1997).

[35]. Mikhail Polyanskiy. Refractive index database (2012). http://refractiveindex.info/?group=GASES&material=Helium.

[36]. R. Benattar, C. Popovics and R. Sigel. *Polarized light interferometer for laser fusion studies*. Review of Scientific Instruments **50**, 1583 –1586 (1979).

[37]. Eugene Hecht. *Optics*. Addison Wesley Longman 3 edition (1998).

[38]. Tannhauser Lipson, Lipson. *Optik*. Springer, Berlin 1 edition (1997).

[39]. W. S. Porter and Jr. E. M. Bock. *Faraday Effect in a Plasma*. American Journal of Physics **33**, 1070–1073 (1965).

[40]. Shen. *The Principles of Nonlinear Optics*. Wiley Interscience (2003).

[41]. Gary D. Schmidt, Hugh C. Harris, James Liebert, Daniel J. Eisenstein, Scott F. Anderson, J. Brinkmann, Patrick B. Hall, Michael Harvanek, Suzanne Hawley, S. J. Kleinman, Gillian R. Knapp, Jurek Krzesinski, Don Q. Lamb, Dan Long, Jeffrey A. Munn, Eric H. Neilsen, Peter R. Newman, Atsuko Nitta, David J. Schlegel, Donald P. Schneider, Nicole M. Silvestri, J. Allyn Smith, Stephanie A. Snedden, Paula Szkody and Dan Vanden Berk. *Magnetic White Dwarfs from the Sloan Digital Sky Survey: The First Data Release*. The Astrophysical Journal **595**, 1101 (2003).

[42]. R. Lichters, J. Meyer ter Vehn and A. Pukhov. *Short-pulse laser harmonics from oscillating plasma surfaces driven at relativistic intensity*. Physics of Plasmas **3**, 3425–3437 (1996).

[43]. M. C. Kaluza, H.-P. Schlenvoigt, S. P. D. Mangles, A. G. R. Thomas, A. E. Dangor, H. Schwoerer, W. B. Mori, Z. Najmudin and K. M. Krushelnick. *Measurement of Magnetic-Field Structures in a Laser-Wakefield Accelerator*. Physical Review Letters **105**, 115002 (2010).

[44]. I. H. Hutchinson. *Principles of Plasma Diagnostics*. Cambridge University Press 2 edition (2005).

[45]. Sergio E Segre. *A review of plasma polarimetry - theory and methods*. Plasma Physics and Controlled Fusion **41**, R57 (1999).

[46]. C.K. Birdsall. *Particle-in-cell charged-particle simulations, plus Monte Carlo collisions with neutral atoms, PIC-MCC*. Plasma Science, IEEE Transactions **19**, 65 –85 (1991).

[47]. W. Lu, M. Tzoufras, C. Joshi, F. S. Tsung, W. B. Mori, J. Vieira, R. A. Fonseca and L. O. Silva. *Generating multi-GeV electron bunches using single stage laser wakefield acceleration in a 3D nonlinear regime*. Physical Review Special Topics - Accelerators and Beams **10**, 061301 (2007).

[48]. S. P. D. Mangles, C. D. Murphy, Z. Najmudin, A. G. R. Thomas, J. L. Collier, A. E. Dangor, E. J. Divall, P. S. Foster, J. G. Gallacher, C. J. Hooker, D. A. Jaroszynski, A. J. Langley, W. B. Mori, P. A. Norreys, F. S. Tsung, R. Viskup, B. R. Walton and K. Krushelnick. *Monoenergetic beams of relativistic electrons from intense laser-plasma interactions*. Nature **431**, 535 (2004).

[49]. C. G. R. Geddes, Cs. Toth, J. van Tilborg, E. Esarey, C. B. Schroeder,

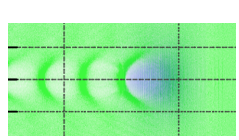

D. Bruhwiler, C. Nieter, J. Cary and W. P. Leemans. *High-quality electron beams from a laser wakefield accelerator using plasma-channel guiding.* Nature **431**, 538 (2004).

[50]. J. Faure, Y. Glinec, A. Pukhov, S. Kiselev, S. Gordienko, E. Lefebvre, J.-P. Rousseau, F. Burgy and V. Malka. *A laserplasma accelerator producing monoenergetic electron beams.* Nature **431**, 541 (2004).

[51]. E. Esarey, R. F. Hubbard, W. P. Leemans, A. Ting and P. Sprangle. *Electron Injection into Plasma Wakefields by Colliding Laser Pulses.* Physical Review Letters **79**, 2682–2685 (1997).

[52]. J. Faure, C. Rechatin, A. Norlin, Y. Lifschitz, A. andGlinec and V. Malka. *Controlled injection and acceleration of electrons in plasma wakefields by colliding laser pulses.* Nature **444**, 737 (2006).

[53]. V. Malka, J. Faure, C. Rechatin, A. Ben-Ismail, J. K. Lim, X. Davoine and E. Lefebvre. *Laser-driven accelerators by colliding pulses injection: A review of simulation and experimental results.* Physics of Plasmas **16**, 056703 (2009).

[54]. A. Beck, X. Davoine and E. Lefebvre. *Scaling laws for electron cold injection in the narrow collision pulse approximation.* New Journal of Physics **13**, 093016 (2011).

[55]. K. Schmid, A. Buck, C. M. S. Sears, J. M. Mikhailova, R. Tautz, D. Herrmann, M. Geissler, F. Krausz and L. Veisz. *Density-transition based electron injector for laser driven wakefield accelerators.* Physical Review Special Topics - Accelerators and Beams **13**, 091301 (2010).

[56]. J. Faure, C. Rechatin, O. Lundh, L. Ammoura and V. Malka. *Injection and acceleration of quasimonoenergetic relativistic electron beams using density gradients at the edges of a plasma channel.* Physics of Plasmas **17**, 083107 (2010).

[57]. A. Pak, K. A. Marsh, S. F. Martins, W. Lu, W. B. Mori and C. Joshi. *Injection and Trapping of Tunnel-Ionized Electrons into Laser-Produced Wakes.* Physical Review Letters **104**, 025003 (2010).

[58]. C. McGuffey, A. G. R. Thomas, W. Schumaker, T. Matsuoka, V. Chvykov, F. J. Dollar, G. Kalintchenko, V. Yanovsky, A. Maksimchuk, K. Krushelnick, V. Yu. Bychenkov, I. V. Glazyrin and A. V. Karpeev. *Ionization Induced Trapping in a Laser Wakefield Accelerator.* Physical Review Letters **104**, 025004 (2010).

[59]. E. Esarey, P. Sprangle, J. Krall and A. Ting. *Overview of plasma-based accelerator concepts.* Plasma Science, IEEE Transactions **24**, 252 –288 (1996).

[60]. A. Butler, D. J. Spence and S. M. Hooker. *Guiding of High-Intensity Laser Pulses with a Hydrogen-Filled Capillary Discharge Waveguide.* Physical Review Letters **89**, 185003 (2002).

[61]. W. P. Leemans, B. Nagler, A. J. Gonsalves, Cs. Tth, K. Nakamura, C. G. R. Geddes, E. Esarey, C. B. Schroeder and S. M. Hooker. *GeV electron beams from a centimetre-scale accelerator.* Nature Physics **2**, 696 (2006).

[62]. S. Karsch, J. Osterhoff, A. Popp, T. P. Rowlands-Rees, Zs. Major, M. Fuchs, B. Marx, R. Hörlein, K. Schmid, L. Veisz, S. Becker, U. Schramm, B. Hidding, G. Pretzler, D. Habs, F. Grüner, F. Krausz and S. M. Hooker. *GeV-scale electron acceleration in a gas-filled capillary discharge waveguide.* New Journal of Physics **9**, 415 (2007).

[63]. Chunmei Wang, Ji Li, Jun Sun and Xisheng Luo. *Shock-wave-based density down ramp for electron injection.* Physical Review Special Topics - Accelerators and Beams **15**, 020401 (2012).

[64]. Wolfgang Demtröder. *Experimentalphysik 1* vol. 1. Springer 2 edition (1998).

[65]. S. C. Wilks, A. B. Langdon, T. E. Cowan, M. Roth, M. Singh, S. Hatchett, M. H. Key, D. Pennington, A. MacKinnon and R. A. Snavely. *Energetic proton generation in ultra-intense laser–solid interactions.* Physics of Plasmas **8**, 542–549 (2001).

[66]. V. S. Rastunkov and V. P. Krainov. *Electron Stochastic Heating in the Interaction of a Short Laser Pulse with Overdense Plasma.* Laser Physics **15**, 262 (2005).

[67]. Feng He, Wei Yu, Peixiang Lu, Han Xu, Liejia Qian, Baifei Shen, Xiao Yuan, Ruxin Li and Zhizhan Xu. *Ponderomotive acceleration of electrons by a tightly focused intense laser beam.* Physical Review E **68**, 046407 (2003).

[68]. Erik Lefebvre and Guy Bonnaud. *Nonlinear electron heating in ultrahigh-intensity-laser-plasma interaction.* Physical Review E **55**, 1011–1014 (1997).

[69]. J. P. Freidberg, R. W. Mitchell, R. L. Morse and L. I. Rudsinski. *Resonant Absorption of Laser Light by Plasma Targets.* Physical Review Letters **28**, 795–799 (1972).

[70]. F. Brunel. *Not-so-resonant, resonant absorption.* Physical Review Letters **59**, 52–55 (1987).

[71]. J. Psikal, V. T. Tikhonchuk, J. Limpouch and O. Klimo. *Lateral hot electron transport and ion acceleration in femtosecond laser pulse interaction with thin foils.* Physics of Plasmas **17**, 013102 (2010).

[72]. P. McKenna, D. C. Carroll, R. J. Clarke, R. G. Evans, K. W. D. Ledingham, F. Lindau, O. Lundh, T. McCanny, D. Neely, A. P. L. Robinson, L. Robson, P. T. Simpson, C.-G. Wahlström and M. Zepf. *Lateral Electron Transport in High-Intensity Laser-Irradiated Foils Diagnosed by Ion Emission.* Physical Review Letters **98**, 145001 (2007).

[73]. S. Buffechoux, J. Psikal, M. Nakatsutsumi, L. Romagnani, A. Andreev, K. Zeil, M. Amin, P. Antici, T. Burris-Mog, A. Compant-La-Fontaine, E. d'Humières, S. Fourmaux, S. Gaillard, F. Gobet, F. Hannachi, S. Kraft, A. Mancic, C. Plaisir, G. Sarri, M. Tarisien, T. Toncian, U. Schramm, M. Tampo, P. Audebert, O. Willi, T. E. Cowan, H. Pépin, V. Tikhonchuk, M. Borghesi and J. Fuchs. *Hot Electrons Transverse Refluxing in Ultraintense Laser-Solid Interactions.* Physical Review Letters **105**, 015005 (2010).

[74]. I. M. Frank and V. L. Ginzburg. *Radiation from a uniformly moving electron passing from one medium to another.* Journal of Physics-USSR **9**, 353 (1945).

[75]. J. J. Santos, F. Amiranoff, S. D. Baton, L. Gremillet, M. Koenig, E. Martinolli, M. Rabec Le Gloahec, C. Rousseaux, D. Batani, A. Bernardinello, G. Greison and T. Hall. *Fast Electron Transport in Ultraintense Laser Pulse Interaction with Solid Targets by Rear-Side Self-Radiation Diagnostics.* Physical Review Letters **89**, 025001 (2002).

[76]. NIST. PSTAR : Stopping Power and Range Tables for Protons (2012). http://physics.nist.gov/cgi-bin/Star/ap_table.pl.

[77]. Victor Malka, Sven Fritzler, Erik Lefebvre, Emmanuel d'Humières, Régis Ferrand, Georges Grillon, Claude Albaret, Samuel Meyroneinc, Jean-Paul Chambaret, Andre Antonetti and Danièle Hulin. *Practicability of protontherapy using compact laser systems.* Medical Physics **31**, 1587–1592 (2004).

[78]. Ute Linz and Jose Alonso. *What will it take for laser driven proton accelerators to be applied to tumor therapy?* Physical Review Special Topics - Accelerators and Beams **10**, 094801 (2007).

[79]. M. Allen, Y. Sentoku, P. Audebert, A. Blazevic, T. Cowan, J. Fuchs, J. C. Gauthier, M. Geissel, M. Hegelich, S. Karsch, E. Morse, P. K. Patel

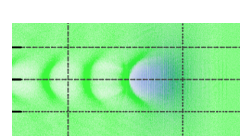

and M. Roth. *Proton spectra from ultraintense laser–plasma interaction with thin foils: Experiments, theory, and simulation.* Physics of Plasmas **10**, 3283–3289 (2003).

[80]. H. Schwoerer, S. Pfotenhauer, O. Jäckel, K.-U. Amthor, B. Liesfeld, W. Ziegler, R. Sauerbrey, K. W. D. Ledingham and T. Esirkepov. *Laser-plasma acceleration of quasi-monoenergetic protons from microstructured targets.* Nature **439**, 445 (2006).

[81]. A. V. Brantov, V. T. Tikhonchuk, O. Klimo, D. V. Romanov, S. Ter-Avetisyan, M. Schnürer, T. Sokollik and P. V. Nickles. *Quasi-monoenergetic ion acceleration from a homogeneous composite target by an intense laser pulse.* Physics of Plasmas **13**, 122705 (2006).

[82]. B. M. Hegelich, B. J. Albright, J. Cobble, K. Flippo, S. Letzring, M. Paffett, H. Ruhl, J. Schreiber, R. K. Schulze and J. C. J. C. Fernández. *Laser acceleration of quasi-monoenergetic MeV ion beams.* Nature **439**, 441 (2006).

[83]. Wolfgang Demtröder. *Experimentalphysik 3* vol. 1. Springer 2 edition (1998).

Papers

Paper I

Hollow microspheres as targets for staged laser-driven proton acceleration

M. Burza, A. Gonoskov, G. Genoud, A. Persson, K. Svensson, M. Quinn, P. McKenna, M. Marklund and C.-G. Wahlström.

New Journal of Physics **13**, 013030 (2011).

New Journal of Physics
The open-access journal for physics

Hollow microspheres as targets for staged laser-driven proton acceleration

M Burza[1,5], A Gonoskov[2,3], G Genoud[1], A Persson[1], K Svensson[1], M Quinn[4], P McKenna[4], M Marklund[2] and C-G Wahlström[1]

[1] Department of Physics, Lund University, PO Box 118, SE-221 00 Lund, Sweden
[2] Department of Physics, Umeå University, SE-901 87 Umeå, Sweden
[3] Institute of Applied Physics, Russian Academy of Sciences, 46 Ulyanov Street, Nizhny Novgorod 603950, Russia
[4] SUPA Department of Physics, University of Strathclyde, Glasgow, G4 0NG, UK
E-mail: matthias.burza@fysik.lth.se

New Journal of Physics **13** (2011) 013030 (14pp)
Received 21 July 2010
Published 21 January 2011
Online at http://www.njp.org/
doi:10.1088/1367-2630/13/1/013030

Abstract. A coated hollow core microsphere is introduced as a novel target in ultra-intense laser–matter interaction experiments. In particular, it facilitates staged laser-driven proton acceleration by combining conventional target normal sheath acceleration (TNSA), power recycling of hot laterally spreading electrons and staging in a very simple and cheap target geometry. During TNSA of protons from one area of the sphere surface, laterally spreading hot electrons form a charge wave. Due to the spherical geometry, this wave refocuses on the opposite side of the sphere, where an opening has been laser micromachined. This leads to a strong transient charge separation field being set up there, which can post-accelerate those TNSA protons passing through the hole at the right time. Experimentally, the feasibility of using such targets is demonstrated. A redistribution is encountered in the experimental proton energy spectra, as predicted by particle-in-cell simulations and attributed to transient fields set up by oscillating currents on the sphere surface.

[5] Author to whom any correspondence should be addressed.

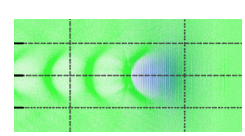

Contents

1. Introduction

Laser-driven ion acceleration is an area of research that currently attracts significant scientific interest. The ion beams produced in these experiments have several attractive characteristics, such as very low transverse emittance and small virtual source size [1] together with a short pulse duration (at the source). Proposed applications of this possibly compact ion beam source include ion radiotherapy for cancer treatment [2, 3], isotope production for medical imaging techniques [4], proton radiography of inertial fusion plasmas [5] and implementation as injectors for future ion accelerators.

In a typical experiment, a high-power laser pulse of short duration, $\leqslant$ps, is focused on the surface of a thin foil to an intensity exceeding $10^{19}\,\mathrm{W\,cm^{-2}}$. The laser interacts with target electrons and a population of hot electrons with a Maxwellian temperature of typically a few MeV is generated. A large fraction of these electrons traverse the target and build up exceptionally high electrostatic fields, $\sim\mathrm{TV\,m^{-1}}$, at the rear surface of the foil, in a direction normal to the target surface. Atoms on the target surface are rapidly field ionized and accelerated. This is referred to as target normal sheath acceleration (TNSA) [6]. Because of the presence of hydrocarbon and water vapour on the surfaces of the foils (in typical vacuum conditions $\sim 10^{-5}$ mbar), protons are the dominating ion species. Due to their high charge-to-mass ratio, protons are more efficiently accelerated than heavier ions.

The acceleration of protons behind the target foil is very rapid, due to the high field strength. However, this field is present during a short time only, limiting the maximum energy reached by the protons. The energy spectra of these proton beams exhibit a longitudinal emittance comparable to that of conventional accelerators, with a quasi-exponential shape and a distinct cut-off energy [6]. The divergence of the proton beam is typically $\sim 30^{\circ}$ half-angle. Significant theoretical and experimental efforts have been devoted to the exploration of a means of boosting the maximum proton energy without the use of increasingly larger laser systems [7, 8].

Practical limitations in laser size and costs, laser materials and repetition rate are necessitating alternative or modified laser acceleration schemes and targets in order to further increase the peak proton energy. It has been found that the maximum proton energy and laser-to-ion energy conversion is enhanced by the use of ultra-thin targets in combination with laser pulses of high temporal contrast [9]. Staging, i.e. combining two or more accelerator stages in series,

may be one way to post-accelerate a selected portion of the protons accelerated in a preceding TNSA stage and thus raise the maximum proton energy and reduce the energy spread [10]. In parallel, extensive studies on controlling beam parameters such as collimation and means to produce quasi-monoenergetic energy distributions have been carried out [11, 12]. In particular, mass-limited targets can be used to reduce the energy spread of the protons [13]–[15]. Curved target foils [16], electrostatic charging of specially shaped targets [17] and separate focusing cylinders [18] enable spatial shaping of the proton beam.

In addition, experiments and numerical modelling have shown that while part of the hot electron distribution is passing through the target foil, a significant part is also spreading laterally along the target. McKenna *et al* [19] found that, when these electrons reach the target edges, after a time determined by the geometrical size of the target and the lateral electron transport velocity, they establish quasi-static electric fields, similar to the one produced behind the target during TNSA, resulting in ion acceleration from the edges. Normally, this mechanism just represents a loss of absorbed laser energy, which is converted to hot electrons but not contributing to the quasi-static sheath built up at the target rear side. In a recent study [15], however, using very small diameter targets, the refluxing of transversely spreading electrons was found to enhance and smooth the sheath field for TNSA from the rear surface.

In this paper, we discuss the use of hollow microspheres, as novel targets for laser acceleration of protons. With this target, several of the above features are combined, which may facilitate improved laser-to-proton efficiency, eventually leading to increased proton energy and reduced divergence. Lateral electron transport is here utilized to set up a post-acceleration field for staged acceleration.

The basic idea behind our approach is to use hollow microspheres with diameters of about 10–50 μm and sub-micrometer wall thickness. In each sphere a small circular opening is made. We refer to the position of this opening as the 'north pole' (see figure 1). A short pulse laser irradiates the sphere at the 'south pole', where TNSA takes place. The primary proton direction will be along the z-axis, defined as the axis from the south pole passing through the north pole of the sphere. The spherical surface, with TNSA taking place from the concave side, results in a collimated or even converging proton beam. Therefore, all the protons can be made to pass through the opening at the north pole. In addition—and this is the key point—electrons leaving the laser focus laterally in any direction along the sphere surface will be guided on different longitudes over the sphere and eventually reach the edge of the opening at the north pole simultaneously after some given time. A very strong quasi-static electric field is then formed in the opening, along the z-axis. This quasi-static field will post-accelerate protons passing through the opening at the correct time.

In our approach to test this idea, theoretical and experimental studies go hand in hand:

To test the experimental feasibility, we perform experiments, at the Lund High Power Laser Facility, with commercially available hollow microspheres of 50 μm diameter.[6] The walls of these spheres are made of glass with a thickness of 0.5–1 μm and coated with a $\sim$50 nm silver layer (see the inset of figure 1), which facilitates the optical alignment and guiding of electrons along the sphere surface. Openings of different sizes are laser micromachined. We present these experiments in section 2, including target preparation, fixation and alignment in the experimental setup together with first results.

[6] Such spheres are very low weight and low cost objects. They weigh only some tens of ng each and cost $\sim$1 USD for 10^5 Ag-coated spheres. The manufacturing of the hole at the north pole, however, is part of the local target preparation and not included in the price.

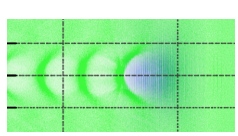

IOP Institute of Physics DEUTSCHE PHYSIKALISCHE GESELLSCHAFT

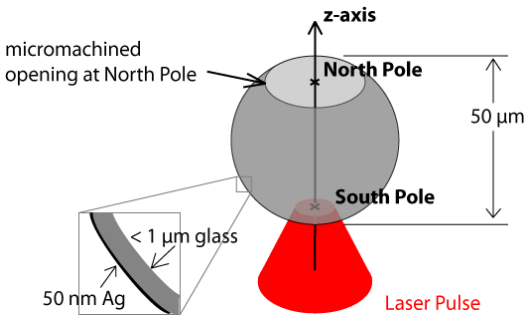

Figure 1. A glass hollow microsphere, with an ∼50 nm silver coating on its $\leqslant 1\ \mu$m thick wall, is struck by a laser pulse at the 'south pole'. TNSA protons are emitted through a circular opening at the 'north pole' and post-accelerated.

In parallel, we perform particle-in-cell (PIC) simulations of hollow conducting spheres with openings, irradiated by short laser pulses. These simulations, presented in section 3, qualitatively describe the dynamics involved.

We discuss the outlook and prospects for further experiments in section 4 and present the conclusions in section 5.

2. Experiment

2.1. Target preparation

Isolated spheres are suspended into a nylon mesh grid, where both the front and back sides of each sphere are accessible for further processing. Openings in the spheres are made with a confocal microscope-based laser micromachining setup. In a two-step process the silver coating is ablated in a well-defined region on the sphere surface, followed by ablation of the glass substrate. This is done with a lateral resolution of about 2 μm utilizing a femtosecond laser system running at 10 Hz repetition rate. Real-time target observation and a high numerical aperture in the setup facilitate both high drilling accuracy and control in the transverse direction, while at the same time preventing the TNSA surface inside the sphere from being damaged in the process.

Afterwards, the target, which is still fixed in the nylon mesh, is mounted in a holder. This also accommodates a gold mesh, placed close to the sphere's north pole, to extract information about proton trajectories, as will be discussed later.

2.2. Experimental setup

The Lund multi-terrawatt laser, which is a Ti : sapphire system based on chirped pulse amplification (CPA), is used for this experiment. In this experiment, it is tuned to 850 mJ pulse energy at 805 nm centre wavelength with a typical pulse duration of 42 fs FWHM. Due to the sub-micron thickness of the sphere walls and the thin silver coating on them, an amplified spontaneous emission (ASE) contrast better than 10^8 some tens of picoseconds prior to the pulse peak is desirable.

IOP Institute of Physics DEUTSCHE PHYSIKALISCHE GESELLSCHAFT

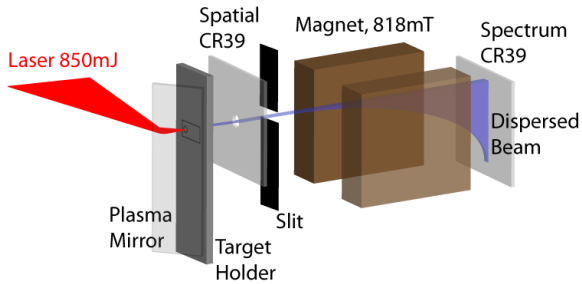

Figure 2. The laser pulse (red) is impinging on the PM at Brewster's angle, which reflects the pulse onto the target at normal incidence. After some centimetres of free passage the resulting particle beam (blue) reaches a CR-39 detector plate, which has the function of providing a lateral image of the beam profile and at the same time enabling a fraction of the beam to enter the slit of a subsequent permanent magnet spectrometer. After traversing the field, a vertically dispersed spectrum is recorded on a second CR-39 plate.

To optimize contrast on a very fast timescale, the convergent, horizontally polarized laser pulse hits a dielectric plasma mirror (PM) at Brewster's angle (3.0 ± 0.2 mm) prior to the primary focus. At this location, the PM is operating at $(8.5 \pm 1.1) \times 10^{15}$ W cm^{-2} spatially averaged peak intensity over the beam diameter (I_{centre}/e^2). When activated, it deflects the laser beam onto the target, at normal incidence (see figure 2).

Plasma mirror characteristics have been investigated by many groups (see e.g. [20]–[22]). A PM assembly, similar to the one applied in the present experiment, was utilized by Neely *et al* [9], using the Lund laser system. In that experiment, proton beams from Al foil targets as thin as 20 nm were observed. Our experiment relates to that one as the very thin silver coating on our target surface is of comparable thickness. Ray tracing, taking a 22 nm FWHM broad Gaussian spectrum and a p-polarized converging beam into account, predicts a contrast increase by a factor of 100 in our experiment (assuming a maximum reflectivity ∼50% from the PM [22]).

Together with a third-order autocorrelation contrast measurement, 2 ps prior to the main pulse, a contrast better than 10^6 on the target can be guaranteed for an intact rear TNSA surface during the first phase of acceleration. This contrast is due to non-perfect compression in the CPA chain and should not be mistaken for the ASE contrast, encountered on a longer picosecond timescale prior to the main pulse, which is of the order 10^{11} on the target.

The infrared (IR) pulse is focused by an $f/3$ off-axis parabolic mirror (OAP) down to a 4.4 μm spot diameter (intensity FWHM), containing 39% of the total energy and reaching a peak intensity of $\sim 3 \times 10^{19}$ W cm^{-2}. Target positioning is accomplished by a confocal imaging system: an expanded HeNe laser beam is superimposed with the IR and a confocal reflection from the silver-coated target surface is imaged, utilizing the OAP as an objective.

The detector system for protons, designed to simultaneously provide a spatial beam profile and a spectrum, is depicted in figure 2. It consists of a primary CR-39 plate at some centimetres distance from the target, which is utilized to characterize the transverse spatial beam profile. This plate is covered by a 6 μm Al foil, which stops protons below 0.5 MeV [23]. At its centre,

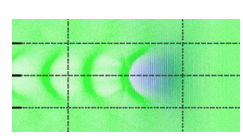

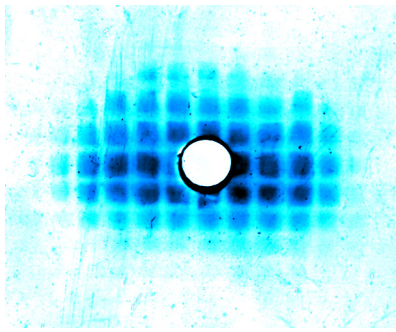

Figure 3. Proton beam profile on a CR-39 plate showing a magnified Au mesh image, recorded (24 ± 0.5) mm distance from the target.

a $\sim$4 mm diameter hole enables protons close to the target normal axis to continue to the momentum dispersive part of the detector and access an 88 μm wide entrance slit of a permanent magnet spectrometer, where they traverse a 51 mm long and 818 mT strong effective field. The vertically dispersed proton spectrum is then recorded by a second CR-39 plate with an accuracy of $\pm$0.2 MeV at 4 MeV proton energy. By this arrangement, spectra can be correlated to the lateral position within the particle beam.

2.3. Experimental measurements and results

After optimization of the PM working distance with the help of proton beams originating from flat 400 nm thick Al foil targets, shots were taken on machined and unmachined microspheres as well as on 0.9 μm thick Mylar foil targets.

Several shots were taken on machined microspheres with holes of typically 18 μm diameter. An example of a proton beam imprint originating from such a sphere on the spatial CR-39 plate, covered by 6 μm Al and located at (24.0 ± 0.5) mm distance from the target, can be seen in figure 3.

One can see a slightly oval beam profile. This slight asymmetry can be attributed either to a non-uniform Ag coating on the sphere's south pole or to grazing incidence of the laser energy around the z-axis due to the curved sphere surface: at a given latitude, the linear polarization of the laser pulse will be incident as p- or s-polarization on the spherical surface, depending on the azimuthal angle. Polarization effects will also facilitate different strengths of the surface currents, depending on the longitude where electrons propagate around the sphere [24].

One can further see the imprint of the earlier mentioned Au mesh on the spatial proton beam image, which is introduced into the proton beam path close to the target. This rectangularly shaped 4 μm thick mesh features squared holes with a nominal aperture of 11×11 μm^2 and a lateral wire width of 5 μm. It is fixed at (165 ± 2) μm distance from the rim of the opening of the microsphere. The motivation to introduce this mesh is twofold: firstly, it verifies that protons contributing to the signal on the spatial CR-39 plate are not due to edge emission at the north pole, which would have resulted in a distinctively different shadow image. Secondly, thanks to this mesh the protons can be shown to come from a virtual source located (54 ± 12) μm from the inner sphere TNSA surface, i.e. very close to the opening. This estimate is valid for the majority

IOP Institute of Physics DEUTSCHE PHYSIKALISCHE GESELLSCHAFT

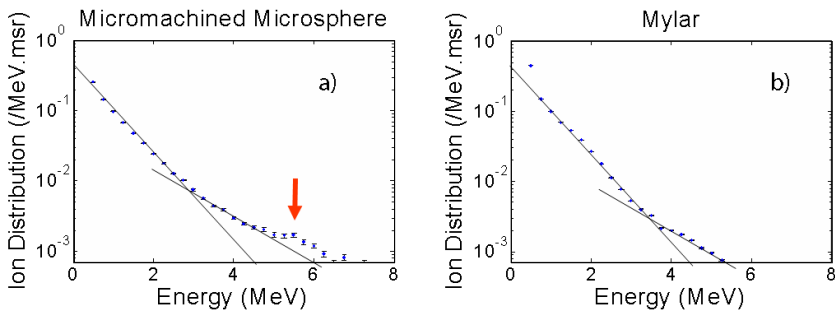

Figure 4. Normalized proton spectra from a microsphere target (a) and a Mylar plane foil (b). The red arrow in (a) indicates a region of constant yield in contrast to the strictly decreasing number density from plane foil TNSA experiments, such as the one depicted in (b); black lines are a dual-temperature guide to the eye.

of particles traversing the opening at late times, where we expect the surface oscillations to have vanished. In order to visualize the effects of a transient field emanating from the rim of the microsphere opening, one would have to filter this image to the appropriate energy. However, as will be discussed later, with our present experimental parameters, we expect only the fastest particles to be affected by these fields, so a filtered signal would become very weak.

By neglecting Coulomb repulsion between protons in the beam, and tracing proton trajectories further back, one can make a rough estimate about the proton emission surface. We find that proton emission seems to occur from a solid angle covering $\approx 140\pi$ msr of the inner shell, measured from the centre of the sphere. This compares to a focal spot, covering $\approx 8\pi$ msr (intensity FWHM), and is consistent with previous observations of the TNSA surface source area being considerably larger than the laser focus [25, 26]. The virtual proton source in a flat foil TNSA experiment [27] was pinpointed to several hundreds of microns distance before the target front side, i.e. the laser-irradiated side. A spherical target, such as the one used for isochoric heating [28, 29], combines ballistic proton propagation with target curvature and an altered electron distribution. A particle focus near the north pole is consistent with these findings.

To further verify that the protons are indeed emitted from the sphere interior, we irradiate closed hollow microspheres that have not gone through the laser micromachining stage. Lacking hydrogenic contaminations, such as water vapour, on the interior surface of the sphere, TNSA of protons is not expected to occur there. Indeed no protons with energies sufficient to be recorded by our diagnostics ($E_{\mathrm{proton}} > 0.8$ MeV) are observed. In addition, lacking the opening and retaining the silver coating, return currents will prevent the formation of a strong edge field at the north pole. This will be further discussed in section 3.1.

Spectra from sphere targets with openings between 18 and 20 μm were taken and a typical spectrum can be seen in figure 4(a). A clear high-energy 'cut off' is not visible in the data, and values above 8 MeV are ignored to ensure that the data presented here are at least one order of magnitude above the noise level. Reference shots are taken on flat 0.9 μm thick Mylar foil targets. A typical proton spectrum can be seen in figure 4(b). Even though the laser absorption

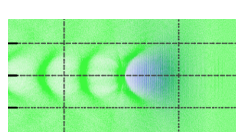

and particle yield are expected to be different as compared to the silver-coated glass surface of the microspheres (∼30 times higher particle number), those shots provide reference spectra, enabling the identification of special features in the microsphere spectra.

All microsphere spectra from the experimental study look very similar, but with an integrated particle yield varying by a factor of 4, which is twice as much as for the Mylar targets. There are indeed features present that could possibly be attributed to a secondary field interaction and a post-acceleration by a secondary field at the sphere opening, which is still prevailing during arrival of the fastest protons. In all microsphere spectra, there is a slight modification of particle yield between 5.5 and 6.5 MeV, where the counts per energy bin remain nearly constant (figure 4(a), red arrow) as compared to the strictly decreasing dual exponential decay observed from the flat foil targets, shot under the same experimental conditions (figure 4(b)). (Likewise, previous experiments carried out with various planar targets using the Lund laser system [30] have resulted in spectra very similar to the ones presented here for Mylar foils.) The plateau in the microsphere spectra can be understood in terms of a spectral redistribution of the order of 1 MeV of proton energies as a result of a secondary field interaction near the opening. Looking at the experiment the other way around, we can regard the protons as a probe for intracavity fields as well. A two-temperature curve fit provides comparable temperatures for low energies for both the targets ((0.6 ± 0.1) MeV and (0.5 ± 0.3) MeV for spheres and Mylar, respectively) but larger values for the high-energy component from the microsphere spectra ((2.0 ± 0.1) MeV) as compared to the foil spectra ((1.6 ± 0.3) MeV).

In the following section, we will discuss the modelling of the present experiment, giving insights into the dynamic processes of hot electron transport on the sphere surface and motivate the observed spectral features. Beyond that, we will consider a means to enhance the post-acceleration mechanism.

3. Simulations

To improve our understanding of the underlying dynamic processes, we have carried out a number of numerical experiments with the parallel PIC code Extreme Laser–Matter Interaction Simulator (ELMIS), developed by the SimLight group [31]. ELMIS is a relativistic code, which uses a parallel fast Fourier transform (FFT) technique to solve Maxwell's equations.

The processes involved in the setup are essentially of two-dimensional (2D) nature. Thus, we perform 2D simulations in order to retain the appropriate space and time scales while still not compromising the physical outcome. However, the 2D nature restricts the interpretation of these results to a qualitative level as scaling laws behave differently in 2D as compared to 3D space.

In the simulations a linearly polarized TEM00 laser pulse (where electric field lies in the plane of simulation) with $\tau_l = 50$ fs duration (Gaussian profile, FWHM) and a total energy of 1 J is focused to a 10 μm spot on the target surface. The laser field reaches a maximum field strength equal to $\sim 3.5\, a_{\mathrm{rel}}$, where $a_{\mathrm{rel}} = 2\pi mc^2/(e\lambda) \approx 3.2 \times 10^{12}\ \mathrm{V\,m^{-1}}$, e and m are the electron charge and mass, respectively, c is the speed of light and $\lambda = 1\ \mu$m is the laser wavelength. This corresponds to a maximum intensity of $2 \times 10^{19}\ \mathrm{W\,cm^{-2}}$. The target consists of a hollow metal sphere with $D_S = 32\ \mu$m diameter and a 10 μm opening. It has a 0.5 μm thick wall, which in our 2D PIC simulation was considered as a (cylindrical) overdense plasma with the electron density of $50\, n_{\mathrm{crit}}$ and an Au^{6+} ion density of $50\, n_{\mathrm{crit}}/6$, where $n_{\mathrm{crit}} = \pi mc^2/(\lambda^2 e^2) \approx 1.1 \times 10^{21}\ \mathrm{cm^{-3}}$ is the critical density for $\lambda = 1\ \mu$m.

To simulate TNSA, we consider a 100 nm contaminant layer of protons and electrons with a density $10\,n_{\rm crit}$, covering the internal surface of the target. The simulation is done for a box size of $64\,\mu$m $\times$ $64\,\mu$m (4096×4096 cells) with absorbing boundaries for the fields and accumulating boundaries for the particles. The initial plasma temperature is set to 16 keV, and the cell size is 15.625 nm, which is approximately 4 times the Debye length for the considered plasma. In the simulation, 100 virtual particles per cell are used for the electrons and Au^{6+} ions and 20 particles per cell are used for the protons; the total number of virtual particles is 4×10^7. The time steps are set to $(2\pi/\omega_{\rm p})/16 \approx 3 \times 10^{-17}$ s, where $\omega_{\rm p} = (4\pi e^2 50 n_{\rm crit}/m)^{1/2}$ is the plasma frequency. The duration limit of the simulation is set to when the leading protons in the accelerating bunch reach the simulation box boundary.

3.1. Simulation results

As the laser pulse reaches the target at the south pole it is reflected from the outer overdense plasma surface, initiating electron heating. This time is set to $t = 0$ in the simulation. Subsequently, protons undergo TNSA from the internal surface and move towards the north pole. A part of the heated electrons leave the plasma, thereby producing an electric field retaining part of the electrons to the target surface. Those trapped hot electrons move along the plasma layer, recirculating near the wall and conserving their momentum in the direction along the surface. Eventually they will arrive at the edge of the sphere opening, where they will leave and return to the plasma layer, thus setting up a charge separation field. This process, albeit for a flat target, was discussed and experimentally observed by McKenna *et al* [19]. Due to the relativistic intensity of the laser pulse, the electrons move with a speed close to c, thus forming a bunch size comparable to the longitudinal extension of the laser pulse ($c\tau_l = 15\,\mu$m). This bunch does not effectively carry any charges due to cold return currents within the plasma. However, due to the absence of a return current at the edges, the bunch produces a charge separation field. The simulation shows that this wave is then reflected from the opening at the north pole and heads back to the south pole, where it refocuses, passes through (collisionlessly) and continues moving towards the opening at the north pole again.

The dynamics are illustrated in figure 5(a), where the radial electric field at $3\,\mu$m distance from the sphere surface is plotted over time and latitude angle (180° corresponds to the south pole, while 0° represents the north pole). Figure 5(b) depicts the electric field component E_z along the z-axis, using red and blue colours. The evolution of the proton density along the z-axis is visualized by the grey distributions, in equidistant frames. In both pictures, one can identify large charge separation fields, set up at the rim due to the absence of a return current.

One can identify certain frames where the field becomes large, alternatingly at the north and the south pole. The periodicity can be estimated as $T_{\rm d} \approx \pi D_{\rm S}/v_{\rm e}$, where v_e is the velocity of the surface dipole wave. From our simulations we obtain $T_{\rm d} \approx 380$ fs, corresponding to a frequency of 2.64 THz and an electron wave velocity of $v_{\rm e} \approx 0.9\,c$.

When the surface dipole wave reaches the opening it produces electric field maxima at the north pole at times t_1, t_2, t_3 (see labels in figure 5(b)), which can be utilized for proton post-acceleration, i.e. staging. Those maxima exist only during relatively short periods. Thus, the timing of the proton bunch and the electron dipole wave is important. In order to have an effective post-acceleration, one would like protons to be pre-accelerated by the TNSA mechanism in such a way that they traverse the vicinity of the north pole when a maximum in accelerating field is present, resulting in a redistribution of the proton energy spectrum.

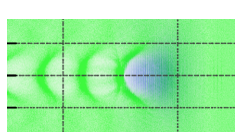

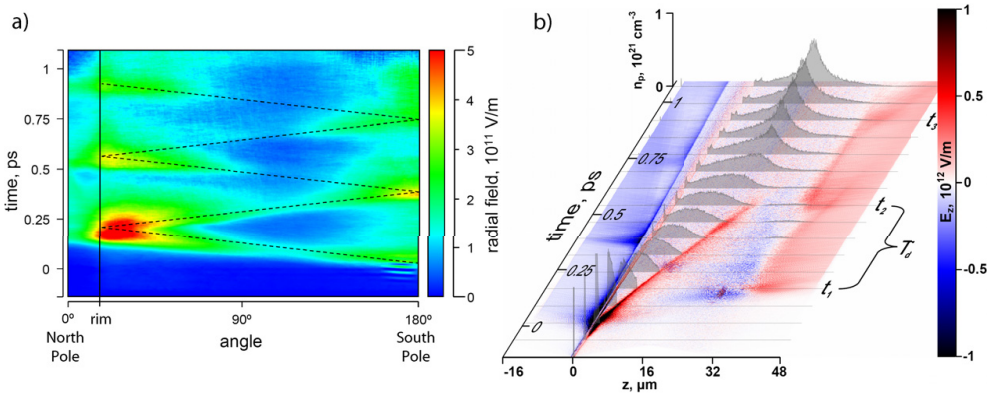

Figure 5. (a) Radial electric field strength, encountered at 3 μm distance from the surface as a function of time. (b) Electric field component E_z along the z-axis; grey plots depict the proton density evolution along the z-axis in equidistant frames.

It should be noted that the surface dipole wave oscillation amplitude decays, which implies that fewer oscillations prior to the proton passage provide a stronger post-acceleration. Additionally to the maxima, a weaker quasi-constant accelerating background field occurs at the opening from t_1 onwards, showing no significant decay on this timescale. Post-acceleration by this background field, which occurs due to a charge up of the sphere during laser irradiation, does not require an accurate timing for the proton passage. However, it provides smaller field strengths as compared to the surface dipole wave oscillations. The effect from both contributions can be seen in figure 6 in the upper marked region, labelled the 'post-acceleration stage', where the evolution of the proton energy distribution is displayed as a function of time. (Note that, due to the limited number of particles, modulations in these spatially integrated spectral distributions manifest themselves as lines that could easily be misinterpreted as trajectories.)

The final state of this simulation is summarized in figure 7 together with the emission angle–energy distribution in the inset, taking all protons into account. From this figure it can be seen that the considered geometry provides additional energy of several MeV for a part of the protons that form a bunch with a small divergence of about 8° half-angle.

4. Discussion and outlook

In the present simulation, a fraction of the protons, with kinetic energies around 9 MeV, reach the opening at time t_3 and pass through a spike in the accelerating field of the post-acceleration stage. However, the acceleration exerted on the protons by this field is relatively small. In 2D simulations, the charge increase due to refocusing of electron trajectories at the north pole is not fully reproduced. Even though qualitatively correct, the simulations are therefore expected to underestimate the field effects.

However, a larger fraction of the particles could be post-accelerated if the relative timing between the surface dipole wave and the proton arrival could be controlled. This could be done

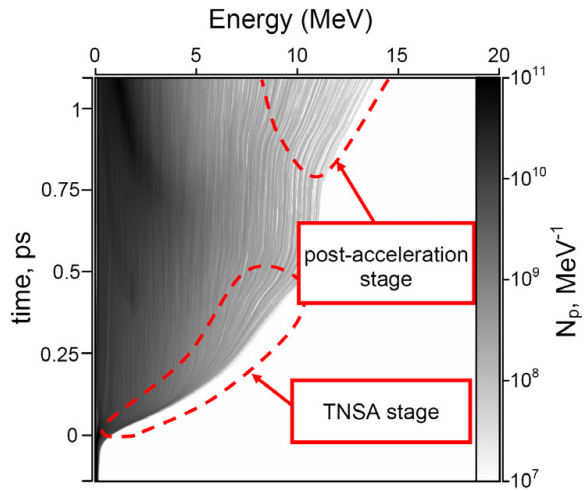

Figure 6. Spatially integrated proton energy distribution along the z-axis with colour-coded number density and its evolution in time.

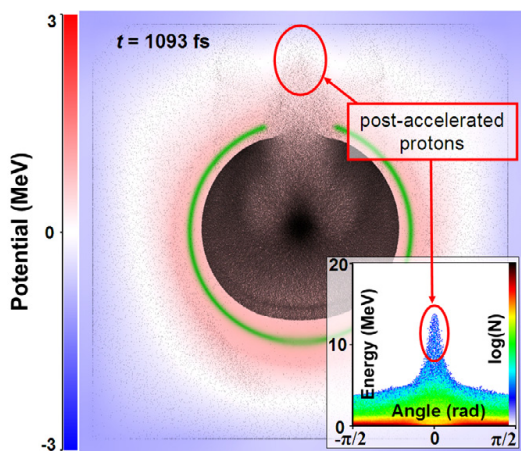

Figure 7. The final instant of the simulation and the corresponding angle–energy distribution of the protons.

either by making use of smaller spheres or oblate spheroidal targets to compensate for their different propagation velocities or by simply increasing the proton temperature in the TNSA stage as they are still moving non-relativistically. In the latter case, an energy of 9 MeV is sufficient for protons to reach the north pole at time t_3, while 37 MeV would be required for a passage at t_2 and GeV energies for t_1. TNSA acceleration to the GeV regime is not feasible, but 37 MeV should be within reach of short-pulse laser systems at intensities below $I_{\text{laser}} = 10^{21}\,\text{W cm}^{-2}$ [32, 33]. In addition, one might be able to reduce the velocity of the surface electron wave by surrounding the sphere with an appropriate dielectric.

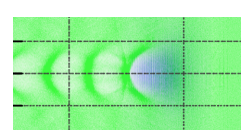

With spheroids the advantages of spheres are conserved, but the relative distance for protons and electrons to propagate can be varied. Simulations with oblate spheroidal surfaces, performed as for the spherical targets above, show both stronger acceleration and a narrower collimation of the protons. Experimentally, however, such targets are not as easily available as spheres.

In the experiment, we irradiated the target at normal incidence to obtain maximum symmetry and facilitate direct comparison with our simulations. However, it is well known that by irradiating the target with p-polarized light at an angle, the efficiency of coupling laser energy to the plasma increases. This should, in our case, enhance both TNSA at the south pole and drive a significantly stronger transverse electron current along the target surface [24]. An extension of both simulation and experimental geometry to allow for non-normal incidence irradiation will be a topic for further study.

Finally, we would like to point out that our target has additional interesting features. One of them is an intermediate particle focus slightly outside the spatial boundaries of the target. This could be used for experiments in fundamental physics that require high proton flux, inherently synchronized with a high-power laser beam line. Additionally, as the microsphere acts as a cavity for electron surface dipole waves, it could provide an efficient means to produce THz radiation with high-intensity lasers. In such an experiment almost all the incident laser energy can be absorbed by irradiating the sphere through the opening at the north pole, launching an electron surface wave from the inside.

5. Conclusions

We have introduced a new scheme for staged laser-driven proton acceleration, using hollow microspheres as targets. On the one side of a microsphere, protons are accelerated by TNSA from the concave inner surface of the sphere. Laser-heated electrons that are spreading transversely in the target, as a charge wave, are refocused on the opposite side of the sphere, where they produce a strong but transient charge separation field in an opening located there. Protons passing through the opening at the correct time can thus be post-accelerated. We have done 2D PIC simulations that confirm that this process indeed occurs and that the electrons spread over the sphere as a charge wave. This wave was found to oscillate back and forth over the sphere while decaying in amplitude, forming charge separation fields in the opening at regular intervals. These simulations also show that protons arriving at the correct time, i.e. those protons that have the right kinetic energy, are post-accelerated. Experimentally we have demonstrated the technical feasibility of preparing and irradiating this type of target. In addition, the preliminary results show some signatures of post-acceleration, although the timing between the electron charge wave and the TNSA protons was far from optimal in this first experiment. Further work with improved relative timing is needed for fully exploring the potential of this new scheme and target geometry.

Acknowledgments

We acknowledge support from the Swedish Research Council (including contract no. 2007-4422 and the Linnaeus grant to the Lund Laser Centre), the Marie Curie Early Stage Training Site MAXLAS (MEST-CT-2005-020356) within the 6th European Framework Programme, the Knut and Alice Wallenberg Foundation, the Swedish National Infrastructure for Computing (SNIC)

and the EPSRC (grant no. EP/E048668/1). This research was further partially supported by the European Research Council under contract no. 204059-QPQV. We also thank D C Carroll for processing the CR-39 plates.

References

[1] Cowan T E *et al* 2004 Ultralow emittance, multi-MeV proton beams from a laser virtual-cathode plasma accelerator *Phys. Rev. Lett.* **92** 204801
[2] Malka V *et al* 2004 Practicability of protontherapy using compact laser systems *Med. Phys.* **31** 1587
[3] Linz U *et al* 2007 What will it take for laser driven proton accelerators to be applied to tumor therapy? *Phys. Rev. ST Accel. Beams* **10** 094801
[4] Spencer I *et al* 2001 Laser generation of proton beams for the production of short-lived positron emitting radioisotopes *Nucl. Inst. Methods Phys. Res.* B **183** 449
[5] Mackinnon A J *et al* 2006 Proton radiography of a laser-driven implosions *Phys. Rev. Lett.* **97** 045001
[6] Wilks S C *et al* 2001 Energetic proton generation in ultra-intense laser–solid interactions *Phys. Plasmas* **8** 542
[7] Glinec Y *et al* 2008 Evolution of energy spectrum from laser-accelerated protons with a 100 fs intense prepulse *Appl. Phys.* B **93** 317
[8] McKenna P *et al* 2008 Effects of front surface plasma expansion on proton acceleration in ultraintense laser irradiation of foil targets *Laser Part. Beams* **26** 591
[9] Neely D *et al* 2006 Enhanced proton beams from ultra thin targets driven by high contrast pulses *Appl. Phys. Lett.* **89** 021502
[10] Jaeckel O *et al* 2009 Staged laser ion acceleration *Proc. Conf. on Lasers and Electro-Optics 2009 and 2009 Conf. on Quantum Electronics and Laser Science (CLEO/QELS 2009) (Baltimore, MD, 2–4 June 2009)* pp 1–2
[11] Allen M *et al* 2003 Proton spectra from ultraintense laser–plasma interaction with thin foils: experiments, theory and simulation *Phys. Plasmas* **10** 3283
[12] Brantov A V *et al* 2006 Quasi-mono-energetic ion acceleration from a homogeneous composite target by an intense laser pulse *Phys. Plasmas* **13** 122705
[13] Schwoerer H *et al* 2006 Laser–plasma acceleration of quasi-monoenergetic protons from microstructured targets *Nature* **439** 445
[14] Sokollik T *et al* 2009 Directional laser-driven ion acceleration from microspheres *Phys. Rev. Lett.* **103** 135003
[15] Buffechoux S *et al* 2010 Hot electrons transverse refluxing in ultraintense laser–solid interactions *Phys. Rev. Lett.* **105** 015005
[16] Roth M *et al* 2002 Energetic ions generated by laser pulses: a detailed study on target properties *Phys. Rev. ST Accel. Beams* **5** 061301
[17] Kar S *et al* 2008 Dynamic control of laser-produced proton beams *Phys. Rev. Lett.* **100** 105004
[18] Toncian T *et al* 2006 Ultrafast laser-driven microlens to focus and energy-select mega-electron volt protons *Science* **312** 410
[19] McKenna P *et al* 2007 Lateral electron transport in high-intensity laser-irradiated foils diagnosed by ion emission *Phys. Rev. Lett.* **98** 145001
[20] Dromey B *et al* 2004 The plasma mirror—a subpicosecond optical switch for ultra high power lasers *Rev. Sci. Instrum.* **75** 3
[21] Doumy G *et al* 2004 Complete characterization of a plasma mirror for the production of high-contrast ultraintense laser pulses *Phys. Rev.* E **69** 026402
[22] Ziener Ch *et al* 2003 Specular reflectivity of plasma mirrors as a function of intensity, pulse duration and angle of incidence *J. Appl. Phys.* **93** 768

[23] National Institute of Science and Technology *PSTAR Database* http://www.physics.nist.gov/PhysRefData/Star/Text/PSTAR.html
[24] Psikal J *et al* 2010 Lateral hot electron transport and ion acceleration in femtosecond laser pulse interaction with thin foils *Phys. Plasmas* **17** 013102
[25] Roth M *et al* 2002 The generation of high-quality, intense ion beams by ultra-intense lasers *Plasma Phys. Control. Fusion* **44** 99
[26] Schreiber J *et al* 2004 Source-size measurements and charge distributions of ions accelerated from thin foils irradiated by high-intensity laser pulses *Appl. Phys.* B **79** 1041
[27] Borghesi M *et al* 2004 Multi-MeV proton source investigations in ultraintense laser–foil interactions *Phys. Rev. Lett.* **92** 055003
[28] Roth M *et al* 2005 Laser accelerated ions in ICF research prospects and experiments *Plasma Phys. Control. Fusion* **47** B841
[29] Patel P K *et al* 2003 Isochoric heating of solid-density matter with an ultrafast proton beam *Phys. Rev. Lett.* **91** 125004-1
[30] McKenna P *et al* 2006 High-intensity laser-driven proton acceleration: influence of pulse contrast *Phil. Trans. R. Soc.* A **364** 711
[31] http://www.ipfran.ru/english/structure/lab334/simlight.html
[32] Fuchs J *et al* 2006 Laser-driven proton scaling laws and new paths towards energy increase *Nat. Phys.* **2** 48
[33] Zeil K *et al* 2010 The scaling of proton energies in ultrashort pulse laser plasma acceleration *New J. Phys.* **12** 045015

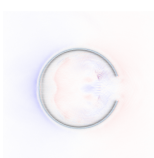

Paper II

Effect of lattice structure on energetic electron transport in solids irradiated by ultraintense laser pulses

P. McKenna, A. P. L. Robinson, D. Neely, M. P. Desjarlais, D. C. Carroll, M. N. Quinn, X. H. Yuan, C. M. Brenner, M. Burza, M. Coury, P. Gallegos, R. J. Gray, K. L. Lancaster, Y. T. Li, X. X. Lin, O. Tresca and C.-G. Wahlström.

Physical Review Letters **106**, 185004 (2011).

PRL 106, 185004 (2011) PHYSICAL REVIEW LETTERS week ending 6 MAY 2011

Effect of Lattice Structure on Energetic Electron Transport in Solids Irradiated by Ultraintense Laser Pulses

P. McKenna,[1,*] A. P. L. Robinson,[2] D. Neely,[2] M. P. Desjarlais,[3] D. C. Carroll,[1] M. N. Quinn,[1] X. H. Yuan,[1] C. M. Brenner,[1,2] M. Burza,[4] M. Coury,[1] P. Gallegos,[1,2] R. J. Gray,[1] K. L. Lancaster,[2] Y. T. Li,[5] X. X. Lin,[5] O. Tresca,[1] and C.-G. Wahlström[4]

[1]*SUPA, Department of Physics, University of Strathclyde, Glasgow G4 0NG, United Kingdom*
[2]*Central Laser Facility, STFC Rutherford Appleton Laboratory, Oxfordshire OX11 0QX, United Kingdom*
[3]*Sandia National Laboratories, P.O. Box 5800, Albuquerque, New Mexico 87185, USA*
[4]*Department of Physics, Lund University, P.O. Box 118, S-22100 Lund, Sweden*
[5]*Beijing National Laboratory of Condensed Matter Physics, Institute of Physics, CAS, Beijing 100190, China*

(Received 21 March 2011; published 6 May 2011)

The effect of lattice structure on the transport of energetic (MeV) electrons in solids irradiated by ultraintense laser pulses is investigated using various allotropes of carbon. We observe smooth electron transport in diamond, whereas beam filamentation is observed with less ordered forms of carbon. The highly ordered lattice structure of diamond is shown to result in a transient state of warm dense carbon with metalliclike conductivity, at temperatures of the order of 1–100 eV, leading to suppression of electron beam filamentation.

DOI: 10.1103/PhysRevLett.106.185004 PACS numbers: 52.38.Kd

Improving our understanding of the physics of energetic (''fast'') electron transport in dense matter is critical for many applications in high energy density physics, including the fast ignition approach to inertial confinement fusion [1], the development of laser-driven ion sources [2], and for laboratory astrophysics. It is well established that in the interaction of an ultraintense ($> 10^{19}$ W cm^{-2}) laser pulse with a solid target, a significant fraction of the laser energy is absorbed, producing a multi-mega-ampere current of relativistic electrons, and that the propagation of these fast electrons within the target is subject to transport instabilities giving rise to filamentation of the beam. Previous studies have shown that a number of plasma instabilities can cause filamentation, including the Weibel [3,4], two-stream [5], and resistive filamentation instabilities [6]. However, the precise causal agents and the circumstances under which filamentation is suppressed are not well understood.

It is well known from solid state physics that the conductivity of a material is strongly affected by its lattice structure [7]. The propagation of a high current of fast electrons in a solid target irradiated by a high energy picosecond laser pulse requires, by charge neutrality, a ''return'' current of thermal electrons which are collisional and rapidly, on the order of picoseconds, heat a significant volume of the target to temperatures in the range 1–100 eV. This results in a nonequilibrium state of warm dense matter (WDM) in which the electrons are ''warm'' (1–100 eV) but the ions remain essentially cold and maintain temporarily the structural arrangement they possessed in the condensed matter state. The conductivity of the material in this transient nonequilibrium state is strongly affected by the retained lattice structure.

In this Letter, we demonstrate for the first time, using various allotropes of a single element, carbon, that lattice structure alone can determine whether or not fast electron beam filamentation occurs in solid targets irradiated by intense picosecond laser pulses. It is shown that the highly ordered arrangement of carbon atoms in diamond results in a transient state of warm dense carbon with metalliclike conductivity, whereas disordered allotropes of carbon under similar rapid thermal loading are poorly conducting. Thus it is demonstrated that the choice of a particular allotrope of a given element enables the material conductivity in the temperature range 1–100 eV to be tailored to produce a given fast electron transport pattern.

The experiment was performed using the Vulcan laser, delivering pulses of 1.053 μm wavelength light, with an energy of 200 J (on target) and duration equal to 1 ps, FWHM. The p-polarized pulses were focused to an 8 μm diameter FWHM spot, to a calculated peak intensity of 2×10^{20} W cm^{-2}. The main target samples were three different allotropes of carbon: (1) single-crystalline diamond, (2) vitreous carbon (disordered), and (3) pyrolytic carbon, which is similar to graphite but with some degree of covalent bonding between its graphene sheets, thus presenting an intermediate degree of atomic ordering. Aluminum and plastic (Mylar) targets were also used as reference materials due to the differences in their ordering and room temperature electrical conductivity. The target size in all cases was 5 mm $\times$ 5 mm and 500 μm thick. We diagnosed the fast electron transport pattern by recording and analyzing the spatial-intensity profile of beams of protons accelerated from the rear surface of the target by an electrostatic sheath field established there by the fast electrons [2]. Filamentation of the electron beam within

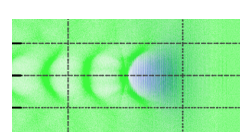

the target produces modulations in the sheath field, which are mapped into the expanding proton beam spatial-intensity distribution, as demonstrated by Fuchs *et al.* [8] and discussed later. The proton beam profile measurements were made using stacked dosimetry film, which enables measurement of the dose deposited by the proton beam at discrete energies given by the stopping range of protons within the stack. Each piece of film was optically scanned and the modulations within the proton dose were quantified.

The key finding of our experiment is that the different allotropes of carbon produce very different fast electron transport patterns. This is demonstrated in Fig. 1, which shows example proton beam spatial-intensity profiles for diamond and vitreous carbon. Figure 1(c) shows the variance in proton dose (normalized to the average dose level) for the range of targets explored. Larger variance values correspond to a more structured proton beam and therefore more filamentation of the electron beam. From left to right in Fig. 1(c), as the degree of ordering of the atoms (in the cold state) increases, the proton beam becomes more uniform, indicating less filamentation. The fast electron transport pattern in diamond is smooth and free of filamentation, and is very similar to that measured for aluminum. By contrast, heavy filamentation is observed for vitreous carbon. Pyrolytic carbon and Mylar, with intermediate degrees of atomic ordering, produce intermediate levels of beam filamentation. Repeat shots were taken on each of the carbon allotropes and the results are fully reproducible, as shown in Fig. 1(c).

These results clearly show a correlation between the degree of lattice structure and the extent of fast electron beam filamentation in targets of the same element. The findings are explained by the effect of lattice structure on electrical conductivity and the fact that the structure is temporarily maintained during rapid thermal excitation of the material [9]. To investigate this in more detail, we modeled the electronic structure and electrical conductivity of two different allotropes of carbon: diamond [tetrahedral lattice; Fig. 2(a)] and vitreous carbon [disordered; Fig. 2(b)] as a function of temperature. The electrical conductivities were derived using quantum molecular dynamics calculations with VASP, a plane-wave density functional code [10]. The atomic configurations were sampled from the configurations in 300 K simulations for each allotrope. The electronic temperature was then varied from 1 to 20 eV in subsequent static Kubo-Greenwood conductivity calculations [11] with the sampled configurations.

Figure 2(c) shows the calculated conductivity as a function of temperature for both carbon allotropes. Diamond is strongly insulating at room temperatures due to the large gap between its valence and conductance bands. However, the electrical conductivity rises sharply with the electronic temperature as soon as the electrons are excited enough to reach above the band gap. The peak in the diamond conductivity corresponds to the onset of ionization for $2s$ electrons and an average of approximately one electron per atom thermally occupying states above the band gap. In contrast, the conductivity of vitreous carbon, which is low but finite at ambient conditions, rises only weakly with increasing electronic temperature, even when heated in the same way. In the transient WDM regime (~ 10 eV), the electrical conductivity of diamond becomes nearly 2 orders of magnitude greater than that of disordered carbon. At even higher temperatures (> 100 eV), the conductivities rise sharply for both materials.

The physical origin of the effects of ionic ordering on electrical conductivity can be understood in the following way. The form of the conductivity-temperature curve in the nonequilibrium regime is critically determined by

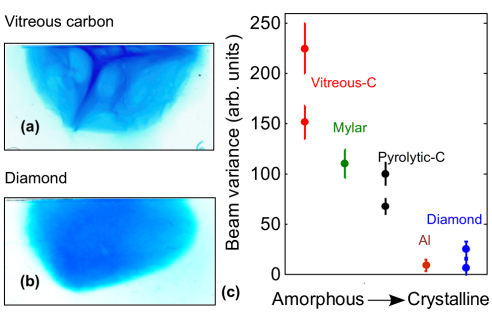

FIG. 1 (color online). Spatial-intensity profile measurements (lower half) of the proton beam, at energy 10 MeV, for (a) vitreous carbon and (b) diamond. (c) Variance in the proton signal (mean of 10 samples) near the center of the proton beam, for given target materials with increasing atomic ordering from left to right. Error bars correspond to statistical variations over the multiple samples.

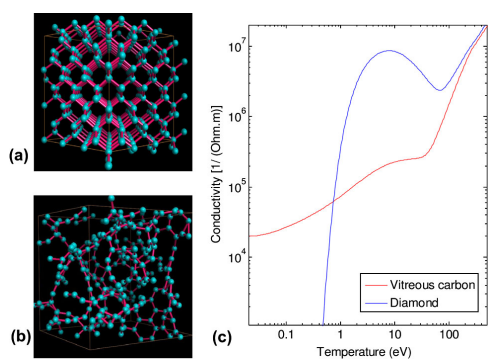

FIG. 2 (color online). Structure of (a) diamond and (b) vitreous carbon. (c) Electrical conductivity as a function of temperature for both carbon allotropes. The curves are calculated as described in the main text.

the electron mean free path in the material [7]. If the ions are highly disordered, then electrons will scatter incoherently and the electron mean free path will be limited to the mean interionic distance, leading to a low conductivity. If, however, the ions are in a well-ordered geometric lattice, then constructive interference of the scattering of the wave function from multiple ions results in a mean free path considerably longer than the mean interionic distance. Thus, for an ordered structure of ions the material conductivity is larger than for a disordered material of the same atomic element, and similar density. At very high temperatures (> 100 eV) the scattering cross sections diminish rapidly with increasing mean electron momentum, typical of Coulomb scattering processes, and hence the conductivity increases irrespectively of ionic ordering.

Next we consider how the calculated differences in electrical conductivity affect the propagation of fast electrons by performing simulations using the 3D ZEPHYROS particle-based hybrid code [12]. A $200 \times 200 \times 200$ μm^3 box with cell size equal to $1 \times 1 \times 1$ μm^3 was used. The laser-to-fast electron conversion efficiency was set to 0.3, the peak laser intensity to 2×10^{20} W cm^{-2}, and the pulse duration to 1 ps. An exponential distribution of electron energies was used with temperature equal to 5.7 MeV (ponderomotive scaling [13]). Example simulation results are shown in Fig. 3, in which 2D slices of the fast electron density in the x-y midplane and the y-z rear plane are plotted. The laser irradiates the targets in the y-z plane at $x = 0$ and the fast electron beam propagates in the x direction. In the simulation of diamond, the fast electron beam is smooth and nonfilamented along its whole length and in its transverse profile at the rear surface. In clear contrast to this, the results of simulations for vitreous carbon show a beam that is filamented along most of its length and exhibits a strongly filamented transverse profile at the rear surface. By carrying out modifications of the simulation parameters we conclude that this result is not a consequence of a particular choice of parameters. A wide range of initial divergence angles gives the same result, as do different choices of the absorption fraction and fast electron temperature scaling. We therefore conclude that these two outcomes reflect a significant qualitative difference between the two materials. The simulations start at a temperature of 1 eV and the conductivity curves converge at >100 eV, and therefore the predicted differences in electron transport result entirely from the differences in conductivity of the two targets in the transient WDM regime.

The sensitivity of the fast electron transport pattern to the target conductivity can be explained in terms of a linear instability analysis of resistive filamentation. The resistive filamentation growth rates were calculated as follows [6]. If we denote

$$\alpha = \frac{e^2 u_f^2 n_f^2 \eta k^2}{\gamma m_e} \qquad (1)$$

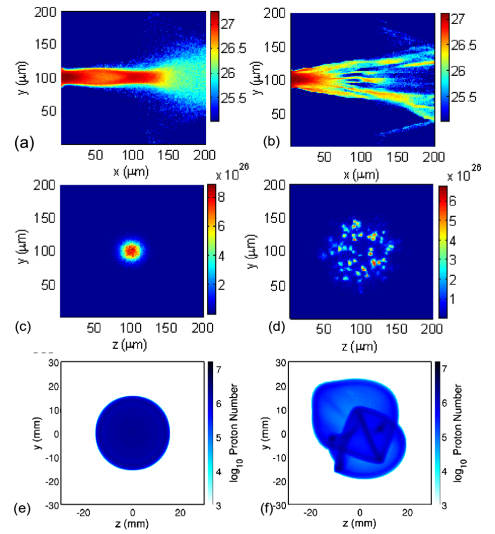

FIG. 3 (color online). Fast electron transport simulation results (electron density) for (a),(c) diamond and (b),(d) vitreous carbon; (a) and (b) show the fast electron density distribution within the target (laser incident from left side) at 1.0 ps; (c) and (d) show the same at the rear of the targets after 1.5 ps (when the main part of the current has reached the rear surface). Smooth transport is observed with diamond, compared to heavily filamented transport in vitreous carbon. The calculated spatial-intensity distribution of the resulting proton beam is shown in (e) and (f), respectively.

and

$$\beta = \frac{eT_\perp k^2}{\gamma m_e}, \qquad (2)$$

where u_f, n_f, $T_\perp$, and γ are the fast electron velocity, density, transverse temperature, and Lorentz factor, respectively, η is the resistivity, and k is the wave number of the filamentation mode, then the growth rate of the resistive filamentation mode is

$$\Gamma = (\alpha/2 - \sqrt{D})^{1/3} - (\sqrt{D} - \alpha/2)^{1/3}, \qquad (3)$$

where $D = (\beta/3)^3 + (\alpha/2)^2$. By choosing representative fast electron parameters the resistive filamentation growth rates in the WDM regimes of the two materials (vitreous carbon, $\eta \approx 4 \times 10^{-6}$ Ωm; diamond, $\eta \approx 2 \times 10^{-7}$ Ωm) can be examined. We choose typical values of $n_f = 10^{26}$ m^{-3}, $u_f = c$, $\gamma = 10$ and find that the filamentation growth rate is much larger for vitreous carbon than for diamond. In vitreous carbon, the time for one e-folding of the resistive filamentation instability is on the order of a few tens of femtoseconds. This means that for electron transport driven by a 1 ps laser pulse, strong filamentation should occur—as observed in the hybrid simulations and

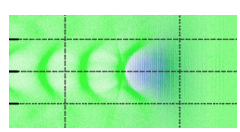

experimentally. In diamond the *e*-folding time is at least a few hundred femtoseconds, so the beam is much less likely to filament. Thus the absence of filamentation observed experimentally for diamond compared to other allotropes of carbon results from its much higher conductivity at WDM temperatures, which in turn results due to the highly ordered arrangement of carbon atoms.

Finally, to demonstrate the correlation between the fast electron density distribution at the target rear and the spatial-intensity distribution of the proton beam, an analytical model was developed to compute the evolution of the sheath field, the proton front, and the projection of the protons to the detector plane. The fast electron distributions resulting from the hybrid electron transport simulations [Fig. 3(c) and 3(d)] were used to calculate the electric field distributions. The temporal evolution of the field and the spreading of the electrons on the target surface were modeled using a similar approach to that described by Yuan *et al.* [14]. Field ionization of hydrogen is assumed to produce the protons and their projection to the detector plane is calculated using the local gradients in the proton front. The methodology will be described in detail in a separate publication. Figures 3(e) and 3(f) show the calculated proton beam spatial-intensity distributions corresponding to the fast electron density distributions in Figs. 3(c) and 3(d), respectively. These are in good qualitative agreement with the measurements in Fig. 1.

In summary, these results show, for the first time, that in the interaction of a short high intensity laser pulse with a solid target the effects of lattice structure in defining the electrical conductivity of the induced transient WDM state plays a key role in the transport of fast electrons within the target. This has implications for the many potential applications of high power laser-solid interactions involving the conduction of large currents of energetic electrons. It shows that the choice of allotrope of a given element is important, which impacts on the choice of materials used in the fabrication of advanced targets for fusion (such as the cone, cone wire, and other variant targets proposed for the fast ignition scheme [15]) and in targets for laser-driven ion acceleration. Our finding that diamond produces smooth electron transport is particularly interesting from an applications viewpoint because of its unique material properties, including high hardness and thermal conductivity.

Furthermore, our analysis shows that the rate of fast electron beam filamentation depends sensitively on electrical conductivity. This suggests that resistive filamentation is the dominant instability mechanism for the parameters explored.

We acknowledge the expert support of the staff at the Central Laser Facility of the Rutherford Appleton Laboratory and the use of computing resources provided by the STFC e-Science Facility. We also acknowledge discussions with Professor R. Bingham and Professor A. R. Bell. This work is supported by EPSRC (Grants No. EP/E048668/1 and No. EP/E035728/1), the HiPER project, the Swedish Research Council, and by the National Basic Research Program of China (program 973; Grant No. 2007CB815101).

*paul.mckenna@strath.ac.uk

[1] M. Tabak *et al.*, Phys. Plasmas **1**, 1626 (1994).
[2] M. Borghesi *et al.*, Fusion Sci. Technol. **49**, 412 (2006).
[3] E. S. Weibel, Phys. Rev. Lett. **2**, 83 (1959).
[4] Y. Sentoku *et al.*, Phys. Rev. Lett. **90**, 155001 (2003).
[5] B. Hao *et al.*, Phys. Rev. E **79**, 046409 (2009).
[6] L. Gremillet, G. Bonnaud, and F. Amiranoff, Phys. Plasmas **9**, 941 (2002).
[7] J. M. Ziman, Adv. Phys. **16**, 551 (1967).
[8] J. Fuchs *et al.*, Phys. Rev. Lett. **91**, 255002 (2003).
[9] V. Recoules *et al.*, Phys. Rev. Lett. **96**, 055503 (2006).
[10] G. Kresse and J. Hafner, Phys. Rev. B **47**, 558 (1993).
[11] M. P. Desjarlais, J. D. Kress, and L. A. Collins, Phys. Rev. E **66**, 025401 (2002).
[12] S. Kar *et al.*, Phys. Rev. Lett. **102**, 055001 (2009).
[13] S. C. Wilks and W. L. Kruer, IEEE J. Quantum Electron. **33**, 1954 (1997).
[14] X. H. Yuan *et al.*, New J. Phys. **12**, 063018 (2010).
[15] R. Kodama *et al.*, Fusion Sci. Technol. **49**, 316 (2006).

Paper III

Influence of laser irradiated spot size on energetic electron injection and proton acceleration in foil targets

M. Coury, D. C. Carroll, A.P.L. Robinson, X. H. Yuan, C. M. Brenner, M. Burza, R. J. Gray, M. N. Quinn, K. L. Lancaster, Y. T. Li, X. X. Lin, O. Tresca, C.-G. Wahlström, D. Neely and P. McKenna.

Applied Physics Letters **100**, 074105 (2012).

APPLIED PHYSICS LETTERS **100**, 074105 (2012)

Influence of laser irradiated spot size on energetic electron injection and proton acceleration in foil targets

M. Coury,[1] D. C. Carroll,[1] A. P. L. Robinson,[2] X. H. Yuan,[1,a)] C. M. Brenner,[1,2] M. Burza,[3] R. J. Gray,[1] M. N. Quinn,[1] K. L. Lancaster,[2] Y. T. Li,[4] X. X. Lin,[4] O. Tresca,[1] C.-G. Wahlström,[3] D. Neely,[2] and P. McKenna[1,b)]
[1]*Department of Physics, SUPA, University of Strathclyde, Glasgow G4 0NG, United Kingdom*
[2]*Central Laser Facility, STFC Rutherford Appleton Laboratory, Oxfordshire OX11 0QX, United Kingdom*
[3]*Department of Physics, Lund University, P.O. Box 118, S-22100 Lund, Sweden*
[4]*Beijing National Laboratory of Condensed Matter Physics Institute of Physics, CAS, Beijing 100190, China*

(Received 6 December 2011; accepted 30 January 2012; published online 15 February 2012)

The influence of irradiated spot size on laser energy coupling to electrons, and subsequently to protons, in the interaction of intense laser pulses with foil targets is investigated experimentally. Proton acceleration is characterized for laser intensities ranging from $2 \times 10^{18} - 6 \times 10^{20}$ W/cm^2, by (1) variation of the laser energy for a fixed irradiated spot size, and (2) by variation of the spot size for a fixed energy. At a given laser pulse intensity, the maximum proton energy is higher under defocus illumination compared to tight focus and the results are explained in terms of geometrical changes to the hot electron injection. © *2012 American Institute of Physics*. [doi:10.1063/1.3685615]

The acceleration of ions to multi-MeV/nucleon energies in the interaction of intense laser pulses with thin solid targets has been actively investigated by many groups since the discovery of the phenomenon over a decade ago.[1,2] Target normal sheath acceleration (TNSA) (Ref. 3) is the dominant acceleration mechanism for laser intensities, I_L, ranging from 1×10^{18} to $\sim 10^{21}$ W/cm^2 and for target thicknesses ranging from microns to millimeters. The resulting pulses of energetic protons are ultra-bright, have low emittance,[4] and have potential applications in a number of areas, including medicine[5] and advanced schemes for inertial fusion energy.[6]

In the TNSA mechanism, a large population of hot (relativistic) electrons generated at the focus of the high power laser pulse is injected into the target and propagates through it, forming a sheath with a ~TV/m field at the rear surface, resulting in ionization and ion acceleration. The need to optimize and control the properties of the resulting high energy ion beam has motivated numerous studies on the influence of laser pulse parameters on ion acceleration—see for example Refs. 7–9. Despite the significant progress made, the functional dependencies of TNSA-ion beam parameters on the laser irradiation conditions are still far from fully understood. Recent investigations employing large laser irradiated spots (defocused irradiation), for example, suggest that the laser irradiated spot size may play an important and previously unexplored role in defining the properties of beams of laser-accelerated protons (beyond simply being a parameter in defining the laser intensity).[10–12]

In this Letter, measurements of the sensitivity of the maximum proton energy, E_{max}, to the laser irradiated spot size are reported for picosecond laser pulses in the intensity range $2 \times 10^{18} - 6 \times 10^{20}$ W/cm^2. Under defocus illumination, higher proton energies are obtained compared to tight focus for a given laser pulse intensity. The results are interpreted in terms of geometrical effects on hot electron injection and transport.

The experiment was performed using the Vulcan laser at the Rutherford Appleton Laboratory. This laser provides pulses with energy up to ~400 J in a duration, $\tau_L = 1$ ps, at a wavelength, λ_L, of 1.054 μm. The laser pulse energy (on target), E_L, was varied in the range 3-150 J and the irradiated spot radius, r_L, was varied in the range 4–40 μm. The p-polarized laser beam was focused, at an incident angle θ_L, of 23° (with respect to target normal), using an f/3 off-axis parabolic mirror. A limited number of data shots were taken with $\theta_L = 7°$ and 48° to test the effect of incident angle on E_{max}. The planar targets were 2 mm × 2 mm and consisted of a layer of 100 μm Al (interaction and propagation layer), a 5 μm Cu fluorescent layer, and a 1 μm Al rear surface layer.

Kα x-ray emission from the Cu fluorescent layer was imaged using a spherically bent Bragg crystal with a FujiFilm BAS image plate detector. This provided a time-integrated measurement of the spatial extent of the hot electron distribution near the target rear surface.[13] The magnification was set to 10, giving a spatial resolution of 20 μm at source. The proton beam spatial-intensity distribution and spectrum were measured using stacked dosimetry film (RCF), positioned 5 cm from the rear of the target. The stacks covered an energy range from 1.2–40 MeV. The proton beam properties are deduced from the dose deposited in the RCF (HD-810).[14]

The laser pulse intensity was varied in two separate scans. In the first, referred to hereafter as the *energy scan*, E_L was varied from 3 to 150 J at a fixed laser spot radius $r_L \sim 4$ μm (half width at half maximum in the plane of the laser beam). In the second scan, referred to as the *focus scan*, r_L was varied from 4 to 40 μm, by defocusing, at fixed $E_L = 150$ J.

Fig. 1(a) shows the measured E_{max} for both scans. It is clear that E_{max} is higher in the case of the focus scan compared to the energy scan at a given laser intensity (except at the highest intensity, corresponding to the smallest spot size at best focus). The E_{max} scaling for the focus scan is

a)Present address: Key Laboratory for Laser Plasmas (Ministry of Education) and Department of Physics, Shanghai Jiao Tong University, Shanghai 200240, China.
b)Electronic mail: paul.mckenna@strath.ac.uk.

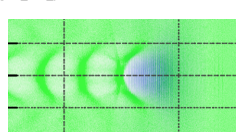

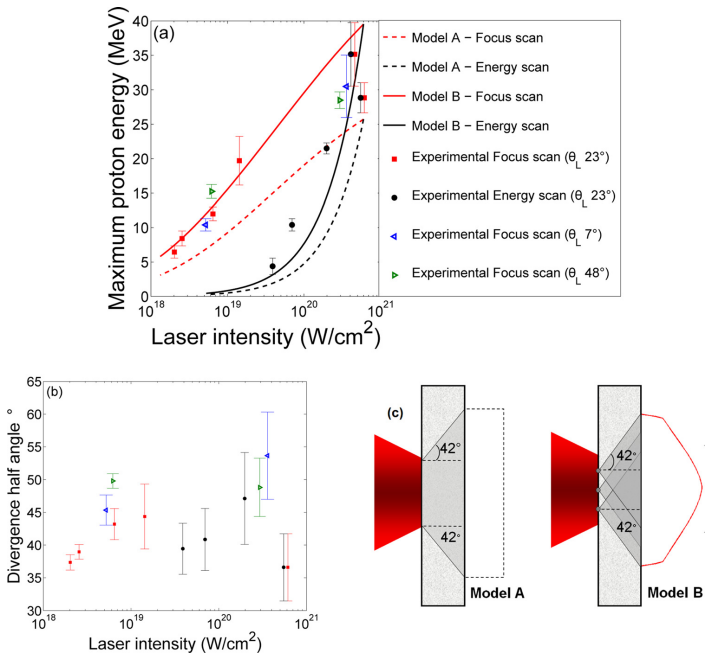

FIG. 1. (Color online) (a) Measured maximum proton energy as a function of laser intensity, by variation of laser energy for fixed irradiated spot ("Energy scan") and by variation of irradiated spot size for fixed energy ("Focus scan"), at given angles; (b) The hot electron beam divergence half-angle, based on the Cu Kα emission, as a function of laser intensity for both scans; (c) Schematic illustrating the hot electron injection and the density distribution at the target rear surface for models A and B.

consistent with the results presented in Brenner *et al.*,[11] also obtained by spot size variation, but with a much shorter laser pulse duration of 40 fs and lower laser intensities ($\sim 10^{16}$ to $\sim 10^{18}$ W/cm^2). Thus the laser irradiated spot size is shown to be important in TNSA-ion acceleration over a wide parameter range. In addition to the differences in the maximum proton energy, the number of protons accelerated is higher for the focus scan (due to the higher E_L), compared to the same intensity achieved via the energy scan. These results are consistent with the observations of Green *et al.*[12] that the number of low energy protons increases with laser irradiated spot size. The spectral shape and therefore temperature is, however, similar at a given I_L for both scans.

Measurements of the lateral extent of the Kα source near the rear surface of the target suggest only small changes in the hot electron beam divergence half-angle θ for both scans, as shown in Fig. 1(b). The average value of θ is 42° (standard deviation 4°).

To explain the measured trends in E_{max}, a simple model of ballistic hot electron transport through the target is adopted and the Mora 1D isothermal plasma expansion formulae[15] used to provide a theoretical E_{max} for given hot electron beam properties at the target rear surface.

In this model, $E_{max} = 2kT_e[\ln(\tau) + \sqrt{(\tau^2+1)}]^2$, where $\tau = \omega_{pi}t_{acc}/\sqrt{2\exp(1)}, \omega_{pi} = \sqrt{n_e e^2/m_i\epsilon_0}, m_i$ is the ion mass, e is the elementary charge, ϵ_0 is the vacuum permittivity, exp(1) is the numerical constant 2.71828., n_e is the hot electron beam density at the target rear surface, kT_e the hot electron beam temperature, and t_{acc} the ion acceleration time. E_{max} is principally defined by three input variables: kT_e, t_{acc}, and n_e. The beam temperature is given by the ponderomotive scaling,[16] and thus by I_L. A finite $t_{acc} = 1.3\,\tau_L$, as used previously by Fuchs *et al.*[8] for similar laser and target parameters, is assumed. We therefore infer that the differences in E_{max} between the two scans are given by differences in n_e. n_e can be expressed as $n_e = n_{front} \times F(\theta, r_L, L)$, where n_{front} is the hot electron beam density at the source (laser focus) and $F(\theta, r_L, L)$ is a transport factor which is a function of θ, r_L, and L, the target thickness. F represents the effects of the fast electron beam injection and the transport mechanism on the on-axis beam density at the target rear surface. The transport is assumed to be ballistic in this study. The hot electron beam density at the source is given by: $n_{front} = \eta_{L-e}E_L/(kT_e\pi r_L^2 c\tau_L)$, where η_{L-e} is the laser to electron energy conversion efficiency and c is the speed of light. Varying the laser incident angle, at a given laser intensity, did not significantly change either E_{max} or the Kα source size, at either tight focus or under defocus irradiation, as shown in Fig. 1. Thus justifying the choice of a fixed η_{L-e}, which is set at 0.2, consistent with the work of Nilson *et al.*[17] for similar laser and target parameters.

We begin by using a method similar to previous proton acceleration scaling studies,[8] in which the hot electron beam is considered to arise from a laminar source. This is hereafter referred to as model A. The hot electrons are accelerated over the laser pulse duration and propagate ballistically through the target with a fixed divergence half-angle θ, as shown in Fig. 1(c) (where $\theta = 42°$). The rear sheath profile is a top hat function where the electrons are spread evenly over the laser pulse duration ($c\tau_L$), with radius (HWHM)

$r_S = r_L + L \tan\theta$. In this model, the transport factor is $F(\theta, r_L, L) = [r_L/(r_L + L\tan\theta)]^2$, giving a flat hot electron rear density profile. Using this approach, n_e is calculated as a function of the laser pulse intensity for the two parameter scans, and the results are presented in Fig. 2(c). An average half-angle, $\theta = 42°$, is used in these calculations, as inferred from the Kα measurements. Fig. 1(a) shows that the calculated values for E_{max} are lower than the measured ones for both scans.

Another approach to calculate n_e (referred to hereafter as model B) is to consider the hot electrons as arising from a diffuse source, which can be described as a summation of elements,[18] each of which injects electrons into the target with the same divergence half-angle $\theta = 42°$, as illustrated schematically in Fig. 1(c). The hot electrons are transported ballistically within the target, as with model A. The on-axis transport factor in this approach is $F_0(\theta, r_L, L) = \ln(1 + r_L^2/L^2)/(2(1 - \cos\theta))$, for $\theta > \arctan(r_L/L)$. F_0 is derived by integrating the electron flux contribution from each element of the source at the target front side, to obtain the flux on-axis at the rear side. It is assumed that the total front side flux is uniformly distributed over the laser focal spot area (of radius r_L) and that the flux within the cone of half angle θ is uniform, but the different geometrical path lengths from each source element to the on-axis point of interest is taken into account.

Application of model B has the effect of changing the hot electron density distribution at the target rear surface to a parabolic-like profile, in agreement with the conclusions of Romagnani *et al.*[19] and Brambrink *et al.*[20] Thus the on-axis density is enhanced compared to the equivalent uniform injection distribution (model A), leading to higher maximum proton energies. As shown in Fig. 1(a), the diffuse source model reproduces the trend observed experimentally for both scans. We also note that a parabolic-like density profile will produce a proton beam divergence similar to that measured experimentally.[21] Although a uniform density is implicit in the 1D Mora expansion model, the use of this model is appropriate even in the case of model B as the variation in n_e is small in the region of the peak density. For example, n_e is reduced by only 3% at 20 μm from the central axis, a distance much larger than the Debye length, resulting in a reduction in E_{max} by 2%.

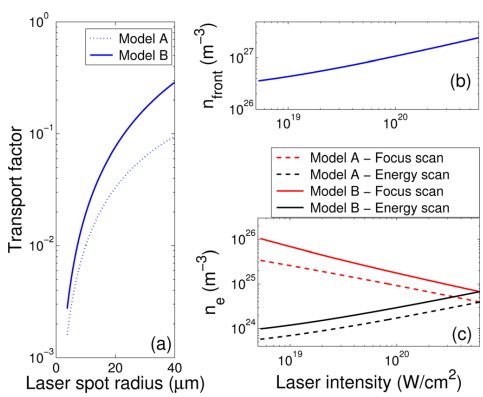

FIG. 2. (Color online) (a) Transport factor, F, for the two models, as a function of laser spot radius; (b) Maximum hot electron density at source as a function of laser intensity; (c) Calculated maximum hot electron density on-axis at the target rear surface as a function of laser intensity, for the two different models and parameter scans.

In model B, since θ and L are constant, the transport factor F varies only with r_L. In the energy scan, F is therefore constant and n_{front} increases with I_L, as shown in Fig. 2(b), so that n_e and therefore the maximum proton energy vary rapidly with I_L, as shown in Figs. 2(c) and 1(a), respectively. By contrast, in the focus scan, F increases with r_L (Fig. 2(a)), and therefore decreasing intensity. Even though n_{front} decreases at the same rate as it does in the energy scan, n_e increases with decreasing intensity, as shown in Fig. 2(c), due to the increase in F and constant E_L. The reduction in kT with intensity means that the maximum proton energy still decreases, but at a much slower rate than in the energy scan.

It is thus shown: (1) there is a slower decrease in the measured maximum proton energy as a function of decreasing intensity in the focus scan, compared to the energy scan at best focus, which cannot be accounted for by differences in the laser pulse energy alone; and, (2) a diffuse source geometry gives a better approximation of hot electron beam injection and propagation. These results should be factored into scaling studies for the optimization of TNSA-ions.

We acknowledge financial support from the EPSRC (Grant numbers EP/E048668/1 and EP/E035728/1) and the Swedish Research Council. We also acknowledge the support of staff at the Central Laser Facility and discussions with Dr. B. Ersfeld (University of Strathclyde).

[1]E. L. Clark, K. Krushelnick, J. R. Davies, M. Zepf, M. Tatarakis, F. N. Beg, A. Machacek, P. A. Norreys, M. I. K. Santala, I. Watts *et al.*, Phys. Rev. Lett. **84**, 670 (2000).
[2]R. A. Snavely, M. H. Key, S. P. Hatchett, T. E. Cowan, M. Roth, T. W. Phillips, M. A. Stoyer, E. A. Henry, T. C. Sangster, M. S. Singh *et al.*, Phys. Rev. Lett. **85**, 2945 (2000).
[3]S. C. Wilks, A. B. Langdon, T. E. Cowan, M. Roth, M. Singh, S. Hatchett, M. H. Key, D. Pennington, A. MacKinnon, and R. A. Snavely, Phys. Plasmas **8**, 542 (2001).
[4]T. E. Cowan, J. Fuchs, H. Ruhl, A. Kemp, P. Audebert, M. Roth, R. Stephens, I. Barton, A. Blazevic, E. Brambrink *et al.*, Phys. Rev. Lett. **92**, 204801 (2004).
[5]C.-M. C. Ma, R. L. Maughan, and C. G. Orton, Med. Phys. **33**, 571 (2006).
[6]M. Roth, T. E. Cowan, M. H. Key, S. P. Hatchett, C. Brown, W. Fountain, J. Johnson, D. M. Pennington, R. A. Snavely, S. C. Wilks *et al.*, Nat. Phys. **86**, 436 (2001).
[7]C. Perego, A. Zani, D. Batani, and M. Passoni, Nucl. Instrum. Methods Phys. Res. A, **653**, 89 (2011).
[8]J. Fuchs, P. Antici, E. d'Humières, E. Lefebvre, M. Borghesi, E. Brambrink, C. A. Cecchetti, M. Kaluza, V. Malka, M. Manclossi *et al.*, Nat. Phys. **8**, 48 (2006).
[9]L. Robson, P. Simpson, P. McKenna, K. Ledingham, R. Clarke, T. McCanny, D. Neely, O. Lundh, F. Lindau, C.-G. Wahlström *et al.*, Nat. Phys. **3**, 58 (2007).
[10]M. Passoni, L. Bertagna, and A. Zani, New J. Phys. **12**, 045012 (2010).
[11]C. M. Brenner, J. S. Green, A. P. L. Robinson, D. C. Carroll, B. Dromey, P. S. Foster, S. Kar, Y. T. Li, K. Markey, C. Spindloe *et al.*, Laser Part. Beams **29**, 345 (2011).
[12]J. S. Green, D. C. Carroll, C. Brenner, B. Dromey, P. S. Foster, S. Kar, Y. T. Li, K. Markey, P. McKenna, D. Neely *et al.*, New J. Phys. **12**, 085012 (2010).
[13]J. A. King, K. Akli, B. Zhang, R. R. Freeman, M. H. Key, C. D. Chen, S. P. Hatchett, J. A. Koch, A. J. MacKinnon, P. K. Patel *et al.*, Appl. Phys. Lett. **86**, 191501 (2005).
[14]F. Nürnberg, M. Schollmeier, E. Brambrink, A. A. Blažević, D. C. Carroll, K. Flippo, D. C. Gautier, M. Geiß, K. Harres, B. M. Hegelich *et al.*, Rev. Sci. Instrum. **80**, 033301 (2009).

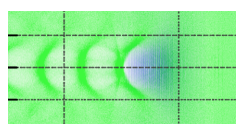

[15]P. Mora, Phys. Rev. Lett. **90**, 185002 (2003).
[16]S. C. Wilks, W. L. Kruer, M. Tabak, and A. B. Langdon, Phys. Rev. Lett. **69**, 1383 (1992).
[17]P. M. Nilson, W. Theobald, J. Myatt, C. Stoeckl, M. Storm, O. V. Gotchev, J. D. Zuegel, R. Betti, D. D. Meyerhofer, and T. C. Sangster, Phys. Plasmas **15**, 056308 (2008).
[18]Warren J. Smith, *Modern Optical Engineering: The Design of Optical Systems*, 4th ed. (McGraw-Hill, New York, 2008), p. 257.
[19]L. Romagnani, J. Fuchs, M. Borghesi, P. Antici, P. Audebert, F. Ceccherini, T. Cowan, T. Grismayer, S. Kar, A. Macchi *et al.*, Phys. Rev. Lett. **95**, 195001 (2005).
[20]E. Brambrink, M. Roth, A. Blazevic, and T. Schlegel, Laser Part. Beams **24**, 163 (2006).
[21]D. C. Carroll, P. McKenna, O. Lundh, F. Lindau, C.-G. Wahlström, S. Bandyopadhyay, D. Pepler, D. Neely, S. Kar, P. T. Simpson *et al.*, Phys. Rev. E **76**, 065401 (2007).

Paper IV

Megagauss magnetic field generation at relativistic intensities using 35 femtosecond laser pulses

A. Gopal, S. Minardi, M. Burza, G. Genoud, I. Tzianaki, A. Karmakar, P. Gibbon, M. Tatarakis, A. Persson and C.-G. Wahlström.

Manuscript.

MegaGauss magnetic field generation at relativistic intensities using 35 femtosecond laser pulses

A Gopal[1,3], S Minardi[1,3], M Burza[2], G Genoud[2], I Tzianaki[3], A Karmakar[4] P Gibbon[4], M Tatarakis[3], A Persson[2], C-G Wahlström[2]

1.Faculty of Physics and Astronomy, Friedrich-Schiller University, Max-Wien Platz 1, D-07743, Jena, Germany
2.Department of Physics, Lund University, Lund, Sweden
3. Centre for Plasma Physics & Lasers, Department of Electronics, TEI of Crete, Chania, GR-73133, Greece
4. Juelich Supercomputing Centre, Institute for Advanced Simulation Research Centre Juelich, 52425 Juelich, Germany

E-mail: amrutha.gopal@uni-jena.de

Abstract. We report the experimental studies on magnetic field generation using a 35 femtosecond laser at relativistic intensities. The polarisation change in the self generated harmonics has been recorded to estimate the magnetic field. A parameter scan was performed by varying the input laser intensity as well as the contrast ratio. External optical probing diagnostics were performed using the second harmonic of the incident laser. Additionally, the Optical Transition Radiation(OTR) from the rear of the target was also recorded.

PACS numbers: 00.00, 20.00, 42.10

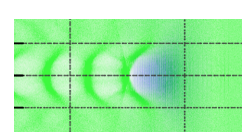

1. Introduction

Since their first observation [1], self-generated magnetic fields in laser-produced plasmas have become an active area of research. The relevance of a detailed understanding of the dynamics of such magnetic fields is manifold. Temperatures and densities achieved in laser produced plasmas can be similar to those expected in the interiors of stars or other unaccessible astrophysical environments [2] where magnetic fields can significantly affect the transport properties or the kinematic of the plasma. Such is the case of the magnetic reconnection phenomena occurring during stellar flares [3,4]. Moreover, lasers of extremely high intensity ($I > 10^{19}$ W/cm^2) have been reported to generate magnetic fields of the order of several hundreds of MGauss [5], thus enabling the unique possibility to reproduce in a laboratory experimental conditions similar to those occurring in the neighborhood of a neutron star [6]. On a more applicative level, the characterization of the plasma dynamics in the presence of magnetic fields is crucial for the optimization of future nuclear fusion schemes using inertial confinement [7]. Of particular relevance is the understanding of the effect of X-ray yield in the plasma in the presence of interacting magnetic fields generated by multiple heating beams in gold holraums or on the surface of fusion pellets [3, 4].

Among the various mechanisms identified by the generalised Ohm's law which give rise to magnetic fields in laser-produced solid plasmas, three are of great significance. *i)* Non-parallel temperature and density gradients (thermoelectric effect) are responsible for a slowly time-varying B field usually observed in the under-critical density region [13]. *ii)* The fast electron current generated in the target during the interaction is a source of axial magnetic fields within the dense plasma [12, 16, 17]. Finally *iii)* the huge radiation pressure (ponderomotive) associated with the incident laser pulse can generate azimuthal magnetic fields in the critical density region [14]. Experiments performed up-to date have usually explored these magnetic fields independently, leaving the observation of the evolution and interaction of the self-generated magnetic field mostly unexplored [10]. Moreover, little is known about the dependence of the magnetic field strength as a function of the laser parameters such as the pulse energy and temporal contrast. The magnetic field production in the ultrashort heating pulse regime ($\tau < 100$ fs) is also little explored.

Various diagnostic methods have been used previously to study these huge fields, such as Faraday rotation of an external optical probe beam [11, 13], cotton-mouton effect on the self generated harmonics [5], properties of the proton beam emitted at the rear surface [12] etc. The highest magnetic field reported in the literature, 0.7 GG has been associated with the dc current generated by the laser radiation pressure and it is comparable to the amplitude of the magnetic field associated with the interacting laser pulse [18]. Depolarisation of the self generated harmonics while propagating through the magnetised plasma was used to detect those fields. Faraday rotation of the second

harmonic of the incident laser beam was employed to measure the coronal magnetic fields of the order of several tens of MG [11]. Clark etal have observed proton emission from the rear surface of a thin target to measure the magnetic field generated inside the dense target [12]. In this paper, we present a systematic study on the magnetic field generation in laser produced plasmas in the relativistic regime using 35 fs, 30 TW laser pulses. For the first time, we have gauged simultaneously the magnetic fields due to thermoelectric, ponderomotive and fast-electron effects using suitably designed optical diagnostics. Experimental results from simultaneous and independent diagnostic show self-generated magnetic fields of the order of 2 MG in the coronal plasma and 100 MG near the critical density surface. Strong collimation of the optical radiation from the target rear surface indicates the formation of strong internal magnetic fields.

2. Set-up and experimental methods

The experiment was performed on the multi tera watt laser system at the Lund Laser Centre (LLC). The LLC laser delivers pulses upto 1.0 Joule on target at 800 nm, 35 fs and 10Hz repetition rate. The main beam was split with a 97 : 3 ratio. The p-polarised

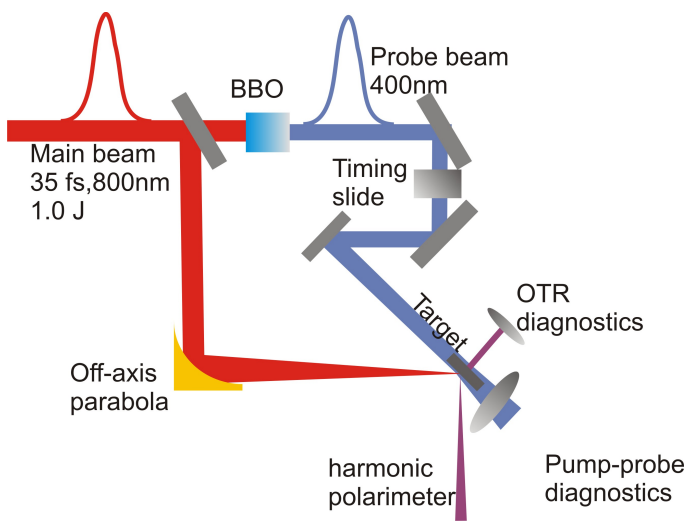

Figure 1: Top: Schematic of the experimental setup.

higher energy beam (97%) was focused onto an optically polished glass target inside the vacuum chamber using a 45°, $f/3$ off-axis parabolic mirror resulting in a 4μm spot size and an estimated peak intensity of 8×10^{19}W/cm^2. The low power beam (remaining 3%) was frequency doubled using a BBO crystal and sent perpendicularly to the target normal to backlight the plasma (see Figure 1) for spatially resolved optical diagnostic. A time slide was included to allow accurate time delay between the heating pulse and

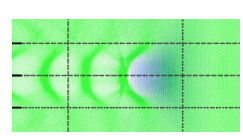

the probe pulse.

To gain an overall picture of the laser-plasma interaction and to measure the magnetic field strength three main diagnostics were implemented, namely: the harmonic polarimeter, spatially-temporally resolved optical diagnostics, and an imaging system for the optical transition radiation. They are described in the following section.

2.1. Harmonic polarimeter

In order to measure magnetic fields generated by the laser ponderomotive force we implemented the harmonic polarimetry technique [19]. The incident heating pulse was polarised (p-polarised) in the plane perpendicular to the target surface. Thus, the harmonics are generated with the same polarisation at the critical density surface, where the highest B-field occurs. As the linearly polarised harmonics propagate through the magnetised plasma with their k vector perpendicular to the B-field they will experience birefringence. By measuring the induced birefringence it is possible to extract the magnitude of the B-field. The polarisation state of electromagnetic radiation can be expressed in terms of the Stokes parameters. In order to obtain the complete polarisation state it is necessary to use a four channel polarimeter. However, the magnetic field strength can also be obtained using only any two of the polarisation states assuming that initially the harmonics are completely linearly polarised. This was indeed confirmed by by taking laser shots at low intensities. A complete description of the polarimeter and the calculation of Stokes parameters can be found in references [8, 9].

In our set-up, self-generated optical harmonics were collected in the specular reflection direction of the pump beam using a two inch diameter fused silica lens with 50 cm focal length. The collimated harmonics were taken out of the vacuum chamber through a fused silica window. The third ($\lambda_0 = 266$ nm) or the fourth harmonic ($\lambda_0 = 200$ nm) could be selected by means of interference filters placed at the entrance of a 3-channel polarimeter outside the chamber (see Figure 2a). The incident angles on the beam splitters and mirror were kept small to avoid the depolarisation of the harmonics due to the optical components. All channels of the polarimeter were imaged on a 16 bit CCD camera.

2.2. Spatiotemporally resolved diagnostic

The $\lambda_0 = 400$ nm probe beam was collected using a high resolution double lens system and was relayed through a fused silica window to a spatially resolved optical diagnostics box, placed outside the experimental chamber. An interference filter ($\lambda_c = 400$ nm, $\Delta\lambda = 10$ nm) and two dielectric mirrors were placed at the entrance of the diagnostic box to reduce in the plasma continuum background emission. The optical diagnostics box included a shadowgraphic, a Faraday rotation and an interferometric channel (cf. Figure 2b). We used the shadowgraphy channel *i)* to monitor the spatio-temporal expansion of the plasma, and *ii)* as a reference for the Faraday rotation channel. The Faraday

rotation channel was employed to measure the B-field generated by the thermoelectric effect in the low density coronal plasma. It consisted of a Glan-Taylor polariser at 12.5°

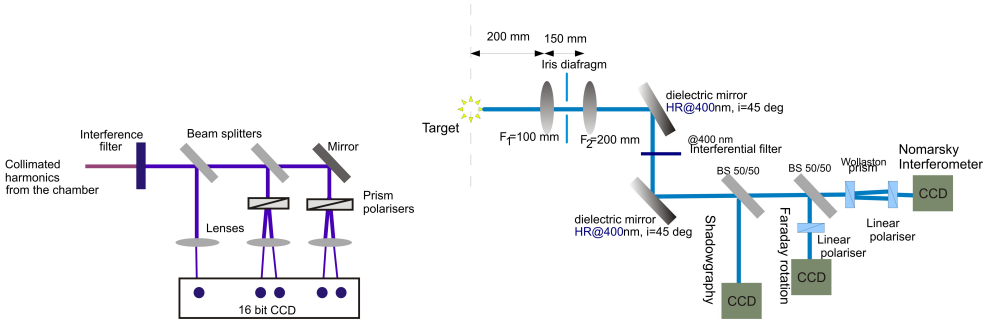

Figure 2: Lay out of the harmonic polarimeter (left) and the optical diagnostics (right).

off-crossed position from the initial polarisation plane of the probe beam. For measuring the electron plasma density we have used a Nomarski interferometric setup [21]. 10-bit charge coupled devices were used as detectors. The probe pulse was sent at various time delays with respect to the main interaction beam so that we could obtain a full time sequence of the plasma expansion.

2.3. Optical Transition Radiation monitor

A qualitative evaluation of the magnetic field generated inside the target by the hot electron current can be extracted from images of the optical transition radiation at the rear side of the target (OTR) [28]. In fact the collimation of the electron beam, and thus of the OTR pattern, depends on the magnetic field generated by the electron beam itself [28]. In our setup, a 50 mm diameter fused silica lens with 20 cm focal length was placed at the rear of the target in the target normal direction. The collected optical radiation from the rear surface was relayed outside the interaction chamber through the fused silica window and was imaged onto a CCD. Best images were obtained by using a 400nm band pass interference filter was placed in the channel.

3. Results

For every laser shot we have simultaneously recorded a shadowgram, an interferogram, a Faraday rotation polarogram, a self generated harmonic polarogram and an OTR image. This provides cross-calibration of the results and a complete characterisation of the plasma for every shot.

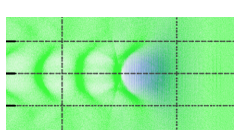

3.1. Self generated harmonics and harmonic polarimetry

The polarisation of the optical harmonics were recorded while varying the laser intensity. This was achieved by moving the target along the focal axis of the parabola. The total yield of the third and fourth harmonics is found to be maximum at the highest laser intensity, i.e.at the Gaussian focus, a clear indication of the higher driving laser field for the electrons at the critical density surface (see Fig.3). We also varied the laser

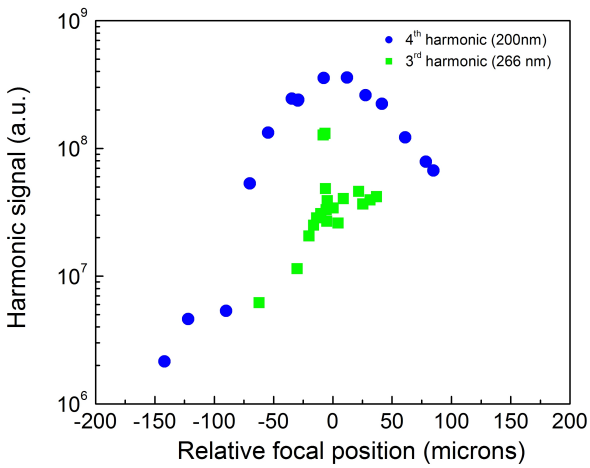

Figure 3: a) Total harmonic yield for 3^{rd} and 4^{th} harmonics while varying the laser intensity.

temporal contrast by adjusting the delay of one of the pockel cells in the final amplifier chain of the laser system. For high contrast incident laser pulses (10^{-8}), the harmonic yield is maximum at the focus, corresponding to the highest field associated with the incident laser which drives the electrons at the critical density surface. However, it was found that at lower contrast ratios (2×10^{-7}) of the interacting pulse the harmonic emission is not following the laser intensity pattern. The emission is peaked on both sides of maximum intensity (see Fig 4). This is expected and is an indication of a strong preplasma formation.

From the depolarisation measurements, the Stokes parameters of the self generated harmonics were calculated. Measurements carried out at relatively low intensities (10^{18} W/cm^2) where the magnetic field is very small, showed that the harmonics are initially linearly polarised (p-polarised). At higher intensities the strength of the magnetic field increases, thus the harmonics experience birefringence as they propagate through the plasma. The polarisation state of the harmonics has been found from the polarimeter data and is plotted on the Poincaré sphere as shown in Figure 5. It is clear that harmonics are highly depolarised at intensities above 10^{19} W/cm^2.

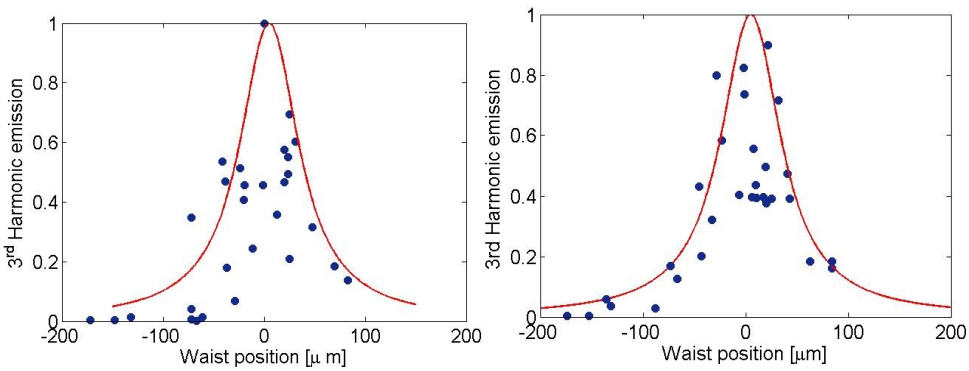

Figure 4: Total harmonic yield for 3^{rd} harmonic for low contrast(10^{-7}) (left) and high contrast (10^{-8}) (right) of the incident laser pulse. Red lines indicate the Gaussian fit for the incident laser pulse intensity.

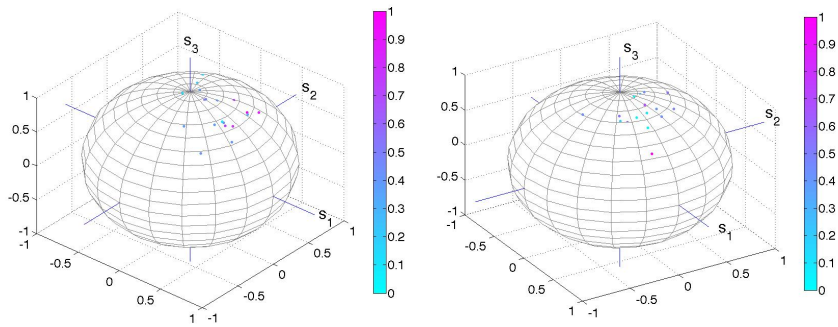

Figure 5: Measured polarisation of the harmonics plotted on the Poincaré sphere. Left: Third harmonic 266nm. Right: Fourth harmonic 200 nm.

The plasma transition matrix was calculated using the plasma density and scale length calculated from the shadowgraphy and interferometry diagnostics. The experimentally determined plasma transition matrix was compared with the theoretical one for both third and fourth harmonic to retrieve the magnetic field strength. The maximum field (Figure 6) we measured at intensities 8×10^{19} W/cm^2 is 100 ± 10 MG.

3.2. Optical diagnostics

Images taken in the shadowgraphy channel were used to estimate the plasma density scale length and expansion rate. At incident intensities of the order of $5 \times 10^{19} W/cm^2$

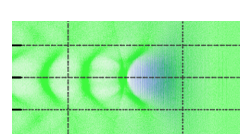

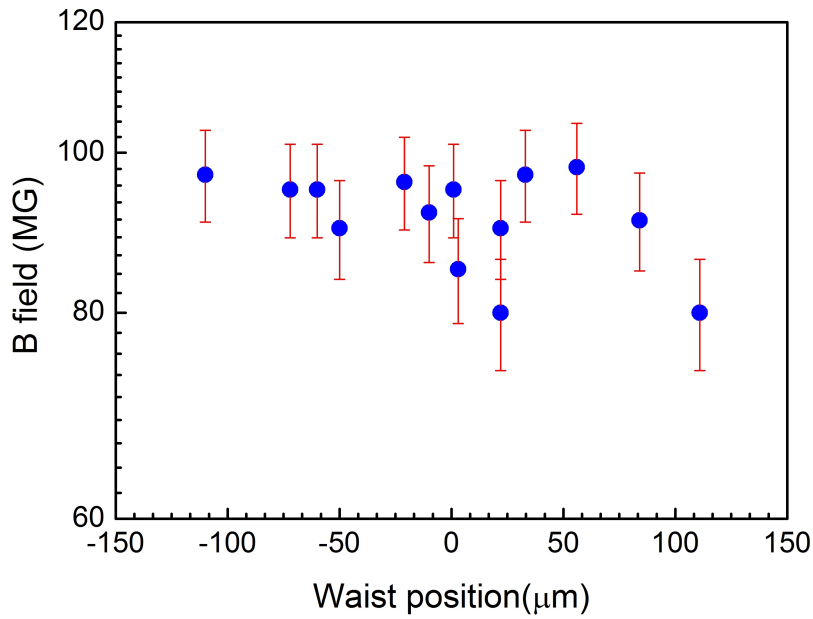

Figure 6: The magnitude of the self generated dc magnetic field due to laser ponderomotive force calculated from the depolarisation of the 4^{th} harmonic (200)nm of the incident laser.

the estimated expansion rate of the critical density surface is is 1.9 ± 0.2 μm per picosecond (see Figure 7a). Interferograms were processed using the Interferometric Data Evaluation Algorithms (IDEA) [15]. The density profiles were retrieved after Abel inversion of the processed interferograms. A horizontal lineout of the density profile shows peak densities of the order of 10^{25} m^{-3} in the coronal plasma. Plasma density and scale length measurements from interferometry and shadowgraphy measurements were used for the calculation of the corresponding B field from the polarograms recorded by the Faraday rotation channel. The polariser and analyser were aligned 12.5° off crossed position. The polarograms show signatures (dark and bright patterns) of toroidal magnetic field in the coronal plasma on both sides of the laser interaction. Figure 7c shows the background subtracted Faraday rotation polarograms. For analysis the self-emission region is masked. Rotation angle is presented in figure 7d by taking a horizontal line out along the region where intensity variations are observed. Maximum rotation (0.7°) is observed in the darker region where the field is localised in a region of 15 micrometer diameter. The brighter region experience a rotation of $-0.22°$ in a region of 36 micrometer diameter. The asymmetry in the observation arises from the oblique incidence of the interaction pulse. The strength of the peak magnetic field was calculated from the rotation angle to be 1.9 MG.

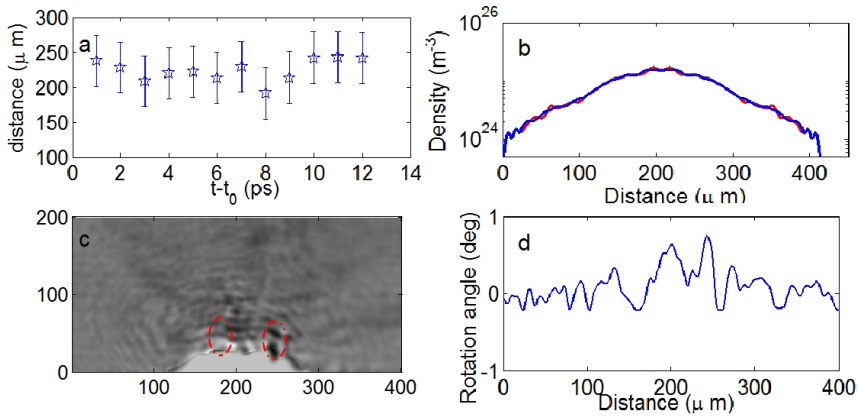

Figure 7: a.Estimation of the expansion velocity of the critical density surface b. Horizontal profile of the density where the thermoelectric B field lies. c. Faraday rotation polarogram at a probe delay of 2.2 ps showing the intensity variations, hence the presence of azimuthal B field generated by thermoelectric effect. d. estimated rotation angle.

3.3. Optical Transition Radiation

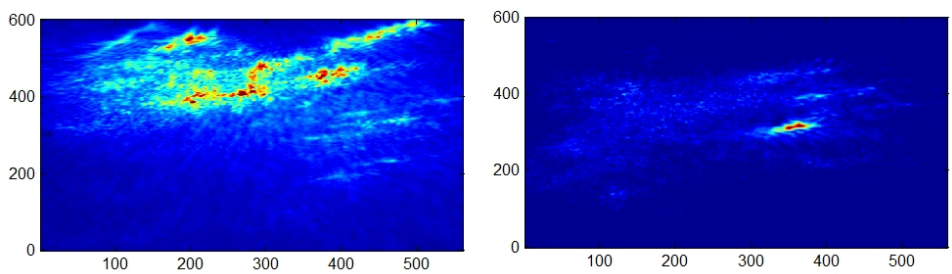

Figure 8: Optical transition radiation at 400 nm from the rear of the target. The emission is well collimated at high intensities where the internal magnetic field is also stronger. Corresponding P/S ratios are 2.44 and 0.2.

In order to understand the internal magnetic fields generated by the electron current inside the target the emission of optical transition radiation from the target rear surface was imaged. With a RG715 filter (which tranmsits above 700nm) in the channel no OTR radiation could be detected, suggesting the observed radiation is generated during the interaction. Figure 8 shows the OTR emission at different laser intensities. Near the optimum laser focus, the emission seems to be more localised with higher B field expected to be generated by the higher electron current inside the target. The polarisation ratio

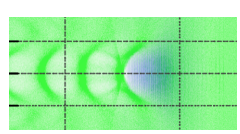

(P/S) of the harmonics observed from the front surface also decreased below 1 indicating strong magnetic field generation due to ponderomotive force of the laser near the critical density surface. As the intensity on target is decreased the emission is defocussed and less intense. At the peak intensity the emission is localised to 15 micrometer diameter much smaller than the electron beam diameter (500 μm) at the target rear surface. The strong localisation of OTR from the rear surface is believed to be due to the electron beam collimation by the internal magnetic field, similar to the observation by Storm et al [28] from thick metal targets.

4. Particle-in-cell (PIC) simulation

In order to validate the experimental evidences we performed 2D PIC simulations using the EM code EPOCH [30]. A simulation domain of size 25 $\times$ 15 microns meshed by 4096 $\times$ 1024 rectangular grid cells was taken. There were 16 particles per cell and no collisions were included in the PIC module. A sharp density profile was chosen where the density rises exponentially from 0 to $30n_c$ within a narrow ramp of 1 micron. A laser pulse of focused intensity 8×10^{19} W/cm^2 was incident at an angle of 45° at the front surface of the target. The laser pulse was p-polarized and of Gaussian profile with a time duration of 35 fs. The pulse enters the simulation box from the center of the left hand boundary with a focal waist of 4μ m. The DC magnetic fields are calculated averaging the instantaneous field over a few laser periods. The results show generation of very strong magnetic field of peak value of the order of 100 Megagauss at around 96 fs as shown in Figure 9. The time evolution of the field was also recorded, showing no current of hot electrons entering the target after the laser pulse is gone, thereby reaching magnetic fields of the order of 100 MG compared to 300 MG as observed in the case of longer incident pulse (greater than 500 fs). This could explain the observation of low magnetic fields in the experiments using lasers of similar intensity but different pulse duration [19].

5. Conclusions

In summary, we simultaneously measured the magnetic fields generated by the three mechanisms described above when a high intensity sub 100 femtosecond laser pulse interacts with solid targets. Toroidal magnetic fields of the order of 1.9 MG were measured in the coronal plasma using Faraday rotation polarimetry of an external probe beam. Self generated 4^{th} harmonic radiation was used to measure the B field due to ponderomotive force near the critical density region. Peak fields of the order of 100 MG were detected. OTR measurements from the target rear surface show localisation of OTR radiation at the highest laser intensities suggesting the presence of strong and collimating B fields generated by electron current inside the target.

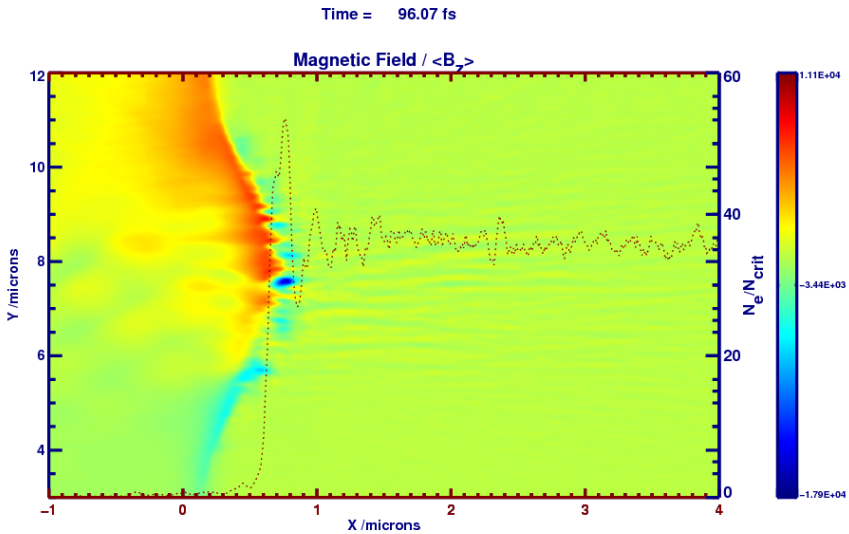

Figure 9: 2D Simulation results showing the generation of strong self- generated DC magnetic fields. Magnetic field topology in the interaction regime at 96 fs after the laser pulse interacts. The broken line shows the density profile changing from 0 to 30 n_c within a narrow ramp.

6. Acknowledgements

We acknowledge the support of the Swedish Research Council, the Knut and Alice Wallenberg Foundation, the EU Access to Research Infrastructures activity (grant agreement no. 212025 Laserlab Europe).

References

[1] J.A. Stamper, B.H. Ripin 1975 Faraday-Rotation Measurements of Megagauss Magnetic Fields in Laser-Produced Plasmas *Phys. Rev. Lett.* **34** 138

[2] Remington B A, Arnett D, Drake R P, Takabe H 1999 Modeling Astrophysical Phenomena in the Laboratory with Intense Lasers *Science* **284** 1488

[3] Nilson P M *et al* 2006 Magnetic Reconnection and Plasma Dynamics in Two-Beam Laser-Solid Interactions *Phys. Rev. Lett.* **97** 255001

[4] Nilson P M *et al* 2008 Bidirectional jet formation during driven magnetic reconnection in two-beam laser-plasma interactions *Phys. Plasmas* **15** 092701

[5] Tatarakis M *et al* 2002 Measuring huge magnetic fields Nature **415** 280

[6] Moon S J *et al* 2005 A neutron star atmosphere in the laboratory with petawatt lasers *Astrophysics and Space Science* **298** 293

[7] Atzeni S and Meyer-ter-Vehn J 2004 The Physics of Inertial Fusion Beam plasma interaction, hydrodynamics dense plasma physics Clarendon Press - Oxford University Press Oxford

[8] Gopal A 2004 Measurements of Ultra strong magnetic fields in laser produced plasmas *Ph.D Thesis* University of London

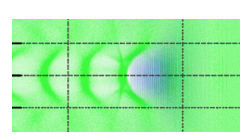

[9] Azzam R M A and Bashara N M 1987 Ellipsometry and polarised light North- Holland Physics Publishing Amsterdam

[10] Gopal A *et al* 2008 Temporally and spatially resolved measurements of multi-megagauss magnetic fields in high intensity laser-produced plasmas *Phys. Plasmas* **15** 122701

[11] Borghesi M *et al* 1998 Megagauss magnetic field generation and plasma jet formation on solid targets irradiated by an ultraintense picosecond laser pulse *Phys. Rev. Lett.* **81** 112

[12] Clark E L *et al* 2000 Measurements of Energetic Proton Transport through Magnetized Plasma from Intense Laser Interactions with Solids *Phys. Rev. Lett.* **84** 670

[13] Stamper J A *et al* 1971 Spontaneous Magnetic Fields in Laser-Produced Plasmas *Phys. Rev. Lett.* **26** 1012

[14] Sudan R N 1993 Mechanism for the generation of 10^9 G magnetic fields in the interaction of ultraintense short laser pulse with an overdense plasma target *Phys. Rev. Lett.* **70** 3075

[15] http://optics.tu-graz.ac.at/idea/idea.html

[16] Davies J R, Bell A R, and Tatarakis M 1999 Magnetic focusing and trapping of high-intensity laser-generated fast electrons at the rear of solid targets *Phys. Rev. E* **59** 6032

[17] Tatarakis M *et al* 1998 Plasma Formation on the Front and Rear of Plastic Targets due to High-Intensity Laser-Generated Fast Electrons *Phys. Rev. Lett.* **81(5)** 999

[18] Wagner *et al* 2004 Laboratory measurements of 0.7 GG magnetic fields generated during high-intensity laser interactions with dense plasmas *Phys. Rev. E* **70 (2)** 026401

[19] Tatarakis M *et al* 2002 Measurements of ultra strong magnetic fields during relativistic laser-plasma interactions *Phys. Plasmas* **9** 3642

[20] Ruhl H Mulser P 1995 Relativistic Vlasov simulation of intense fs laser pulse-matter interaction *Physics Letters A* **205** 388

[21] Hutchinson I H 2002 Principles of plasma diagnostics 2^{nd} edition CUP Cambridge

[22] Bellei C 2010 *et al* Micron-scale fast electron filaments and recirculation determined from rear side optical emission in high-intensity laser solid interactions *New Journal of Physics* **12** 073016

[23] Sandhu A S *et al* 2002 Laser-Generated Ultrashort Multimegagauss Magnetic Pulses in Plasmas *Phys.Rev. Lett.* **89** 225002

[24] Cai H *et al* 2007 Generation of quasistatic magnetic fields in interactions of ultraintense and short laser pulses with over dense plasma targets *Phys.Rev. E* **76** 036403

[25] Krainov V P 2003 Generation of high magnetic fields in an atomic plasma by irradiation with super intense femtosecond laser pulse. *J.Phys.B:At.Mol.Opt. Phys.* **36** 3187

[26] Beiersdorfer P, Scofield J H, and Osterheld A L 2003 X-ray line diagnostic of Magnetic field strength for high temperature Plasmas *Phys. Rev. Lett.* **90** 235003

[27] Sinha J *et al* 2008 Mapping of magnetic fields around dense solid plasmas by high-resolution magneto-optical microscopy *Phys. Rev. E* **77** 046118

[28] Storm M *et al* 2009 High-Current, Relativistic Electron-Beam Transport in Metals and the Role of Magnetic Collimation *Phys.Rev. Lett.* **102** 235004

[29] Yuan X H *et al* 2010 Effect of self-generated magnetic fields on fast-electron beam divergence in solid targets *New Journal of Physics* **12** 063018

[30] Extendable PIC Open Collaboration project UK - http://ccpforge.cse.rl.ac.uk/gf/project/epoch/

Paper V

Staged laser wakefield acceleration using double density ramps

M. Burza, K. Svensson, A. Gonoskov, F. Wojda, A. Persson, O. Lundh, M. Marklund and C.-G. Wahlström.

Manuscript.

Staged Laser Wakefield Acceleration Using Double Density Ramps

M. Burza,[1] A. Gonoskov,[2,3] K. Svensson,[1] F. Wojda,[1] A. Persson,[1] M. Hansson,[1]
G. Genoud,[1] M. Marklund,[2] C.-G. Wahlström[1] and O. Lundh[1]

[1] *Department of Physics, Lund University, P.O. Box 118, SE-221 00 Lund, Sweden*
[2] *Department of Physics, Umeå University, SE-901 87 Umeå, Sweden*
[3] *Institute of Applied Physics, Russian Academy of Sciences, 46 Ulyanov Street, Nizhny Novgorod 603950, Russia*

(Dated: April 21, 2012)

A novel approach to implement and control electron injection into the accelerating phase of a laser wakefield accelerator (LWFA) is presented. It utilizes a wire, which is introduced into the flow of a supersonic gas jet creating shock waves and three regions of differing plasma density. If tailored correctly, electron acceleration takes place in four separate stages: Laser self-compression, electron injection, bunch transfer into the second bucket of the plasma wake, and acceleration. Compared to self-injection by wavebreaking of a nonlinear plasma wave in a constant density plasma, this scheme increases beam charge by up to one order of magnitude. Electron acceleration in the second bucket reduces electron beam divergence by $\approx 25\,\%$, and the localized injection at the density downramp shock wave results in quasi-monoenergetic spectra with $\lesssim 1\,\%$ relative spread.

In plasma based laser-driven electron accelerators, strong longitudinal fields, $\sim 100\,\mathrm{GV/m}$, can be sustained in the plasma oscillation produced in the wake of an intense laser pulse [1]. This gives an advantage over conventional accelerators using RF cavities regarding the relatively compact high-power table-top laser systems readily available [2]

In most experiments, injection of electrons into the accelerating structure relies on breaking of the plasma wave, which can thus self-inject electrons. This scheme is rather simple and quasi-monoenergetic beams have been produced in this way [3–5]. Electron beams of low spectral spread and divergence are necessary in order for these accelerators to be attractive for applications [6–8]. However, the wavebreaking process is highly nonlinear, and in order to achieve higher quality beams, mean to control the injection process are necessary. Both, the amount of charge and the time of electron injection from the background plasma into the accelerating and focusing phase of the wakefield are crucial [9–11]. In this respect self-injection [12–14] is inferior to most schemes with external injection control, such as colliding pulse techniques [15–18], ionisation injection [19, 20] or density gradients [21–23], which are used in this experiment. At the downwards gradient the plasma wavelength increases rapidly enough for the plasma wave to break as a result of the wave-phase irregularity created at the transition.

Shock waves resulting in very abrupt density transitions, have been produced previously with a knife edge introduced into a supersonic gas flow [24]. By this, a well defined shock wave and a density downwards gradient is provided on the laser axis. Alternatively, an auxiliary pulse produced an electron depleted region by a formation of an ionization channel followed by hydrodynamic expansion [25, 26]. Our experiment relates to these, as plasma densities are modulated on the laser axis to control injection externally.

A thin wire, as a novel tool, introduced into a gas jet, can produce extremely sharp density transitions and shock waves to facilitate gradient injection. These transitions may be of only some microns length [27]. Additionally, the pulse may propagate in the undisturbed plasma prior to reaching the shock waves and thus match itself to the plasma conditions by relativistic self-focusing, self-modulation and compression, with only a negligible amount of charge being trapped (stage 1). After a variable length, adjustable by the wire position along the optical axis, the laser intersects the first shock front, originating from the wire, where gradients enable injection (stage 2). However, a key feature of this experiment, never utilized before, is the possibility of a controlled charge transfer of the injected electron bunch to a later bucket of the plasma wake. At the transition from the density-diluted region right above the wire to the final constant density region, the plasma wavelength shrinks rapidly and due to their inertia electrons may thus be transferred to a later bucket (stage 3). This filters the previously injected bunch and isolates it from the laser field during acceleration (stage 4), which improves their longitudinal and transverse emittance. Stage 4 is driven by the same already matched laser pulse from stage 1. The wire injection scheme presented in this article is thus a novel, staged, four step, laser wakefield accelerator.

The experiment was conducted at the Lund Laser Centre, Sweden, where a Ti:Sa CPA laser system provides pulses at 800 nm central wavelength with 42 fs duration at an energy of approximately 1 J on target. A deformable mirror provides a nearly diffraction limited focal spot with of an $f/15$ off-axis parabolic mirror $\approx 700\,\mu\mathrm{m}$ above the orifice of a 3 mm diameter supersonic gas nozzle, which provides the target gas. The laser is focused at the boundary of the gas jet producing a spot with $\approx 15\,\mu\mathrm{m}$ intensity FWHM diameter. A motorized holder positions a wire above the nozzle but below the laser optical axis. This produces three distinct plasma density regions for the laser interaction as illustrated by the white broken line function in Fig. 6 b)). To tailor and model plasma densities, interferometric measurements have been carried out using hydrogen at 9 bar backing pressure. Initially the laser pulse encounters a region of approximately constant density (region I), which has been determined to $\approx 6\times10^{18}\,\mathrm{cm}^{-3}$. After $\sim 1\,\mathrm{mm}$ it encounters the first shock wave and downwards gradient,

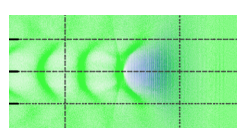

followed by region II, where the plasma density is reduced to only $\approx 3 \times 10^{18}\,\mathrm{cm}^{-3}$ for $\sim 300\,\mu$m. After a second shock wave transition, region III,whose density is approximately the same as in region I, provides the acceleration distance, until the end of the gas jet is reached. By adjustments of wire position, thickness and Mach number, gradients and density ratios between region I and II can be tailored to match the requirements for electron injection and laser guidance. Shock wave divergence angle and density ramps have been found to be symmetric as long as the wire is < 0.5 mm off the nozzle centre. Without wire, the plasma density is comparable to that at the plateau regions I and III.

As diagnostics serve a top view camera as well as a permanent magnet electron spectrometer equipped with a Lanex screen (Kodak Lanex Regular), whose emission is recorded by a 16 bit CCD camera. Based on previous work [28, 29] the electron spectrometer is calibrated in absolute charge. The setup is depicted in Fig. 1.

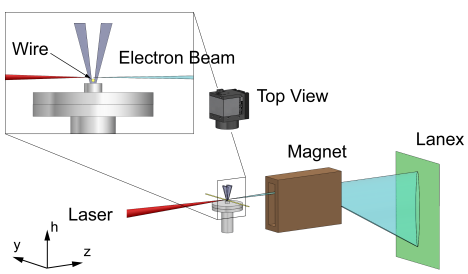

FIG. 1: Experimental setup: The laser pulse enters from the left and impinges on the gas jet ≈ 0.7 mm above the nozzle. The wire is positioned ≈ 0.2 mm above the orifice. Top-view and a permanent magnet Lanex electron spectrometer serve as primary diagnostics. The position z=0 along the laser axis is centred above the nozzle.

Stainless steel wires with $300\,\mu$m, $200\,\mu$m, $50\,\mu$m and $25\,\mu$m diameter were tested, but only the latter two can trigger injection, with a much improved performance of the $25\,\mu$m wire. Thicker wires inevitably increase the length and depth of the density-diluted region II, promoting diffraction and making it difficult to maintain a sufficiently strong laser pulse for region III. Hydrogen and helium have both been tested as target gas but with the wire present, only hydrogen produced electron beams.

A wire height scan revealed, that probability for the production of electron beams increases with reduced distance to the optical axis. However, closer than 0.65 mm dramatically reduces the lifetime of the wire. As no improved performance on the production of electron beams could be observed in the range between 0.35 mm and 0.50 mm, the latter position was chosen.

A z-scan conducted with the $25\,\mu$m wire at 0.50 mm distance and with a backing pressure around the threshold for self-injection reveals the sensitivity of the wire position along the optical axis on the production of electron beams (threshold is defined here as plasma density resulting in beams with $< 10\,\%$ of the maximum charge observed during a pressure scan). This window was found to be $\sim 200\,\mu$m wide only. Outside this, the beam charge is comparable to the self-injection case without density modulation.

Pressure scans were carried out at what was found to be the optimum spatial parameters, employing a $d_{opt} = 25\,\mu$m diameter wire at 0.50 mm distance to the optical axis and at a longitudinal position $z_{opt} = -0.07$ mm. The wire injection scheme was found to be rather robust with regard to backing pressure. Below the self-modulated LWFA regime at ≈ 11 bar, beam charge is increased by one order of magnitude, as shown in Fig. 2. Divergence during injection utilizing the wire seems to be unaffected by the pressure but is on average only 75 % of the value encounterd in the self-injection case.

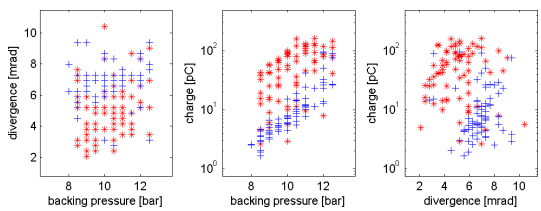

FIG. 2: Comparison of divergence, charge and brightness of electron beams. Red stars represent shots with the wire 0.5 mm below the laser axis, and blue crosses represent LWFA with nonlinear wave-breaking and self-injection. Every data point corresponds to one shot. Failure rate with wire is below 5 % and thus comparable to the wireless self-injection.

Example spectra can be seen in Fig. 3, showing the spectral range from ≈ 43 MeV to infinity. The effects of the wire are threefold: It injects a charge ~ 10 times higher than that available without wire while at the same time providing beams with a quasi-monoenergetic spectra and reduced divergence, thus brightness is increased dramatically. A weak self-injected background charge can be identified in most of the shots. Within limits, energy tuning becomes possible by altering the z-position of the wire as shown in Fig. 3. From this a field gradient of ~ 250 GV/m may be estimated.

From the same data, a relative spectral spread $\frac{\Delta E}{E} \leq 4\,\%$ can be calculated. Note however, that spectrometer dispersion and divergence have not been deconvoluted yet. In fact, 4 mrad (see Fig. 2) produces an apparent $\frac{\Delta E}{E} \approx 4\,\%$ at 100 MeV, thus the real relative spectral spread is expected to $\lesssim 1\,\%$. Electron beam mean energies are generally lower with wire.

Figure 4 compares spectra with and without wire at backing pressures, for the resulting beam charge to be comparable in both cases. Thus self-injection at 12 bar backing pressure is compared to wire injection at 9 bar. The tendency of decreasing peak energy with increasing charge due to beam loading [10], which is clearly visible in the wire injection case, indicates that injection probably occurs at the same z-position.

The 3D fully relativistic parallel PIC code *ELMIS* [30] is

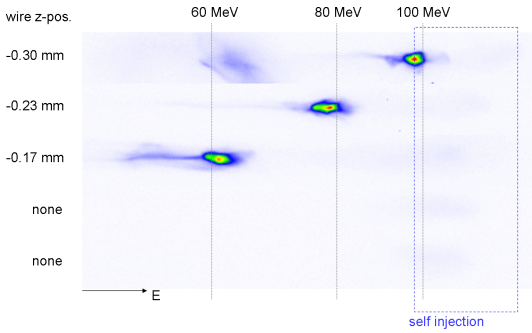

FIG. 3: Example spectra with comparable charge and variable wire position as recorded on the Lanex screen using 9.5 bar backing pressure. Besides the rather strong peak when the wire is present, weak background self-injection can be seen in all spectra.

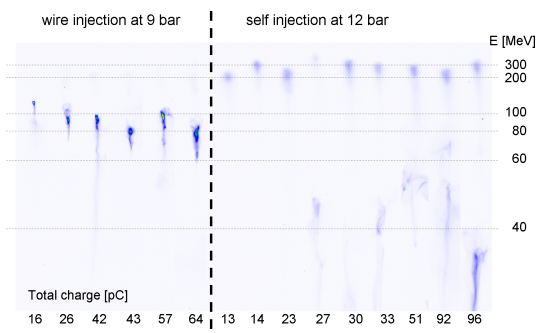

FIG. 4: Example spectra of beams with variable charge and fixed wire position; left: wire injection at 9 bar backing pressure; right: self-injection at 12 bar backing pressure to compensate for the charge increase in the wire injection case as indicated in Fig. 2. Each group has been sorted according to integrated charge

used to investigate the physical mechanisms. 140 attoseconds correspond to one time step in the simulation and an $80\,\mu\text{m}\times80\,\mu\text{m}\times80\mu\text{m}$ box is represented by $1024\times256\times256$ cells. The ions (H^+) are mobile. During the simulation the average number of virtual particles of both types is 0.5 billion. Laser parameters are taken from the experiment. As the measured gradients are blurred $\sim 100\,\mu$m, the exact density distribution is unknown but two extreme cases can be considered, that both give rise to the same interferometric data.

In case one, inspired by Wang *et al.* [31], shock waves are placed to the outwards expanding front. The corresponding densities are approximated by the broken-line function in Fig. 5. When traversing region I, the laser pulse gets focused transversely and generates a highly nonlinear plasma wave, which does not reach breaking and thus facilitates neither longitudinal nor transverse electron self-injection. In line with previous studies [21, 23, 32] at the density downramp, the leading cavity of the nonlinear plasma wave rapidly expands behind

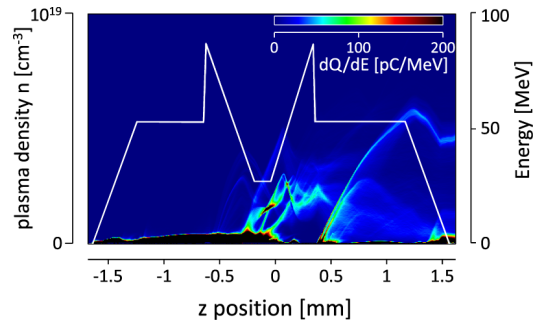

FIG. 5: Electron energy distribution as a function of the laser pulse z-position and plasma density distribution (white curve).

the laser pulse and thereby catches electrons accumulated between the buckets. In region II these electrons form an electron bunch. At the entry to region III, the cavity size shrinks rapidly. With these gradients however, electrons are dephased at the transition and cannot be accelerated further. In contrast, the outward density shock wave enables injection of a new bunch into the second bucket, which is accelerated in region III.

In case two, sharp density transitions are assumed at the inward boundaries to region II. This might resemble the flow of a particularly cold gas or when shooting closer to the wire. The dynamics are comparable to case one above, except that electron injection occurs into the first bucket during the transition from region I to region II. However upon reaching the boundary to region III, the previously injected electron bunch is moved to the second bucket but not necessarily to its accelerating phase. Therefore electrons may now decelerate and fall further behind until they reach the acceleration phase of the second bucket, as depicted in Fig. 6 a). If the distance between the laser pulse and the electron bunch remains constant while passing the density upramp, the size of the plasma cavity in the high density region should ideally be half the size of what it has been in the low density region in order to match acceleration phases. Thus densities should roughly differ by a factor four under the premise that either the laser pulse can traverse region II with sufficient guiding by the plasma or region II being sufficiently short. However, the allowed density regime is not too sensitive to actual plasma densities and gradients. For the case of non-matched wire injection conditions, electrons in region III may first decelerate but eventually they will reach the proper position for further acceleration.

As measured gas jet temperatures are $\lesssim 50$ K, we assume that the real density distribution is a compromise between these two extreme cases. The initial dephasing or renewed injection of electrons upon entering region III, followed by a rapid acceleration over no more than half a millimetre, until the end of the gas jet, explains the rather short acceleration lengths that can be deduced from the field estimates related to Fig. 3. This also leads to the observed lower final energy

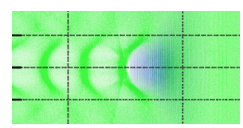

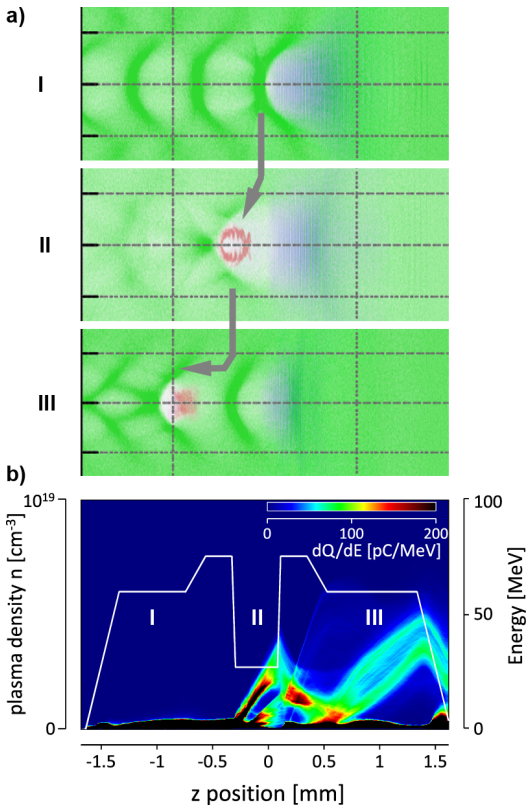

FIG. 6: a) Plasma electron density distribution (green), accelerated electron bunch (red) and laser pulse (blue) shown at the axial section for the instant of laser pulse passing the corresponding density regions I-III. b) same as in Fig. 5.

of the electrons compared to the self-injection case. At the same time it can explain why electron acceleration can only be observed when laser interaction takes place at a certain distance to the wire as this affects the encountered density ratios. Should the electrons due to a density mismatch end up in the decelerating phase and not manage to reach the accelerating phase before the end of the gas jet, no beams of high energy electrons are observed. This is particularly true for helium, whose measured density ratios and gradients were smaller as a result of its fluid characteristics, while working with similar plasma densities, Mach number and void lengths. Generally, a matched wire injection scheme has to be the one of the goals of future attempts utilizing the wire as means to inject and accelerate electrons.

If acceleration takes place in the first bucket, an effect of the laser field acting directly on the accelerating electron bunch can be observed [33]. Thus electron acceleration in the second bucket, isolated from the laser pulse, may as well explain the experimentally observed reduced divergence. Additionally simulations show a filtering effect during the transition from region II to region III, seemingly reducing the transverse spread of the bunch. Note that the number of injected electrons is sensitive to the plasma density gradient [34].

In conclusion, the wire injection scheme has successfully been demonstrated as an alternative to more complex setups facilitating controlled injection. Beam features include a by $\approx 25\,\%$ reduced divergence and one order of magnitude charge increase if compared to the nonlinear self-injection case. Their spectra are quasi-monoenergetic features with $\lesssim 1\,\%$ relative spread. For enhanced performance, a matched wire injection regime is proposed, omitting the initial deceleration in the second high density region by adjusting the prevailing density ratios.

We acknowledge the Swedish Research Council, the Knut and Alice Wallenberg Foundation, the Lund University X-Ray Centre, the European Research Council contract number 204059-QPQV, the Swedish Research Council contract number 2010-3727 and the Swedish National Infrastructure for Computing.

[1] T. Tajima *et al.*, Phys. Rev. Lett. **43**, 267 (1979).
[2] S. Backus *et al.*, Rev. Sci. Instrum. **69**, 1207 (1998).
[3] C. G. R. Geddes *et al.*, Nature **431**, 538 (2004).
[4] J. Faure *et al.*, Nature **431**, 541 (2004).
[5] S. P. D. Mangles *et al.*, Nature **431**, 535 (2004).
[6] K. Nakajima *et al.*, Nature Phys. **4**, 92 (200).
[7] H.-P. Schlenvoigt *et al.*, Nature Phys. **4**, 130 (2008).
[8] M. Fuchs *et al.*, Nature Phys. **5**, 826 (2009).
[9] M. Tzoufras *et al.*, Phys. Rev. Lett. **101**, 145002 (2008).
[10] C. Rechatin *et al.*, Phys. Rev. Lett. **103**, 194804 (2009).
[11] C. Rechatin *et al.*, Phys. Rev. Lett. **102**, 164801 (2009).
[12] I. Kostyukov *et al.*, Phys. Rev. Lett. **103**, 175003 (2009).
[13] S. V. Bulanov *et al.*, Phys. Rev. Lett. **78**, 4205 (1997).
[14] A. Zhidkov *et al.*, Physics of Plasmas **11**, 5379 (2004).
[15] E. Esarey *et al.*, Phys. Rev. Lett. **79**, 2682 (1997).
[16] V. Malka *et al.*, Physics of Plasmas **16**, 056703 (2009).
[17] A. Beck *et al.*, New Journal of Physics **13**, 093016 (2011).
[18] J. Faure *et al.*, Nature **444**, 737 (2006).
[19] A. Pak *et al.*, Phys. Rev. Lett. **104**, 025003 (2010).
[20] C. McGuffey *et al.*, Phys. Rev. Lett. **104**, 025004 (2010).
[21] S. Bulanov *et al.*, Phys. Rev. E **58**, R5257 (1998).
[22] C. G. R. Geddes *et al.*, Phys. Rev. Lett. **100**, 215004 (2008).
[23] H. Suk *et al.*, Phys. Rev. Lett. **86**, 1011 (2001).
[24] K. Schmid *et al.*, Phys. Rev. STAB **13**, 091301 (2010).
[25] J. Faure *et al.*, Phys. Plasmas **17**, 083107 (2010).
[26] C.-T. Hsieh *et al.*, Phys. Rev. Lett. **96**, 095001 (2006).
[27] D. Philpott *et al.*, *Mechanics of Flight* (Paperback, 2006).
[28] Y. Glinec *et al.*, Rev. Sci. Instrum. **77**, 103301 (2006).
[29] A. Buck *et al.*, Rev. Sci. Instrum. **81**, 033301 (2010).
[30] URL `http://www.ipfran.ru/english/structure/lab334/simlight.html`.
[31] C. Wang *et al.*, Phys. Rev. STAB **15**, 020401 (2012).
[32] R. G. Hemker *et al.*, Phys. Rev. STAB **5**, 041301 (2002).
[33] S. P. D. Mangles *et al.*, Phys. Rev. Lett. **96**, 215001 (2006).
[34] A. A. Soloviev *et al.*, Nucl. Instrum. Meth. A. **653**, 35 (2011).

Paper VI

Controlling the spectrum of x-rays generated in a laser-plasma accelerator by tailoring the laser wavefront

S. P. D. Mangles, G. Genoud, S. Kneip, M. Burza, K. Cassou, B. Cros, N. P. Dover, C. Kamperidis, Z. Najmudin, A. Persson, J. Schreiber, F. Wojda and C.-G. Wahlström.

Applied Physics Letters **95**, 181106 (2009).

APPLIED PHYSICS LETTERS **95**, 181106 (2009)

Controlling the spectrum of x-rays generated in a laser-plasma accelerator by tailoring the laser wavefront

S. P. D. Mangles,[1,a)] G. Genoud,[2] S. Kneip,[1] M. Burza,[2] K. Cassou,[3] B. Cros,[3] N. P. Dover,[1] C. Kamperidis,[2] Z. Najmudin,[1] A. Persson,[2] J. Schreiber,[1] F. Wojda,[3] and C.-G. Wahlström[2]

[1]*Blackett Laboratory, Imperial College London, London SW7 2AZ, United Kingdom*
[2]*Department of Physics, Lund University, P.O. Box 118, S-22100 Lund, Sweden*
[3]*Laboratoire de Physique des Gaz et des Plasmas, Centre National de la Recherche Scientifique, Université Paris XI, 91405 Orsay, France*

(Received 1 September 2009; accepted 13 October 2009; published online 4 November 2009)

By tailoring the wavefront of the laser pulse used in a laser-wakefield accelerator, we show that the properties of the x-rays produced due to the electron beam's betatron oscillations in the plasma can be controlled. By creating a wavefront with coma, we find that the critical energy of the synchrotronlike x-ray spectrum can be significantly increased. The coma does not substantially change the energy of the electron beam, but does increase its divergence and produces an energy-dependent exit angle, indicating that changes in the x-ray spectrum are due to an increase in the electron beam's oscillation amplitude within the wakefield. © *2009 American Institute of Physics*. [doi:10.1063/1.3258022]

The use of intense laser pulses to excite plasma waves with a relativistic phase velocity is a possible route to the development of compact particle accelerators. Using this laser-wakefield acceleration technique, experiments have produced quasimonoenergetic 0.1 to 1 GeV electron beams in distances on the order of 1 cm.[1–3] Such compact particle sources have a clear potential as a source of x-rays. The plasma waves produced in current generation experiments not only have a strong accelerating field but also have strong focusing fields. These focusing fields can cause electrons within the wakefield to oscillate transverse to their acceleration direction, in "betatron orbits." This motion generates x-ray radiation which can have properties, in particular peak brightness, similar to those achievable with conventional "3rd generation" light sources.[4] This is, in part, due to the ultrashort-pulse nature of these x-ray sources, which are thought to be at least as short as the laser pulse involved in the interaction,[5] i.e., on the order of tens of femtoseconds. Such x-ray sources could be used for a wide range of studies into the structure of matter. The ultrashort duration of the x-ray pulse and the possible femtosecond synchronization with other photon and particle sources driven by the same laser offer significant benefits.

Studies to date have concentrated on characterizing the properties of this x-ray source in terms of the spectrum, angular distribution, source size, and its ultrashort nature.[4–7] In this letter we demonstrate an ability to control the spectral properties of the betatron x-ray source by controlling the laser wavefront.

In Ref. 8, a correlation between the energy of the electron beam and the angle at which it exited the plasma was attributed to betatron oscillations caused by off-axis injection of the electrons. It was hypothesized that this was caused by an aberration in the focal spot. However, in that study, no direct control of the excitation of the betratron motion was attempted, nor was the effect on x-ray production measured. In this work we use a deformable mirror to tailor the laser wavefront and show that the x-ray spectrum can be changed significantly, in particular we show that a coma wavefront produces more high-energy photons than a flat wavefront. This change in the photon spectrum is due to an increase in the strength of the plasma wiggler, a direct result of off-axis injection.

In the blow-out regime relativistic electrons with energy $\gamma m_e c^2$ undergo transverse (or betatron) oscillations at the betatron frequency $\omega_\beta = \omega_p/\sqrt{2\gamma}$, with a wavenumber $k_\beta = \omega_\beta/c$ (where $\omega_p = \sqrt{n_e e^2/m_e \epsilon_0}$ is the plasma frequency of a plasma of electron density n_e). The wiggler (or betatron) strength parameter for an electron oscillating with an amplitude r_β is $K = \gamma k_\beta r_\beta$. For sufficiently large oscillations ($K > 1$) the radiation is broadband and well characterized by a synchrotronlike spectrum,[4,9] i.e., close to the axis ($\theta = 0$) the spectrum takes the form of $d^2I/(dEd\Omega)_{\theta=0} \propto \xi^2 \mathcal{K}_{2/3}^2(\xi/2)$, where $\mathcal{K}_{2/3}(x)$ is a modified bessel function of order 2/3 and $\xi = E/E_c$. The shape of this spectrum is characterized by a single parameter, the critical energy E_c. The on-axis spectrum is broadband and peaked close to E_c, with approximately half the energy radiated below E_c (note the present definition of E_c is different to that used in Refs. 7 and 9 but consistent with Refs. 4, 6, and 10). For fixed γ and n_e, the critical energy is directly proportional to the oscillation amplitude. $E_c = \frac{3}{4}\hbar\gamma^2\omega_p^2 r_\beta/c$. Thus increasing the oscillation amplitude of the electrons within the wakefield is expected to have a significant effect on the x-ray photon spectrum.

The experiment was performed using the multi-terawatt laser at the Lund Laser Centre, which provided 0.6 J energy pulses on target with a full width at half maximum (FWHM) duration of 45 ± 5 fs at a central wavelength of 800 nm. The laser was focused onto the edge of a 2 mm supersonic helium gas jet using an $f/9$ off-axis parabolic mirror. The plasma density was held constant at 1.5×10^{19} cm^{-3}, at which the laser pulse length is approximately 1.5 times the wavelength of the relativistic plasma wave $\lambda_p = 2\pi c/\omega_p = 9$ μm.

a)Electronic mail: stuart.mangles@imperial.ac.uk.

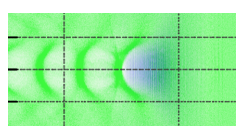

The laser wavefront was measured using a wavefront sensor (Phasics SID4). A 32 actuator deformable mirror (Night N Adaptive Optics DM2-65-32), placed before the focusing optic was used to correct for wavefront errors present in the laser system, defining our flat wavefront. The deformable mirror could be adjusted to tailor the wavefront. The wavefront discussed here is coma, defined on a unit circle by the Zernike polynomial $Z(r,\theta)=\sqrt{8}C(3r^3-2r)\cos\theta$ for horizontal coma. (where C is the rms. amplitude of the coma in units of the laser wavelength λ).

The intensity distribution of the focal spot was recorded on a 12 bit charge coupled device (CCD) camera using a microscope objective. The flat wavefront setting produced a focal spot with a $1/e^2$ intensity radius, or waist, of $w_0=12\pm1$ μm. 42% of the pulse energy was within the FWHM. This corresponds to a peak intensity of 4.0×10^{18} W cm^{-2} or a normalized vector potential of $a_0\simeq1.4$, where $a_0=eA_0/(m_ec)\simeq eE_0/(m_e\omega_0c)$ (A_0 and E_0 are the amplitude of the vector potential and electric field of the laser and ω_0 is the laser frequency). For $C=0.175\lambda$ horizontal coma the peak intensity reduced to 2.1×10^{18} W cm^{-2}, or a normalized vector potential of $a_0\simeq1$. The energy contained within the FWHM reduced to 25%. Horizontal coma elongates the focal spot in the horizontal (x) direction, but it does not do so symmetrically. For $C=0.175\lambda$ and $x<0$ the waist is close to the flat wavefront case with $w_{x<0}=13\pm1$ μm. However, for $x>0$ the waist is significantly increased to $w_{x>0}=18\pm1$ μm. Horizontal coma leaves the vertical (y) beam waist unaffected.

To diagnose the effect of coma on the electron beam profile a scintillator screen (Kodak Lanex regular) was placed in the beam path and imaged onto a 12 bit CCD camera. A permanent magnet ($B=0.7$ T, length 100 mm) could be moved into position between the gas jet and the scintillator screen to sweep the electrons away from the laser axis. The magnetic field dispersed the electrons in the vertical direction, the vertical (y) position of the electron beam on the scintillator screen is then a function of the beam energy (E) so that, taking into account the nonlinear dispersion dy/dE and the response of the lanex to high-energy electrons[11] the electron energy spectrum dN/dE can be calculated.

X-rays generated by betatron oscillations in the wake were recorded by an x-ray sensitive 16 bit CCD camera (Andor 434-BN). The CCD chip had 1024×1024 pixels and was placed on the laser axis. The chip collection angle corresponded to 20×20 mrad^2. The x-rays were only recorded when the magnet was in position to prevent the electron beam striking the CCD chip. An array of filters (Al, Zn, Ni, and Fe) were placed directly in front of the CCD chip. Using the known transmission of x-rays[12] through the filters, and the CCD sensitivity, we find the critical energy E_c which best describes the x-ray photon spectrum using a least-squares method.[7]

The variation in E_c with coma amplitude is shown in Fig. 1(a). For the flat wavefront we observed $E_c=1.5\pm0.5$ keV. As the coma amplitude increases, a clear shift in the x-ray spectrum toward higher photon energies is observed, reaching $E_c=4.0\pm1.5$ keV for 0.175 λ coma. The electron spectra shows a constant mean electron energy of $\langle\gamma\rangle=144\pm7$ for all the coma settings, implying that the change in E_c is due to a change in the oscillation amplitude,

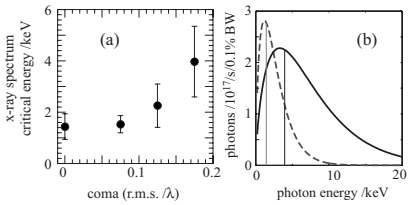

FIG. 1. (a) Variation in the observed x-ray spectrum critical photon energy, E_c with the amplitude of coma. For larger coma no x-rays or were observed. (b) best-fit synchrotron spectra for a flat wavefront (dashed line) and 0.175 λ amplitude coma (solid line). The curves take into account the expected change in beam divergence and assume the duration of the x-rays is that of the laser pulse. The vertical lines indicate the position of E_c.

r_β. We calculate that the oscillation amplitude increases from $r_\beta=1.0\pm0.4$ μm to $r_\beta=3\pm1$ μm corresponding to an increase in the wiggler strength parameter from $K=5\pm2$ to $K=17\pm6$. The largest oscillation amplitudes are slightly less than the radius of the wakefield (approximately $\lambda_p/2=4.5$ μm) and indicate that almost the whole width of the plasma channel is being used for radiation generation. Oscillations larger than this would not be supported and may indicate why, when larger amplitude coma wavefronts were used, no electrons or x-rays were observed.

Integrating the signal recorded on the CCD and taking into account the expected photon beam divergence, $\theta\approx K/\gamma$, we estimate that as the coma is increased the number of photons remains approximately constant at $(3\pm1)\times10^7$ photons per shot. The energy in the x-ray beam therefore increases, as expected for an increase in K. Two x-ray spectra are shown in Fig. 1(b). While the peak intensity is reduced for the case of 0.175 λ coma, there is significantly more intensity at the higher photon energies.

The source of the change in the x-ray spectrum can be elucidated by examining the effect of coma on the electron beam. Figure 2 shows the variation in the electron beam profile and energy spectrum with the amplitude of coma. The electron beam profile images (each representing an average

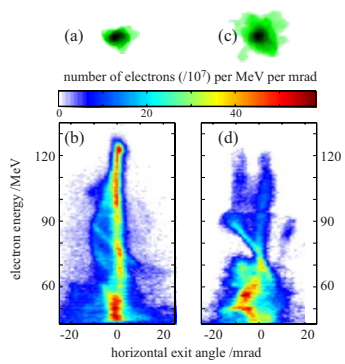

FIG. 2. (Color online) Effect of coma on the electron beam. [(a) and (b)] Flat wavefront, [(c) and (d)] coma=0.175λ, (a) and (c) show the electron beam profile (average from several shots), (b) and (d) show the electron energy spectrum (from a single shot). The vertical axis is a linear energy scale and the horizontal scale represents the exit angle in the nondispersion plane.

of five shots) show that the electron beam divergence increases with the amplitude of coma from $\simeq$10 mrad (FWHM) for the flat wavefront to $\simeq$20 mrad for 0.175λ coma. The images of the electron energy spectrum (each from a single shot) show the electron energy spectrum dN/dE as a function of the horizontal angle at which the beam exits the plasma. For shots with the flat wavefront and $n_e = 1.5 \times 10^{19}$ cm^{-3} the electron spectrum is broadband, extending in energy to $\simeq$120 MeV. For the flat wavefront the electrons have an approximately constant exit angle, indicating a small betatron amplitude. With coma we observe an energy-dependent exit angle, indicating a large betatron oscillation amplitude. This occurs because, for broad energy-spread beams, an electron's energy can be mapped to its phase within the plasma wave. Different energy electrons will therefore be at a different phase of their betatron orbit as they exit the plasma, resulting in an oscillatory dependence of the exit angle with energy, as observed.

The electron beam diagnostics show that, by tailoring the wavefront to create an asymmetric focal spot, the wake dynamics are sufficiently perturbed so as to increase the amplitude of the betatron oscillations. This is likely due to the promotion of off-axis injection due to the generation of an asymmetric wakefield by the asymmetric focal spot. Images of self-scattered radiation show that a long wavelength hosing of the channel sometimes occurred; the likelihood of observing this hosing increased with coma. However, the hosing wavelength was significantly longer than the plasma wavelength so would not produce an energy-dependent exit angle, and no correlation between the amplitude of the hosing and x-ray spectrum was observed.

By tailoring the laser wavefront to produce an asymmetric focal spot we have demonstrated an ability to change the energy spectrum of the x-ray photons from a laser-plasma wiggler; increasing the number of high-energy ($E \gtrsim 5$ keV) photons without the need to increase the laser power or electron beam energy. This offers an alternative route to higher energy laser-based x-ray sources without the significant cost of petawatt laser facilities. On some shots we observe that the effect of the coma on the electron beam divergence is predominantly in the plane of the laser asymmetry. If this effect can be controlled then it also offers a mechanism for producing polarized x-rays with a laser-plasma wiggler.

We acknowledge support from The Royal Society, the Marie Curie Early Stage Training Site MAXLAS (Grant No. MEST-CT-205-02936), the Swedish Research Council, and the EuroLEAP network.

[1]W. P. Leemans, B. Nagler, A. J. Gonsalves, C. Toth, K. Nakamura, C. G. Geddes, E. Esarey, C. B. Schroeder, and S. M. Hooker, Nat. Phys. **2**, 696 (2006).
[2]S. Karsch, J. Osterhoff, A. Popp, T. P. Rowlands-Rees, Z. Major, M. Fuchs, B. Marx, R. Horlein, K. Schmid, L. Veisz, S. Becker, U. Schramm, B. Hidding, G. Pretzler, D. Habs, F. Gruner, F. Krausz, and S. M. Hooker, New. J. Phys. **9**, 415 (2007).
[3]S. Kneip, S. R. Nagel, S. F. Martins, S. P. D. Mangles, C. Bellei, O. Chekhlov, R. J. Clarke, N. Delerue, E. J. Divall, G. Doucas, K. Ertel, F. Fiuza, R. Fonseca, P. Foster, S. J. Hawkes, C. J. Hooker, K. Krushelnick, W. B. Mori, C. A. J. Palmer, K. Ta Phuoc, P. P. Rajeev, J. Schreiber, M. J. V. Streeter, D. Urner, J. Viera, L. O. Silva, and Z. Najmudin, Phys. Rev. Lett. **103**, 035002 (2009).
[4]A. Rousse, K. T. Phuoc, R. Shah, R. Fitour, and F. Albert, Eur. Phys. J. D **45**, 391 (2007).
[5]K. Ta Phuoc, R. Fitour, A. Tafzi, T. Garl, N. Artemiev, R. Shah, F. Albert, D. Boschetto, A. Rousse, D. E. Kim, A. Pukhov, V. Seredov, and I. Kostyukov, Phys. Plasmas **14**, 080701 (2007).
[6]A. Rousse, K. T. Phuoc, R. Shah, A. Pukhov, E. Lefebvre, V. Malka, S. Kiselev, F. Burgy, J. P. Rousseau, and D. Umstadter, Phys. Rev. Lett. **93**, 135005 (2004).
[7]S. Kneip, S. R. Nagel, C. Bellei, N. Bourgeois, A. E. Dangor, A. Gopal, R. Heathcote, S. P. D. Mangles, J. R. Marques, A. Maksimchuk, P. M. Nilson, K. Ta Phuoc, S. Reed, M. Tzoufras, F. S. Tsung, L. Willingale, W. B. Mori, A. Rousse, K. Krushelnick, and Z. Najmduin, Phys. Rev. Lett. **100**, 105006 (2008).
[8]Y. Glinec, J. Faure, A. Lifschitz, J. M. Vieira, R. A. Fonseca, L. O. Silva, and V. Malka, Europhys. Lett. **81**, 64001 (2008).
[9]E. Esarey, B. A. Shadwick, P. Catravas, and W. P. Leemans, Phys. Rev. E **65**, 056505 (2002).
[10]J. D. Jackson, *Classical Electrodynamics* 3rd ed. (Wiley, New York, 1999).
[11]Y. Glinec, J. Faure, A. Guemnie-Tafo, V. Malka, H. Monard, J. P. Larbre, V. De Waele, J. L. Marignier, and M. Mostafavi, Rev. Sci. Instrum. **77**, 103301 (2006).
[12]J. Hubbell and S. Seltzer, N.I.S.T., Gaithersburg, MD, http://physics.nist.gov/xaamdi, 2004.

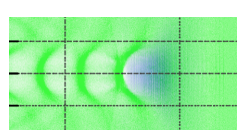

Paper VII

Self-injection threshold in self-guided laser wakefield accelerators

S. P. D. Mangles, G. Genoud, M. S. Bloom, M. Burza, Z. Najmudin, A. Persson, K. Svensson, A. G. R. Thomas and C.-G. Wahlström.

Physical Review Special Topics - Accelerators and Beams **15**, 011302 (2012).

PHYSICAL REVIEW SPECIAL TOPICS - ACCELERATORS AND BEAMS **15**, 011302 (2012)

Self-injection threshold in self-guided laser wakefield accelerators

S. P. D. Mangles,[1] G. Genoud,[2] M. S. Bloom,[1] M. Burza,[2] Z. Najmudin,[1]
A. Persson,[2] K. Svensson,[2] A. G. R. Thomas,[3] and C.-G. Wahlström[2]

[1]*The Blackett Laboratory, Imperial College London, SW7 2AZ, United Kingdom*
[2]*Department of Physics, Lund University, P.O. Box 118, S-22100 Lund, Sweden*
[3]*Center for Ultrafast Optical Science, University of Michigan, Ann Arbor, Michigan 48109, USA*
(Received 7 January 2011; published 19 January 2012)

A laser pulse traveling through a plasma can excite large amplitude plasma waves that can be used to accelerate relativistic electron beams in a very short distance—a technique called laser wakefield acceleration. Many wakefield acceleration experiments rely on the process of wave breaking, or self-injection, to inject electrons into the wave, while other injection techniques rely on operation without self-injection. We present an experimental study into the parameters, including the pulse energy, focal spot quality, and pulse power, that determine whether or not a wakefield accelerator will self-inject. By taking into account the processes of self-focusing and pulse compression we are able to extend a previously described theoretical model, where the minimum bubble size $k_p r_b$ required for trapping is not constant but varies slowly with density and find excellent agreement with this model.

DOI: 10.1103/PhysRevSTAB.15.011302 PACS numbers: 52.38.Kd, 41.75.Jv, 52.35.Mw

Laser wakefield acceleration, where an intense laser pulse drives a plasma wave with a relativistic phase velocity, is a promising technique for the development of compact, or ''tabletop,'' particle accelerators and radiation sources. Plasma waves driven in moderate density plasmas can support electric fields over a thousand times stronger than those in conventional accelerators. Laser driven plasma waves have demonstrated electron acceleration to $\simeq 1$ GeV in distances $\simeq 1$ cm [1–3]. These compact particle accelerators have significant potential as bright x-ray sources [4–6] offering peak brightness comparable to 3rd generation synchrotron sources in x-ray flashes on the order of just 10 fs.

At the heart of the laser wakefield acceleration concept is the fact that electron plasma waves with relativistic phase velocities are driven to very large amplitudes, where they become highly nonlinear. If the plasma wave is driven beyond a threshold amplitude, the wave breaks. When the wave is driven far beyond the wave breaking threshold, the wave structure is destroyed and large amounts of charge can be accelerated to high energy but with a broad energy spread [7]. With appropriately shaped laser pulses this normally catastrophic process of wave breaking can be tamed to produce high quality beams of electrons. This is because close to the wave breaking threshold the nature of wave breaking changes—some electrons from the background plasma can become trapped in the wave without destroying the wave structure, a process called self-injection.

The highly nonlinear broken wave regime [8] is used in many experiments to produce quasimonoenergetic electron beams [9–11]. In such experiments a threshold plasma density is commonly observed, below which no electron beams are produced. Because of the inverse scaling of the electron beam energy with plasma density, the highest energy beams achievable with a given laser system are achieved just above the threshold, and it is well known that many of the beam parameters including the spectrum and stability are also optimized just above the threshold density [12,13]. It is also well known that to achieve self-injection at lower densities higher power lasers are required—although the exact scaling of the threshold with laser power is not well known. A number of techniques to improve the electron beam parameters including stability and total charge have recently been demonstrated by using alternative injection schemes [14–18]. Crucially these schemes all rely on operating the laser wakefield accelerator (LWFA) below the self-injection threshold. A number of recent purely theoretical papers have addressed the dynamics of wave breaking or self-injection [19–22]. Clearly a good understanding of the self-injection threshold is important for the development of laser wakefield accelerators. We report here on a series of experiments which identify the key laser and plasma parameters needed to predict the density threshold and we develop a model capable of predicting the self-injection threshold density for a given set of experimental parameters.

In LWFA experiments the laser pulse self-focuses due to the transverse nonlinear refractive index gradient of the plasma [23,24] and the spot size decreases towards a matched spot size. This matched spot size occurs when the ponderomotive force of the laser balances the space charge force of the plasma bubble formed. In situations

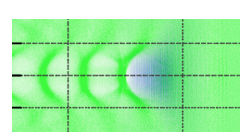

where there is no loss of energy during self-focusing, nor any change in the pulse duration, the final matched spot size, and hence the final intensity, is simply a function of $\alpha P/P_c$. P is the laser power; α is the fraction of laser energy within the full width at half maximum intensity of the focal spot—important because energy in the wings of the spot are not self-focused by the plasma wave and so do not contribute; P_c is the laser power where relativistic self-focusing dominates over diffraction, $P_c = (8\pi\epsilon_0 m_e^2 c^5/e^2)(n_c/n_e) \simeq 17 n_c/n_e$ GW (where n_e is the background plasma electron density and n_c is the critical density for propagation of the laser in the plasma). We might therefore expect that the self-injection threshold would occur at a fixed value of $\alpha P/P_c$ [25]. However, it is also known that the longitudinal nonlinear refractive index gradient also has a significant effect on the pulse properties [26,27] and we expect this to have an affect on the self-injection threshold.

The experiment was carried out using the multi-TW laser at the Lund Laser Centre. The laser delivered pulse energies of up to 0.7 J in pulses as short as 40 fs, corresponding to a peak power of 18 TW. An f/9 off-axis parabolic mirror was used to focus the pulse. A deformable mirror was used to optimize the focal spot, producing a spot size of 16 ± 1 μm FWHM. For a Gaussian focal spot the theoretical maximum fraction of energy within the FWHM is $\alpha = 1/2$, the best focus that we obtained had $\alpha = 0.48$. The focal plane was positioned onto the front edge of a supersonic helium gas jet with an approximately flat top profile of length 1.8 ± 0.1 mm.

To investigate the self-injection threshold, we studied the effect of the plasma density n_e, the total laser energy E, the focal spot quality α, and the pulse duration τ on the amount of charge in the electron beam. We chose to use the total charge in the electron beam as the diagnostic of self-injection as it provides a clear unambiguous signal of an electron beam.

The charge was measured using an electron beam profile monitor, consisting of a Lanex screen placed on the back surface of a wedge (which was used to collect the transmitted laser light). The wedge was 1 cm thick and made of glass and therefore prevented electrons below approximately 4 MeV reaching the Lanex. The Lanex screen was imaged onto a 12 bit CCD camera. To reduce the amount of background light from the interaction, a narrow band interference filter matched to the peak emission of the Lanex screen was placed in front of the camera. In addition, the camera was triggered several microseconds after the interaction but within the lifetime of the Lanex fluorescence. The Lanex screen was calibrated using the absolute efficiency data, absolute response of the CCD camera, and the details of the imaging system [28]. A beam profile monitor was used in preference to an electron spectrometer due to the fact that it has a higher sensitivity (i.e. the signal produced by a low charge beam dispersed inside a spectrometer will drop below the background level, whereas the same low charge beam will produce a bright image on the profile monitor). Also close to the threshold we do not expect the electrons to have particularly high energy (i.e. injection could be occurring but the electron beam energy could be outside the range of the electron spectrometer).

The gas jet could produce electron densities up to $n_e = 5 \times 10^{19}$ cm^{-3}. The laser pulse energy was varied by altering the energy pumping the final laser amplifier. We used the deformable mirror to reduce α by adding varying amounts of spherical aberration. Spherical aberration has the effect of decreasing α without introducing asymmetry to the focal spot and without significantly affecting its size. Degrading the focal spot symmetrically was desirable as asymmetric pulses can drive asymmetric wakes which can have a strong effect on the dynamics of self-injection [29]. The pulse duration was altered by changing the separation of the gratings in the compressor. Changing the grating separation introduced both a chirp to the pulse spectrum and a skew to the pulse envelope. To take this into account, we investigated both positive and negative chirps.

Figure 1 shows the effect of varying the laser pulse energy within the focal spot on the self-injection threshold. Keeping the total laser energy constant and degrading the focal spot (i.e. lowering α) moves the threshold to higher plasma densities. We also observe an increase in the threshold density when we keep α constant and reduce the laser pulse energy. In fact, we find that the two effects are equivalent, i.e., that the threshold shifts according to the product αE. This demonstrates that it is only the energy within the FWHM of the focal spot that contributes to driving the plasma wave. This emphasizes the importance

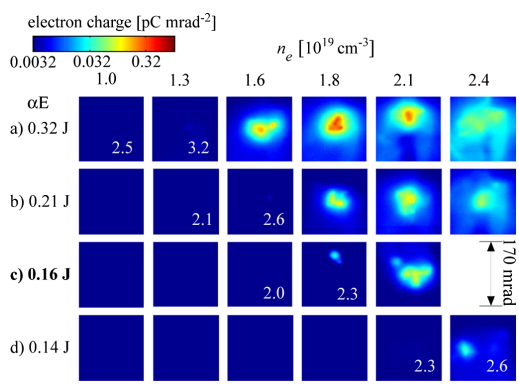

FIG. 1. Electron beam profiles for various plasma densities for different values of the amount of laser energy within the FWHM of the focal spot. (a), (b), and (d) kept the total laser energy constant but varied α whereas (c) reduced the laser energy. Each panel is an average of five shots and is displayed on a logarithmic color scale.

of laser focal spot quality in LWFA experiments [30], which are often performed with $\alpha \approx 0.3$ [2,25]. Improving the focal spot could therefore result in a significant increase in the electron beam energy achievable from a given laser system.

The observed variation of the threshold with αE is as expected for one based on $\alpha P/P_c$ but this can only be confirmed by the behavior of the threshold when we vary the laser pulse duration, keeping αE constant. When we do this we see markedly different behavior.

We kept the plasma density constant, at a value just above the threshold density for the optimally compressed pulse. At this density ($n_e = 1.6 \times 10^{19}$ cm^{-3}), with full laser energy ($\alpha E = 0.32$ J) and the fully compressed pulse ($\tau = 42$ fs) we observed a bright electron beam. When we reduced either the plasma density or the pulse energy by a small factor (20%–25%) this beam disappeared, i.e., we dropped below the threshold. Even after increasing the pulse duration by a factor of 2, electrons are clearly still injected, as shown in Fig. 2. This is true regardless of the chirp of the laser pulse, however we do see an enhancement of the total charge using positively chirped (red at the front) pulses as reported previously [31]. These pulses have a fast rising edge indicating that the precise shape of the pulse may play a role in the total charge injected. The direction of chirp of the pulse may also affect the rate at which pulse compression occurs [32]. For both directions of chirp the fact that the threshold behavior is so significantly different to that observed when varying αE suggests that pulse compression is indeed playing an important role in determining whether or not the accelerator reaches wave breaking.

In Fig. 3 we plot the total charge observed on the profile monitor screen for the various data sets. Figure 3(a) shows the total charge, plotted against the pulse power normalized to the critical power for self-focusing, for the data sets where we varied the plasma density and the energy within the focal spot (either by varying the spot quality α or total pulse energy E). The charge rises rapidly with increasing $\alpha P/P_c$ until eventually reaching a plateau at

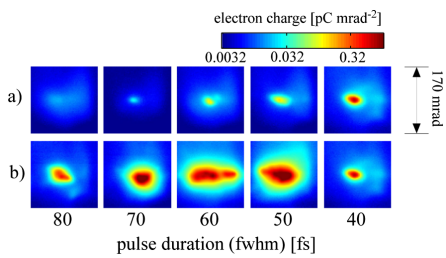

FIG. 2. Electron beam profiles for various pulse durations at fixed αE and at a plasma density just above the threshold density for injection for 40 fs pulses. The pulse duration was varied by changing the compressor grating separation which introduces a chirp to the pulse: (a) negative chirp; (b) positive chirp.

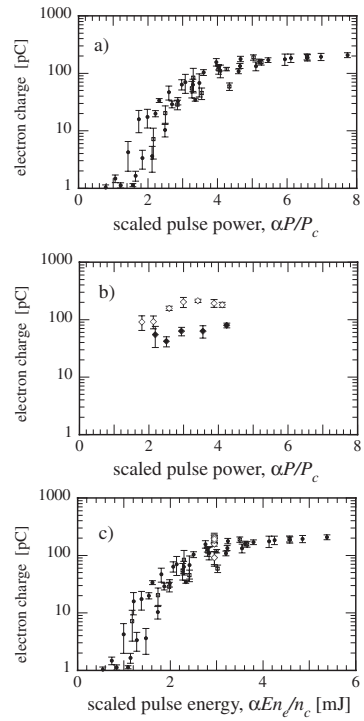

FIG. 3. (a) Electron charge (>4 MeV) versus $\alpha P/P_c$ keeping the pulse duration constant but varying focal spot quality and plasma density (closed circles) or total pulse energy and plasma density (open squares) but keeping pulse duration constant. (b) Electron charge versus $\alpha P/P_c$ varying pulse duration while keeping plasma density and energy in focal spot constant. (c) Data from (a) and (b) plotted versus $\alpha E n_e/n_c$. Each data point is an average of five shots and the error bars represent 1 standard deviation.

around $\alpha P/P_c \approx 4$. There is an increase in the total charge of a factor of 10 between $\alpha P/P_c = 2$ and $\alpha P/P_c = 4$ for both sets of data. The fact that both data sets lie on the same curve confirms the fact that it is the energy within the focal spot which determines the wakefield behavior. This supports the hypothesis that energy in the wings of the focal spot is not coupled into the accelerator: energy in the wings of the spot is effectively wasted.

Figure 3(b) shows the charge plotted against $\alpha P/P_c$ for a data set where we kept the plasma density and αE constant but varied the pulse duration (by introducing either positive or negative chirp). The markedly different behavior is once again apparent: rather than the rapid increase of charge between $\alpha P/P_c = 2$ and $\alpha P/P_c = 4$ the charge is approximately constant for each data set.

Figure 3(c) plots all of the data sets (varying α, E, and τ) against a scaled pulse energy $\alpha E n_e/n_c$ rather than the

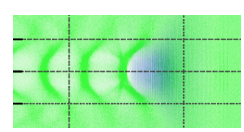

scaled pulse power. The fact that the pulse duration data set now fits closely with the αE data sets confirms that pulse compression is playing an important role in determining whether or not the wakefield accelerator reaches self-injection.

A recent paper that examined the trajectory of electrons inside the plasma bubble [21] predicts that self-trapping will occur when the radius of the plasma bubble (r_b) is larger than a certain value given by

$$k_p r_b > 2\sqrt{\ln(2\gamma_p^2) - 1}, \tag{1}$$

where $\gamma_p \approx \sqrt{n_c/(3n_e)}$ [33] is the Lorentz factor associated with the phase velocity of the bubble. When this condition is met, an electron starting at rest a distance r_b from the laser axis and following an elliptical trajectory in the bubble fields (thus defining the edge of the bubble) will be accelerated by the bubble fields up to $\gamma_p m_e c^2$ by the time it reaches the back of the bubble. A key feature of this model is that the normalized bubble size required for self-injection $k_p r_b$ is not constant with density. As Eq. (1) depends only on the plasma density and bubble size, we can determine the minimum pulse properties required to reach the threshold by noting that the radius of the bubble is related to the pulse energy and duration through [34]

$$k_p r_b = 2\sqrt{2}\left(\frac{\alpha E}{\tau P_c}\right)^{1/6}. \tag{2}$$

Combining Eqs. (1) and (2) yields an expression for the minimum pulse energy required to reach self-injection:

$$\alpha E > \frac{\pi \epsilon_0 m_e^2 c^5}{e^2}\left[\ln\left(\frac{2n_c}{3n_e}\right) - 1\right]^3 \frac{n_c}{n_e}\tau(l), \tag{3}$$

where $\tau(l)$ is the pulse duration after a propagation length l. A simple model for the rate of pulse compression was put forward in Ref. [27] based on the fact that the front of the pulse travels at the group velocity of the laser in the plasma and the back of the pulse travels in vacuum, this produces $\tau(l) \approx \tau_0 - (n_e l)/(2cn_c)$. The interaction length will be limited by either the length of the plasma target or the pump depletion length $l_{\mathrm{pd}} \simeq c\tau_0 n_c/n_e$ [34]. For the depletion limited case Eq. (3) reduces to

$$\frac{\alpha P}{P_c} > \frac{1}{16}\left[\ln\left(\frac{2n_c}{3n_e}\right) - 1\right]^3. \tag{4}$$

The threshold density for self-injection for a given experiment can be calculated from (3) and (4). This model requires knowledge of the initial pulse energy, pulse duration, and the length of the plasma to predict the threshold. As Eqs. (3) and (4) are transcendental, the density threshold for a given laser system must be found numerically.

A previous study showed that, at low density, the threshold is approximately $\alpha P/P_c > 3$ [25], this can be rearranged into a similar form to Eq. (3):

$$\alpha E > 3\frac{\pi \epsilon_0 m_e^2 c^5}{e^2}\frac{n_c}{n_e}\tau_0. \tag{5}$$

We can then use Eq. (5) to predict the density threshold for specific experimental conditions. To use this model only the initial pulse power is required to calculate the threshold density. Combining $\alpha P/P_c > 3$ and Eq. (2) reveals that this threshold model is also equivalent to stating that the minimum bubble size for self-trapping is constant with density ($k_p r_b > 3.4$) in contrast to Eq. (1).

In Fig. 4 we plot the variation of the observed threshold density with laser energy (αE). We have defined the experimentally observed threshold density as lying in the region between the highest density where we observe no electron beam and the lowest density where we clearly observe a beam. We also show the theoretical threshold density based on Eqs. (3) and (4), and the predicted threshold based on Eq. (5). Its agreement with the experimental data indicates that our model accurately predicts the self-injection threshold, confirming that the threshold is reached because the laser pulse undergoes intensity amplification due to a combination of pulse compression and self-focusing.

Our measurements of the threshold density for self-injection have been made with only moderate laser pulse energies ~1 J. Many laser wakefield experiments are now being performed with pulse energies ~10 J and the validity of this model at these higher laser energies can be verified by applying it to previously published data. We restrict ourselves to data obtained from experiments with gas jets as guiding structures can affect the trapping threshold by changing the way pulse evolution occurs [30] or by introducing additional effects such as ionization injection [35]. To calculate the density threshold for a particular set of experimental parameters, the following information is required: the laser energy E, the focal spot quality α, the initial pulse duration τ, and the maximum plasma length l. Equations (3) and (4) or Eq. (5) can then be used to calculate the expected density threshold for the two models. Kneip *et al.* [2], using a 10 J, 45 fs, 800 nm laser pulse

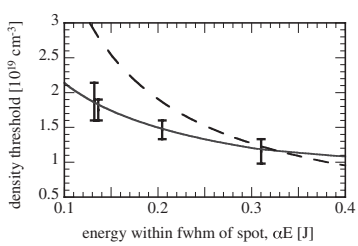

FIG. 4. Observed density threshold as a function of laser energy (αE) for our experiment. The solid curve represents our threshold model. The dashed curve represents a threshold based on $\alpha P/P_c > 3$.

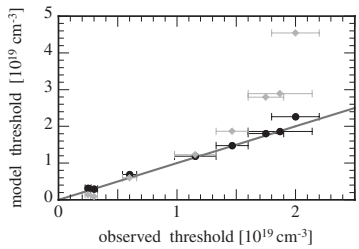

FIG. 5. Plot of reported density threshold, n_t, versus predicted density threshold, n_{model}, for this and other published experiments [2,11,25,36]. Circles show the predictions of our model, diamonds show the threshold based on $\alpha P/P_c > 3$. The line indicates $n_t = n_{\mathrm{model}}$.

with $\alpha = 0.3$, observed a threshold density of $n_e = 2$–3×10^{18} cm^{-3} in an 8.5 mm long plasma; our model predicts that the threshold density for self-injection should occur at $n_e \approx 3 \times 10^{18}$ cm^{-3}. Froula *et al.* [25], using a 60 fs, 800 nm laser with $\alpha E \approx 6$ J, observed a threshold density of $n_e \approx 3 \times 10^{18}$ cm^{-3} in an 8.0 mm plasma; our model also predicts $n_e \approx 3 \times 10^{18}$ cm^{-3}. Schmid *et al.* [36] using an 8 fs, 840 nm laser with $\alpha E \approx 15$ mJ, observed electron beams at a density of $n_e \approx 2 \times 10^{19}$ cm^{-3} in a plasma 300 μm long; our model predicts a threshold of $n_e \approx 2.2 \times 10^{19}$ cm^{-3}. Faure *et al.* [11], using a 33 fs, 820 mn laser, reported a dramatic decrease in the number of accelerated electrons at $n_e \approx 6 \times 10^{18}$ cm^{-3} in a 3 mm gas jet with $\alpha E \approx 0.5$ J. Our model predicts a threshold density of $n_e \approx 7 \times 10^{18}$ cm^{-3}.

These additional data points, together with those from this experiment, are presented in Fig. 5. Because of the fact that our model does not depend on a single experimental parameter, we plot the experimentally observed density threshold n_t for each experiment on the x axis and against the calculated threshold n_{model} obtained using either Eqs. (3) and (4) or Eq. (5). Figure 5 shows that our model is in good agreement with experiments over nearly 3 orders of magnitude in laser energy, whereas the threshold based on Eq. (5) matches the observed threshold over only a very limited range of pulse energies: it overestimates the threshold density for low energy laser systems and, on the other hand, would significantly underestimate the threshold for very high energy laser systems.

We note that simulations by Yi *et al.* [22] show that, at very low density and an initial laser spot size less than the matched spot size, diffraction of the laser pulse leads to a lengthening of the bubble which plays a role in determining self-injection. In that work they see self-injection with a 200 J, 150 fs laser pulse at a density of $n_e = 10^{17}$ cm^{-3}. Our model predicts that the threshold would be $n_e \approx 4 \times 10^{17}$ cm^{-3}—actually in reasonable agreement with [22], however our model relies on pulse compression occurring over ≈ 10 cm whereas Yi *et al.* show that in their simulations injection occurs after just 5 mm. This indicates that our model is only valid for initial laser spot sizes *greater than or equal to* the matched spot size (as is the case for the experiments shown in Fig. 5).

We now use our model to predict the self-injection threshold density for lasers currently under construction. For example, our model predicts that a 10 PW laser (300 J in 30 fs, $\lambda = 0.9$ μm, such as the Vulcan 10 PW laser at the Rutherford Appleton Lab, or the ELI Beamlines facility in the Czech Republic) could produce electron injection at as low as $n_e \approx 2 \times 10^{17}$ cm^{-3} (assuming $\alpha = 0.5$) in a 6 cm long plasma. For a 1 PW laser (40 J in 40 fs, $\lambda = 0.8$ μm, such as the Berkley Lab Laser Accelerator, BELLA), our model predicts that self-injection will occur at a density of $n_e \approx 9 \times 10^{17}$ cm^{-3} in 2.4 cm.

The lower the threshold density of a wakefield accelerator, the higher the maximum beam energy. However, for self-injecting accelerators there must be acceleration after injection, requiring operation at densities slightly above this threshold so that injection occurs earlier in the interaction.

In summary, we have measured the effect of various laser parameters on the self-injection threshold in laser wakefield accelerators. The simple model we use relies on the fact that pulse compression and self-focusing occur and that only the energy within the FWHM of the focal spot contributes towards driving the plasma wave. We find that in cases where the interaction is limited by pump depletion, the threshold can be expressed as a ratio of P/P_c, but this ratio is not the same for all laser systems: for higher power lasers the threshold occurs at a higher value of P/P_c than for lower power lasers. When the plasma length is shorter than the pump depletion length, we find that the length of the plasma is an important parameter in determining the injection threshold.

ACKNOWLEDGMENTS

This work was supported by the Royal Society, EPSRC (Grant No. EP/I014462/1); the Swedish Research Council (including the Linné grant to the LLC); the Knut and Alice Wallenberg Foundation; the EU Access to Research Infrastructures activity, FP7 Grant Agreement No 228334: Laserlab Europe, the Lund University X-ray Centre (LUXC); and the Marie Curie Early Stage Training Site MAXLAS (Contract No. MEST-CT-2005-020356).

[1] W. P. Leemans *et al.*, Nature Phys. **2**, 696 (2006).
[2] S. Kneip *et al.*, Phys. Rev. Lett. **103**, 035002 (2009).
[3] C. E. Clayton *et al.*, Phys. Rev. Lett. **105**, 105003 (2010).
[4] A. Rousse *et al.*, Phys. Rev. Lett. **93**, 135005 (2004).
[5] S. Kneip *et al.*, Nature Phys. **6**, 980 (2010).
[6] M. Fuchs *et al.*, Nature Phys. **5**, 826 (2009).
[7] A. Modena *et al.*, Nature (London) **377**, 606 (1995).

[8] A. Pukhov and J. Meyer-ter Vehn, Appl. Phys. B **74**, 355 (2002).
[9] S. P. D. Mangles *et al.*, Nature (London) **431**, 535 (2004).
[10] C. G. R. Geddes *et al.*, Nature (London) **431**, 538 (2004).
[11] J. Faure *et al.*, Nature (London) **431**, 541 (2004).
[12] V. Malka *et al.*, Phys. Plasmas **12**, 056702 (2005).
[13] S. P. D. Mangles *et al.*, Phys. Plasmas **14**, 056702 (2007).
[14] J. Faure *et al.*, Nature (London) **444**, 737 (2006).
[15] C. McGuffey *et al.*, Phys. Rev. Lett. **104**, 025004 (2010).
[16] A. Pak *et al.*, Phys. Rev. Lett. **104**, 025003 (2010).
[17] C. G. R. Geddes *et al.*, Phys. Rev. Lett. **100**, 215004 (2008).
[18] K. Schmid *et al.*, Phys. Rev. ST Accel. Beams **13**, 091301 (2010).
[19] S. Kalmykov *et al.*, Phys. Rev. Lett. **103**, 135004 (2009).
[20] I. Kostyukov *et al.*, Phys. Rev. Lett. **103**, 175003 (2009).
[21] A. G. R. Thomas, Phys. Plasmas **17**, 056708 (2010).
[22] S. A. Yi, V. Khudik, S. Kalmykov, and G. Shvets, Plasma Phys. Controlled Fusion **53**, 014012 (2011).
[23] A. G. R. Thomas *et al.*, Phys. Rev. Lett. **98**, 095004 (2007).
[24] J. E. Ralph *et al.*, Phys. Rev. Lett. **102**, 175003 (2009).
[25] D. H. Froula *et al.*, Phys. Rev. Lett. **103**, 215006 (2009).
[26] J. Faure *et al.*, Phys. Rev. Lett. **95**, 205003 (2005).
[27] J. Schreiber *et al.*, Phys. Rev. Lett. **105**, 235003 (2010).
[28] Y. Glinec *et al.*, Rev. Sci. Instrum. **77**, 103301 (2006).
[29] S. P. D. Mangles *et al.*, Appl. Phys. Lett. **95**, 181106 (2009).
[30] T. P. A. Ibbotson *et al.*, Phys. Rev. ST Accel. Beams **13**, 031301 (2010).
[31] W. P. Leemans *et al.*, Phys. Rev. Lett. **89**, 174802 (2002).
[32] E. S. Dodd and D. Umstadter, Phys. Plasmas **8**, 3531 (2001).
[33] C. D. Decker *et al.*, Phys. Plasmas **3**, 2047 (1996).
[34] W. Lu *et al.*, Phys. Rev. ST Accel. Beams **10**, 061301 (2007).
[35] T. P. Rowlands-Rees *et al.*, Phys. Rev. Lett. **100**, 105005 (2008).
[36] K. Schmid *et al.*, Phys. Rev. Lett. **102**, 124801 (2009).

Paper VIII

Active control of the pointing of a multi-terawatt laser

G. Genoud, F. Wojda, M. Burza, A. Persson and C.-G. Wahlström.
Review of Scientific Instruments **82**, 033102 (2011).

REVIEW OF SCIENTIFIC INSTRUMENTS **82**, 033102 (2011)

Active control of the pointing of a multi-terawatt laser

G. Genoud,[1] F. Wojda,[1,2] M. Burza,[1] A. Persson,[1] and C.-G. Wahlström[1,a)]
[1]*Department of Physics, Lund University, P.O. Box 118, S-22100 Lund, Sweden*
[2]*Laboratoire Physique Gaz et Plasmas (UMR 8578) – Université Paris-Sud 11, F-91405 Orsay Cedex, France*

(Received 30 July 2010; accepted 28 January 2011; published online 7 March 2011)

The beam pointing of a multi-terawatt laser wave laser is stabilized on a millisecond time scale using an active control system. Two piezo mirrors, two position sensing detectors, and a computer based optimization program ensure that both near- and far-field are stable, even during single shot operation. A standard deviation for the distribution of laser shots of 2.6 μ rad is achieved. © *2011 American Institute of Physics*. [doi:10.1063/1.3556438]

I. INTRODUCTION

In recent years, high power lasers have made tremendous progress and allowed scientists to access new and exciting fields of research. The advent of the chirped pulse amplification technique[1] allowed relativistic intensities to be reached even with compact laser systems. However, in order to fully utilize the potential of available high-power lasers, some quality issues still need to be addressed. In particular, the stability of laser parameters such as beam pointing, wavefront, and pulse energy are crucial in order for these lasers and their applications to benefit a broader community of scientific users. This paper addresses one of these issues, as the beam pointing of a multi-terawatt (TW) laser is actively stabilized.

The production of laser pulses of multi-TW peak power frequently causes the environment to become very noisy (electronically and mechanically). This makes the project particularly challenging in comparison with similar projects on more conventional lasers. In addition, experiments using multi-TW lasers usually require single-shot operation. Active beam pointing stabilization has been previously addressed for less powerful lasers, with high repetition rate, e.g., a 1 kHz Ti:sapphire femtosecond laser.[2] The principle used then is similar to ours, but it cannot operate in single-shot and only one piezo mirror was used, whereas in the work presented here single-shot operation is possible and two mirrors are used. More advanced schemes have also been demonstrated,[3,4] but are not suitable to the present situation. In Ref. 3, the pointing stability is controlled using neural networks and a feedforward algorithm. However, this cannot be used in single-shot operation. On the other hand, the method described in Ref. 4 can be used in a single-shot mode, but since it is based on image rotation and sum-frequency generation it is not suitable for high power lasers.

The driving force for the present work was to improve the feasibility of electron acceleration experiments, with laser driven plasma waves in dielectric capillary tubes.[5,6] Laser plasma wake fields can accelerate electrons to relativistic energies over a very short distance.[7] However, in order to increase the energy of the electrons to the GeV range and above, the interaction length must be increased. With the help of guiding structures, such as dielectric capillaries or plasma discharge channels, diffraction effects can be circumvented and plasma waves can be excited over several centimeters.[5,8] The requirement of good laser beam pointing is crucial to achieve good guiding in this kind of structure.[9] Good pointing stability is particularly important when using dielectric capillary tubes with inner diameter similar to the laser spot size to prevent damaging the capillary opening. In addition, the stability of the resulting electron beam depends on the pointing stability of the driving laser, among other parameters. Thus, in order to reach a good electron beam stability, the pointing of the driving laser beam must be controlled.

At the Lund Laser Centre, extensive work has been devoted to improve the pointing of its multi-TW laser. The first step was to improve it passively. The laser beam path was covered as much as possible to avoid air turbulences. Mechanical vibrations were also reduced. However, to further reduce remaining pointing instabilities, active control was necessary. This paper presents the active stabilization system developed at the Lund Laser Centre. The stabilization system was designed for single shot operation. Thus, corrections need to be made for both slow and fast effects that may have happened since the previous shot, which may be seconds, minutes, or even hours ago. The sources of pointing instabilities can be divided into three different types: (1) thermal drifts (on the time scale of minutes, hours), (2) air turbulence and slow mechanical vibrations (on the time scale of seconds, $>$10 ms), and (3) mechanical vibrations ($>$10 Hz). According to the Nyquist sampling theorem, in order to detect (and then correct) fluctuations with a given frequency, sampling has to be made at at least twice the frequency. The first type is, thus, very easily taken care of. Slow mirrors can be used to compensate for such drifts. The active stabilization system needs to be fast in order to correct for the two other types of fluctuations. The goal of our beam stabilization system is to take care of all of the first and the second type of instabilities and part of the third.

II. SETUP

The basic setup for the active stabilization system consists of two piezo mirrors and two position sensing detectors (PSDs). Each PSD records the offset of the laser beam from

a)Electronic mail: claes-goran.wahlstrom@fysik.lth.se.

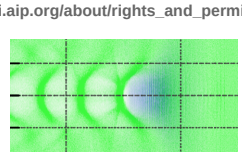

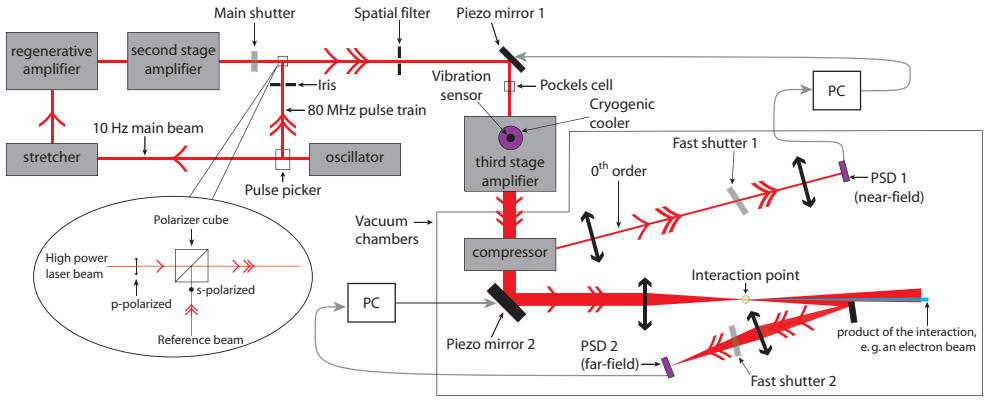

FIG. 1. (Color online) Schematic view of the beam pointing stabilization system of the Lund Laser Centre multi-TW laser (details in the text). The inset shows a side view of the injection point of the reference beam. The system works in the following way: two piezo mirrors are compensating for fluctuations in the beam pointing, one controls the near-field and other the far-field. Right before a main laser pulse arrives, the mirrors are fixed while fast shutters close to protect the detectors from the high power laser pulse. Once the laser pulse has passed the shutters open and the system starts regulating again.

the desired position and provides a voltage proportional to this offset. A fast computer and a custom made program is used to read the signals from the detector and to send appropriate voltages to the piezo mirror. For each mirror two signals are sent: one for corrections in the horizontal direction and one for the vertical direction. In order to get the beam axis right and not only the far-field position, one piezo mirror regulates the near-field while the other one takes care of the far-field.

A schematic view of the active control setup is given in Fig. 1. The high-intensity Ti:sapphire based chirped pulse amplification laser system at the Lund Laser Centre delivers up to 40 TW onto the target, with a FWHM pulse duration down to 35 fs and a beam diameter before focusing of 50 mm. The laser repetition rate is 10 Hz. Therefore, it is not possible to use the laser beam itself as a reference, if we want to correct for fluctuations faster than 5 Hz. Another reference beam is necessary that follows the same path as the TW beam. For this purpose we use part of the oscillator beam. This beam is at 80 MHz, which on the time scale we want to correct for, can be considered as continuous. A pulse picker takes ten pulses per second from this oscillator beam to be amplified, but all the remaining pulses can be used. This beam is injected into the laser system, after the second amplification stage, and follows the same path as the main laser beam. Both beams are going through a spatial filter, placed right after the injection point, and the reference beam is aligned on an iris used for the alignment of the main beam. This ensures that from this point both beams are colinear.

The reference beam is apertured by an iris before entering into the spatial filter, and the diameter of the focused beam is significantly larger than the hole of the spatial filter. Fluctuations in the pointing of the reference beam prior to the filter are, therefore, not transmitted. As the spatial filter is not diffraction limited for the main beam, fluctuations of the main beam occurring before the spatial filter are transmitted. The system compensates only for fluctuations experienced by the main beam after the spatial filter. Before the spatial filter, two slow piezo mirror systems using the 10 Hz beam itself as a reference are used to compensate for slow drifts and to keep the laser well aligned up to the spatial filter. The reference beam has a polarization perpendicular to the main beam polarization and the two beams can, therefore, be combined using a polarizing cube, where the main laser beam is transmitted and the reference beam is reflected (see inset in Fig. 1). Later in the laser chain, before the third and final amplification stage, a Pockels cell rotates the plane of polarization of the amplified pulse, while most of the time, between the laser shots, the reference beam is not affected. Thus, both beams have the same polarization further on.

The two-dimensional PSDs used in this setup are duolateral PSDs (from SiTek Electro Optics), which have four terminals, two on the back side and two on the front side, where the terminals on the back side are placed perpendicular to the terminals on the front side. The photoelectric current, generated by the incident light, flows through the device and the relationship between the currents on the four terminals gives the light spot position. Unlike quadrant sensors, which require overlap in all quadrants, this kind of PSD provides the position of any spot within the detector region, independent of beam shape, size, and power distribution. They have very good resolution and linearity. Their fast response (400 kHz bandwidth) gives them an advantage over CCD cameras.

Two different types of piezo mirrors are used in the setup, as the beam has different size at the position of the mirrors. The first mirror (a 1 inch optic) sits in a piezoelectric mount (KC1-PZ from Thorlabs). The second mirror is a 4 inches optic and is mounted into a Piezo Tip/Tilt-Platform (S-340 from Physik Instrumente). Each mirror mount must be firmly mounted, or the movements of the piezo may drive the mirror mount itself into resonance. This is especially

important for the second mirror due to its large size and weight. The limiting factor of the hardware is the resonance frequency of the large piezo mirror, which is about 500 Hz.

The detectors need to record both the near- and far-field positions of the reference beam without blocking the path for the main pulse as it arrives. The first detector, for the near-field, monitors the zeroth order reflection from the first grating of the the laser pulse compressor, placed under vacuum. The second detector monitors an image of the laser focal spot at the final interaction point. The first PSD controls a piezo mirror placed before the final stage of amplification. As this PSD monitors the near-field, a two lens system is used to project the transverse position of the full beam onto the PSD. The first lens (2 m focal length) focuses the beam in order to make the full beam small enough to fit on the PSD. The second lens (5 cm focal length) is used to image the position of the beam on the first lens onto the PSD. The second detector controls the large piezo mirror placed after the pulse compressor. PSD 2 is placed in the image plane of a lens collecting the light after the interaction point and, therefore, monitors the far-field. The lens is imaging the focal point onto the PSD with a magnification of two in order to increase the sensitivity. In many experiments using this kind of laser, the laser beam is focused into a gas jet. Part of the reference beam can then be collected after the focus point by a mirror and sent to the lens and the PSD. As the center part of the laser beam is not collected, the product of the interaction, e.g., an electron beam, can still pass through. For other types of experiments, other arrangement to image the focal spot of the reference beam might be needed. For the results presented below, the focusing optics had a focal length of 47.5 cm and the imaging lens a focal length of 20 cm. One should notice that the two piezo-controlled mirrors are far apart from each other in order to uncouple their actions.

In order for the active stabilization system to work efficiently, it must be optimized for speed. A properly adapted software must be use. We chose LABVIEW field-programmable gate array (FPGA) for its reliability, determinism, and parallelism. In addition, proportional-integral-derivative (PID) controllers were implemented in the code, which allows for faster corrections than simple proportional controllers.[10] The PID loop runs at a fast rate and corrections were sent to the mirrors at 4 and 2 kHz for the small and large piezo mirrors, respectively. These rates are higher than the resonance frequencies of the mirrors and, thus, the output signal is smoothened. In addition, in order to reduce the step-like behavior of the output signal, the program interpolates between the consecutive points of the output signal.

Filtering of the detector signal is also necessary to eliminate high frequency components above the resonance frequencies of the piezo mirrors. If fed to the piezo mirrors, these high frequency components drive the mirrors unstable, disturbing the stabilization. However, filter always introduces a time delay between the observed error and the correction. In order to operate the stabilization system at a fast rate, this delay must be minimized. This is done using low-pass finite impulse response digital filters. Such filters produce much shorter delays than conventional ones and have the advantage of producing the same delay for all frequencies.[11]

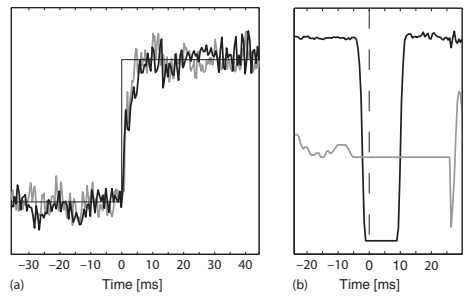

FIG. 2. (a) Typical step responses of the system. The gray and black curves are the signals recorded by the horizontal axis of the PSDs monitoring the far-field and near-field, respectively. In (b) the timing of the fast shutter used to protect the detectors is described. The black line shows the intensity recorded by the PSD and the gray line is the voltage sent to the piezo mirror. The dashed line corresponds to the time when the TW laser pulse arrives.

The time response of the system has been investigated by recording the error signal from the PSDs inside the loop. By frequency analysis of the open- and close-loop signals, it is found that frequency components up to 150 Hz for the near-field mirror and up to 100 Hz for the far-field mirror are successfully attenuated by the feedback loop. The response to set point changes was also investigated. A step of the order of the pointing fluctuations (corresponding to 6.8 μrad for the far-field and 900 μm for the near-field) was introduced in the set point value as shown in Fig. 2(a). We observe that it takes about 5 ms for the system to settle to the new set point values in both the far-field and the near-field. These are evidences that the system is able to act on a millisecond time scale.

In order to avoid the PSD to be destroyed by the high power laser shots, fast mechanical shutters (approximately millisecond response time, VS14 from Uniblitz) are protecting the PSDs when the main laser shots arrive. Each piezo mirror is regulating until just before the shutter closes and then holds the voltage, as described in Fig. 2(b). The delay between the laser shot and the end of regulation is very short, typically only a few ms, and the introduced error is, therefore, negligible. The timing between the shutter and the laser is shown in Fig. 2(b), where it is seen that the piezo mirrors are held at a fixed voltage 5 ms before the laser shot and the shutter starts closing 4 ms before the shot.

Some fluctuations are too dominant to be efficiently compensated for by the active control system. For example, the cryogenic cooler produces short but intense burst of high frequency vibrations that are difficult to handle because of their high frequency. We instead circumvent these vibration bursts. The cryogenic cooler is used to cool the crystal of the final stage of amplification. A pump circulates helium to the crystal at a rate of 1 Hz. During its operating cycle, when the piston reaches its stop, it makes the optical table vibrate. Given that the cycle consists of the piston going back and forth, there are two stops, giving a repetition frequency of 2 Hz for these bursts. After each shock, the optical table reacts and vibrates for some hundred milliseconds while damping the waves, as

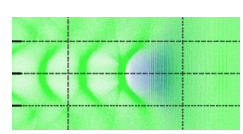

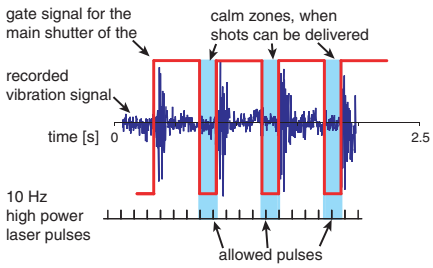

FIG. 3. (Color online) Filtering of the laser shots is necessary to avoid the short but intense burst of high frequency vibrations produced by the cryogenic cooler. The main shutter of the laser delivers shots only when the vibrations are minimal.

illustrated in Fig. 3. The vibrations are recorded and a gate signal is produced which allows the main shutter of the laser to deliver shots only when the vibrations are minimal. The calm period starts about 400 ms after the beginning of the shock and lasts 100 ms. This allows a laser shot to be delivered during this calm period. The dominant fluctuations are thus simply avoided. The control loop runs all the time but it is not able to regulate well during the shocks. However when the calm period starts, it has enough time to settle before the laser shot arrives. This mode of operation works well for single shot operation or repetition rate below 2 Hz. This is indeed the case for most types of ultrahigh intensity experiments. Modifications will be necessary if 10 Hz operation is required.

To summarize, the system works in the following way: two piezo mirrors are regulating and compensating for fluctuations in the beam pointing, one controls the near-field and one the far-field. When a high power laser shot is requested, the main shutter delivers a pulse during the calm time window of the cryogenic cooler. Right before the pulse comes, the voltages to the mirrors are fixed while fast shutters close to protect the detectors from the high power laser shot. Once the laser pulse has passed, the shutters open and the mirrors start regulating again.

III. EXPERIMENTAL RESULTS AND DISCUSSION

In order to assess the quality of the beam stabilization, signals recorded with the reference beam on the PSDs are not enough, actual laser shots must be recorded. To do so, a beam splitter was placed in the beam and the focal spot imaged by a 40 times microscope objective and recorded with a CCD camera. Two hundred consecutive laser shots in the high power configuration (the laser was attenuated, but everything else was running in the full power experimental conditions) were recorded with 3 s between each shot. The results are presented in Fig. 4. In the panels on the left, each point represents one laser shot. The origin (0,0) corresponds to the mean position of all the points. The positions recorded by the CCD camera are divided by the focal length of the laser focusing optics used and the scales are, therefore, shown in μrad, which is

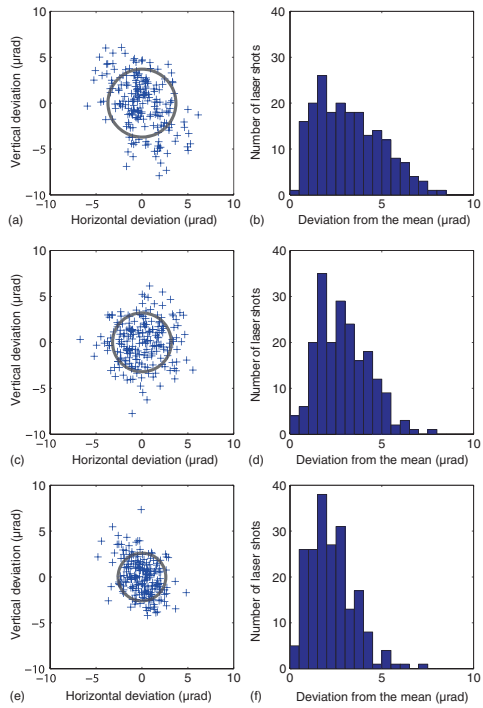

FIG. 4. (Color online) Pointing of 200 consecutive laser shots recorded by a microscope objective and a CCD camera. On the right side corresponding distributions of deviations from the mean. In (a) and (b) no active stabilization is used, in (c) and (d) the laser shots are gated in time in order to avoid firing when intense vibrations are produced by the cryogenic cooler in the laser amplifier. Finally, in (e) and (f), active stabilization is added with the help of two piezo mirrors. The circle represents the deviation corresponding to one standard deviation and its radius decreases for each step of the stabilization.

independent of the focusing optic used. In (a) no active stabilization is used. The beam pointing is, however, already fairly good thanks to all the work done on passive stabilization of the laser system. (c) Shows laser shots recorded with the gating system, delivering shots only in the calm section of the vibration cycle of the cryogenic cooler. (e) Presents shots with both gating and piezo mirror stabilization active. Each step of the stabilization shows an improvement in both the extremes and the mean of the distances between the laser shots.

On the right-hand side in Fig. 4, the distribution of the laser shots as function of their distance from the mean position is presented. This gives a better understanding of the effect of each step of the stabilization. We see that the gating of the shots already reduce the extreme points. The active stabilization further reduces it and no laser shots are more than 7.3 μrad away from the center. If we calculate the standard deviation of the distribution, we also observe a clear improvement: 3.7 μrad for (a), 3.2 μrad in (c), and 2.6 μrad in (e), which corresponds to an overall improvement of 30%. At the beginning of this project, i.e., before passive stabilization, the

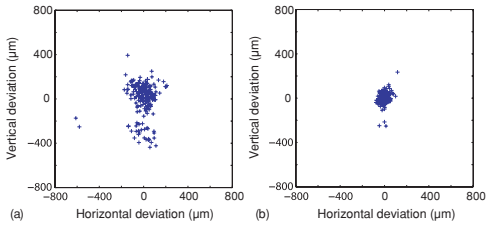

FIG. 5. (Color online) Near-field position of the reference beam for 200 consecutive shots recorded by a CCD camera imaging the position of the beam on the focusing optics. In (a) no active stabilization is used and in (b) the active stabilization is added.

mean was 6.7 μrad. It shows the importance of doing passively what can be done first. It is interesting to compare the obtained pointing fluctuations with the focal spot size. In the experiments reported in Refs. 5 and 6, using a $f = 1.5$ m focusing mirror, the focal spot size was 40 μm (radius of the first minimum of an Airy-like pattern). The mean of the resulting pointing fluctuations with this focusing optics would be 3.9 μm. The resulting pointing fluctuations, thus, correspond to only 10% of the focal spot size.

When only the second piezo mirror is regulating, the standard deviation is 2.8 μrad, which is similar to the value obtained with two piezo mirrors. This is expected as the CCD is monitoring the position of the beam in the focal plane, i.e., the far-field, and the second piezo mirror regulates only the far-field. In this case, the laser beam is hitting the right point in the focal plane but not necessarily along the correct axis. The use of two mirrors improves the overall pointing stability. This further shows that the use of two piezo mirrors in this configuration does not produce any interference effect.

The stability of the near-field was also investigated. To do so, a lens was placed after the focal spot to image the position of the beam on the parabolic mirror onto the CCD camera. To avoid problems with varying intensity profile, we assess the near-field stability of the reference beam instead of the main beam. Figure 5 shows the effect of the active stabilization on the position of the reference beam on the focusing optics, i.e., the near-field. In (a) there is no stabilization active, whereas in (b) the system is regulating. It is clearly observed that the near-field position of the beam is well stabilized and that the reference beam can be used to keep the main beam axis stable, as its intensity profile is very stable.

Depending on the requirements of the experiment, one might not need any active stabilization or one might want to use only one mirror. When only far-field stability is needed. For guiding experiments in capillaries, one mirror is enough in order not to damage the entrance of the capillary and it was used in this configuration in Refs. 5 and 6 with PSD 1 acting as a far-field detector. With two mirrors it should be possible to achieve even better guiding.[9] In gas jet experiments for electron acceleration, pointing stabilization is not crucial for the generation of the electron beams. However, in order to obtain an electron beam with good pointing stability, the laser pointing stability of both the near- and far-field is important. Experiments on solid target (for example, target normal sheath acceleration on flat foils) might not require very high pointing stability, however, for mass-limited targets one may need fast active stabilization with at least one mirror.

IV. CONCLUSION AND OUTLOOK

A system that actively stabilizes both the near-field and the far-field beams pointing of a multi-TW laser on the few millisecond time scale is introduced. The work presented above shows that a beam stabilization system can be implemented on an existing TW laser system without modifying its layout despite the high power laser pulses delivered and the resulting noisy environment due to the production of such pulses. Laser shots can be contained within a circle of 7.3 μrad radius with a standard deviation of 2.6 μrad. In addition, both the near- and far-field are stabilized. The results on monomode guiding in dielectric capillaries presented in Refs. 5 and 6 were possible thanks to this work. This opens prospects for further experiments, where the beam pointing is an important parameter.

Of course, this stabilization system can further be improved. Sources of high frequency vibrations should be isolated better from the laser system. The implementation of a feed-forward loop could predict the position of the beam in the gap between the shutter closing and the laser shot. When designing a new laser system, issues related to beam pointing can be taken into account from the start, making the implementation of such stabilization system much easier.

ACKNOWLEDGMENTS

The authors would like to acknowledge the fruitful discussions and collaboration within Lund University with L. Österman, B. Lundberg, B. Wittenmark, K. J. Åström, A. Cervin, and L. Sörnmo. The authors acknowledge the financial support from the Swedish Research Council and the Knut and Alice Wallenberg Foundation. This research was supported by the Marie Curie Early Stage Training Site MAXLAS (Contract No. MEST-CT-2005-020356) within the 6th European Community Framework Programme and the NEST Activity under the FP6 Structuring the European Research Area programme (project EuroLEAP, Contract No. 028514).

[1]D. Strickland and G. Mourou, Opt. Commun. **56**, 219 (1985).
[2]T. Kanai, A. Suda, S. Bohman, M. Kaku, S. Yamaguchi, and K. Midorikawa, Appl. Phys. Lett. **92**, 061106 (2008).
[3]F. Breitling, R. S. Weigel, M. C. Downer, and T. Tajima, Rev. Sci. Instrum. **172**, 1339 (2001).
[4]Y. Wu, D. French, and I. Jovanovic, Opt. Lett. **35**, 250 (2010).
[5]F. Wojda, K. Cassou, G. Genoud, M. Burza, Y. Glinec, O. Lundh, A. Persson, G. Vieux, E. Brunetti, R. Shanks, D. Jaroszynski, N. E. Andreev, C.-G. Wahlström, and B. Cros, Phys. Rev. E **80**, 066403 (2009).
[6]N. E. Andreev, K. Cassou, F. Wojda, G. Genoud, M. Burza, O. Lundh, A. Persson, B. Cros, V. E. Fortov, and C.-G. Wahlström, New J. Phys. **12**, 045024 (2010).
[7]S. P. D. Mangles, C. D. Murphy, Z. Najmudin, A. G. R. Thomas, J. L. Collier, A. E. Dangor, E. J. Divall, P. S. Foster, J. G. Gallacher, C. J. Hooker, D. A. Jaroszynski, A. J. Langley, W. B. Mori, P. A. Norreys, F. S. Tsung, R. Viskup, B. R. Walton, and K. Krushelnick, Nature (London) **431**, 535 (2004); C. G. R. Geddes, C. Toth, J. van Tilborg, E. Esarey, C. B. Schroeder, D. Bruhwiler, C. Nieter, J. Cary, and

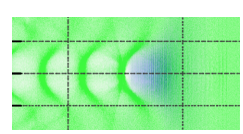

W. P. Leemans, Nature (London) **431**, 538 (2004); J. Faure, Y. Glinec, A. Pukhov, S. Kiselev, S. Gordienko, E. Lefebvre, J.-P. Rousseau, F. Burgy, and V. Malka, Nature (London) **431**, 541 (2004).
[8]W. P. Leemans, B. Nagler, A. J. Gonsalves, C. Tóth, K. Nakamura, C. G. R. Geddes, E. Esarey, C. B. Schroeder, and S. M. Hooker, Nat. Phys. **2**, 696 (2006).
[9]M. Veysman, N. E. Andreev, K. Cassou, Y. Ayoul, G. Maynard, and B. Cros, J. Opt. Soc. Am. B **27**, 1400 (2010).
[10]K. J. Åström and R. M. Murray, *Feedback Systems: An Introduction for Scientists and Engineers* (Princeton University Press, Princeton, NJ, 2008).
[11]S. K. Mitra and J. Kaiser, *Handbook for Digital Signal Processing* (Wiley, New York, 1993).

Paper IX

Laser-driven plasma waves in capillary tubes

F. Wojda, K. Cassou, G. Genoud, M. Burza, Y. Glinec, O. Lundh, A. Persson, G. Vieux, E. Brunetti, R. P. Shanks, D. Jaroszynski, N. E. Andreev, C.-G. Wahlström and B. Cros.

Physical Review E **80**, 066403 (2009).

PHYSICAL REVIEW E **80**, 066403 (2009)

Laser-driven plasma waves in capillary tubes

F. Wojda,[1] K. Cassou,[1] G. Genoud,[2] M. Burza,[2] Y. Glinec,[2] O. Lundh,[2] A. Persson,[2] G. Vieux,[3] E. Brunetti,[3] R. P. Shanks,[3] D. Jaroszynski,[3] N. E. Andreev,[4] C.-G. Wahlström,[2] and B. Cros[1,*]

[1]*Laboratoire Physique Gaz et Plasmas, CNRS–Université Paris-Sud 11, F-91405 Orsay Cedex, France*

[2]*Department of Physics, Lund University, P.O. Box 118, S-22100 Lund, Sweden*

[3]*Department of Physics, University of Strathclyde, Glasgow G4 0NG, United Kingdom*

[4]*Joint Institute for High Temperatures, Russian Academy of Sciences, Moscow 125412, Russia*

(Received 8 July 2009; revised manuscript received 3 November 2009; published 4 December 2009)

The excitation of plasma waves over a length of up to 8 cm is demonstrated using laser guiding of intense laser pulses through hydrogen-filled glass capillary tubes. The plasma waves are diagnosed by spectral analysis of the transmitted laser radiation. The dependence of the spectral redshift—measured as a function of filling pressure, capillary tube length, and incident laser energy—is in excellent agreement with simulation results. The longitudinal accelerating field inferred from the simulations is in the range of 1–10 GV/m.

DOI: 10.1103/PhysRevE.80.066403 PACS number(s): 52.38.Kd, 41.75.Jv, 52.35.Mw, 52.38.Hb

Electrons accelerated in laser wakefield accelerators (LWFAs) [1–3] acquire momentum from the electrostatic fields of a plasma density wave or wake, excited by an intense laser pulse passing through plasma. As they can achieve ultrarelativistic energies over very short distances, they have attracted great interest as novel routes to a new generation of ultracompact accelerators, which could be relevant to a wide range of applications, including high-energy physics and compact free-electron lasers. At high laser intensities large amplitude plasma waves with longitudinal electric fields, up to hundreds of GV/m, are excited, which are several orders of magnitude higher than those possible in conventional accelerators. When electrons are injected into the accelerating regions of such plasma waves, either from an external source [4] or by self-trapping of plasma electrons by nonlinear effects, they have been observed to reach energies up to hundreds of MeV over acceleration distances of only a few mm [5–8]. However, even with fields as high as 100 GV/m, the acceleration distance must be extended to tens of cm in order to reach electron energies of, say, tens of GeV. This is a range not yet realized experimentally.

There are two main requirements that must be fulfilled before a viable multi-GeV LWFA can be realized. First, the intense laser pulse driving the plasma wave must be guided over the full length of the accelerator. Second, the dephasing length, which is the distance over which the accelerating electrons outrun the accelerating region of the plasma wave, must be at least as long as the accelerating medium. To date, most experiments have been performed with a few mm long gas jets, where self-guiding due to relativistic self-focusing provides a simple guiding solution. However, the threshold power for self-focusing is, for a given laser wavelength, inversely proportional to the plasma density, thus requiring a minimum density for a given laser. As an example, for a laser with 10 TW peak power and 800 nm wavelength, this density is $n_e \approx 3\times 10^{18}$ cm^{-3}. An alternative approach is to guide the laser in a preformed plasma channel produced by an electric discharge in a gas-filled capillary tube. In this way guiding up to several centimeter long plasma waveguide has been demonstrated [9]. However, this approach is limited to plasma densities in excess of $n_e \sim 10^{18}$ cm^{-3}. Long dephasing lengths require very low plasma densities [3], which is clearly in conflict with the density requirements for relativistic self-guiding and guiding by discharge-formed plasma channels.

A method of guiding the intense laser pulse over long distance, while allowing very low plasma density, is thus required. This can be realized using capillary tubes as waveguides [10] where guiding is achieved by reflection from the walls. Laser guiding through gas-filled capillary tubes allows for a smooth transverse profile in monomode propagation [11] and a minimum attenuation of the laser pulse through refraction losses. As a first step in developing the waveguide as a medium for a wakefield accelerator, we have characterized the properties of the plasma wave in the moderately nonlinear regime over several centimeters. Working in the linear or moderately nonlinear regime allows control of the amplitude of the plasma waves while providing a focal spot of sufficient dimensions to effectively create quasi-one-dimensional longitudinal oscillations as shown by theoretical studies [12,13]. This regime enables a controlled and reproducible injection of an external electron bunch into the accelerating field, which provides a means of attaining high stability and reproducibility for future staging of several LWFA stages.

In this paper, we report on an observation of plasma waves excited by a guided high-intensity laser pulse inside hydrogen-filled capillary tubes with lengths up to 8 cm. The plasma wave excitation is diagnosed using a method based on spectral modifications of the laser pulse, due to local spatiotemporal variations of the density of the plasma [14].

An experiment was performed using the high-intensity Ti:sapphire laser system at the Lund Laser Centre which delivers up to 40 TW onto the target, with a full width at half maximum (FWHM) pulse duration down to $\tau_L = 35$ fs. The setup is shown schematically in Fig. 1. The 30-mm-diameter beam was focused with an $f = 1.5$ m spherical mirror at the entrance of a capillary tube. A deformable mirror was placed after the compressor (not shown) to correct the main aberrations of the phase front in the focal plane.

*brigitte.cros@u-psud.fr

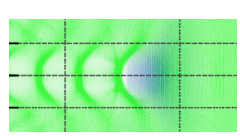

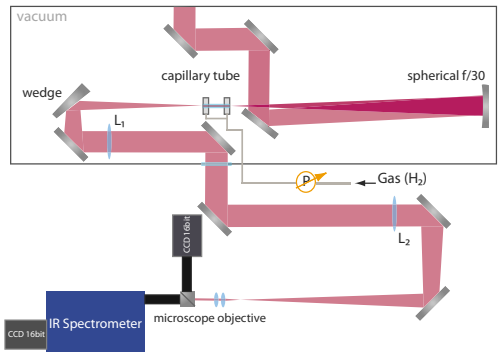

FIG. 1. (Color online) Schematic view of the experiment setup. Elements within the gray line box are under vacuum.

The laser beam transmitted through the capillary tube was attenuated by reflecting it on an optically flat glass wedge and then collimated by an achromatic $f_1=1$ m lens (L_1), which could be translated in vacuum along the beam axis to collect light either from the focal plane (i.e., with the capillary tube removed) or from the exit plane of the tube. The beam was then focused by a $f_2=1$ m achromatic lens (L_2) and magnified $10\times$ by a microscope objective. The beam was split in two parts. Focal spot or capillary tube output images were recorded by a 16-bit charge-coupled device (CCD). The transmitted part was sent to a visible to near-infrared imaging spectrometer equipped with a 16-bit CCD camera. The spectral resolution was 0.1 nm.

Glass capillary tubes with inner radius $r_c=50$ μm and length varying between 1.2 and 8.1 cm were used. Hydrogen gas flowed into the tubes through two thin (~ 100 μm) slits located between 2.5 and 5 mm from each end of the tube. The filling pressure was varied between 0 and 70 mbar. Each capillary tube could be used for at least 100 laser shots, when the laser beam remained well centered at the capillary entrance. Pointing variations due to thermal drifts and mechanical vibrations were therefore minimized or compensated for. Laser guiding at input intensities up to 10^{18} W/cm^2 was achieved with more than 90% energy transmission in evacuated or hydrogen-filled gas tubes up to 8 cm long.

For the data presented here, in order to investigate the moderately nonlinear regime, the input intensity was kept lower than 3×10^{17} W/cm^2. The laser pulse duration was $\tau_L=45\pm 5$ fs and the associated bandwidth was approximately 25 nm (FWHM); each pulse had a small negative linear chirp (-550 fs^2), i.e., short wavelengths preceded longer wavelengths, and the center wavelength was 786 nm. The energy distribution in the focal plane exhibited an Airy-like pattern with a radius at first minimum of $r_0=40\pm 5$ μm.

Spectra of the laser light transmitted through gas-filled capillary tubes exhibit blue and red broadening. In the range of parameters relevant to this experiment, spectral modifications of the wake-driving laser pulse—after propagating in the plasma over a large distance—are mainly related to changes in the index of refraction of the plasma during the creation of the plasma wave. The front of the laser pulse creates an increase in electron density, leading to a blueshift at the front of the pulse, while the rear of the pulse creates a decrease in electron density with larger amplitude, and thus a redshift of the spectrum. This effect has been proposed [14] to determine the amplitude of the electron plasma density perturbation in the linear or moderately nonlinear regime.

An averaged wavelength shift $\Delta\lambda(l)$ is calculated from the experimentally measured spectra $S(\lambda,l)$ at the exit of a capillary of length l and is defined as

$$\Delta\lambda(l)=\frac{\int_0^\infty \lambda S(\lambda,l)d\lambda}{\int_0^\infty S(\lambda,l)d\lambda}-\lambda_L, \tag{1}$$

where $\lambda_L=[\int_0^\infty S(\lambda,l=0)d\lambda]^{-1}\int_0^\infty \lambda S(\lambda,l=0)\simeq 2\pi c/\omega_L$ is the center wavelength of the incident laser pulse in vacuum and ω_L is the laser frequency. For an underdense plasma and laser intensity well above the ionization threshold, when the blueshift due to gas ionization inside the interaction volume V can be neglected and the wavelength shift given by Eq. (1) remains small compared to λ_L, this shift is directly related to the energy of the plasma wave electric field E_p excited in the plasma [14],

$$\frac{\Delta\lambda(l)}{\lambda_L}\simeq\frac{1}{16\pi\mathcal{E}_{out}}\int_V E_p^2 dV, \tag{2}$$

where $\mathcal{E}_{out}$ is the total energy of the transmitted pulse. For monomode propagation of a laser pulse with Gaussian time envelope, generating a wakefield in the weakly nonlinear regime, the wavelength shift can be expressed analytically. For small energy losses, it is proportional to the peak laser intensity on the capillary axis and to the length of the capillary and exhibits a resonantlike dependence on gas pressure described by the function $D(\Omega)$ as

$$\Delta\lambda(l)\simeq\left[0.178+1.378\frac{c^2}{(\omega_p r_c)^2}\right]\left(\frac{\omega_p}{\omega_L}\right)^3 a_L^2 D(\Omega)l, \tag{3}$$

where $a_L=eE_L/m_e\omega_L c$ is the normalized amplitude of laser electric field E_L, $D(\Omega)=\Omega\exp(-\Omega^2/4)$ with $\Omega=\omega_p\tau_L/\sqrt{2\ln 2}$, and $\omega_p=\sqrt{n_e e^2/\epsilon_0 m_e}$ is the electron plasma frequency.

The value of the wavelength shift $\Delta\lambda$ obtained from measured spectra is plotted as a series of black squares in Fig. 2 for a tube of length 7.1 cm as a function of filling pressure. Nonlinear laser pulse propagation in the gas-filled capillary tube including optical field ionization of gas, wakefield generation, and the self-consistent laser pulse spectrum modification was simulated numerically using the code described in [12]. The parameters used at the capillary entrance are $\tau_L=51$ fs, with a negative chirp, and an incident laser energy $\mathcal{E}_L=0.12$ J, with a radial profile corresponding to the one measured in the focal plane in vacuum, averaged over the angle. Simulation results are plotted as a red triangle curve in Fig. 2. For comparison, the analytical behavior given by Eq. (3) is plotted as a blue dashed curve, for the same $(\tau_L,\mathcal{E}_L)$. The simulated wavelength shifts fit closely the experimen-

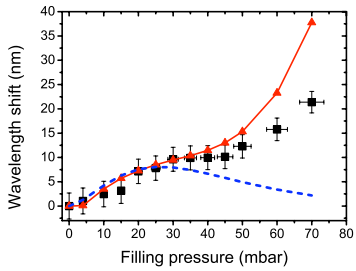

FIG. 2. (Color online) Wavelength shift as a function of hydrogen H_2 filling pressure at the exit of a 7.1-cm-long capillary tube obtained from experimental data (black squares); simulation results (red triangle curve) with $(\tau_L, \mathcal{E}_L)$=(51 fs, 0.12 J) and a negative chirp; analytical result from Eq. (3) for the same parameters (dashed blue line).

tally measured ones up to a filling pressure of 50 mbar. Analytical curve and measured and modeled wavelength shifts have the same behavior up to the linear resonant pressure of 25 mbar ($n_e \simeq 1.2 \times 10^{18}$ cm^{-3}). For pressures higher than 25 mbar, the experimental data and simulation exhibit a larger redshift than the analytical prediction. The analysis of the pulse evolution in the simulation shows that a steepening of the laser pulse front edge, due to propagation in the ionizing gas [15], occurs followed in time by pulse self-modulation [12]. A steepened pulse front is more efficient than a Gaussian time envelope to generate the wakefield at pressures larger than the resonant one. The values of the wavelength shift in the simulation are larger than the measured ones for pressures above 50 mbar. This behavior is related to the assumption of cylindrical symmetry used in the simulation, which leads to more pronounced nonlinear effects including laser pulse shortening [12,16].

Figure 3 shows examples of the spectra of the laser pulse measured (black lines) in the focal plane in vacuum [Fig. 3(a)] and at the output of the 7.1 cm capillary tube and the corresponding simulated spectra (dashed red lines) for filling pressures of 30 mbar [Fig. 3(b)] and 40 mbar [Fig. 3(c)]; two different shots are shown for each pressure.

All spectra are normalized to their maximum amplitude and integrated over the radial coordinate. The spectral modifications in the experiment and the simulations are in excellent agreement over a large range of amplitude. This agreement on the detailed structure of the spectra confirms the one, shown in Fig. 2, achieved on the wavelength shift, which is an integrated and averaged quantity.

The wavelength shift measured at the output of the capillary tubes as a function of the tube length is plotted in Fig. 4 for different filling pressures as well as the corresponding simulated results. A linear behavior of the wavelength shift as a function of length is observed at 20 mbar. The fit of experimental data by simulation results demonstrates that the plasma wave is excited over a length as long as 8 cm. As the pressure is increased, the nonlinear laser pulse evolution is amplified with the propagation length leading to a larger plasma wave amplitude.

The wavelength shift as a function of input laser energy is

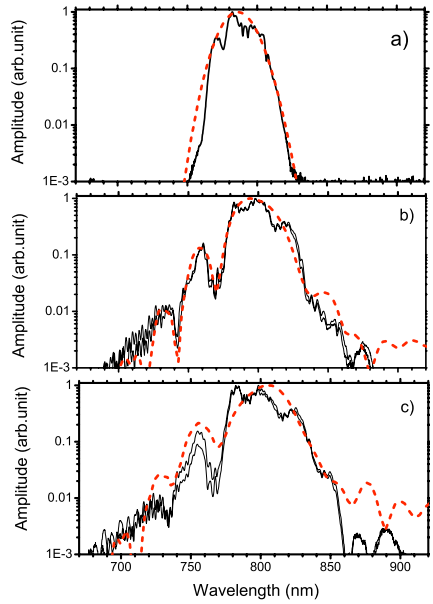

FIG. 3. (Color online) Spectra measured (black lines) (a) in the focal plane in vacuum and at the output of the 7.1 cm capillary tube for filling pressures of (b) 30 and (c) 40 mbar; two shots are shown for each pressure; corresponding simulated spectra (red dashed line).

shown in Fig. 5 at the exit of a 7.1-cm-long capillary tube for a filling pressure of 40 mbar, obtained from experimental data, simulation results, and analytical prediction. For $\mathcal{E}_L > 0.1$ J, the growth of the wavelength shift is faster than the linear one predicted analytically and the experimental and numerical results are in excellent agreement. For lower energy ($\simeq$0.05 J), gas ionization occurs closer to the maximum of the pulse and, combined with radial structure, leads to a more pronounced steepening of the front edge of the pulse and increased wakefield amplitude and wavelength

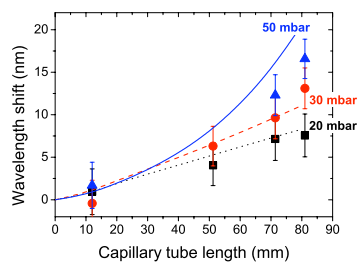

FIG. 4. (Color online) Wavelength shift measured at the output of the capillary tubes as a function of the tube length for filling pressures of 20 mbar (black square), 30 mbar (red dots), and 50 mbar (blue triangles) and the corresponding simulated shifts (dotted, dashed, and solid lines).

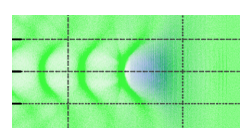

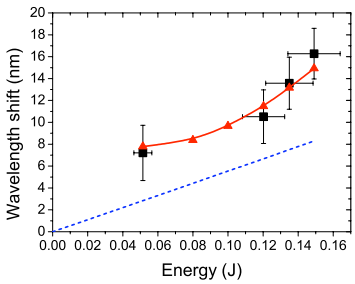

FIG. 5. (Color online) Wavelength shift as a function of input energy, at the exit of a 7.1-cm-long capillary tube for a filling pressure of 40 mbar obtained from experimental data (black squares), simulation results (red triangle curve), and analytical prediction (blue dashed curve).

shift compared to the analytical prediction [Eq. (3)].

In conclusion, we have generated and characterized a laser-driven plasma wave in the moderately nonlinear regime over a distance as long as 8 cm inside dielectric capillary tubes. An excellent agreement is found between the measured wavelength shift and the results from simulations as concerns pressure, length, and energy dependences. In the linear and weakly nonlinear regimes, this diagnostic provides a robust and reproducible measurement of the plasma wave amplitude over a long distance. The value of the longitudinal accelerating field in the plasma obtained from the simulation is in the range of 1–10 GV/m. The average product of gradient and length achieved in this experiment is on the order of 0.4 GV at a pressure of 50 mbar; it could be increased to several GV by extending the length and diameter of the capillary tube with higher laser energy.

We acknowledge the support of the European Community-New and Emerging Science and Technology Activity under the FP6 "Structuring the European Research Area" program (project EuroLEAP, Contract No. 028514) and Marie Curie Early Stage Training Site MAXLAS (Contract No. MEST-CT-2005-020356). This work was also supported by the Swedish Research Council, the Knut and Alice Wallenberg Foundation, the EU Access to Research Infrastructures activity (Contract No. RII3-CT-2003-506350, Laserlab Europe), the Russian Foundation for Basic Research (Project No. 07-02-92160), and the EPSRC U.K.

[1] T. Tajima and J. M. Dawson, Phys. Rev. Lett. **43**, 267 (1979).
[2] P. Sprangle *et al.*, Appl. Phys. Lett. **53**, 2146 (1988).
[3] E. Esarey *et al.*, IEEE Trans. Plasma Sci. **24**, 252 (1996).
[4] F. Amiranoff *et al.*, Phys. Rev. Lett. **81**, 995 (1998).
[5] S. Mangles *et al.*, Nature (London) **431**, 535 (2004).
[6] C. Geddes *et al.*, Nature (London) **431**, 538 (2004).
[7] J. Faure *et al.*, Nature (London) **431**, 541 (2004).
[8] W. Leemans *et al.*, Nat. Phys. **2**, 696 (2006).
[9] D. J. Spence and S. M. Hooker, Phys. Rev. E **63**, 015401(R) (2000).
[10] F. Dorchies *et al.*, Phys. Rev. Lett. **82**, 4655 (1999).
[11] B. Cros, C. Courtois, G. Matthieussent, A. Di Bernardo, D. Batani, N. Andreev, and S. Kuznetsov, Phys. Rev. E **65**, 026405 (2002).
[12] N. E. Andreev, Y. Nishida, and N. Yugami, Phys. Rev. E **65**, 056407 (2002).
[13] N. E. Andreev *et al.*, Phys. Plasmas **9**, 3999 (2002).
[14] N. E. Andreev and M. Chegotov, JETP **101**, 56 (2005).
[15] N. E. Andreev *et al.*, JETP **96**, 885 (2003).
[16] S. A. Skobelev *et al.*, JETP Lett. **89**, 540 (2009).

Paper X

Analysis of laser wakefield dynamics in capillary tubes

N. E. Andreev, K. Cassou, F. Wojda, G. Genoud, M. Burza, O. Lundh, A. Persson, B. Cros, V. E. Fortov and C.-G. Wahlström.

New Journal of Physics **12**, 045024 (2010).

New Journal of Physics
The open-access journal for physics

Analysis of laser wakefield dynamics in capillary tubes

N E Andreev[1,2,5], K Cassou[3], F Wojda[3], G Genoud[4], M Burza[4], O Lundh[4], A Persson[4], B Cros[3], V E Fortov[1,2] and C-G Wahlstrom[4]

[1] Joint Institute for High Temperatures of RAS, Russian Academy of Sciences, Moscow 125412, Russia
[2] Moscow Institute of Physics and Technology (State University), Moscow 113303, Russia
[3] Laboratoire de Physique des Gaz et des Plasmas, CNRS – Université Paris-Sud 11, F-91405 Orsay Cedex, France
[4] Department of Physics, Lund University, PO Box 118, S-22100 Lund, Sweden
E-mail: andreev@ras.ru

New Journal of Physics **12** (2010) 045024 (17pp)
Received 28 November 2009
Published 30 April 2010
Online at http://www.njp.org/
doi:10.1088/1367-2630/12/4/045024

Abstract. A general approach to the modifications of the spectrum of a laser pulse interacting with matter is elaborated and used for spectral diagnostics of laser wakefield generation in guiding structures. Analytical predictions of the laser frequency red shift due to the wakefield excited in a capillary waveguide are confirmed by self-consistent modeling results. The role of ionization blue shift, and nonlinear laser pulse and wakefield dynamics on the spectrum modification, is analyzed for recent experiments on plasma wave excitation by an intense laser pulse guided in hydrogen-filled glass capillary tubes up to 8 cm long. The dependence of the spectral frequency shift, measured as a function of filling pressure, capillary tube length and incident laser energy, is in excellent agreement with the simulation results, and the associated longitudinal accelerating field is in the range 1–10 GV m^{-1}.

[5] Author to whom any correspondence should be addressed.

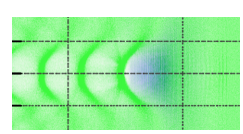

Contents

1. Introduction

The interaction of short, intense laser pulses with plasmas produces large amplitude wakes. The high-field amplitude associated with these wake waves can be used to accelerate particles to high energies over very short lengths compared with the conventional accelerator technology [1]–[3]. In linear or moderately nonlinear regimes, these fields are of the order of 1–10 GV m^{-1}, and relativistic electrons injected into the wave can acquire an energy of the order of 1 GeV over a length of the order of a few centimeters. The control of the characteristics of the electron beam as it is accelerated is crucial for achieving a usable laser–plasma accelerator unit. It is linked to the control of the accelerating electric field structure over several centimeters in a plasma. Diagnostics providing a detailed knowledge of the field structure and time evolution are therefore important for the progress of accelerator development.

Several diagnostics methods have been used to measure plasma waves created by the laser wakefield, in particular multi-shot or single-shot frequency domain interferometry [4, 5]. They rely on the interference in the frequency domain of two separate probe pulses and have been used to measure density perturbations over lengths of the order of a few millimeters. The dispersion effects on the probe pulse and the variations of the phase velocity of the exited plasma wave make these diagnostic techniques difficult to use over longer propagation distances [6]. Modifications of the spectrum of a single probe pulse propagating in a time- and space-varying plasma density [7] can be used to diagnose the laser wakefields [6, 8] without restrictions to the wake wave amplitude and dispersion effects.

The amplitude of the plasma wave excited by the laser pulse over a large length can be obtained in a single shot by the analysis of the modifications of the spectrum of the driving pulse. This method, proposed in [9, 10] and compared with the experimental measurements for a supersonic helium gas jet target of sub-millimeter length in [11], relies on the modifications of the spectrum induced by the time-varying plasma density within the pulse duration. Recently, it has been used successfully to measure the plasma wave excited in the wake of an intense laser guided in a gas-filled capillary tube over 8 cm [12].

In this paper, analytical expressions for the frequency shift due to the laser wakefield excited in a capillary tube are derived and compared with self-consistent modeling including gas ionization, nonlinear laser pulse and wakefield dynamics. A detailed comparison with experimental data shows that excellent agreement is obtained in a broad range of plasma densities, which allows us to determine the value of the accelerating field amplitude.

2. Analytical theory (general approach)

The general frequency momentum theory [13] describes the relation between the frequencies, ω, averaged over the spectrum of incident and output radiation of intensity $I_\alpha(\omega, R)$ from the interaction volume V:

$$\langle\omega^2\rangle_\alpha = \oint_S \int_0^{+\infty} \omega^2 I_\alpha(\omega, \mathbf{R}) \mathrm{d}\omega\, \mathbf{n}\mathrm{d}\mathbf{s} \left[\oint_S \int_0^{+\infty} I_\alpha(\omega, \mathbf{R}) \mathrm{d}\omega\, \mathbf{n}\mathrm{d}\mathbf{s}\right]^{-1}, \quad \alpha = \text{in, out}, \tag{1}$$

where d$\mathbf{s}$ is the vector element normal to the surface S and $\mathbf{n}$ is the unit Poynting vector at a given point on the surface S. It can be shown without any restrictions on the radiation intensity and geometry that the frequency shift of the output radiation $\langle\omega^2\rangle_{\text{out}}$ relative to the incident one, $\langle\omega^2\rangle_{\text{in}} = \omega_0^2$, has the form [9, 13]

$$\langle\omega^2\rangle_{\text{out}} - \omega_0^2 = \frac{1}{\varepsilon_{\text{out}}} \left\{ \int_V \mathrm{d}^3\mathbf{r} \int_{-\infty}^{+\infty} \mathrm{d}t \left[\omega_0^2 \mathbf{E}\,\mathbf{j} - \frac{\partial \mathbf{E}}{\partial t}\frac{\partial \mathbf{j}}{\partial t}\right] + \frac{1}{8\pi}\int_V \mathrm{d}^3\mathbf{r} \right.$$
$$\left. \times \left[\omega_0^2 \left(\mathbf{E}^2 + \mathbf{B}^2\right) - \left(\left(\frac{\partial \mathbf{E}}{\partial t}\right)^2 + \left(\frac{\partial \mathbf{B}}{\partial t}\right)^2\right)\right]\Bigg|_{t=-\infty}^{t=+\infty} \right\}, \tag{2}$$

where $f|_{t=-\infty}^{t=+\infty} \equiv f(t=+\infty) - f(t=-\infty)$, $\mathbf{E}$ ($\mathbf{B}$) and $\mathbf{j}$ are the electric (magnetic) field and the current in the medium of volume V, respectively, ε_{in} is the energy of incident radiation and ε_{out} is the energy of radiation coming out of the volume V. The zero-frequency moment of Maxwell equations gives the energy conservation law for ε_{in} and ε_{out}:

$$\varepsilon_{\text{out}} = \varepsilon_{\text{in}} - \int_V \mathrm{d}^3\mathbf{r} \int_{-\infty}^{+\infty} \mathrm{d}t\, \mathbf{E}\,\mathbf{j} - \frac{1}{8\pi}\int_V \mathrm{d}^3\mathbf{r}\, (\mathbf{E}^2 + \mathbf{B}^2)\Big|_{t=-\infty}^{t=+\infty}. \tag{3}$$

The first integral term in (2) describes in particular a blue frequency shift due to optical field ionization (OFI), while the last summands in (2) and (3) account for the plasma wave existing after the laser pulse. When the peak pulse intensity is much higher than the one corresponding to the optical ionization threshold, ionization and wakefield generation are separated in space and time. In this case, it can be shown that the total frequency shift due to both processes is the sum of the shift $\delta\omega_{\text{ion}}$ due to ionization and the shift $\delta\omega_{\text{wf}}$ associated with wakefield generation:

$$\frac{\delta\omega}{\omega_0} \equiv \frac{\langle\omega^2\rangle_{\text{out}} - \omega_0^2}{2\omega_0^2} \cong \frac{\delta\omega_{\text{ion}}}{\omega_0} + \frac{\delta\omega_{\text{wf}}}{\omega_0}, \tag{4}$$

where, in accordance with (2), the shift due to plasma wake generation is determined from the energy of the wake electric field, E_{p}, excited in the plasma [10]:

$$\frac{\delta\omega_{\text{wf}}}{\omega_0} \cong -\frac{1}{\varepsilon_{\text{out}}}\frac{1}{16\pi}\int_V \mathbf{E}_{\text{p}}^2\, \mathrm{d}V. \tag{5}$$

Assuming that the pulse intensity distribution is cylindrically symmetric with a characteristic radius larger than the plasma skin depth $k_{\text{p}}^{-1} = c/\omega_{\text{p}}$ (where c is the speed of light and $\omega_{\text{p}} = \sqrt{4\pi e^2 n_0/m}$ is the electron plasma frequency, where e, m and n_0 are the electron charge,

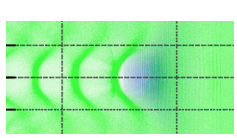

mass and background plasma density), the plasma wakefields can be found with the help of the equation for the wakefield potential, Φ, [14]

$$\left\{\left(\Delta_\perp - k_\mathrm{p}^2\right)\frac{\partial^2}{\partial\xi^2} - \frac{\partial \ln n_0}{\partial r}\frac{\partial^3}{\partial r\,\partial\xi^2} + k_\mathrm{p}^2\Delta_\perp\right\}\Phi - \frac{k_\mathrm{p}^4}{2}\left[1 - \frac{1+|\boldsymbol{a}|^2/2}{(\Phi+\delta\Phi_\mathrm{S})^2}\right] = \frac{k_\mathrm{p}^2}{4}\Delta_\perp|\boldsymbol{a}|^2, \tag{6}$$

where $\Delta_\perp = (1/r)\partial/\partial r(r\partial/\partial r)$ is the transverse part of the Laplace operator, $\xi = z - ct$, $\boldsymbol{a}(\xi, z, r) = e\mathbf{E}_\mathrm{L}/(mc\omega_0)$ is the normalized complex envelope of the laser field, related to the high-frequency laser field by

$$\tilde{\mathbf{E}}_\mathrm{L}(\mathbf{r}, t) = \mathrm{Re}\left\{\mathbf{E}_\mathrm{L}(\xi, z, r)\exp\left(\mathrm{i}k_0\xi\right)\right\}, \tag{7}$$

where $k_0 = \omega_0/c = 2\pi/\lambda_0$ is the vacuum laser wave vector and $\delta\,\Phi_\mathrm{S}$ describes the effect of OFI on wakefield generation [14]. In the weakly relativistic approximation ($|\boldsymbol{a}| \ll 1$, $|\delta\Phi| \equiv |\Phi - 1| \ll 1$), assuming that the contribution due to ionization is negligible, and for the background plasma density n_0 uniform in space (or weakly inhomogeneous over lengths of the order of k_p^{-1}), the equation for the potential derived from (6) is

$$\left(\frac{\partial^2}{\partial\xi^2} + k_\mathrm{p}^2\right)\delta\Phi = \frac{1}{4}|\boldsymbol{a}|^2. \tag{8}$$

With the help of $\partial\Phi/\partial\xi = eE_{\mathrm{p},z}/m_\mathrm{e}c^2$ and $\partial\Phi/\partial r \cong eE_{\mathrm{p},r}/m_\mathrm{e}c^2$, equation (8) yields the wakefield amplitude $\mathbf{E}_\mathrm{p}$ [10]:

$$\mathbf{E}_{\mathrm{p,max}}^2 = \frac{m^2c^2}{e^2}\frac{\omega_\mathrm{p}^2}{16}\left\{k_\mathrm{p}^2\left|\int_{-\infty}^{\infty}\mathrm{d}\xi\,\mathrm{e}^{-\mathrm{i}k_\mathrm{p}\xi}|\boldsymbol{a}|^2\right|^2 + \left|\frac{\partial}{\partial r}\int_{-\infty}^{\infty}\mathrm{d}\xi\,\mathrm{e}^{-\mathrm{i}k_\mathrm{p}\xi}|\boldsymbol{a}|^2\right|^2\right\}. \tag{9}$$

An expression similar to (9) was obtained for the electron density perturbations in [15] (see also [2]).

In order to obtain an analytical expression for the frequency shift of (5), a simplified expression for the laser pulse envelope is used in (9), where the reciprocal effect of the wakefield plasma wave on pulse propagation is neglected. Let us consider a Gaussian laser pulse focused at the capillary entrance, $z = 0$, as

$$\boldsymbol{a}(\xi, r, z = 0) = \boldsymbol{a}_0\exp\left[-\frac{r^2}{r_0^2} - \frac{(\xi-\xi_0)^2}{c^2\tau^2}\right], \tag{10}$$

where $a_0 \cong 0.86\times10^{-9}(I_0[\mathrm{W\,cm^{-2}}])^{1/2}\,\lambda_0[\mu\mathrm{m}]$ is the normalized laser pulse amplitude (I_0 is the laser peak intensity). When the focal spot size of the laser pulse r_0 is matched to the inner radius of the capillary tube, R_cap, i.e. when $r_0 \cong 0.65R_\mathrm{cap}$, about 98% of the incident energy is transferred to the fundamental capillary mode, which can be described as [8, 14, 16,]

$$|\boldsymbol{a}(\xi, z, r)|^2 = |a_0|^2\exp\left(-2\delta\,k_{z1}''z - 2\frac{(\xi-\xi_0)^2}{c^2\tau^2}\right)J_0^2\left(b_1\frac{r}{R_\mathrm{cap}}\right), \tag{11}$$

where $b_1 \cong 2.405$ is the first root of $J_0(\mathrm{x}) = 0$, J_0 is the Bessel function of integer order 0 and $\delta k_{z1}''$ is the damping coefficient associated to the loss of energy by refraction through the capillary wall with dielectric constant ε_w:

$$\delta\,k_{z1}'' = \frac{b_1^2}{2k_0^2R_\mathrm{cap}^3}\frac{1+\varepsilon_\mathrm{w}}{\sqrt{\varepsilon_\mathrm{w}-1}}.$$

Using (11) and (9) in (5), the frequency shift as a function of the laser pulse propagation distance z can be written as

$$\frac{\delta\omega_{\rm wf}(z)}{\omega_0} = -\frac{1}{64}\sqrt{\frac{\pi}{2}}\left(C_1 + \frac{C_2}{k_{\rm p}^2 R_{\rm cap}^2}\right)\left(\frac{\omega_{\rm p}}{\omega_0}\right)^2 |a_0|^2 D(\Omega)\,\frac{k_{\rm p}}{\delta\, k''_{z1}}\left[1 - \exp\left(-4\delta\, k''_{z1} z\right)\right], \tag{12}$$

where the constants C_1 and C_2 are determined by the radial laser intensity distribution for the fundamental mode

$$C_1 \equiv \int_0^{b_1} x J_0^4(x)\,{\rm d}x \left(\int_0^{b_1} x J_0^2(x)\,{\rm d}x\right)^{-1} \cong 0.5655,$$

$$C_2 \equiv 4b_1^2 \int_0^{b_1} x J_0^2(x)\, J_1^2(x)\,{\rm d}x \left(\int_0^{b_1} x J_0^2(x)\,{\rm d}x\right)^{-1} \cong 4.361,$$

and the function $D(\Omega) = \Omega\exp(-\Omega^2/4)$, with $\Omega = \omega_{\rm p}\tau$, reflects the resonant behavior of wakefield generation, depending on the laser pulse duration with Gaussian time envelope in (11). Note that for a small energy loss by refraction through the capillary wall, when $\delta k''_{z1} z \ll 1$, the frequency shift (12) grows linearly with the capillary length z.

In the following sections, the analytical prediction for the frequency shift due to wakefield generation of (12) will be compared with the results of fully self-consistent modeling, including gas ionization and nonlinear multi-mode laser pulse propagation in a capillary tube.

3. Modeling results and comparison with analytical predictions

To describe nonlinear laser pulse propagation in a gas-filled capillary, the following wave equation for the pulse envelope was used [14]

$$\left\{2ik_0\frac{\partial}{\partial z} + 2\frac{\partial^2}{\partial z\partial\xi} + \Delta_\perp\right\} a = k_0^2\left(\frac{n}{n_{\rm c}\gamma}a - iG^{(\rm ion)}\right), \tag{13}$$

where n is the slowly varying electron density, $n_{\rm c} = m\omega_0^2/(4\pi e^2)$ is the critical density for the laser frequency ω_0, $\gamma = [1 + (\mathbf{p}/mc^2 + |a|^2/2]^{1/2}$ is the relativistic factor of plasma electrons with momentum $\mathbf{p}$ slowly varying in time and the last term on the right-hand side of (13) is the normalized ionization current, which represents the laser energy losses in the process of OFI [17]. In the quasi-static approximation [18], the relativistic plasma response n/γ can be expressed through a single scalar function, the potential Φ determined by (6) [14]:

$$\frac{n}{\gamma} = n_0\frac{1 + k_{\rm p}^{-2}\Delta_\perp\Phi}{\Phi + \delta\,\Phi_{\rm S}}. \tag{14}$$

When the laser pulse propagates in ionizing gas, equations (13), (14) and (6) should be supplemented with the equations for ionization kinetics, which determine the electron density $n_0(\mathbf{r}, \xi)$ produced by OFI [14, 17, 19]

$$\frac{\partial n_0}{\partial\xi} = -\frac{1}{c}\sum_{k=0}^{Z_n-1}\bar{W}_k N_k, \tag{15}$$

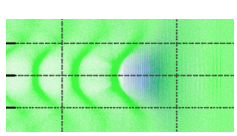

where N_k and $\bar{W}_k$ are the averages over the laser period of the ion densities and probabilities of tunneling ionization of ions [20] with charge state k, $k = 0, 1, \ldots, Z_n$ and Z_n is the atomic charge number.

For the numerical modeling of laser pulse propagation and wakefield generation inside a gas-filled capillary tube by (6) and (13), boundary conditions have to be supplied. For linearly polarized laser pulses, the following boundary condition at the capillary tube wall, $r = R_{\rm cap}$, is used:

$$\frac{\partial a}{\partial r} = 2ik_0 \frac{(\varepsilon_{\rm w} - 1)^{1/2}}{\varepsilon_{\rm w} + 1} \left(1 - \frac{\mathrm{i}}{k_0} \frac{\partial}{\partial \xi}\right) a, \tag{16}$$

which describes correctly the structure of eigenmodes and their damping due to the energy loss through the capillary walls (see [14, 16]). The boundary conditions for the wakefield potential are $\Phi = 1$ in the unperturbed gas in front of the laser pulse, $\xi \to +\infty$, and at the capillary wall $r = R_{\rm cap}$.

Taking into account (7), the mean-square frequency, defined by (1), at a distance z in the capillary is expressed using the laser envelope as follows:

$$\langle \omega^2 \rangle (z) \equiv \left(\int_{-\infty}^{\infty} \int_0^{R_{\rm cap}} |\boldsymbol{a}(\omega, r, z)|^2 \, r \, \mathrm{d}r \, \mathrm{d}\omega \right)^{-1} \int_{-\infty}^{\infty} (\omega + \omega_0)^2 \int_0^{R_{\rm cap}} |\boldsymbol{a}(\omega, r, z)|^2 \, r \, \mathrm{d}r \, \mathrm{d}\omega, \tag{17}$$

where $\boldsymbol{a}(\omega, r, z)$ is the dimensionless laser pulse envelope in Fourier space. The corresponding frequency shift is defined as

$$\delta\omega(z) = \frac{\langle \omega^2 \rangle (z) - \omega_0^2}{2\omega_0}. \tag{18}$$

The solution to the system of equations (13)–(16) and (6) permits us to also obtain the normalized spectrum of the propagating laser field, centered at the carrier frequency ω_0, integrated over the transverse cross section:

$$I(\omega + \omega_0, z) \equiv \left(\max_{\omega} \int_0^{R_{\rm cap}} |\boldsymbol{a}(\omega, r, z)|^2 \, r \, \mathrm{d}r \right)^{-1} \int_0^{R_{\rm cap}} |\boldsymbol{a}(\omega, r, z)|^2 \, r \, \mathrm{d}r. \tag{19}$$

This solution and spectrum (19) will be analyzed below and the resulting frequency shift given by (18) will be compared with the analytical expression (12), and to the experimental results in section 5. In order to compare with the experimental results, it is useful to define the relative wavelength shift. For a mean-square frequency shift $\delta\omega$ small compared with ω_0, determined by (1), (4) and (17), (18), the relative wavelength shift and the relative frequency shift are of opposite signs:

$$\frac{\Delta\lambda z}{\lambda_0} \equiv \left[\frac{1}{\Delta\omega(z)/\omega_0 + 1} - 1 \right] \cong -\frac{\Delta\omega(z)}{\omega_0} \cong -\frac{\delta\omega(z)}{\omega_0}, \tag{20}$$

where

$$\Delta\lambda(z) \equiv \left(\int_0^{\infty} I(\lambda, z) \, \mathrm{d}\lambda \right)^{-1} \int_0^{\infty} \lambda I(\lambda, z) \, \mathrm{d}\lambda - \lambda_0 \tag{21}$$

and $\Delta\omega(z) \equiv (\int_0^{\infty} I(\omega, z) \, \mathrm{d}\omega)^{-1} \int_0^{\infty} \omega I(\omega, z) \, \mathrm{d}\omega - \omega_0$ are the averaged wavelength and frequency shifts and $I(\lambda, z)$ and $I(\omega, z)$ are the spectral intensity, averaged over the radius, as functions of wavelength and frequency, respectively.

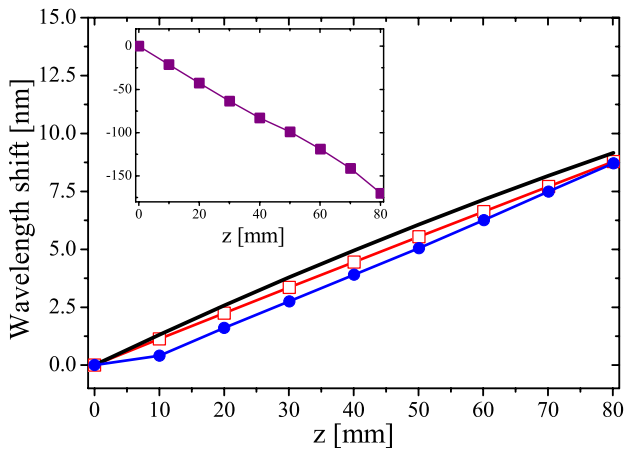

Figure 1. Wavelength shift calculated with (12), the solid line (not marked), and obtained in simulations as functions of the laser propagation distance in a capillary filled with 20 mbar of hydrogen; lines with markers: OFI included (dots) and pre-ionized plasma (open squares). The inset shows the wavelength shift for the same parameters but in a capillary filled with helium. Parameters are indicated in the text.

The results of self-consistent modeling by (13)–(16) and (6) are illustrated in figures 1–4 for quasi-monomode laser pulse propagation, when the Gaussian laser pulse of (10) is focused at the entrance of a capillary of radius $R_{\rm cap} = 50\,\mu$m, with the matched spot size $r_0 = 0.67R_{\rm cap} = 33.5\,\mu$m and $a_0 = 0.24$; for a full-width at half-maximum (FWHM) pulse duration $\tau_{\rm FWHM} = \sqrt{2\ln 2}\,\tau = 51$ fs and $\lambda_0 = 0.8\,\mu$m, it corresponds to a laser pulse energy of 0.12 J and an intensity $I_0 = 1.3 \times 10^{17}\,{\rm W\,cm^{-2}}$.

The red wavelength shift (20) due to wakefield generation in a capillary filled with hydrogen at a pressure of 20 mbar is shown in figure 1 by lines with markers for OFI included (marked by dots) and for a pre-ionized plasma (marked by open squares). The corresponding spectra are shown in figure 2. They are in good agreement with the analytical prediction from (12) shown in figure 1 by a solid line (not marked). At this laser pulse intensity, well above the threshold value for the OFI of hydrogen gas, the laser pulse propagates in the capillary in the quasi-monomode regime over a few centimeters without substantial distortions and visible influence of ionization to the laser spectrum.

For the same parameters, when the capillary is filled with helium (with an atomic density half that of hydrogen in order to get the same free electron density at full ionization), the wavelength shift is determined completely by OFI: it is blue (negative) and of much larger amplitude than the red shift in hydrogen, as seen in the inset of figure 1 and in figure 2 for the lines marked by solid squares. Note that the integral wavelength shift (see (17), (18) and (20)) is determined not only by the shift of the maximum of the spectrum, but also by the 'blue tail' of the spectrum, not seen completely in figure 2 and extending in this case up to 400 nm. The laser pulse and the wakefield generated in the capillary filled with helium reveal in this case

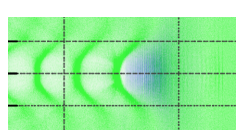

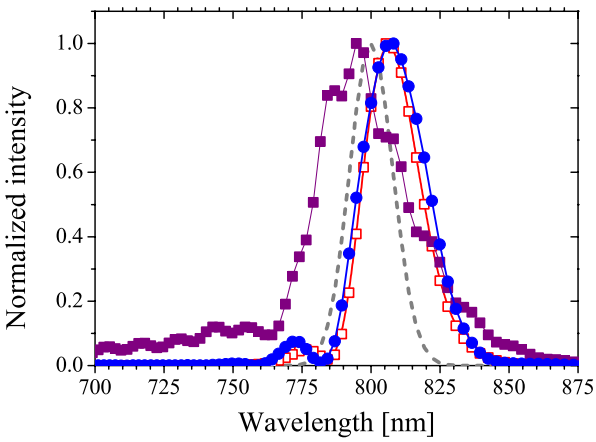

Figure 2. Spectra of transmitted laser pulses integrated over the radius obtained in simulations after propagation over a length of 70 mm in a capillary filled with 20 mbar of hydrogen: OFI included (marked by dots) and pre-ionized plasma (open squares); the same for capillary filled with helium, the line is marked by solid squares. The dashed line shows the spectrum at the capillary entrance. Parameters are the same as in figure 1.

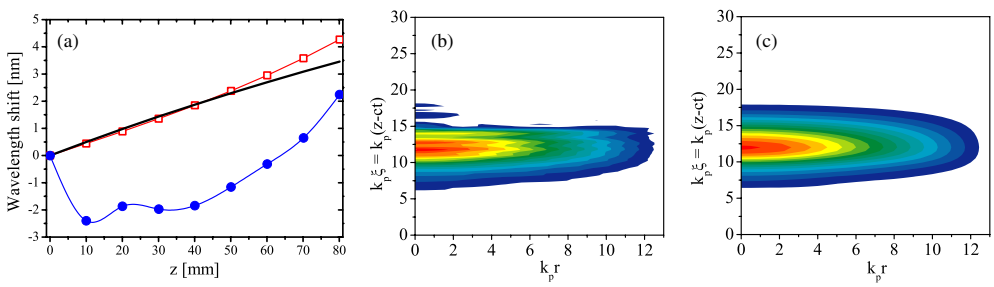

Figure 3. (a) Wavelength shift calculated with (12), unmarked solid line, and obtained in simulations as functions of the laser propagation distance in a capillary filled with 40 mbar of hydrogen, for $\varepsilon_L = 50$ mJ: OFI included (marked by dots) and pre-ionized plasma (open squares). (b) Normalized laser pulse envelope $|a(r, \xi)|$ after propagating in a capillary of 50 mm long filled with 40 mbar of hydrogen (OFI included). All parameters are the same as in (a). (c) The same as in (b), but in pre-ionized plasma.

a pronounced longitudinal and radial modulation caused by the variation of electron density produced self-consistently by the OFI of helium [14, 21].

For higher gas pressure and lower laser pulse intensities, gas ionization starts to play a substantial role in the laser pulse spectrum modification even for capillaries filled with hydrogen. As an example, figure 3(a) shows the wavelength shifts for a capillary filled with

IOP Institute of Physics DEUTSCHE PHYSIKALISCHE GESELLSCHAFT

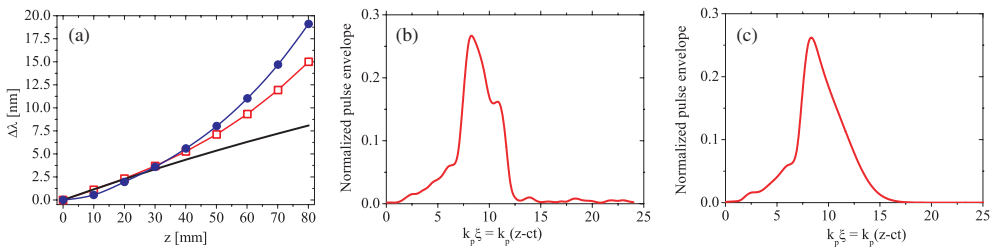

Figure 4. (a) The same as in figure 3(a) for a capillary filled with 40 mbar of hydrogen and laser pulse intensity $I_0 = 1.3 \times 10^{17}\,\mathrm{W\,cm^{-2}}$ and an energy of 0.12 J. (b) Normalized laser pulse envelope $a(r = 0, \xi)$ on the axis at a distance of 70 mm with OFI included. All parameters are the same as in (a). (c) The same as in (b), but in pre-ionized plasma.

40 mbar of hydrogen, a laser pulse energy of 50 mJ, and intensity $I_0 = 0.54 \times 10^{17}\,\mathrm{W\,cm^{-2}}$. All other parameters are the same as for figure 1. Ionization dominates the spectrum modification and leads to a net blue shift for capillary lengths smaller than 70 mm. The shift due to ionization is partly compensated by the shift due to wakefield, whose amplitude increases with pressure and capillary length as nonlinear effects modify the pulse shape. Note that the laser pulse intensity in this case is still well above the threshold value for the OFI of hydrogen (of the order of $10^{14}\,\mathrm{W\,cm^{-2}}$), but the OFI contributes substantially to the laser pulse dynamic and spectrum modification. Figures 3(b) and (c) exhibit the amplitude of the normalized laser pulse envelope $|a(r, \xi)|$ at a distance $z = 50$ mm for the same parameters as figure 3(a). In figure 3(b), where ionization is included, the front of the pulse at $k_p\xi \simeq 17$ is eroded due to refraction-induced ionization [21]. At the same time, there is no significant influence of the nonlinearity of pre-ionized plasma on the pulse propagation, as seen in figures 3(a) and (c).

For the same pressure of hydrogen (40 mbar), but higher laser intensity, $I_0 = 1.3 \times 10^{17}\,\mathrm{W\,cm^{-2}}$, the plasma nonlinearity starts to play a substantial role in the pulse dynamics and transmitted laser spectrum, as illustrated in figure 4.

Comparison of figures 4(b) and (c) shows that the OFI of gas leads to the shortening and sharpening of the front of the pulse [21]; in addition, the self-phase modulation and nonlinear group velocity dispersion in the plasma causes a sharpening of the pulse tail just after the intensity maximum [22] (see figure 4(b)). Both these effects lead to pulse shortening that increases the wakefield generation [14, 23] and the subsequent red wavelength shift, as seen in figure 4(a), as the initial pulse length for this pressure was about twice as long as the linear resonant one.

4. Experimental arrangement

An experiment was performed using the multi-TW Ti:sapphire laser system at the Lund Laser Centre, which provided up to 0.5 J energy pulses onto the target, with an FWHM pulse duration of 40 ± 5 fs at a central wavelength of $\lambda_0 = 786$ nm. The experimental setup scheme is presented in figure 5. The 30 mm-diameter laser beam was focused with an $f = 1.5$ m spherical mirror

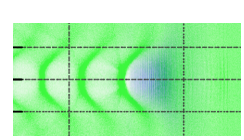

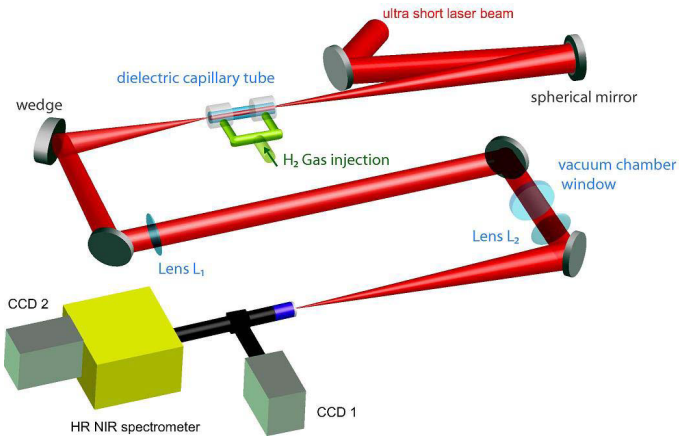

Figure 5. Schematic view of the experimental setup. All the elements up to the vacuum chamber window were under vacuum.

at the entrance of a capillary tube. In order to correct the aberrations of the phase front, a deformable mirror was used after the compressor. The laser beam transmitted through the capillary tube was attenuated by reflecting it from a glass wedge and then collimated by an achromatic $f_1 = 1$ m lens (L_1), which could be translated in vacuum along the beam axis to collect light either from the focal plane (i.e. with the capillary tube removed) or from the exit plane of the tube. The beam was then focused by an $f_2 = 1$ m achromatic lens (L_2) and magnified $10\times$ by a microscope objective. The beam was split into two parts. Focal spot or capillary tube output images were recorded by a 16-bit charged-couple device (CCD 1 in figure 5). The transmitted part was sent to a visible-to-near-infrared imaging spectrometer equipped with a 16-bit CCD camera (CCD 2 in figure 5). The spectral resolution was 0.1 nm. The laser beam path up to the vacuum chamber window was under vacuum. Glass capillary tubes with inner radius $R_{cap} = 50 \pm 1\ \mu$m and length varying between 1.2 and 8.1 cm were used. Hydrogen gas (H_2) was injected into the tubes through two thin ($\cong 100\ \mu$m) slits located between 2.5 and 5 mm from each end of the tube. The filling pressure was varied between 0 and 80 mbar. Each capillary tube could be used for at least a hundred laser shots, when the laser beam remained well centered at the capillary entrance. Pointing variations due to thermal drifts and mechanical vibrations were therefore minimized or compensated for. Laser guiding at input intensities up to 10^{18} W cm^{-2} was achieved with more than 90% energy transmission in evacuated or hydrogen-filled gas tubes up to 8 cm long.

For the data presented here, in order to investigate the moderately nonlinear regime, the input intensity was kept lower than 3×10^{17} W cm^{-2}. The laser pulse duration was $\tau_0 = 45 \pm 5$ fs and the associated bandwidth was approximately 25 nm (FWHM); each pulse had a small negative linear chirp, i.e. short wavelengths preceded longer wavelengths. The energy distribution in the focal plane exhibited an Airy-like pattern with a radius at first minimum of $r_0 = 40 \pm 5\ \mu$m.

IOP Institute of Physics DEUTSCHE PHYSIKALISCHE GESELLSCHAFT

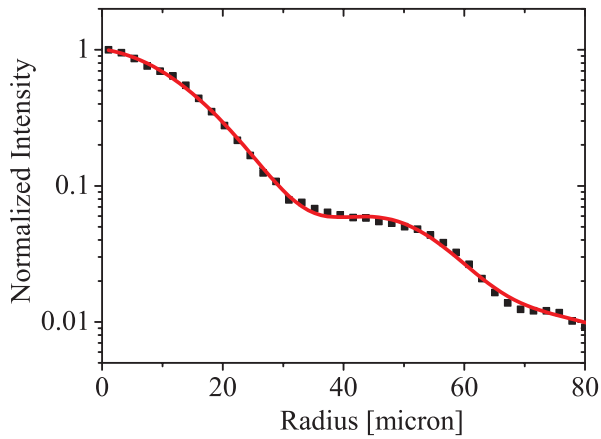

Figure 6. Normalized laser intensity distribution averaged over the azimuthal angle measured in the experiment (squares) and its multi-picks approximation used in simulations (the solid line).

5. Comparison between modeling results and experimental data

To model wakefield generation and laser pulse spectrum modifications with initial conditions as close as possible to the experimental ones, the measured radial laser intensity distribution was approximated by a radial profile averaged over the azimuthal angle as shown in figure 6. This approximation was used for all the modeling results shown below. In the simulations, the FWHM laser pulse duration was 51 fs with a linear negative chirp of $-550\,\mathrm{fs}^2$, which corresponds to the experimentally measured laser spectrum width at the focal plane in vacuum.

Figure 7 shows the wavelength shift (21) measured in the experiment (squares with error bars) and obtained in the modeling (line with circles) for the experimentally measured radial distribution of laser intensity at the capillary entrance as a function of the laser pulse energy for a 7 cm-long capillary filled with hydrogen molecular gas at a pressure of 40 mbar. The dashed line is the analytical prediction (12) with the on-axis laser pulse amplitude adjusted so that the laser pulse energy in the main mode (11) equals the experimental measurement. The measured and modeled red wavelength shifts are in a good agreement in all the energy range shown in figure 7 and they are larger than the linear analytical prediction (12). At this gas pressure, above the linear resonant one equal to 25 mbar, and for laser pulse energies higher than 100 mJ, both ionization and nonlinear group velocity dispersion are responsible for the laser pulse shortening and consequently are more effective for wakefield generation as shown in figure 4. For energies lower than 100 mJ, the sharpening of the front edge of the pulse due to ionization is combined with the transverse modification of the structure of the laser pulse guided in the capillary; the use of the non-Gaussian distribution of figure 6 at the entrance thus induces a larger wavelength shift. This can be seen by comparison with figure 3(a) where the wavelength shift obtained for an initially Gaussian pulse in transverse direction is almost zero at 70 mm, whereas in figure 7 it is of the order of 7 nm for 50 mJ.

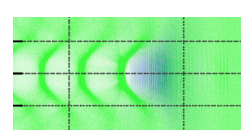

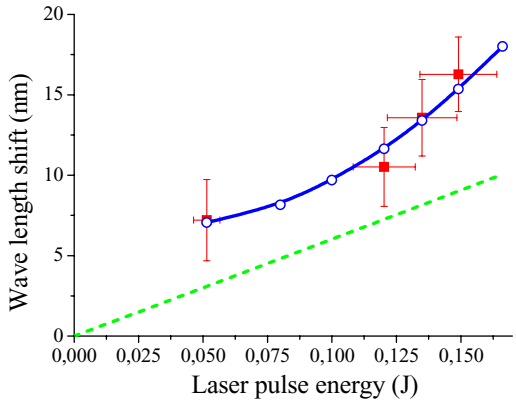

Figure 7. Wavelength shift measured in the experiment (squares with error bars) and obtained in the modeling (line with circles) as functions of the laser pulse energy for a 70 mm-long capillary filled with hydrogen gas at a pressure of 40 mbar. The dashed line is the analytical prediction (12).

The agreement between modeled and measured red shifts observed in figure 7 is supported by the agreement achieved for the transmitted laser pulse spectra shown in figure 8 for laser pulse energies 50, 120 and 150 mJ measured for different shots (black and gray solid lines in figures 8(a) and (c)) and obtained in full-scale modeling (dashed lines). The blue solid line in figure 8(b) shows a spectrum averaged over four shots. This shows that not only the pulse broadening but also the growth of the amplitude of the modulations can be reproduced by the simulations when the energy is increased.

The wavelength shifts as functions of pressure for different lengths of a capillary are shown in figure 9 at a laser pulse energy 120 mJ. For short, 12 mm-long capillaries the measured, modeled and analytically predicted shifts are close to zero as the ionization blue shift roughly cancels the wakefield red shift as can be seen for 20 mbar in figure 1(a). For longer capillaries, when wakefield generation has a substantial effect on the transmitted laser spectra, the measured and modeled dependences shown in figures 9(b)–(d) closely follow analytical predictions up to a pressure of the order of 25 mbar, which corresponds to the value determined by the linear resonant condition for the wakefield generation, $\omega_p \tau = 2$, for the Gaussian time envelope (10).

For higher pressures, in excess of 40 mbar and for capillaries longer than 50 mm, the measured and modeled red shifts grow with increasing pressure as opposed to the drop in the analytical behavior caused by the departure from the resonance between the laser pulse length and plasma wavelength (see figure 9, dashed lines). An increase of the wakefield generation and corresponding red wavelength shift for pressures higher than that determined by the linear resonant condition is caused by nonlinear laser pulse shortening. For monomode laser pulse propagation and 70 mm capillary length, this process is illustrated in figure 4(a) for a hydrogen pressure of 40 mbar. For the radial distribution of figure 6 and for higher pressure, the propagation in the capillary is multi-mode, leading to a more important pulse shortening as shown in figure 10 for the capillary length 71 mm and pressure 60 mbar (see also [24]). However, it should be noted that even for this strong nonlinear modification of the laser pulse,

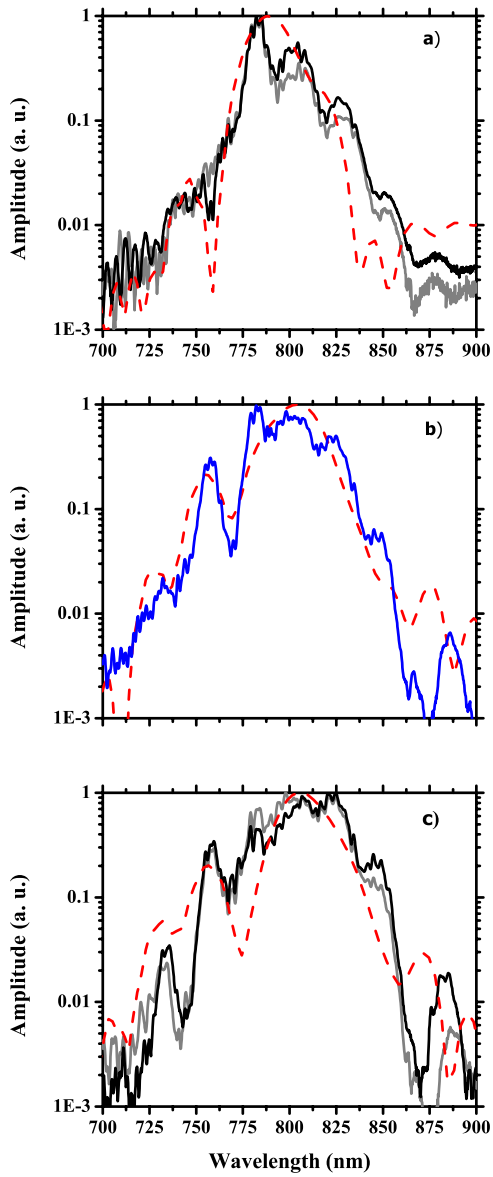

Figure 8. Laser pulse spectra for pulse energies 50 (a), 120 (b) and 150 mJ (c) measured in the experiment (solid lines are for different shots in (a) and (c) and the average of 4 shots is shown in (b)) and obtained in simulations (dashed lines). Parameters are indicated in the text.

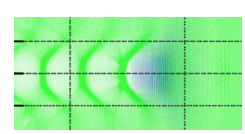

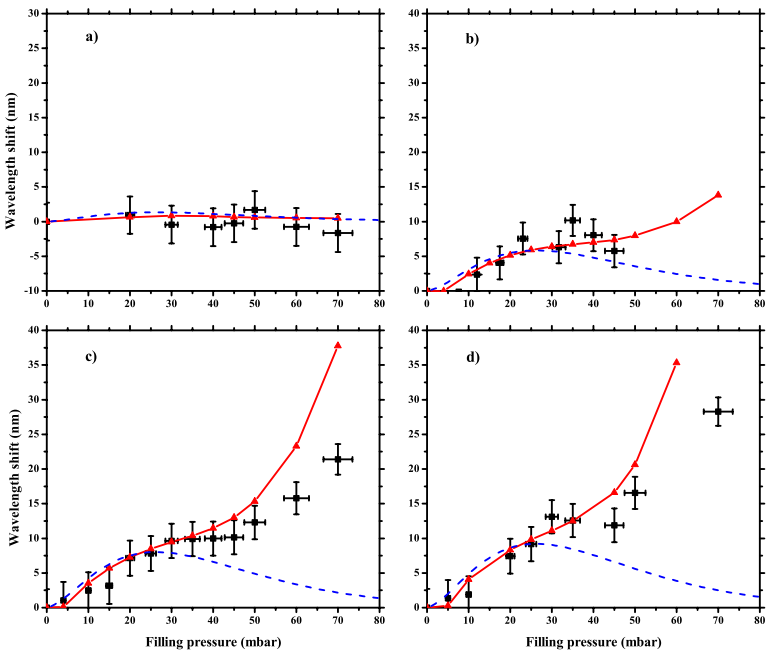

Figure 9. Wavelength shifts as functions of pressure at a laser pulse energy of 120 mJ for different lengths of capillary $L_{cap} = 12$ (a); 50 (b); 71 (c) and 81 mm (d). Squares with error bars are experimentally measured values, solid lines are the results of modeling and dashed lines are for analytical prediction (12).

the wakefield generated along the capillary tube is very regular as can be seen in figure 10(c), where the radial distribution of the wakefield potential as a function of the local time in the co-moving frame (moving with the speed of light) is shown by the color map. The zero of the local time corresponds to the time when the laser pulse maximum reaches the capillary entrance, see figure 10(a). The increasing deviations of the modeled red shift from the one measured as the pressure and the capillary length are increased (see figure 9) are attributed to the asymmetry of the focal spot in the experiment, whereas cylindrical symmetry, assumed in the model, leads to more pronounced nonlinear effects.

Figure 11 shows the wavelength shifts as functions of the length of the capillary filled with hydrogen gas, measured in the experiment and obtained in the modeling for pressures of 20 and 40 mbar and a laser pulse energy of 120 mJ. The wavelength shift grows linear as a function of length for the 20 mbar case, in agreement with analytical prediction (12). The fit of experimental data by simulation results demonstrates that the plasma wave is excited over a length as long as 8 cm. As the pressure is increased, the nonlinear laser pulse evolution is amplified with the propagation length leading to larger plasma wave amplitude.

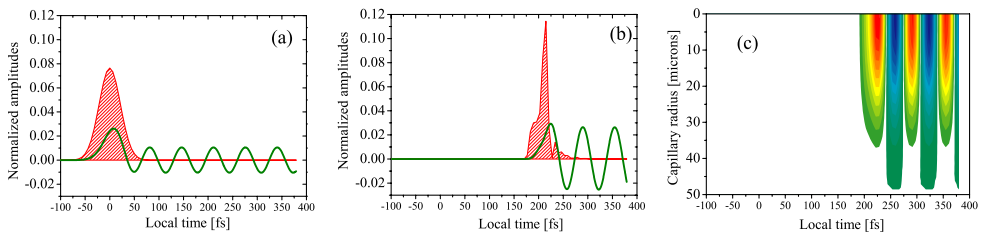

Figure 10. Normalized laser pulse intensity (the hatched area) and wakefield potential (the solid line) on the axis at the entrance (a) and after propagation in a capillary of length 71 mm (b), as functions of the local time; radial distribution of the wakefield potential in time (c). Parameters of modeling correspond to figure 9(c) at pressure 60 mbar.

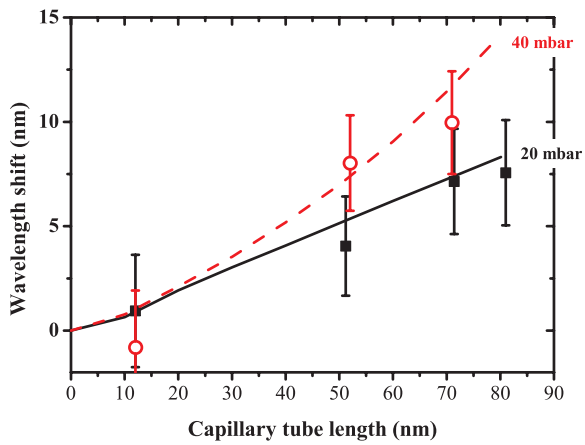

Figure 11. Wavelength shifts as functions of the length of capillary filled with 20 mbar of hydrogen gas measured in the experiment (solid squares with error bars) and obtained in the modelling (solid line); open circles with error bars and dashed line are for a pressure of 40 mbar. Laser pulse energy is 120 mJ.

6. Conclusion

Analytical predictions of the laser pulse frequency red shift based on the general approach of the frequency momentum theory formulated without any restrictions on the radiation intensity and geometry were used to analyze the wakefield generated by a short intense laser pulse propagating in a gas-filled capillary tube. The full-scale self-consistent modeling completely confirms the results obtained analytically in the following conditions: monomode propagation of the laser pulse, in a moderately nonlinear regime, with intensities much higher than the threshold value for the OFI of hydrogen filling the capillary, and gas pressures lower than the value determined by the linear resonant condition for wakefield generation. For higher pressures and laser pulse energies, modeling results exhibit nonlinear pulse shortening, enhanced wakefield

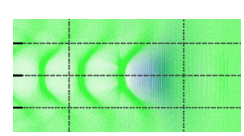

generation and frequency red shift closely fitting experimental results. Even for intensities much higher than the threshold value for the OFI of filling gas, ionization-induced refraction can substantially modify the laser pulse, and the influence of ionization is more pronounced for higher pressures and lower pulse energies.

The agreement between modeled and measured red shifts observed as functions of pulse energy, pressure of hydrogen gas filling the capillary and capillary length is supported by the agreement achieved for the transmitted laser pulse spectra obtained in simulations and experiment. The value of the longitudinal accelerating field in the plasma obtained from the simulation is in the range 1–10 GV m^{-1}. The average product of gradient and length achieved in this experiment is of the order of 0.4 GV at a pressure of 50 mbar; it could be increased to several GV by extending the length and diameter of the capillary tube with higher laser energy.

In conclusion, the outgoing spectra of driving laser pulses measured after propagation in gas-filled capillaries supported by relevant modeling can provide detailed information on laser pulse dynamics and on the main characteristics of the accelerating fields excited in the wake of the laser pulses over the long distances necessary for efficient acceleration of electrons to high energies.

Acknowledgments

This work was supported in part by the Programs on fundamental research of the Russian Academy of Sciences, by the Russian Foundation for Basic Research—CNRS PICS program (grant 07-02-92160), and by the European Community—New and Emerging Science and Technology Activity under the FP6 'Structuring the European Research Area' programme (project EuroLEAP, contract 028514). This work was also supported by the Marie Curie Early Stage Training Site MAXLAS (MEST-CT-2005-020356), the Swedish Research Council and the Knut and Alice Wallenberg Foundation.

References

[1] Tajima T and Dawson J 1979 *Phys. Rev. Lett* **43** 267
[2] Gorbunov L M and Kirsanov V I 1987 *Sov. Phys.—JETP* **66** 290
[3] Esarey E, Sprangle P, Krall J and Ting A 1996 *IEEE Trans. Plasma Sci.* **24** 252
[4] Marques J R *et al* 1996 *Phys. Rev. Lett.* **76** 3566
Siders C W *et al* 1996 *Phys. Rev. Lett.* **76** 3570
[5] Le Blanc S P, Gaul E W, Matlis N H, Rundquist A and Downer M C 2000 *Opt. Lett.* **25** 764
[6] Dias J M, Silva L O and Mendonca J T 1998 *Phys. Rev. ST Accel. Beams* **1** 031301
[7] Wilks S C, Dawson J M, Mori W B, Katsouleas T and Jones M E 1989 *Phys. Rev. Lett* **62** 2600
Esarey E, Ting A and Sprangle P 1990 *Phys. Rev.* **42** 3526–31
[8] Andreev N E, Chegotov M V, Cros B, Mora P and Vieux G 2006 *Phys. Plasmas* **13** 053109
[9] Andreev N E, Fortov V E and Chegotov M V 2003 Spectral analysis of the ultrafast processes by the interaction of short laser pulses with matter *Physics of Extreme States of Matter* ed V E Fortov *et al* (Chernogolovka: Institute of Problems of Chemical Physics RAS) p 11
Chetogov M V 2004 *Proc. Scientific Session of Moscow Institute of Engineering Physics* MIFI-2004 p 163
[10] Andreev N E and Chegotov M V 2005 *J. Exp. Theor. Phys.* **101** 56–63
[11] Murphy C D *et al* 2006 *Phys. Plasmas* **13** 033108
[12] Wojda F *et al* 2009 *Phys. Rev.* **80** 066403

[13] Chegotov M V 2002 *Tech. Phys.* **47** 1002
Chegotov M V 2003 *Quantum Electron.* **33** 370–6
[14] Andreev N E, Nishida Y and Yugami N 2002 *Phys. Rev.* E **65** 056407
Andreev N E, Cros B, Gorbunov L M, Matthieussent G, Mora P and Ramazashvili R R 2002 *Phys. Plasmas* **9** 3999–4009
[15] Leemans W, Siders C W, Esarey E, Andreev N, Shvets G and Mori W B 1996 *IEEE Trans. Plasma Sci.* **24** 331
[16] Dorchies F *et al* 1999 *Phys. Rev. Lett.* **82** 4655
Courtois C, Couairon A, Cros B, Marque's J R and Matthieussent G 2001 *Phys. Plasmas* **8** 3445
Cros B, Courtois C, Matthieussent G, Di Bernardo A, Batani D, Andreev N and Kuznetsov S 2002 *Phys. Rev.* E **65** 026405
[17] Andreev N E, Chegotov M V and Veisman M E 2000 *IEEE Trans. Plasma Sci* **28** 1098
Andreev N E, Veisman M E, Cadjan M G and Chegotov M V 2000 *Plasma Phys. Rep.* **26** 947
[18] Sprangle P, Esarey E and Ting A 1990 *Phys. Rev. Lett.* **64** 2011
[19] Kandidov V P, Kosareva O G and Shlenov S A 1994 *Quantum Electron.* **24** 971
[20] Ammosov M V, Delone N B and Krainov V P 1986 *Sov. Phys.—JETP* **64** 1191
Delone N B and Krainov V P 1998 *Phys.—Usp.* **41** 469
Delone N B and Krainov V P 1998 *Usp. Fiz. Nauk* **168** 531
[21] Andreev N E, Chegotov M V and Pogosova A A 2003 *J. Exp. Theor. Phys.* **96** 885
[22] Esarey E, Schroeder C B, Shadwick B A, Wurtele J S and Leemans W P 2000 *Phys. Rev. Lett* **84** 3081
Hubbard R F, Sprangle P and Hafizi B 2000 *IEEE Trans. Plasma Sci.* **28** 1122
[23] Andreev N E, Kuznetsov S V, Pogosova A A, Steinhauer L C and Kimura W D 2003 *Phys. Rev. ST Accel. Beams* **6** 041301
Kimura W D *et al* 2005 *IEEE Trans. Plasma Sci.* **33** 3–7
[24] Skobelev S A, Kulagin D I, Stepanov A N, Kim A V, Sergeev A M and Andreev N E 2009 *JETP Lett.* **89** 540–6

Paper XI

Laser-plasma electron acceleration in dielectric capillary tubes

G. Genoud, K. Cassou, F. Wojda, H. E. Ferrari, C. Kamperidis, M. Burza, A. Persson, J. Uhlig, S. Kneip, S. P. D. Mangles, A. Lifschitz, B. Cros and C.-G. Wahlström.

Applied Physics B **105**, 309 (2011).

Appl Phys B (2011) 105:309–316
DOI 10.1007/s00340-011-4639-4

Applied Physics B
Lasers and Optics

Laser-plasma electron acceleration in dielectric capillary tubes

G. Genoud · K. Cassou · F. Wojda · H.E. Ferrari · C. Kamperidis · M. Burza · A. Persson · J. Uhlig · S. Kneip · S.P.D. Mangles · A. Lifschitz · B. Cros · C.-G. Wahlström

Received: 25 January 2011 / Revised version: 19 April 2011 / Published online: 29 July 2011

Abstract Electron beams and betatron X-ray radiation generated by laser wakefield acceleration in long plasma targets are studied. The targets consist of hydrogen filled dielectric capillary tubes of diameter 150 to 200 microns and length 6 to 20 mm. Electron beams are observed for peak laser intensities as low as 5×10^{17} W/cm^2. It is found that the capillary collects energy outside the main peak of the focal spot and contributes to keep the beam self-focused over a distance longer than in a gas jet of similar density. This enables the pulse to evolve enough to reach the threshold for wavebreaking, and thus trap and accelerate electrons. No electrons were observed for capillaries of large diameter (250 μm), confirming that the capillary influences the interaction and does not have the same behaviour as a gas cell. Finally, X-rays are used as a diagnostic of the interaction and, in particular, to estimate the position of the electrons trapping point inside the capillary.

G. Genoud · C. Kamperidis · M. Burza · A. Persson · C.-G. Wahlström (✉)
Department of Physics, Lund University, P.O. Box 118, 22100 Lund, Sweden
e-mail: claes-goran.wahlstrom@fysik.lth.se
Fax: +46-46-2224250

K. Cassou · F. Wojda · H.E. Ferrari · A. Lifschitz · B. Cros
Laboratoire Physique Gaz et Plasmas (UMR 8578), Université Paris-Sud 11, 91405 Orsay Cedex, France

H.E. Ferrari
CONICET, Buenos Aires, Argentina

J. Uhlig
Department of Chemical Physics, Lund University, P.O. Box 124, 22100 Lund, Sweden

S. Kneip · S.P.D. Mangles
Blackett Laboratory, Imperial College London, London, SW7 2BZ, UK

1 Introduction

When an intense femtosecond laser pulse interacts with gas, a plasma is formed and the ponderomotive force of the pulse generates a large amplitude plasma wave. This wave can break, trap, and accelerate electrons. The acceleration field can be more than a thousand times higher than those achieved in accelerators based on conventional technology. Laser plasma wakefield accelerators are thus a promising alternative to conventional accelerators, especially because of their compactness and short pulse duration. Quasi-monoenergetic beams of electrons, of hundreds of MeV kinetic energy, have been produced in several experiments [1–5]. The laser pulse can also be externally guided, for example by using either a plasma channel created by a discharge inside a capillary [6] or a dielectric capillary tube. In this article, we discuss the use of gas-filled dielectric capillary tubes to assist guiding and thereby enable wave breaking and self-trapping of electrons at lower laser intensities than required with gas jets, which also have a homogeneous transverse gas profile.

Even when the intensity at the entrance of the plasma is below the threshold for wave-braking and electron trapping, it can be reached through the non-linear evolution of the pulse, undergoing self-focusing and pulse compression. In the experiment reported here, electron beams were observed with peak laser intensities as low as $I = (5 \pm 2) \times 10^{17}$ W/cm^2 (corresponding to a normalized pulse amplitude $a_0 = 0.5$) for a plasma electron density of the order of 10^{18} cm^{-3}. With such a low intensity, the evolution of

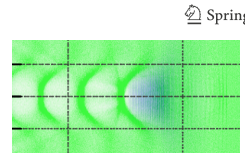

the laser pulse would not be sufficient over the length typical for a gas jet experiment (a few mm). However, capillary tubes longer than 6 mm provide a distance of interaction long enough to achieve electron trapping and acceleration.

The inside walls of the capillary tubes are smooth at the laser wavelength and the laser pulse is guided by Fresnel reflection on the walls. Ultrashort intense laser pulses propagate using eigenmodes of the capillary tubes [7]. For a Gaussian distribution of energy at the entrance of the capillary, with a waist matched to the capillary radius, more than 98% of the incident energy can be transferred into the fundamental capillary mode, inducing quasi-perfect monomode guiding [8]. This can produce linear plasma waves over several centimetres [9] which could be used as an accelerating structure for injected electrons. The electron density in this type of capillary can be arbitrarily low which is an advantage, as the dephasing length can then be made equal or longer than the capillary tube. Dephasing occurs at the point where the electrons outrun the plasma wave and start decelerating. The dephasing length is given by $L_d = (\omega_0/\omega_p)^2\lambda_p$, where ω_0 is the laser frequency, $\omega_p = (n_e e^2/\epsilon_0 m_e)^{1/2}$ the plasma frequency of a plasma of electron density n_e and λ_p the corresponding plasma wavelength. e and m_e are the charge and mass of an electron, respectively. However, when the capillary diameter is too large to match the focal spot, the propagation is not monomode, as higher order modes are then also excited. In the experiment reported here, the focal spot size was deliberately chosen significantly smaller than the tube diameter to allow higher order modes to be excited. This resulted in a regime where external guiding, non-linear pulse evolution and self trapping take place inside the tube.

X-rays can be produced within a wakefield accelerator through a process called betatron oscillations [10]. Transverse fields can cause electrons within the wakefield to oscillate transversely to their acceleration direction and produce X-rays, which have great potential as novel ultra-short radiation sources. Moreover, their observation provides insight into the laser-plasma interaction itself, because their production is directly linked to the trapping and acceleration of electrons. For large amplitude oscillations of electrons, the radiation emitted close to the axis can be shown [11] to have a synchrotron-like spectrum, which is a broadband spectral distribution peaked close to the critical energy $E_c = 3/2\hbar K\gamma^2\omega_\beta$, with $\gamma m_e c^2$ the electron energy [12]. The betatron frequency $\omega_\beta = \omega_p/\sqrt{2\gamma}$ and the betatron strength parameter $K = \gamma r_\beta \omega_\beta/c$ describe the trajectory of an electron oscillating with an amplitude r_β.

2 Experiment

2.1 Experimental arrangement

The experiment was performed using the 10 Hz multi-terawatt Ti:sapphire laser system at the Lund Laser Centre,

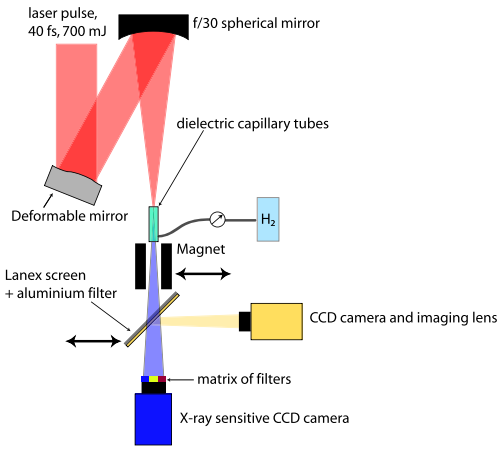

Fig. 1 Schematic view of the experimental setup

which delivered 0.7 J within a focal spot of 50 µm size (radius of the first minimum of an Airy-like pattern) in 40 fs (FWHM) pulse duration at $\lambda_0 = 795$ nm centre wavelength. A schematic view of the experimental arrangement is presented in Fig. 1. The laser pulses were loosely focused at the entrance of dielectric capillary tubes, using a spherical mirror in combination with a deformable mirror, to correct aberrations of the phase front in the focal plane. Glass capillary tubes with inner diameter ranging from $d = 150$ µm to 250 µm and length varying between 6 mm and 20 mm were aligned along the optical axis. Hydrogen gas was filled into the tubes through two thin (∼300 µm) slits located 2.5 mm from each end of the tubes. An electro-magnetic valve controlled the pressure in a reservoir which in turn controlled the flow of gas into the capillary tube. Gas densities inside the capillary corresponding to electron densities in the range 5×10^{17}–1.5×10^{19} cm^{-3}, were achieved and characterized by off-line interferometric measurement. Each capillary tube could be used for a large number of laser shots (∼100 shots in the same capillary), as long as the focused laser beam remained well centered at the capillary entrance. Pointing variations due to thermal drifts and mechanical vibrations were therefore minimized or actively compensated for [13]. The laser pulse was guided in the capillary in the multi-mode regime [7], ionizing the gas and producing a wake. Figure 2 illustrates how the capillary guides the laser beam in vacuum. In (a), the focal spot at the entrance of the capillary tube is shown. In (b), the mode pattern at the exit of the capillary tube shows that the laser pulse was guided in the multi-mode regime. The transmission within the capillary diameter is 70% (capillary of 20 mm long and 200 µm diameter). The symmetry of this multi-mode structure at the exit of the capillary tube is the criterion used for the alignment of the tube on the laser axis.

Electrons from the plasma were trapped, accelerated and then detected on a phosphor screen (Kodak Lanex), placed 59 cm after the laser focus, imaged by a CCD camera. A permanent magnet ($B = 0.7$ T, length 100 mm) could be moved into position between the capillary exit and the phosphor screen to deflect the electrons and thereby allow their energy distribution to be measured. Electrons with energy below 40 MeV did not reach the phosphor screen and were thus not detected. Far-field profiles of the X-rays, generated due to betatron oscillations inside the capillary, were recorded by a 16 bit CCD X-ray camera placed on the laser axis. X-rays and electron spectra were recorded simultaneously when the electron beam was deflected from the axis by the magnet. A matrix of metallic filters was placed over the chip of the camera in order to block laser and visible light and to provide a low resolution measurement of the X-ray spectrum. The camera, an Andor 434-BN CCD chip with 1024×1024 pixels of 13 μm size, was placed 89 cm away from the source, corresponding to a chip collection angle of 15×15 mrad^2.

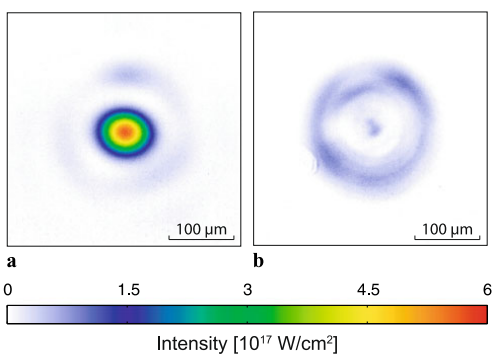

Fig. 2 Transmission trough a capillary tube of 20 mm long and 200 μm diameter in vacuum. In (**a**) the focal spot at the entrance of the capillary tube and (**b**) the multi-mode pattern at the exit of the capillary tube. The transmission within the capillary diameter is 70%

2.2 Electrons

Electron beams, with charge varying in the range 1–100 pC, were observed. The quality of the beam was found to depend very sensitively on the plasma electron density. Individual shots showed peaks with energies up to 170 MeV, with energy spreads as low as 7% and divergence as low as 4 mrad FWHM. At optimum plasma density, monoenergetic features were observed, as illustrated in Fig. 3(a) for $n_e = 3 \times 10^{18}$ cm^{-3}, a capillary length of 20.5 mm and a diameter of 200 μm. At higher densities, trapping occurs at more than one point leading to broad electron spectra, occasionally with multiple peaks as shown in Fig. 3(b) for $n_e = 8 \times 10^{18}$ cm^{-3} in a capillary 11 mm long and of 200 μm diameter. Both spectra were recorded at a peak laser intensity of 6×10^{17} W/cm^2.

The influence of the plasma electron density, laser intensity and capillary parameters, such as diameter and length, are presented in Fig. 4. In (a), the charge above 40 MeV is plotted as a function of the plasma electron density for different capillary diameters, and laser intensities. The capillary length was kept fixed (20.5 mm) and the diameter varied: 180 μm (circles), 200 μm (squares, diamonds) and 250 μm (triangles). The laser intensity was 6×10^{17} W/cm^2 except for the data represented by squares, where the laser intensity was 5×10^{17} W/cm^2. Figure 4(a) shows that for each capillary diameter and laser intensity, there is a narrow range of electron density for which accelerated electrons are produced. In this regime of acceleration, the plasma electron density is a crucial parameter for the trapping and acceleration process. This is also observed in simulations where changes in diameter and intensity significantly change the pulse evolution, as discussed by Ferrari et al. in [14]. In order to fully understand this very complex interaction and, in particular, how the different parameters influence the value of the optimum density, further modelling and systematic studies are required. Here, we merely demonstrate this sensitivity. Finally, for capillaries of 250 μm, diameter no electrons were observed over the entire range of electron densities explored. This suggests that for such large diameter

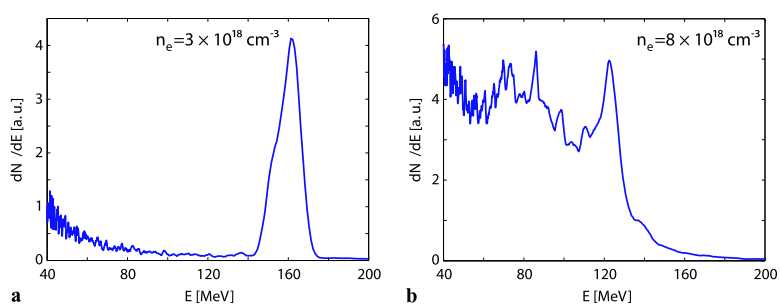

Fig. 3 Experimental electron spectra. In (**a**) a peaked spectrum and in (**b**) a broad spectrum with multiple peaks, with a total charge above 40 MeV of 2.3 pC and 7.7 pC, respectively

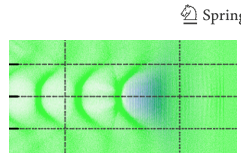

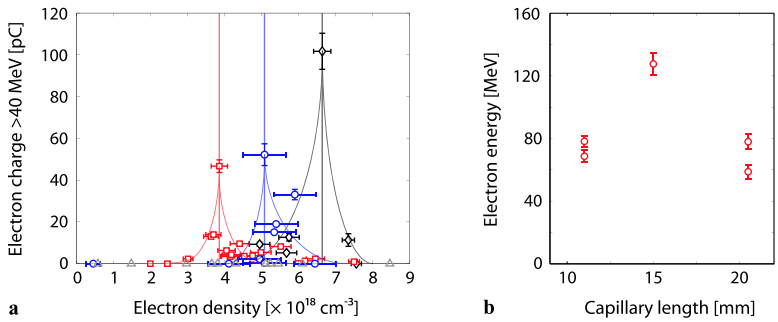

Fig. 4 Influence of the electron density, the laser intensity and the capillary parameters (diameter and length) on the electron beams. In (**a**) the charge above 40 MeV as function of electron density is shown for different capillary diameters: 180 μm (*blue circles*), 200 μm (*red squares*, *black diamonds*) and 250 μm (*grey triangles*) for a laser intensity of 6×10^{17} W/cm^2 except for the points represented by the squares where the laser intensity was 5×10^{17} W/cm^2. Each point corresponds to one laser shot. The graph shows complete data sets and therefore also illustrates the shot to shot fluctuations. The *lines* are drawn to guide the eye. The peak electron energy is plotted as function of the capillary length in (**b**) for $n_e = 5 \times 10^{18}$ cm^{-3}. The effect of dephasing is clearly visible

the capillary acted mainly as a windowless gas cell: the reflection from the wall are not sufficient to contribute significantly to the pulse evolution. In Fig. 3(b), the peak energy as a function of the capillary length is shown at a fixed electron density of 5×10^{18} cm^{-3} for a capillary diameter of 180 μm and laser intensity of 6×10^{17} W/cm^2. The onset of dephasing is observed as the peak energy decreases for the longest capillaries. At this density the theoretical dephasing length is $L_d = 5$ mm. As it is seen in the simulations (see, for example Fig. 8), for the values of densities and power considered, self-focusing is a slow process: it takes 6.4 mm in this example for a_0 to reach an adequate value for electron injection and trapping. Adding the evolution distance to the dephasing length gives a value of the order of what we observe in the experiment. Thus, the maximum electron energy can be reached inside the capillary. Alternatively, pump depletion can also contribute to limit the maximum energy. From simulations (Fig. 6 of [14]), it is estimated that 40% of the laser energy is depleted after 11 mm, where self-focusing stops.

2.3 X-rays

The production of betatron X-rays is directly linked to the trapping and acceleration of electrons. The far-field distribution of X-ray beams were recorded and gave additional insight into the interaction itself. The number of X-ray photons obtained strongly depends on the charge of the electron beam, and thus also on the plasma electron density. We obtained up to $\sim 5 \times 10^4$ photons/mrad^2 over the range 1–10 keV, which is comparable to the results in [10].

Figure 5(a) and (b) show far-field distributions of the X-ray beam for two slightly different electron densities, $n_e = 5.3 \times 10^{18}$ cm^{-3} and $n_e = 5.9 \times 10^{18}$ cm^{-3}, respectively. Both were produced in a capillary 20 mm long and of 180 μm diameter and recorded using a uniform filter (6 μm mylar and 3 μm Al) in front of the CCD chip. Figure 5(c) shows a radial profile, averaged over angles (red curve) of the image of Fig. 5(a), as well as line-outs in two transverse directions (black and grey curves) of a simulated X-ray beam, from simulations discussed in the next section, with $n_e = 5 \times 10^{18}$ cm^{-3}, a capillary diameter of 150 μm and a length of 20 mm for an X-ray photon energy of 1 keV. Figure 5(d) shows the X-ray beam distribution produced in a capillary tube of length 20 mm and diameter 200 μm, $n_e = 7 \times 10^{18}$ cm^{-3}, and a different set of filters (a base of 6 μm mylar and 3 μm Al, with a 3 μm thick vertical stripe of Al and a 3 μm thick horizontal stripe of Sn). Assuming a synchrotron-like spectrum, using the tabulated transmission data of the filters and known CCD sensitivity, an estimate of the critical energy $E_c = 1.3$ keV was deduced using a least-squares method [15].

The shape of the edge of the beam on the images of Fig. 5 shows that the wall of the capillary in the output plane casts a shadow, indicating that the source of the X-rays is inside the tube. The shadow of the wall is observed also on the simulation results and its size is similar to the experimental data. From the different images in Fig. 5, it is clearly observed that the divergence of the X-ray beam varies, which can be related to a different geometry (different capillary tubes) or a different position of the X-ray source along the capillary axis, due for example to a different electron density.

Sources situated at different points along the axis of the capillary produce circular beams of different radii on the detector, as illustrated in Fig. 6. The points closest to the entrance of the tube, situated on the left in Fig. 6, will therefore produce the smallest beam and the point closest to the exit

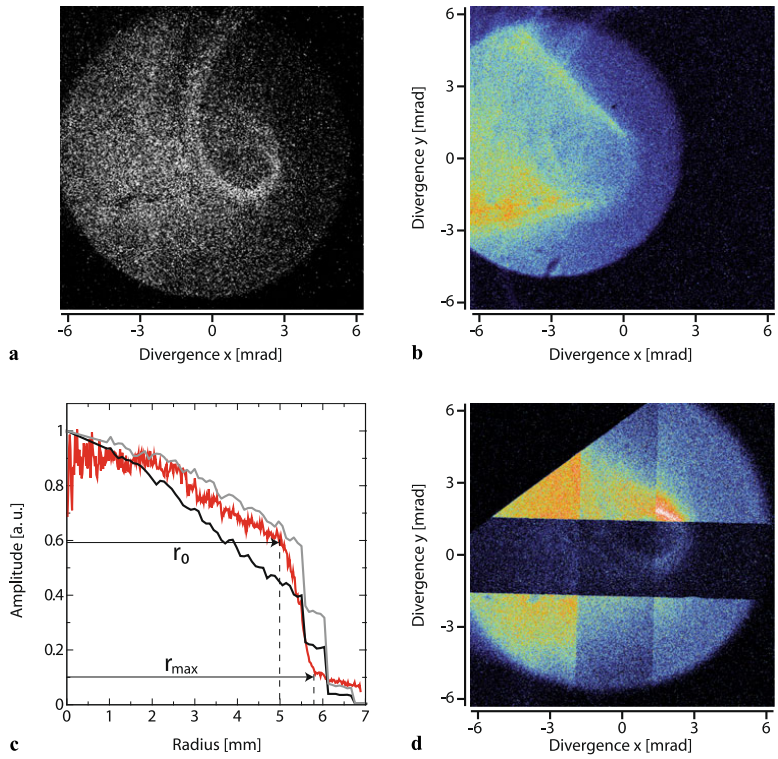

Fig. 5 Far-field distribution of the X-ray beam for two different densities in (**a**) and (**b**). In (**d**) the absorption in additional stripes of metallic foils placed in front of the detector are visible and are use to make a rough estimate of the X-ray spectrum. In (**c**), radial average profile of (**a**) (*red curve*), horizontal (*black curve*) and vertical (*grey curve*) line-outs of a simulated X-ray beam profile are shown

of the tube produces the largest one. This means that the radius, r_0, where the signal starts to decrease corresponds to emission from the point producing the smallest beam, i.e. the point closest to the entrance of the capillary. As shown in Fig. 5(c), r_0 can be obtained from the X-ray image and then using simple geometry, the position of the start of the X-ray emission can be estimated. Assuming that X-rays are not reflected by the capillary walls, the distance on axis between the start of the X-ray source and the exit of the capillary, L_X, can be written as $L_X = L/[(r_0/r_{\mathrm{cap}}) - 1]$ where L is the distance between the capillary output and the CCD camera, and r_{cap} the capillary tube radius. For example in the case of Fig. 5(a), $r_0 = 5$ mm, and the distance from the capillary entrance $L_{\mathrm{cap}} - L_X$ to the beginning of the X-ray emission is then estimated as 4.6 mm.

The shape of the edge of the beam is also an indicator of the extend of the X-ray source, or of the existence of multiple sources. The radius r_{max} corresponds to emission from the point producing the largest beam, i.e. the point closest to the exit of the capillary. Using the same calculation as previously, it is possible to estimate where the X-ray emission stops. For the case in Fig. 5(c), we find $r_{\mathrm{max}} = 5.8$ mm and the position of the end of the source is then estimated to be 6.8 mm from the capillary entrance. The source therefore extends from 4.6 to 6.8 mm after the entrance of the capillary. However, this is only a lower limit for the extend of the source as the detector is not perfect and the signal drops below the noise level. According to [16–19], the transverse source size is expected to be of the order of a few microns which would result in a radius difference of about ∼0.2 mm on the detector. This has been neglected as the radius difference due to the longitudinal source size is much larger.

As the electrons start emitting X-rays as soon as they are trapped, the position of the X-ray source can be used to determine the trapping position. However, due to the filters in front of the CCD camera, only X-rays above 500 eV were detected and only the point where the electrons have been sufficiently accelerated to produce X-rays above 500 eV can be determined. Figure 7 shows the dependence of the position of the onset of the first X-ray emission, determined from the X-ray beam diameter, on the electron density for different capillaries and laser intensities. We observe that for most of the capillaries the X-ray emission starts at a shorter distance when the density is increased. The capillary diameter, as well as the laser intensity, also influences the result, confirming that the whole acceleration process is very sensitive

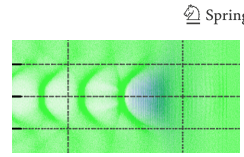

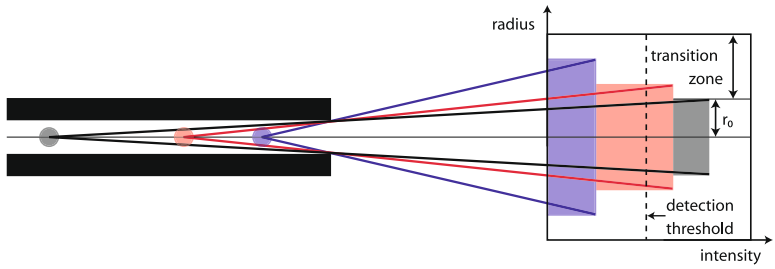

Fig. 6 Schematic explanation of the interpretation of the far-field intensity profiles images of the X-ray beams. The longitudinal spread of the X-ray emission inside the capillary tube is represented as different point sources. Depending on the position of the source, the beams *outside* of the capillary obtain different divergence. The points closest to the entrance in the tube, situated on the left of the figure, produce the smallest radius on the detector. By measuring r_0, it is possible to estimate the start of the X-ray emission and therefore the trapping point of the electrons

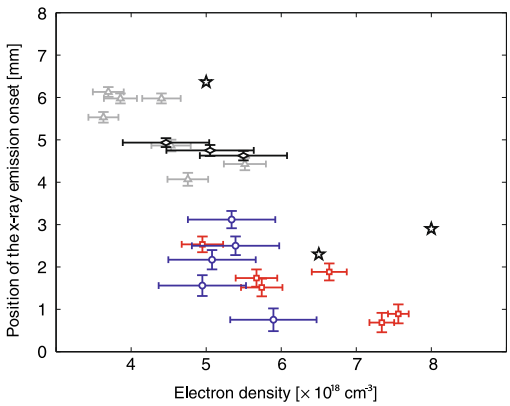

Fig. 7 The diameter of the X-ray image can be used to determine the position of the onset of the first X-ray emission relative to the laser focus inside the capillary. This is done for different capillaries as a function of electron density: a capillary of 20 mm length and 200 µm diameter (*grey triangles*, *red squares*), a capillary of 20 mm length and 180 µm diameter (*blue circles*), a capillary of 15 mm length and 180 µm diameter (*black diamonds*) for a laser intensity of 6×10^{17} W/cm^2 except for the points represented by the triangles and the diamonds where the laser intensity was 5×10^{17} W/cm^2. Each point corresponds to one laser shot. The stars correspond to the trapping points obtained from the simulations described in the next section

to these parameters. This is consistent with the observations of the electron beam, as shown in Fig. 4(a). The points represented by stars in Fig. 7 correspond to the trapping position obtained from the simulations described in the next section. A trend similar to the experimental one is observed.

Superimposed over a more-or-less uniform background, the far-field beam profiles in Fig. 5(a) and (b) show spatial features, which suggest particular trajectories of the electrons [18]. A "spiral-like" feature is observed in the images for many different shots and for different capillaries. Assuming that specular reflections of X-rays from the inside walls are negligible, the spiral shapes might be understood as the X-ray emission characteristics of electrons along a spiral-like trajectory [20]. Features similar to the observed ones correspond to an oscillation amplitude of the order of ∼0.1 µm, which is about one order of magnitude smaller than the ones mentioned in [18, 19]. This much smaller oscillation amplitude might be due to the particular interaction in the capillary tube, as the experiments reporting larger amplitudes were all performed in gas jets.

3 Simulations and discussion

Simulations were carried out in order to better understand the interaction processes [14] for the low laser intensity and low electron density used in the experiment, where one would not expect trapping and acceleration of electrons to occur and consequently no betatron X-rays to be produced. Particle-in-cell (PIC) simulations were performed using the electromagnetic code CALDER-CIRC [21]. To model the propagation of the laser pulse along the capillary tube, a dielectric boundary condition was added to the code. Detailed results of these simulations are presented in [14]. Additional simulations results are shown in this section. They were performed for a 35 fs laser pulse with a radial intensity profile fitting the θ-averaged experimental profile, and a peak normalized laser amplitude of 0.6. The focal plane was located at the capillary entrance. The capillary diameter was 150 µm, its length 20 m. A ramp of 400 µm increased the electron density from 0 to n_e, with n_e being the electron density inside the capillary. Simulations were carried out for three different electron densities $n_e = 5, 6.5$ and 8×10^{18} cm^{-3}.

An example of results is shown in Fig. 8 for $n_e = 5 \times 10^{18}$ cm^{-3}. The solid black curve shows the evolution of the normalized laser amplitude along the axis of the

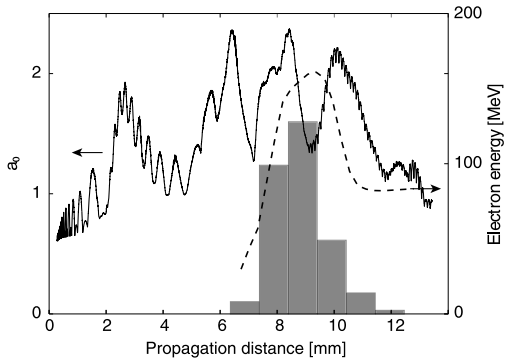

Fig. 8 Simulation of the interaction in the capillary tube using the PIC code CALDER-CIRC. The *solid black curve* shows the evolution of the laser intensity along the capillary length. The *dashed line* shows the energy of the first electron bunch. The corresponding X-ray emission is shown by the *grey bars*, with the total X-ray energy plotted in arbitrary units. The maximum of the X-ray emission coincides with the maximum energy of the electrons

capillary tube. The beam undergoes a slow process of self-focusing, reaching a maximum amplitude of $a_0 = 2.5$ after a propagation of 6.4 mm (i.e. the intensity has increased by a factor 17). This relatively modest amplitude is nevertheless large enough to produce self-injection of electrons, mainly into the first bucket of the wakefield, even at such low density. The capillary confines the energy surrounding the main peak of the focal spot and contributes to maintaining the beam self-focused 2–3 mm longer than without the capillary. The simulations show that the evolution of the laser intensity depends strongly on capillary diameter, initial laser intensity, and electron density, as the mode propagation is quite sensitive to these parameters. This is consistent with our experimental observations, as shown in Figs. 4(a) and 7, where the optimum density and the position of the trapping point depend strongly on these parameters.

After trapping, the electron bunch is accelerated by the plasma wave in the capillary. Simulations show that the electrons reach dephasing, as illustrated by the dashed line in Fig. 8 showing the energy of the first electron bunch. This is also consistent with the experimental electron data (see Fig. 4(b)). At this low density, the dephasing length is ∼5 mm but dephasing is still reached inside the capillary. The extracted electron bunch therefore presents a wide energy spectrum, similar to the experimental spectrum shown in Fig. 3(b). In some cases, the peaks in the simulated electron spectra are more pronounced, but the quasi-mono-energetic features observed experimentally, such as the one shown in Fig. 3(a), are not reproduced in the simulations. Mono-energetic spectra could result from a strongly asymmetric self-injection of electrons, originated in beam asymmetry and eventually associated hosing. Further studies taking into account asymmetrical features are needed to test these hypotheses.

The X-ray spectra generated by accelerated electrons, obtained in the simulations, are found to be synchrotron-like, with a critical energy of about 1 keV in fair agreement with experimental data. The total X-ray energy (integrated from 0 to 10 keV) is also calculated and shown by the grey bars in Fig. 8. It is clearly seen that most of the X-rays are generated in the region where electrons reach their maximum energy. The emitted power scales with γ^4 [11] and, therefore, the X-ray emission is maximum when the electrons have their maximum energy. The spatial profile is calculated with the assumption that the X-rays are absorbed at the capillary wall. The simulated results are very close to the experimental ones, as seen for example in Fig. 5(c). In the simulations, the radius of the X-ray beam is also found to vary as a function of the electron density. This agrees with our explanation that the diameter of the X-ray beam on the detector gives us an indication about the position of the trapping point. For $n_e = 8 \times 10^{18}$ cm^{-3}, the simulations shows that the electrons are trapped early (∼3 mm) and the divergence of the X-ray beam is 9.4 mrad. For $n_e = 5 \times 10^{18}$ cm^{-3}, electrons are trapped later (∼7 mm), and the divergence of the X-ray beam is therefore much bigger (13.6 mrad). The trapping position estimated from the simulation results fairly agree with the experimental determination.

4 Conclusion

Experimental data show that inside dielectric capillaries trapping and acceleration of electrons is possible at lower laser intensities than in gas jets, where in both cases the laser pulse interacts with a neutral gas homogeneous in the transverse direction. It was found that the capillary confines energy located outside the main peak in the focal plane and contributes to the beam self-focusing over longer distances, thus allowing the pulse to evolve enough to reach the threshold for trapping and acceleration of electrons. The interaction was found to depend strongly, and in a complex way, on parameters such as plasma electron density, capillary diameter, and laser intensity. This has been investigated experimentally, both by observing the accelerated electron beam directly and by analysing betatron X-ray radiation as an additional diagnostic of the interaction. Simulations are in good agreement with experimental results. The work presented here shows that the interaction in a capillary tube is different from the interaction in more conventional targets, such as gas jets. This suggests that this kind of structures has interesting properties for electron acceleration. In order to explore the potential of these novel targets for electron acceleration, further studies are required.

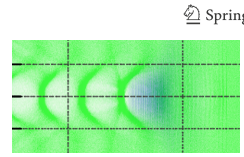

Acknowledgements We acknowledge the support of the European Community—NEST Activity under the FP6 Structuring the European Research Area programme (project EuroLEAP, contract 028514), Marie Curie Early Stage Training Site MAXLAS (MEST-CT-2005-020356), the Lund University X-ray Center (LUXC), the Swedish Research Council (including the Linné grant to the LLC), the Knut and Alice Wallenberg Foundation, the RTRA Triangle de la Physique, and the French Agence Nationale de la Recherche. We also thank the referees for their constructive comments.

References

1. S.P.D. Mangles, C.D. Murphy, Z. Najmudin, A.G.R. Thomas, J.L. Collier, A.E. Dangor, E.J. Divall, P.S. Foster, J.G. Gallacher, C.J. Hooker, D.A. Jaroszynski, A.J. Langley, W.B. Mori, P.A. Norreys, F.S. Tsung, R. Viskup, B.R. Walton, K. Krushelnick, Nature (London) **431**, 535 (2004)
2. C.G.R. Geddes, Cs. Toth, J. van Tilborg, E. Esarey, C.B. Schroeder, D. Bruhwiler, C. Nieter, J. Cary, W.P. Leemans, Nature (London) **431**, 538 (2004)
3. J. Faure, Y. Glinec, A. Pukhov, S. Kiselev, S. Gordienko, E. Lefebvre, J.-P. Rousseau, F. Burgy, V. Malka, Nature (London) **431**, 541 (2004)
4. S.P.D. Mangles, A.G.R. Thomas, M.C. Kaluza, O. Lundh, F. Lindau, A. Persson, F.S. Tsung, Z. Najmudin, W.B. Mori, C.-G. Wahlström, K. Krushelnick, Phys. Rev. Lett. **96**, 215001 (2006)
5. J. Osterhoff, A. Popp, Zs. Major, B. Marx, T.P. Rowlands-Rees, M. Fuchs, M. Geissler, R. Hörlein, B. Hidding, S. Becker, E.A. Peralta, U. Schramm, F. Grüner, D. Habs, F. Krausz, S.M. Hooker, S. Karsch, Phys. Rev. Lett. **101**, 085002 (2008)
6. W.P. Leemans, B. Nagler, A.J. Gonsalves, Cs. Tóth, K. Nakamura, C.G.R. Geddes, E. Esarey, C.B. Schroeder, S.M. Hooker, Nat. Phys. **2**, 696 (2006)
7. B. Cros, C. Courtois, G. Matthieussent, A. Di Bernardo, D. Batani, N. Andreev, S. Kuznetsov, Phys. Rev. E **65**, 026405 (2002)
8. F. Dorchies, J.R. Marquès, B. Cros, G. Matthieussent, C. Courtois, T. Vélikoroussov, P. Audebert, J.P. Geindre, S. Rebibo, G. Hamoniaux, F. Amiranoff, Phys. Rev. Lett. **82**, 4655 (1999)
9. F. Wojda, K. Cassou, G. Genoud, M. Burza, Y. Glinec, O. Lundh, A. Persson, G. Vieux, E. Brunetti, R.P. Shanks, D. Jaroszynski, N.E. Andreev, C.-G. Wahlström, B. Cros, Phys. Rev. E **80**, 066403 (2009)
10. A. Rousse, K.T. Phuoc, R. Shah, A. Pukhov, E. Lefebvre, V. Malka, S. Kiselev, F. Burgy, J.-P. Rousseau, D. Umstadter, D. Hulin, Phys. Rev. Lett. **93**, 135005 (2004)
11. E. Esarey, B. Shadwick, P. Catravas, W. Leemans, Phys. Rev. E **65**, 056505 (2002)
12. J.D. Jackson, in *Classical Electrodynamics*, 3rd edn. (Wiley, New York, 1975), Chap. 14
13. G. Genoud, M. Burza, A. Persson, F. Wojda, C.-G. Wahlström, Rev. Sci. Instrum. **82**, 033102 (2011)
14. H.E. Ferrari, A.F. Lifschitz, B. Cros, Plasma Phys. Control. Fusion **53**, 014005 (2010)
15. S. Kneip, S.R. Nagel, C. Bellei, N. Bourgeois, A.E. Dangor, A. Gopal, R. Heathcote, S.P.D. Mangles, J.R. Marquès, A. Maksimchuk, P.M. Nilson, K.T. Phuoc, S. Reed, M. Tzoufras, F.S. Tsung, L. Willingale, W.B. Mori, A. Rousse, K. Krushelnick, Z. Najmudin, Phys. Rev. Lett. **100**, 105006 (2008)
16. S. Kneip, C. McGuffey, J.L. Martins, S.F. Martins, C. Bellei, V. Chvykov, F. Dollar, R. Fonseca, C. Huntington, G. Kalintchenko, A. Maksimchuk, S.P.D. Mangles, T. Matsuoka, S.R. Nagel, C.A.J. Palmer, J. Schreiber, K.T. Phuoc, A.G.R. Thomas, V. Yanovsky, L.O. Silva, K. Krushelnick, Z. Najmudin, Nat. Phys. **6**, 980 (2010)
17. R.C. Shah, F. Albert, K.T. Phuoc, O. Shevchenko, D. Boschetto, A. Pukhov, S. Kiselev, F. Burgy, J.-P. Rousseau, A. Rousse, Phys. Rev. E **74**, 045401 (2006)
18. K.T. Phuoc, S. Corde, R. Shah, F. Albert, R. Fitour, J.-P. Rousseau, F. Burgy, B. Mercier, A. Rousse, Phys. Rev. Lett. **97**, 225002 (2006)
19. S.P.D. Mangles, G. Genoud, S. Kneip, M. Burza, K. Cassou, B. Cros, N.P. Dover, C. Kamperidis, Z. Najmudin, A. Persson, J. Schreiber, F. Wojda, C.-G. Wahlström, Appl. Phys. Lett. **95**, 181106 (2009)
20. K. Ta Phuoc, S. Corde, R. Fitour, R. Shah, F. Albert, J.-P. Rousseau, F. Burgy, A. Rousse, V. Seredov, A. Pukhov, Phys. Plasmas **15**, 073106 (2008)
21. A.F. Lifschitz, X. Davoine, E. Lefebvre, J. Faure, C. Rechatin, V. Malka, J. Comput. Phys. **228**, 1803 (2009)

Paper XII

Enhancement of x-rays generated by a guided laser wakefield accelerator inside capillary tubes

J. Ju, K. Svensson, A. Döpp, H. E. Ferrari, K. Cassou, O. Neveu, G. Genoud, F. Wojda, M. Burza, A. Persson, O. Lundh, C.-G. Wahlström and B. Cros.

Applied Physics Letters **in press**, (2012).

Enhancement of X-rays generated by a guided laser wakefield accelerator inside capillary tubes

J. Ju,[1] K. Svensson,[2] A. Döpp,[1] H. E. Ferrari,[3] K. Cassou,[1] O. Neveu,[1] G. Genoud,[2] F. Wojda,[2] M. Burza,[2] A. Persson,[2] O. Lundh,[2] C.-G. Wahlström,[2] and B. Cros[1, a)]

[1)] *Laboratoire de Physique des Gaz et des Plasmas, CNRS-Université Paris-Sud 11, 91405, Orsay, France*

[2)] *Department of Physics, Lund University, P.O. Box 118, S-22100 Lund, Sweden*

[3)] *Consejo Nacional de investigaciones científicas y técnicas (CONICET), Argentina*

Electrons accelerated in the nonlinear regime in a laser wakefield accelerator experience transverse oscillations inside the plasma cavity, giving rise to ultra-short pulsed X-rays, also called betatron radiation. We show that the fluence of X-ray can be enhanced by more than one order of magnitude when the laser is guided by a 10 mm long capillary tube instead of interacting with a 2 mm gas jet. X-rays with a synchrotron-like spectrum and associated critical energy ~ 5 keV, with a peak brightness of $\sim 1 \times 10^{21}$ ph/s/mm^2/mrad^2/0.1%BW, were achieved by employing 16 TW laser pulses.

Since their discovery X-rays have contributed to many fields of science and the development of new X-ray sources is an active field of research. Ultra-short X-ray pulses[1,2] can be generated in a laser wakefield accelerator (LWFA). In the so-called blow-out regime of LWFAs, the ponderomotive force of an intense laser pulse focused in a plasma blows the electrons out of a volume of radius similar to the laser focal spot radius. The charge separation between electrons and ions is associated to electric fields with an amplitude of the order of $\sim$100 GV/m. These fields can trap and accelerate longitudinally plasma electrons to high energy, typically hundreds of MeV, over only a few millimetres, and at the same time wiggle the electrons transversely. The X-ray pulses produced by this mechanism have spectra similar to synchrotron radiation and are often called betatron radiation. The betatron radiation has intrinsically striking features for ultra-fast imaging: a pulse duration on the femtosecond scale[3] and a perfect synchronization to the pump laser.

The use of such X-rays sources for imaging applications has already been demonstrated[4,5] with photon energies in the range 1-10 keV and peak brightness of 10^{22} ph/s/mm^2/mrad^2/0.1%BW. As they are produced by relatively compact laser systems, they have a large potential for dissemination among various user communities. Their development has thus attracted a lot of attention in the past few years, mostly to characterize their properties[3,6,7], or to control them[8,9]. Scalings developed for betatron radiation predict that the X-ray photon energy and brightness can be enhanced by increasing the laser intensity or/and decreasing the plasma density[10]. For example, X-rays extending to 50 keV were observed[11]by using a peak focused intensity larger than 10^{20} W/cm^2. The use of laser guiding in capillary tubes has been shown to enable electron acceleration and X-ray emission at low plasma density and low laser intensity[12,13].

In this letter, we report on the ability to increase the number of photons produced in the 2-10 keV range by using a lower density, longer plasma inside capillary tubes, compared to the plasma density and length usually achieved with gas jets. Using 16 TW laser pulses, the generated X-ray peak brightness is multiplied by 30 when the laser beam is guided by a 10 mm long capillary tube instead of using a 2 mm long gas jet.

Experiments were performed at the Lund Laser Centre, Sweden, where a Ti:Sa, 800 nm central wavelength, laser system delivers an energy of up to 1 J in 40 fs full width at half maximum (FWHM) pulses. A deformable mirror is used after compression to compensate for wavefront distortions in the focal plane. The laser beam was focused, using a $f/15$ off-axis parabola, to an Airy-like spot with 19.7$\pm$0.8 μm radius at first minimum. With an energy of 650 mJ in the focal plane, the peak intensity was estimated to be $(5.4 \pm 0.1)\times10^{18}$ W/cm^2, giving a normalized laser strength parameter $a_0 = 1.6$. Capillary tubes filled with hydrogen gas were used to confine the gas and to partially guide the laser beam. The spectra of electrons accelerated in either a gas jet or capillary tubes were measured by a spectrometer, composed of a 10 cm long permanent magnet, with a central magnetic field of 0.7 T, deflecting the electrons subsequently intercepted by a phosphor screen (Kodak Lanex Regular) imaged onto a CCD camera. Electrons below 42 MeV did not reach the phosphor screen and were not detected. The beam charge was obtained by the absolute calibration of the Lanex screen[14]. X-rays generated by betatron oscillations in the LWFAs were recorded by a X-ray CCD camera placed 110 cm away from the capillary exit on the laser axis, providing a collection angle of 12$\times$12 mrad^2. The X-ray camera was located outside the vacuum chamber, behind a 300 μm thick beryllium window, and a 5 mm air gap. A set of metallic filters (V, Fe, Ni, Sn, and Zr), held together by a 30 μm wire grid, was used in front of the camera to determine the critical energy associated to the X-ray spectrum in the range 2-10 keV.

Fig. 1 shows the main characteristics of the electrons and X-rays produced inside a 10 mm long, 178 μm diameter capillary tube for two values of the plasma electron density, n_e. The electron energy spectra in (b) and (e)

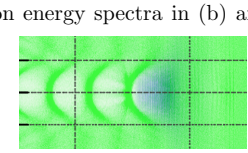

[a)] Electronic mail: brigitte.cros@u-psud.fr

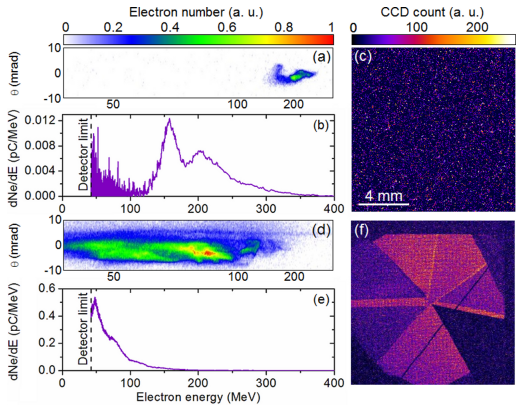

FIG. 1. Single shot raw Lanex images, energy spectra, and X-ray beam images obtained after a 10 mm long, 178 μm diameter capillary tube for two values of the plasma electron density (a) to (c): $n_e = (5.4 \pm 0.3) \times 10^{18}$ cm^{-3}; (d) to (f): $n_e = (8.1 \pm 0.5) \times 10^{18}$ cm^{-3}.

were extracted from the raw Lanex images seen in (a) and (d), respectively, by summing in the vertical direction and rescaling in the horizontal direction to account for magnet dispersion. The electron spectra typically exhibit rather large energy spread and the total charge and maximum energy are strongly dependent on the plasma electron density. The lower density case is close to the density injection threshold[13] and leads to a maximum energy of the order of 300 MeV (measured at 10% of the maximum of the spectrum), with a low beam charge of 0.9 pC, and a divergence FWHM of 5.2 mrad. No X-rays were detected for this shot as seen in Fig. 1(c). At $n_e = (8.1 \pm 0.5) \times 10^{18}$ cm^{-3}, a 18 pC electron bunch was measured with a maximum energy of ∼120 MeV, as shown in Fig. 1(e). The corresponding beam divergence is about 5.8 mrad. Fig. 1(f) shows the associated X-ray beam transmitted through the different filters.

The X-ray spectrum can be characterized by a synchrotron-like[2] spectrum of the form $d^2I/(dEd\Omega)_{\theta=0} \propto (E/E_c)^2 \mathcal{K}^2_{2/3}(E/E_c)$, where $\mathcal{K}_{2/3}$ is the modified bessel function of order 2/3. The critical energy is given by $E_c = 3\hbar K\gamma^2\omega_\beta$, where $K = \gamma r_\beta \omega_\beta/c$ is the wiggler strength parameter with γ, r_β, ω_β denoting the relativistic factor, the amplitude and frequency of betatron oscillation, respectively. The critical energy was evaluated from the transmission of X-rays through the different metal filters with a least squares method[11]. In the case of Fig. 1(f), it was found to be 5.4 keV, which is higher than in previous observations[1,12] with similar laser power.

The maximum X-ray fluence measured is $(5.7 \pm 0.6) \times 10^5$ ph/mrad^2 [Fig. 1(f)]. To estimate the peak brightness of this X-ray source, the source size and duration are needed. The source size can be estimated from the expression of critical energy[15] as $r_\beta = E_c c/3\hbar\gamma^3\omega_\beta^2$. The relativistic factor is determined using the mean energy of the electron spectra $\bar{E}_e$, where $\bar{E}_e$ is the average of electron energies weighted by their respective spectral intensities. For the shot plotted in Fig. 1(e), $\bar{E}_e$ is calculated to be 88±4 MeV, and the source size estimated to be $r_\beta = 2 \pm 0.3$ μm. This estimation is validated by 3D simulations performed with the particle-in-cell code CALDER-CIRC[16], for input parameters close to the experimental ones. They show that the laser pulse non linear evolution in the 178 μm diameter capillary tube leads to a maximum normalized vector potential in the range $4 < a_0 < 5.5$, and produces accelerated electrons with a mean energy of about 130 MeV. The transverse and longitudinal sizes of the electron bunch in the simulation are 1.3 μm and 10 μm (∼35 fs), respectively, in reasonable agreement with the estimation from the measurements. The peak brightness achieved in our experiment is estimated, using $r_\beta = 2$ μm, to be $\sim 1 \times 10^{21}$ ph/s/mm^2/mrad^2/0.1%BW, and the wiggler strength parameter, $K \simeq 10$. Taking into account the divergence of the X-ray beam, $\theta = K/\gamma$, the estimated total photon number over the whole spectrum is of the order of 10^9 per shot.

The X-ray fluence can be changed by varying the plasma density, as presented in Fig. 2 for two different capillaries. In both cases, the X-ray fluence is maximum

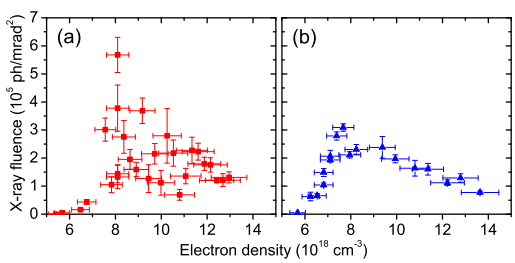

FIG. 2. X-ray fluence as a function of the plasma electron density for (a) a 10 mm long, 178 μm diameter capillary and (b) a 20 mm long, 152 μm diameter capillary; the other parameters are the same as for Fig. 1.

for a density of the order of 8×10^{18} cm^{-3}. The influence of the plasma electron density on the X-ray fluence can be understood as a result of the influence of the density on the laser propagation and related electron injection and acceleration. For the parameters of this experiment, at lower densities, electron trapping is not efficient, resulting in a lower beam charge, as seen in Fig. 1. As the plasma density is increased, trapping becomes more efficient and more charge can be accelerated but the acceleration length and thus the electron energy, become smaller due to the shortening of the electron dephasing and laser depletion lengths. For the given laser intensity, the maximum X-ray fluence is achieved in the 10 mm long capillary tube. Simulations in the 178 μm capillary tube

for the optimum electron density show that the overall process of laser non-linear evolution, electron injection and acceleration, and X-ray emission occur over the first 10 mm of propagation. Fluctuations of the X-ray fluence are smaller at the output of the 152 μm diameter, 20 mm long capillary: this can be attributed to the fact that the capillary diameter is smaller favoring a more stable laser guiding. In this case more X-rays are produced at low densities: it can be due to higher intensities achieved locally inside the capillary, or an evolution of the laser pulse leading to electron injection and acceleration over a distance larger than 10 mm.

The enhancement of the X-ray fluence due to the length and density of the plasma is demonstrated in Fig. 3 by the comparison of the X-ray fluence measured for two targets, 10 mm long capillary tube and 2 mm gas jet, for the same experimental conditions. It shows that for

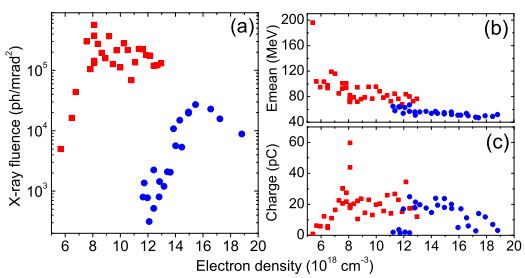

FIG. 3. (a) X-ray fluence, (b) mean energy and (c) charge of electrons as a function of plasma density for the 10 mm long capillary (red squares) and the 2 mm gas jet (blue dots).

the intensity used in this experiment, the use of a capillary tube allows electron self-injection to happen at lower density than in the gas jet. The capillary provides a long distance for laser evolution to the threshold required for self-trapping[12,13], and helps collecting and refocusing the energy initially in the wings of the laser spot[16]; the excitation of multiple modes and their beating can also give rise locally to higher intensity than in vacuum, thus favoring an increase of a_0. For the gas jet, electron trapping starts around $n_e = 11\times10^{18}$ cm^{-3}, which results in lower energy electrons, as electron energy inversely depends on plasma density. In the intermediate density range $(11-13)\times10^{18}$ cm^{-3}, a higher mean electron energy is achieved when the capillary is employed. The maximum X-ray fluence in the capillary corresponds to the density where the maximum electron charge is measured. The maximum X-ray fluence obtained with the gas jet is 2.7×10^4 ph/mrad^2 for $n_e = 15\times10^{18}$ cm^{-3}. Using the values obtained from experimental data, $E_c = 4.6$ keV, $\bar{E}_e = 56$ MeV, the source size is estimated to be 2.4 μm and the corresponding peak brightness is $\sim 3\times10^{19}$ ph/s/mm^2/mrad^2/0.1%BW, similar to the result of Ref. [1].

In conclusion, we demonstrate that betatron radiation is significantly enhanced by guiding the laser in a capillary tube allowing electron acceleration in a low density, long plasma. In particular, to the best of our knowledge, $\sim 1\times10^{21}$ ph/s/mm^2/mrad^2/0.1%BW is the brightest X-ray beam achieved with a <20 TW laser.

This work was supported by LASERLAB-EUROPE (grant agreement 228334), the Triangle de la Physique (grant agreement NEXT-2009-064T), the Lund University X-ray Center (LUXC), the Swedish Research Council (including the Linné grant to LLC), and the Knut and Alice Wallenberg Foundation. J. Ju acknowledges financial support from the Chinese Scholarship Council.

[1] A. Rousse, K. Ta Phuoc, R. Shah, A. Pukhov, E. Lefebvre, V. Malka, S. Kiselev, F. Burgy, J.-P. Rousseau, D. Umstadter, and D. Hulin, Phys. Rev. Lett. **93**, 135005 (2004).
[2] E. Esarey, B. A. Shadwick, P. Catravas, and W. P. Leemans, Phys. Rev. E **65**, 056505 (2002).
[3] K. Ta phuoc, R. Fitour, A. Tafzi, T. Garl, N. Artemiev, R. Shah, F. Albert, D. Boschetto, A. Rousse, D-E. Kim, A. Pukhov, V. Seredov, I. Kostyukov, Phys. Plasmas **14**, 080701 (2007).
[4] S. Kneip, C. McGuffey, F. Dollar, M. S. Bloom, V. Chvykov, G. Kalintchenlko, K. Krushelnick, A. Maksimchuk, S. P. D. Mangles, T. Matsuoka, Z. Najmudin, C. A. J. Palmer, J. Schreiber, W. Schumaker, A. G. R. Thomas, and V. Yanovsky, Appl. Phys. Lett. **99**, 093701 (2011).
[5] S. Fourmaux, S. Corde, K. Ta Phuoc, P. Lassonde, G. Lebrun, S. Payeur, F. Martin, S. Sebban, V. Malka, A. Rousse, and J. C. Kieffer, Opt. Lett. **36**, 2426 (2011).
[6] R. C. Shah, F. Albert, K. Ta Phuoc, O. Shevchenko, D. Boschetto, A. Pukhov, S. kiselev, F. Burgy, J.-P. Rousseau, and A. Rousse, Phys. Rev. E **74**, 045401(R) (2006).
[7] S. Fourmaux, S. Corde, K. Ta Phuoc, P. M. Leguay, S. Payeur, P. Lassonde, S. Gnedyuk, G. Lebrun, C. Fourment, V. Malka, S. Sebban, A. Rousse and J. C. Kieffer, New J. Phys. **13**, 033017 (2011).
[8] S. P. D. Mangles, G. Genoud, S. Kneip, M. Burza, K. Cassou, B. Cros, N. P. Dover, C. Kamperidis, Z. Najmudin, A. Persson, J. Schreiber, F. Wojda, and C.-G. Wahlström, Appl. Phys. Lett. **95**, 181106 (2009).
[9] K. Ta Phuoc, E. Esarey, V. Leurent, E. Cormier-Michel, C. G. R. Geddes, C. B. Schroeder, A. Rousse, and W. P. Leemans, Phys. Plasmas **15**, 063102 (2008).
[10] A. G. R. Thomas, Phys. Plasmas **17**, 056708 (2010).
[11] S. Kneip, S. R. Nagel, C. Bellei, N. Bourgeois, A. E. Dangor, A. Gopal, R. Heathcote, S. P. D. Mangles, J. R. Marquès, A. Maksimchuk, P. M. Nilson, K. Ta Phuoc, S. Reed, M. Tzoufras, F. S. Tsung, L. Willingale, W. B. Mori, A. Rousse, K. Krushelnick, and Z. Najmudin, Phys. Rev. Lett. **100**, 105006 (2008).
[12] G. Genoud, K. Cassou, F. Wojda, H. E. Ferrari, C. Kamperidis, M. Burza, A. Persson, J. Uhlig, S. Kneip, S. P. D. Mangles, A. Lifschitz, B. Cros, and C.-G. Wahlström, Appl. Phys. B **105**, 309 (2011).
[13] H. E. Ferrari, A. F. Lifschitz, G. Maynard, and B. Cros, Phys. Plasmas **18**, 083108 (2011).
[14] Y. Glinec, J. Faure, A. Guemnie-Tafo, V. Malka, H. Monard, J. P. Larbre, V. De Waele, J. L. Marignier, and M. Mostafavi, Rev. Sci. Instrum. **77**, 103301 (2006).
[15] F. Albert, R. Shah, K. Ta Phuoc, R. Fitour, F. Burgy, J.-P. Rousseau, A. Tafzi, D. Douillet, T. Lefrou, and A. Rousse, Phys. Rev. E **77**, 056402 (2008).
[16] H. E. Ferrari, A. Lifschitz, and B. Cros, Plas. Phys. Contr. Fus. **53**, 014005 (2011).